

Self-propelling needles

From biological inspiration to percutaneous interventions

Scali, Marta

DOI

[10.4233/uuid:523e3e5f-08f0-4acb-ab45-abaa7ace3967](https://doi.org/10.4233/uuid:523e3e5f-08f0-4acb-ab45-abaa7ace3967)

Publication date

2020

Document Version

Final published version

Citation (APA)

Scali, M. (2020). *Self-propelling needles: From biological inspiration to percutaneous interventions*. [Dissertation (TU Delft), Delft University of Technology]. <https://doi.org/10.4233/uuid:523e3e5f-08f0-4acb-ab45-abaa7ace3967>

Important note

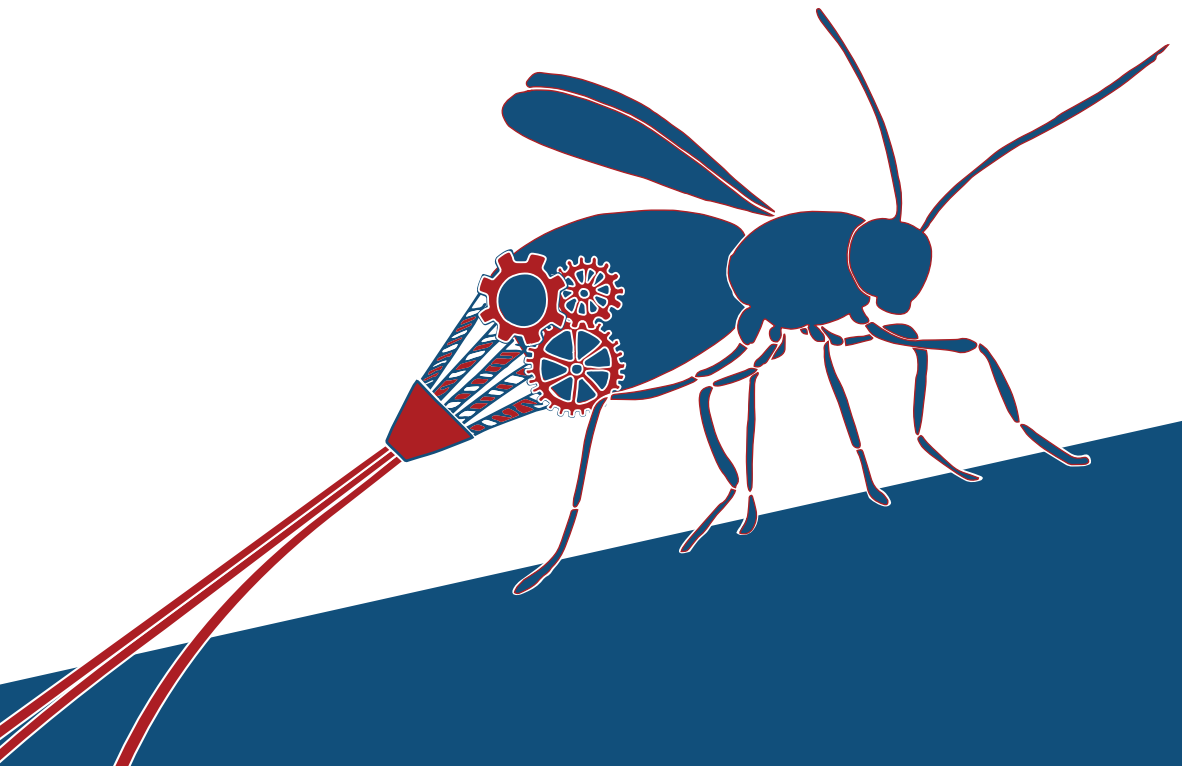
To cite this publication, please use the final published version (if applicable). Please check the document version above.

Copyright

Other than for strictly personal use, it is not permitted to download, forward or distribute the text or part of it, without the consent of the author(s) and/or copyright holder(s), unless the work is under an open content license such as Creative Commons.

Takedown policy

Please contact us and provide details if you believe this document breaches copyrights. We will remove access to the work immediately and investigate your claim.



SELF-PROPELLING NEEDLES

From Biological Inspiration
to Percutaneous Interventions

Marta Scali

Propositions

accompanying the dissertation

SELF-PROPELLING NEEDLES

From biological inspiration to percutaneous interventions

Marta Scali

1. Increasing the number of components decreases the design complexity of a self-propelling needle (This proposition pertains to this dissertation).
2. Science fiction movies facilitate brainstorming sessions for the design of medical instruments.
3. Learning a skill is a skill on its own.
4. Supporting scientists to publish negative results will speed up technological development.
5. Bureaucracy promotes conflict-avoidance behaviour.
6. Peak performance is a delicate balance between rigid discipline and flexible mindset.
7. Creativity is a tool to create new standards.
8. Making working from home obligatory at least once a week is a solution to climate change.
9. Teaching human psychology to researchers, in particular PhD students, will enhance productivity.
10. To facilitate a conversation, the Dutch should learn how to tell a story and the Italians should learn how to ask a question.

These propositions are regarded as opposable and defensible, and have been approved as such by the promotors Prof. dr. ir. P. Breedveld and Dr. D. Dodou.

SELF-PROPELLING NEEDLES

From Biological Inspiration to Percutaneous Interventions

Marta Scali

Cover design by: Marta Scali

Printed by: Gildeprint

© 2020 Marta Scali

All rights reserved. No part of this thesis may be reproduced by any means or transmitted in any form without the written permission of the author or, when appropriate, of the publisher of the publications.

ISBN 978-94-6366-282-6

An electronic version of this dissertation is available at <https://repository.tudelft.nl/>

SELF-PROPELLING NEEDLES

From Biological Inspiration to Percutaneous Interventions

Dissertation

for the purpose of obtaining the degree of doctor
at Delft University of Technology
by the authority of the Rector Magnificus prof.dr.ir. T.H.J. van der Hagen
Chair of the Board for Doctorates
to be defended publicly
Friday 10 July at 10.00 o'clock

by

Marta SCALI

Master of Science in Biomedical Engineering, University of Pisa, Italy
Born in Sinalunga, Italy

This dissertation has been approved by the promotor.

Composition of the doctoral committee:

Rector Magnificus,	chairperson
Prof. dr. ir. P. Breedveld	Delft University of Technology, promotor
Dr. D. Dodou	Delft University of Technology, promotor

Independent members:

Prof. dr. B.H.W. Hendriks	Delft University of Technology
Prof. dr. H.J.C.M. Sterenborg	Amsterdam University Medical Center
Prof. dr. ir. S. Stramigioli	University of Twente
Dr. G.A. Kraan	Reinier de Graaf Hospital
Dr. T.A. Lenau	Technical University of Denmark, Denmark
Prof. dr. J. Dankelman	Delft University of Technology, reserve member



This research is supported by the Netherlands Organization for Scientific Research (NWO), domain Applied and Engineering Sciences (TTW), which is partly funded by the Ministry of Economic Affairs (project number 12712, STW Perspectief Programme iMIT-Instruments for Minimally Invasive Techniques).

Table of Contents

Summary	ix
Samenvatting	xi
1. Introduction	1
1.1. Medical needles and their use.....	2
1.2. Steerable needles.....	3
1.3. Biological inspiration	3
1.4. Biologically inspired needles.....	5
1.5. Needle diameter	5
1.6. Aim and research objectives	6
1.7. Thesis outline	6
2. Needle-Like Instruments for Steering Through Solid Organs – A Review	11
2.1. Introduction	13
2.2. Literature search methods.....	14
2.2.1. Scientific literature search.....	14
2.2.2. Patent literature search.....	15
2.2.3. Eligibility criteria.....	16
2.2.4. Study selection.....	16
2.3. Literature search results.....	16
2.4. Classification of possible mechanical solutions for 3D steering.....	17
2.5. Allocation of the retrieved steerable needle designs in the classification scheme	23
2.5.1. Bevel-tip needles.....	23
2.5.2. One-plane pre-curved needles	24
2.5.3. Two-plane pre-curved needles.....	25
2.5.4. Bevel-tip and one-plane pre-curved needles.....	26
2.5.5. Needles with one on-demand deflection angle	26
2.5.6. Needles with two on-demand deflection angles.....	29
2.5.7. Needles with one on-demand angle and one pre-defined deflection angle.....	30
2.6. Discussion.....	30
2.6.1. Comparative study.....	31
2.6.2. Tissue interaction.....	31
2.6.3. Design choices related to the deflection angle of steerable needles.....	32
2.6.4. Commercially available instruments.....	33
2.6.5. Limitations	34
2.7. Conclusion and future work.....	35

3. Ovipositor-Inspired Steerable Needle: Design and Preliminary Experimental Evaluation	41
3.1. Introduction	43
3.1.1. Steerable needle mechanism.....	43
3.1.2. Biological inspiration for steerable needles.....	44
3.1.3. Aim.....	47
3.2. Needle design	47
3.2.1. Conceptual design.....	47
3.2.2. Needle prototype.....	49
3.2.3. Forward motion and steering of the needle.....	50
3.3. Materials and methods	54
3.3.1. Experimental setup	54
3.3.2. Experiment 1—forward motion	56
3.3.3. Experiment 2—steering	57
3.4. Results	58
3.4.1. Experiment 1—forward motion	58
3.4.2. Experiment 2—steering	58
3.5. Discussion.....	61
3.5.1. Needle design.....	61
3.5.2. Experiment 1—forward motion	62
3.5.3. Experiment 2—steering	63
3.5.4. Limitations	64
3.5.5. Future work.....	65
3.6. Conclusion.....	66
4. Design and Evaluation of a Wasp-Inspired Steerable Needle.....	71
4.1. Introduction	73
4.1.1. Needle steering curvature.....	73
4.1.2. Aim.....	74
4.2. Needle design	75
4.2.1. Conceptual design for reducing wire bifurcation	75
4.2.2. Needle prototype.....	80
4.2.3. Steering motion.....	80
4.3. Materials and methods	81
4.3.1. Experimental setup	81
4.3.2. Experimental design	83
4.4. Results	85
4.4.1. Converging ring	85
4.4.2. Diverging ring.....	86
4.5. Discussion.....	87
4.6. Conclusion.....	89

5. Experimental Evaluation of a Self-Propelling Bio-Inspired Needle in Single- and Multi-Layered Phantoms	93
5.1. Introduction	95
5.2. Materials and methods	99
5.2.1. Needle tip design and prototype.....	99
5.2.2. Actuation unit.....	100
5.2.3. Experimental setup	100
5.2.4. Actuation mode.....	101
5.2.5. Gelatine phantoms.....	101
5.2.6. Self-propelling motion	103
5.2.7. Hypotheses	104
5.2.8. Experimental procedure.....	105
5.2.9. Data analysis	105
5.2.10. Statistical analysis.....	106
5.3. Results	106
5.3.1. Six-wire 0.25-mm prototype, step-by-step motion, three gelatine phantoms.....	106
5.3.2. Six-wire 0.125-mm prototype, step-by-step motion, three gelatine phantoms.....	107
5.3.3. Three-wire 0.25-mm prototype, step-by-step motion, one gelatine phantom.....	107
5.3.4. Statistical analysis.....	109
5.3.5. Additional experiments.....	110
5.4. Discussion.....	112
6. Behavior of an Ovipositor-Inspired Needle in Porcine Tissue: A Preliminary Ex Vivo Study.....	119
6.1. Introduction	121
6.2. Materials and methods	121
6.2.1. Needle prototype and actuation unit	121
6.2.2. Actuation mode.....	121
6.2.3. Experimental setup	122
6.2.4. Biological tissue samples.....	122
6.2.5. Procedure	124
6.2.6. Data analysis	124
6.3. Results	125
6.4. Discussion.....	127
7. Design of an Ultra-Thin Steerable Probe and Preliminary Evaluation in a Gelatine Phantom.....	131
7.1. Introduction	133
7.2. State-of-the-art steerable needles and probes.....	133
7.3. Aim	135
7.4. Design process.....	135

7.4.1. Design requirements	135
7.4.2. Probe design.....	136
7.4.3. Probe prototype.....	136
7.5. Experimental evaluation.....	140
7.5.1. Gelatine phantom	141
7.5.2. Experimental setup.....	141
7.5.3. Actuation modes	142
7.5.4. Experiment 1: Steering direction.....	143
7.5.5. Experiment 2: Final position after steering.....	146
7.6. Results	148
7.6.1. Experiment 1.....	148
7.6.2. Experiment 2.....	149
7.7. Discussion.....	150
7.7.1. Probe performance	150
7.7.2. Limitations and future work	152
7.7.3. Possible applications of the steerable probe.....	154
7.8. Conclusion.....	155
8. Discussion.....	161
8.1. Main findings of this thesis.....	162
8.2. Towards clinical use.....	163
8.3. Other applications	165
8.4. Technical challenges still ahead.....	166
8.5. Towards future bio-inspired needles.....	167
Acknowledgments	173
Curriculum Vitae	175

Summary

During percutaneous interventions, medical needles are inserted through the skin inside the body to collect diagnostic samples or to inject substances in a minimally invasive manner. However, when the target to be reached is located deep inside the body, needle insertion becomes challenging: the needle should be long enough to reach the target, thin (diameter lower than 1 mm) to limit tissue damage, and preferably steerable in order to move around obstructing anatomical structures. No needle currently used in medical practice combines all these characteristics: slender (i.e., long-and-thin) needles are susceptible to buckling, and steerable mechanisms require space, inhibiting miniaturization.

In nature, such needles exist. Some species of parasitic wasps use their slender ovipositor to puncture, advance and steer through solid substrates, such as fruits or wood. These wasps use a push-pull mechanism to advance their ovipositor through the substrate without buckling. Translating that mechanism into a technical system might help to solve the current challenges with medical needles. Accordingly, this thesis aimed to design, develop, and evaluate a new ovipositor-inspired ultra-thin (i.e., submillimetre diameter) and long needle that can move through solid substrates.

First, a comprehensive overview of steerable needle designs and mechanisms is presented (Chapter 2). A classification of mechanical working principles was created to categorize the existing mechanical solutions for 3D steering through solid organs. Two main classes were identified: needles with a simple design, such as pre-curved needles, which are easy to miniaturize, but they need rotation around the body axis to steer in 3D, and cable-actuated needles, which are able to steer omnidirectionally without axial rotation of the body, but they usually have complex designs, hampering miniaturization.

Inspired by the ovipositor of parasitic wasps, a 1.2-mm diameter, 160-mm long needle prototype was developed (Chapter 3). The needle consists of seven flexible Nitinol wires connected at the tip by a straight, flower-shaped ring. The needle was able to move through gelatine with zero net push force and steer omnidirectionally by creating an offset at the tip. A second ovipositor-inspired needle prototype was developed with the aim of increasing the steerability of the first prototype (Chapter 4). In order to do so, the straight ring of the previous prototype was replaced by a tapered flower-shaped ring.

Next, three ovipositor-inspired needle prototypes were developed (Chapter 5), with the goal of miniaturizing the needle design. The prototypes had a length of 300 mm and diameters of 0.8 mm, 0.6 mm and 0.4 mm. The reduction in diameter was achieved by replacing the aluminium flower ring from Chapters 3 and 4 with a thin-walled shrinking tube to keep the Nitinol wires together at the tip. All three prototypes were able to self-propel

through single- and multi-layer tissue-mimicking phantoms without buckling. The 0.8-mm diameter needle prototype was also preliminarily tested *ex vivo*. Results showed that this prototype self-propelled through porcine kidney, liver and brain (Chapter 6).

Chapter 7 describes the design of a 0.5-mm diameter probe which combines the simplicity of the pre-curved needle design with the steering capabilities of cable-actuated needles. The prototype probe was able to steer in 3D without the need of axial rotation through gelatine. The probe was also able to follow a multi-curved path. Ultra-thin submillimetre steerable probes can be advantageous for correcting small deviations from the pre-defined trajectory and for making complex curvatures to avoid sensitive structures into the body.

This thesis demonstrates the value of adopting a biological mechanical solution to solve the challenges with standard needles during percutaneous interventions. The proposed bio-inspired needle design and mechanism of motion hold great promise to improve accuracy and safety during delicate percutaneous procedures and to perform those that are not yet possible.

Samenvatting

Tijdens percutane ingrepen worden medische naalden door de huid in het lichaam ingebracht om diagnostische monsters te nemen of om vloeistoffen op een minimaal invasieve manier te injecteren. Wanneer de beoogde locatie zich echter diep in het lichaam bevindt wordt het inbrengen van de naald een uitdaging: de naald moet namelijk lang genoeg zijn om deze locatie te bereiken, dun zijn (diameter kleiner dan 1 mm) om weefselschade te beperken, en bij voorkeur stuurbaar zijn om versperrende, anatomische structuren te ontwijken. Geen enkele naald die momenteel in de medische praktijk wordt gebruikt, combineert al deze kenmerken: slanke (d.w.z. lange en dunne) naalden hebben de neiging te knikken, en bestuurbare mechanismen vereisen ruimte, waardoor miniaturisatie wordt verhinderd.

In de natuur bestaan dergelijke naalden. Sommige soorten sluipwespen gebruiken hun slanke legboor om door vaste substraten, zoals fruit of hout, te boren en te sturen. Deze wespen gebruiken een trek-duw mechanisme om hun legboor zonder knikken door het substraat te bewegen. Het vertalen van dit mechanisme naar een technisch systeem zou kunnen helpen om de huidige uitdagingen van medische naalden op te lossen. Zodoende was het doel van dit proefschrift om een nieuwe, geïnspireerd door de wesplegboor, ultradunne (d.w.z. sub-millimeter-diameter) en lange naald te ontwerpen, ontwikkelen, en evalueren, die door vaste substraten kan bewegen.

Eerst wordt een uitgebreid overzicht gepresenteerd van bestaande ontwerpen van stuurbare naalden en mechanismen (Hoofdstuk 2). Er wordt een classificatie van de mechanische werkingsprincipes geïntroduceerd waarmee bestaande mechanische oplossingen om in 3D door solide organen te bewegen kunnen worden gecategoriseerd. Er werden twee hoofdklassen geïdentificeerd: naalden met een simpel ontwerp, zoals voorgebogen naalden, die eenvoudig te miniaturiseren zijn maar die rond hun lichaams-as moeten worden gedraaid om in 3D te kunnen bewegen, en kabel-gedreven naalden, die omni-directioneel kunnen sturen zonder rotatie om hun lichaams-as, maar wiens ontwerp doorgaans complex is, waardoor miniaturisering wordt belemmerd.

Geïnspireerd op de legboor van sluipwespen werd een prototype van een naald ontwikkeld met een diameter van 1.2 mm en een lengte van 160 mm (Hoofdstuk 3). De naald bestaat uit zeven flexibele Nitinol draden die aan de tip verbonden zijn door een rechte, bloemvormige ring. De naald was in staat om door gelatine te bewegen met nul netto duwkracht en kon omni-directioneel sturen door het creëren van een offset aan de tip. Een tweede door de legboor geïnspireerde naald prototype werd ontwikkeld met verbeterde

stuurbaarheid als doel (Hoofdstuk 4). Hiervoor werd de rechte ring van het eerste prototype vervangen door een tapse bloemvormige ring.

Vervolgens werden drie, op de legboor geïnspireerde, naaldprototypes ontwikkeld gericht op de miniaturisering van het ontwerp (Hoofdstuk 5). Deze drie prototypes hadden een lengte van 300 mm en een diameter van 0.8 mm, 0.6 mm en 0.4 mm. De reductie in diameter werd mogelijk gemaakt door de aluminium bloem-vormige ring van Hoofdstukken 3 en 4 te vervangen door een dunwandige krimprous om de Nitinol draden bij elkaar te houden aan de tip. Alle drie de prototypes waren in staat om zichzelf zonder te knikken voort te bewegen door enkellaags en meerlaags weefsel-imitaties. Het naaldprototype met een diameter van 0.8 mm diameter werd ook voorlopig ex vivo getest. De resultaten toonden aan dat dit prototype in staat was om zichzelf voort te bewegen door varkensnier, -lever, en -hersenen (Hoofdstuk 6).

Hoofdstuk 7 beschrijft het ontwerp van een sonde met 0.5 mm diameter die de eenvoud van een voorgebogen naald-ontwerp combineert met de stuurbaarheid van kabel-gedreven naalden. De prototype-sonde was in staat om in 3D door gelatine te sturen zonder dat daarvoor een axiale rotatie nodig is. De sonde was ook in staat om een meervoudig gekromd pad te volgen. Ultradunne sub-millimeter, stuurbare sondes maken het mogelijk om kleine afwijkingen van een vooraf bepaald pad te corrigeren, en om complexe krommingen te realiseren waarbij kwetsbare structuren in het lichaam vermeden kunnen worden.

Dit proefschrift toont de waarde aan van het overnemen van een biologisch-mechanische oplossing om de uitdagingen van bestaande medische naalden voor percutane interventies op te lossen. Daarmee zijn het voorgestelde, door de natuur geïnspireerde, naaldontwerp en bewegingsmechanisme erg veelbelovend, zowel om de nauwkeurigheid en veiligheid van delicate percutane procedures te verbeteren, maar ook om nieuwe type interventies mogelijk te maken.

Chapter 1

Introduction

*“A journey of a thousand miles
begins with a single step”*

Lao Tzu

1.1. MEDICAL NEEDLES AND THEIR USE

At the time of the ancient Greeks and Romans, simple hollow tubes were used to administer liquids into natural orifices of the body. It was only in 1844, when Dr. Francis Rynd [1] injected painkillers through the skin of his patient, that the modern medical needle was invented. Since then, the design has basically remained unchanged (Figure 1.1). Designed as a hollow, slender tube with a sharp tip, the medical needle provides access through the skin to internal tissues to carry out diagnostic and therapeutic procedures in a minimally invasive way.

For example, during blood sampling, a needle connected to a syringe is inserted into a vein in the arm, to extract blood for diagnostic analysis. In regional anaesthesia, clinicians inject medication near a group of nerves, to numb the area of the body that requires surgery [2]. During a biopsy procedure, a needle can be used to extract a tissue sample for cancer diagnosis [3]. Needles are also used in brachytherapy [4], to insert radioactive seeds inside the prostate for cancer treatment, or as introduction tool for guidewires [5] and catheters [6]. The success of these procedures relies on the accuracy and precision of needle targeting.

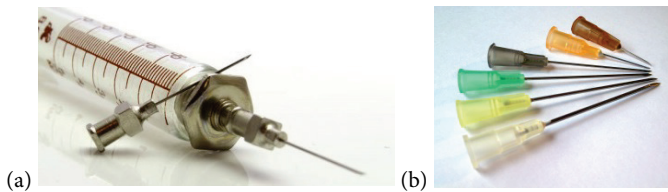


Figure 1.1. Medical needle. (a) Antique needle and syringe [7], (b) Six modern needles with Luer connectors for the syringe. The color indicates the needle diameter [8].

During percutaneous procedures, physiological processes, such as breathing and heart beating, might cause the tissue to move, leading to targeting errors [9]. Furthermore, in these procedures, the needle crosses several tissue types with different mechanical properties (e.g., stiffness), which could cause the needle to deviate from its planned trajectory [10]. Finally, human error, such as wrong needle placement, might compromise the success of the procedure [11]. Clinicians can correct for needle misplacement either by retracting and re-inserting the needle multiple times until the target is reached [12] or by manipulating the base of the needle (i.e., the part of the needle outside the patient) to re-direct the needle [13]. The second option is preferred over the first, because multiple needle insertions might increase procedure time and discomfort for the patient.

In the past years, studies on models estimating needle deflection [14, 15], robotic needle guidance [16, 17], and needle tracking [18, 19] have been presented, to improve the accuracy

in needle targeting by limiting manual corrections. Also, the use of external imaging systems, such as X-ray and ultrasound, helps clinicians to monitor the needle inside the body during the procedure [20, 21].

1.2. STEERABLE NEEDLES

Common needles have a straight, rigid body, meaning that they can in principle only follow a straight path. However, when the target is located deep inside the body, a simple straight trajectory could not be sufficient because of the presence of vulnerable anatomic obstacles such as organs or blood vessels between the entry and the target point. To overcome this limitation, flexible steerable needles have been developed and studied by a number of research groups (a detailed state-of-the-art on this topic is presented in Chapter 2). Steerable needles are able to follow a curved path, which is useful for avoiding anatomical obstacles between the entry and the target point and for compensating for unwanted needle deflections.

A common way to achieve needle steering is via tip asymmetry. A needle with a bevel-tip [22] or a pre-curved tip [23] can steer through tissue because of asymmetric reaction forces at the tip upon insertion. Bevel-tip and pre-curved needles are designed to steer in one direction, meaning that, in order to achieve 3D steering, rotation around the needle axis is necessary. However, the rotation along the long and very slender needle body might not exactly match the rotation applied at the handle [24], which makes the control of the needle trajectory challenging, particularly in the case of large insertion depths. One solution to this problem is the use of tendon-driven steerable needles [25]. This type of needles steer without the use of interaction with the tissue, which opens possibilities for steering in 3D with no need of rotation around the body axis. However, the design of tendon-driven needles is complex, which inhibits their miniaturization.

1.3. BIOLOGICAL INSPIRATION

In nature, needle-like systems are used to puncture and penetrate solid structures for feeding or reproduction [26]. Some species of female parasitic wasps bear a thin and flexible needle-like structure, called ovipositor, used to lay eggs into hosts hidden into solid substrates, such as fruits or wood [27]. The ovipositor consists of three longitudinal parts, called valves: one dorsal valve and two ventral valves (Figure 1.2). A tongue-and-groove mechanism, the olistheter, connects the valves along their length, preventing their separation [28].

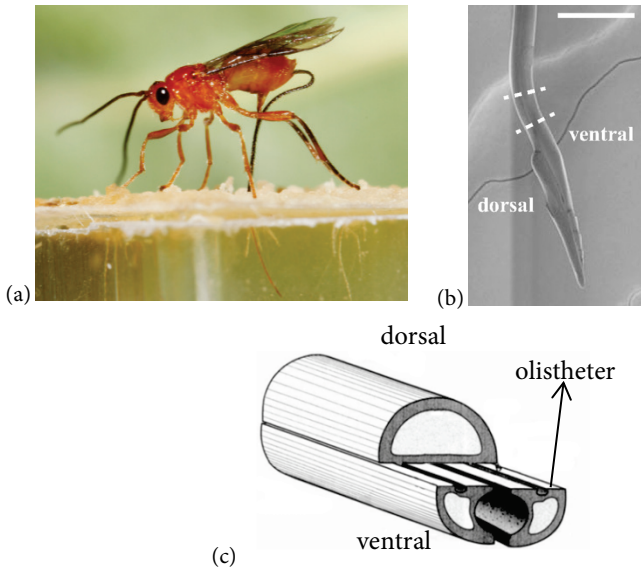


Figure 1.2. Structure and anatomy of the wasp ovipositor. (a) Wasp *Diachasmimorpha longicaudata* (Braconidae) ovipositing into an agar gelatine substrate (Courtesy of Uros Cerkvenik, Sander W.S. Gussekkloo, Johan L. van Leeuwen). (b) SEM image of the ovipositor of *D. longicaudata*. (Scale bar: 100 μm) (adapted with permission from [29]). (c) Cross-section and internal anatomy of the ovipositor (adapted with permission from [28]).

The ovipositor can be few μm thin with a length of few cm. Despite its high aspect ratio (e.g., a 260 length-to-diameter ratio in the wood-probing wasp *Megarhyssa atrata* [30]), the ovipositor advances through substrates as hard as wood without buckling or breaking. The secret of its success is in the mechanism of motion. The ovipositor insertion is done by antagonistically moving the valves: one valve moves forward while the other valves are used as support [31]. Some species have directional serrations at the ovipositor tip, to help the valves anchor against the substrate [32]. In some cases, the wasp pulls backwards two of the three valves, anchoring on the substrate and allowing the third valve to advance through the substrate. This mechanism limits the amount of forward motion of the valve that is protruded and protects the ovipositor from excessive axial load and net push force. Researchers have shown that the wasp is also able to steer the ovipositor to precisely reach the target host [33, 34].

A number of hypotheses have been proposed about the steering mechanism of the wasp ovipositor [33]. During the reciprocal motion of the valves, the relative position between the valves changes, creating an asymmetry at the tip. Because the tip of the valves has a bevel shape, asymmetric forces arise at the tip. These forces might be the cause of the ovipositor bending [29]. Additionally, the steering might be enhanced by the fact that the valves are pre-

curved, that is, they tend to curve in a specific direction when no opposite force is applied. When the valves are aligned, they are “forced” in a straight configuration. As soon as one pre-curved valve is protracted, it will curve.

1.4. BIOLOGICALLY INSPIRED NEEDLES

Engineers in several application fields, from planetary (e.g., Mars) and Earth drills [35] to medical needles and probes [36], have shown interest in the design of the ovipositor of parasitic wasps and the mechanism of advancing and steering through substrates. Rodriguez y Baena and co-workers, for example, developed a probe consisting of four segments, each of them with a bevel-tip, connected with a jigsaw-puzzle interlocking mechanism similar to the olistheter in the wasp ovipositor [36]. In their paper, a series of prototypes are presented, with diameters ranging between 12 mm [37] and 2 mm [38]. The authors showed that the probe is able to self-propel by using a reciprocal actuation sequence and that the use of such probes has the potential to decrease the damage to the tissue and the target displacement as compared to when the probe is directly pushed [39]. Additionally, the probes were able to steer by creating an asymmetry at the tip [40].

At Delft University of Technology, Sprang et al. [41] developed a needle (2-mm thick) consisting of four rigid longitudinal square segments. These authors showed that a needle without directional serration is able to self-propel through gelatine phantoms with zero external pushing force. This is possible when the surface-dependent friction acting on the protruding segment and the cutting force acting at its tip is compensated by the difference in contact area between the stationary and the protruding segments.

1.5. NEEDLE DIAMETER

Although 2 mm thick ovipositor-inspired needles do exist [38], their size is still too big for use in most clinical settings. Typical needle diameters range from 2.1 mm (14 G¹) for tissue sampling, where a part of tissue is removed to be diagnosed [42], to 0.5 mm (27 G) for spinal anaesthesia, where a local anaesthetic is injected in the spinal cord [43]. Smaller diameters are required, for example, in ophthalmology, where needles as thin as 0.3 mm (30 G) are used [44]. Needles with a larger diameter are easier to handle and allow to collect bigger samples, but they also cause more damage to the tissue and pain to the patient. Therefore, when

¹Birmingham gauge: the main system for measuring the outer diameter of needles. Smaller gauge numbers indicate larger outer diameters.

possible, thinner needles (diameter smaller than 1 mm) are preferred over thicker needles [45].

1.6. AIM AND RESEARCH OBJECTIVES

Pushing and steering a thin needle through a solid substrate is challenging. Buckling might occur and unwanted trauma to the tissue might result from the rotation of the needle body used in current steering techniques. Parasitic wasps use an ingenious biological method to protrude and steer a thin and long needle through a solid substrate while avoiding buckling and without the need of rotation of the body. Such a wasp-inspired needle would help doctors reach deep targets into the body avoiding tissue damage and pain for the patient.

The aim of this thesis is *to design, develop, and evaluate a new biologically inspired needle that can steer and self-propel at a submillimeter scale*. The following research objectives were addressed to achieve the above aim:

- To investigate the state-of-the-art of mechanical working principles of steerable needle-like instruments.
- To investigate how the mechanical working principles of the wasp ovipositor can be translated into the design of needles able to self-propel and steer through solid structures.
- To develop self-propelling and steerable needles with a diameter smaller than 1 mm.
- To evaluate the self-propelling behaviour of an ovipositor-inspired needle in single- and multi-layered phantoms.

In this research, we explored the benefits of using an ovipositor-inspired working principle for the development of a new generation of medical needles able to reach targets located deep inside the body accurately and precisely without buckling. Observing the ability of the wasp to move its ovipositor forward and steer through solid substrates, inspired us to develop a series of unique ultrathin self-propelling and/or steerable needle prototypes.

1.7. THESIS OUTLINE

This thesis consists of eight chapters. Chapters 2-5 and Chapter 7 are independent articles, published in peer-reviewed journals or conference proceedings. For this reason, the information presented in the introduction and method sections of these chapters might overlap. To gain insight into steerable needle mechanisms, **Chapter 2** presents a detailed analysis of the mechanical working principles used for steering needle-like instruments through solid organs. The literature study showed that, previously to the work presented in

this thesis, a design of a needle with a diameter smaller than 2 mm, able to steer in 3D without the need of axial body rotation has not been proposed. The next chapters focus on the development and experimental evaluation of a series of biologically inspired needles that aim to fill in this gap. **Chapter 3** describes the design process used to translate the wasp ovipositor into the design of a needle with a diameter of 1.2 mm. The prototype was able to self-propel and steer in 3D without the need of axial body rotation. The two functions, steering and self-propelling, are further investigated in Chapters 4-5. **Chapter 4** presents an experimental evaluation of a second version of the prototype with a different tip design, with the aim to increase the amount of steering. **Chapter 5** describes the parameters that influence the self-propelling motion, looking at the properties of the needle designs and the environment. The performance of three needle designs (diameters 0.8, 0.6, and 0.4 mm) are compared and tested in single- and multi-layer tissue-mimicking phantoms. Each of the prototypes was able to self-propel through the samples. Slip between the needle and the sample was used to compare the performance of the prototypes. **Chapter 6** presents an ex vivo experiment in porcine tissue samples using the 0.8 mm ovipositor-inspired needle described in Chapter 5. **Chapter 7** describes the development of a manually controlled ultra-thin steerable needle (diameter 0.5 mm) the size and morphology of which was inspired by the wasp ovipositor. **Chapter 8** discusses the main findings of the work and gives a number of recommendations for future research.

REFERENCES

1. Rynd F. Description of an instrument for the subcutaneous introduction of fluids in affections of the nerves. *Dublin Quarterly J Med Sci.* 1861; 32(1):13.
2. Chin KJ, Perlas A, Chan VW, Brull R. Needle visualization in ultrasound-guided regional anesthesia: challenges and solutions. *Reg Anesth Pain Med.* 2008; 33(6):532-44.
3. Lindgren P. Percutaneous needle biopsy: a new technique. *Acta Radiol Diagn.* 1982; 23(6):653-6.
4. Alterovitz R, Goldberg K, Pouliot J, Taschereau R, Hsu I-C. Needle insertion and radioactive seed implantation in human tissues: Simulation and sensitivity analysis. *IEEE Int Conf Robot Autom (Cat No 03CH37422)*; 2003 Sept 14-19; Taipei, Taiwan. IEEE; 2003 p. 1793-99.
5. Kipling M, Mohammed A, Medding RN. Guidewires in clinical practice: applications and troubleshooting. *Expert Rev Med Devic.* 2009; 6(2):187-95.
6. Love LJ, Jansen JF, Lloyd PD. Force-based needle insertion for medical applications. *IEEE/RSJ International Conference on Intelligent Robots and Systems (IROS)*; 2009 Oct 10-15; St.Louis, MO, USA. IEEE; 2009 p.2592-97.
7. Old Syringe. Available from: <https://torange.biz/old-syringe-20197>.
8. Hypodermic Needles. Zephyris / CC BY-SA. Available from: <https://commons.wikimedia.org/wiki/File:HypodermicNeedles.jpg>

9. De Jong TL, van de Berg NJ, Tas L, Moelker A, Dankelman J, van den Dobbelsteen JJ. Needle placement errors: do we need steerable needles in interventional radiology? *Med Devices (Auckl)*. 2018; 11:259.
10. Ng KW, Goh JQ, Foo SL, Ting PH, Lee TK, Esuvaranathan K, et al. Needle deflection studies for optimal insertion modeling. *Int J Biosci Biochem Bioinforma*. 2013; 3(6):570.
11. Roberson PL, Narayana V, McShan DL, Winfield RJ, McLaughlin PW. Source placement error for permanent implant of the prostate. *Med Phys*. 1997; 24(2):251–7.
12. Chan C, Lam F, Rohling R. A needle tracking device for ultrasound guided percutaneous procedures. *Ultrasound Med Biol*. 2005; 31(11):1469–83.
13. DiMaio SP, Salcudean SE. Needle steering and motion planning in soft tissues. *IEEE Trans Biomed Eng*. 2005; 52(6):965–74.
14. Park Y-L, Elayaperumal S, Daniel B, Ryu SC, Shin M, Savall J, et al. Real-time estimation of 3-D needle shape and deflection for MRI-guided interventions. *IEEE/ASME Trans Mechatronics*. 2010; 15(6):906–15.
15. Sadjadi H, Hashtrudi-Zaad K, Fichtinger G. Needle deflection estimation: prostate brachytherapy phantom experiments. *Int J Comput Assist Rad*. 2014; 9(6):921–9.
16. Kronreif G, Fürst M, Kettenbach J, Figl M, Hanel R. Robotic guidance for percutaneous interventions. *Adv Robotics*. 2003; 17(6):541–60.
17. Fichtinger G, DeWeese TL, Patriciu A, Tanacs A, Mazilu D, Anderson JH, et al. System for robotically assisted prostate biopsy and therapy with intraoperative CT guidance. *Acad Radiol*. 2002; 9(1):60–74.
18. Shen F, Shinohara K, Kumar D, Khemka A, Simoneau AR, Werahera PN, et al. Three-dimensional sonography with needle tracking: Role in diagnosis and treatment of prostate cancer. *J Ultras Med*. 2008; 27(6):895–905.
19. Krücker J, Xu S, Glossop N, Viswanathan A, Borgert J, Schulz H, et al. Electromagnetic tracking for thermal ablation and biopsy guidance: clinical evaluation of spatial accuracy. *J Vasc Interv Radiol*. 2007; 18(9):1141–50.
20. Abolhassani N, Patel R, Moallem M. Needle insertion into soft tissue: A survey. *Med Eng Phys*. 2007; 29(4):413–31.
21. Chang KJ, Nguyen P, Erickson RA, Durbin TE, Katz KD. The clinical utility of endoscopic ultrasound-guided fine-needle aspiration in the diagnosis and staging of pancreatic carcinoma. *Gastrointest Endosc*. 1997; 45(5):387–93.
22. Swaney PJ, Burgner J, Gilbert HB, Webster RJ. A flexure-based steerable needle: high curvature with reduced tissue damage. *IEEE Trans Biomed Eng*. 2013;60(4):906–9.
23. Okazawa S, Ebrahimi R, Chuang J, Salcudean SE, Rohling R. Hand-held steerable needle device. *IEEE/ASME Trans Mechatron*. 2005; 10(3):285–96.
24. Reed KB, Okamura AM, Cowan NJ. Modeling and control of needles with torsional friction. *IEEE Trans Biomed Eng*. 2009; 56(12):2905–16.
25. van de Berg NJ, Dankelman J, van den Dobbelsteen JJ. Design of an actively controlled steerable needle with tendon actuation and FBG-based shape sensing. *Med Eng Phys*. 2015; 37(6):617–22.
26. Cerkvėnik U, Dodou D, van Leeuwen JL, Gussekloo SW. Functional principles of steerable multi-element probes in insects. *Biol Rev Camb Philos Soc*. 2019; 94(2): 555–574.
27. Kundanati L, Gundiah N. Biomechanics of substrate boring by fig wasps. *J Exp Bio*. 2014; 217(11):1946–54.

28. Rahman MH, Fitton MG, Quicke DL. Ovipositor internal microsculpture in the Braconidae (Insecta, Hymenoptera). *Zool Scr.* 1998; 27(4):319–32.
29. Cerkvenik U, van de Straat B, Gussekloo SW, van Leeuwen JL. Mechanisms of ovipositor insertion and steering of a parasitic wasp. *PNAS.* 2017; 114(37):E7822–E31.
30. Le Lannic J, Nénon J-P. Functional morphology of the ovipositor in *Megarhyssa atrata* (Hymenoptera, Ichneumonidae) and its penetration into wood. *Zoomorphology.* 1999; 119(2):73–9.
31. Vincent J, King M. The mechanism of drilling by wood wasp ovipositors. *Biomimetics (USA).* 1995.
32. Quicke DLJ, Wyeth P, Fawke JD, Basibuyuk HH, Vincent JF. Manganese and zinc in the ovipositors and mandibles of hymenopterous insects. *Zool J Linnean Soc.* 1998; 124(4):387–96.
33. Quicke DLJ, Fitton MG, Harris J. Ovipositor steering mechanisms in braconid wasps. *J Hymenopt Res.* 1995; 4:110–20.
34. Quicke DLJ, Fitton MG. Ovipositor steering mechanisms in parasitic wasps of the families Gasteruptionidae and Aulacidae (Hymenoptera). *Proc R Soc Lond Biol Sci.* 1995; 261(1360):99–103.
35. Gouache T, Gao Y, Gourinat Y, Coste P. Wood wasp inspired planetary and Earth drill. *Biomimetics Learning from Nature: InTech;* 2010.
36. Frasson L, Ko S, Turner A, Parittotokkaporin T, Vincent JF, y Baena FR. STING: a soft-tissue intervention and neurosurgical guide to access deep brain lesions through curved trajectories. *Proc Inst Mech Eng H.* 2010; 224(6):775–88.
37. Ko SY, Frasson L, y Baena FR. Closed-loop planar motion control of a steerable probe with a “programmable bevel” inspired by nature. *IEEE Trans Robot.* 2011; 27(5):970–83.
38. Viridyawan V, Oldfield M, y Baena FR. Laser Doppler sensing for blood vessel detection with a biologically inspired steerable needle. *Bioinspir Biomim.* 2018; 13(2):026009 .
39. Parittotokkaporin T, Frasson L, Schneider A, Huq SE, Davies BL, Degenaar P, et al. Soft tissue traversal with zero net force: feasibility study of a biologically inspired design based on reciprocal motion. 2008 IEEE International Conference on Robotics and Biomimetics; 2009 Feb 22-25; Bangkok Thailand. *IEEE;* 2009 p.80-5.
40. Burrows C, Secoli R, y Baena FR, editors. Experimental characterisation of a biologically inspired 3D steering needle. 2013 13th International Conference on Control, Automation and Systems (ICCAS 2013); 2013 Oct 20-23; Gwangju, South Korea. *IEEE;* 2013.
41. Sprang T, Breedveld P and Dodou D. Wasp-inspired needle insertion with low net push force. In: Lepora N, Mura A, Mangan M, Verschure P, Desmulliez M, Prescott T (eds) *Biomimetic and Biohybrid Systems. Living Machines 2016. Lecture Notes in Computer Science*, vol 9793. 2016; Springer, Cham; p. 307–18.
42. Helbich T, Rudas M, Haitel A, Kohlberger P, Thurnher M, Gnant M, et al. Evaluation of needle size for breast biopsy: comparison of 14-, 16-, and 18-gauge biopsy needles. *AJR Am J Roentgenol.* 1998; 171(1):59–63.
43. Tsen LC, Hepner DL. Needles used for spinal anesthesia. *Expert review of medical devices.* 2006; 3(4):499–508.
44. Thakur Singh RR, Tekko I, McAvoy K, McMillan H, Jones D, Donnelly RF. Minimally invasive microneedles for ocular drug delivery. *Expert Opin Drug Deliv.* 2017; 14(4):525–37.
45. Stewart C, Coldewey J, Stewart I. Comparison of fine needle aspiration cytology and needle core biopsy in the diagnosis of radiologically detected abdominal lesions. *J Clin Pathol.* 2002; 55(2):93–7.

Chapter 2

Needle-Like Instruments for Steering Through Solid Organs – A Review

Published as:

Scali M*, Pusch TP*, Breedveld P, Dodou D. Needle-like instruments for steering through solid organs: a review of the scientific and patent literature. *Proceedings of the Institution of Mechanical Engineers, Part H: Journal of Engineering in Medicine*. 2017; 231(3):250–265. <https://doi.org/10.1177/0954411916672149>.

Copyright © 2017 (SAGE Publishing).

*Authors contributed equally to the realization of this paper

ABSTRACT

High accuracy and precision in reaching target locations inside the human body is necessary for the success of percutaneous procedures, such as tissue sample removal (biopsy), brachytherapy, and localized drug delivery. Flexible steerable needles may allow the surgeon to reach targets deep inside solid organs while avoiding sensitive structures (e.g., blood vessels). This article provides a systematic classification of possible mechanical solutions for three-dimensional steering through solid organs. A scientific and patent literature search of steerable instrument designs was conducted using Scopus and Web of Science Derwent Innovations Index patent database, respectively. First, we distinguished between mechanisms in which deflection is induced by the pre-defined shape of the instrument versus mechanisms in which an actuator changes the deflection angle of the instrument on demand. Second, we distinguished between mechanisms deflecting in one versus two planes. The combination of deflection method and number of deflection planes led to eight logically derived mechanical solutions for three-dimensional steering, of which one was dismissed because it was considered meaningless. Next, we classified the instrument designs retrieved from the scientific and patent literature into the identified solutions. We found papers and patents describing instrument designs for six of the seven solutions. We did not find papers or patents describing instruments that steer in one-plane on-demand via an actuator and in a perpendicular plane with a pre-defined deflection angle via a bevel tip or a pre-curved configuration.

2.1. INTRODUCTION

Medical needles are common devices used in percutaneous procedures, such as tissue sample removal (biopsy) [1], internal radiotherapy (brachytherapy) [2], and localized drug delivery [3]. The success of these procedures depends on the accuracy and precision with which the target site is reached. During biopsy procedures, for example, malpositioning of the medical needle can lead to false diagnosis and healthy tissue damage [4, 5]. Similarly, accurate positioning of radioactive seeds is necessary for brachytherapy [6], and wrong positioning of the needle during peripheral or central anesthesia could cause neurological complications [7]. When the target is reachable via a straight trajectory, rigid needles are typically used. The physician carefully chooses the puncturing angle and pushes the needle forward in order to reach the target. Once the needle is inside the tissue, only small adjustments of the trajectory are possible. Misestimating the puncturing angle requires withdrawing and reinserting the needle, which elongates procedure times and increases patient discomfort.

Flexible steerable needles have the potential to allow the surgeon to reach targets located deep inside the body with higher accuracy and precision than rigid straight needles do. However, several parameters undermine the accurate placement of steerable needles, including needle deflection due to needle-tissue interaction, organ movement due to physiological processes (e.g., breathing), and human error [8, 9].

The navigation of a flexible steerable needle in the human anatomy can be controlled manually or automatically. In the latter case, a robot is used to align the needle with the target location in real time, thereby reducing human error during the pre-insertion phase [10]. Real-time correction of the needle path requires a detailed model of the interaction between the tissue and the needle. Defining the right model for the procedure is challenging due to a vast amount of variables that have to be taken into account, such as needle geometry and tissue properties (for a comprehensive review on this subject, see Gao et al. [11]). Therefore, mainly manually controlled steerable needles are used in percutaneous interventions. Manually controlled needles allow the physician to correct the trajectory of the needle toward the target by, for example, maneuvering the tip of the needle with a joystick, at the cost of inducing human error [12].

The steerability of a flexible needle depends on the mechanical design of the needle and the control strategy used, with the latter having been more broadly investigated than the former [13] (for a review, see Abolhassani et al. [14]). So far, needle steerability in terms of mechanical design has been investigated in two reviews [15, 16]. Cowan et al. [15] distinguished between three steering methods: (1) tip-based steering, relying on an asymmetric needle tip for deflection, (2) lateral manipulation, in which the base of the needle is moved perpendicularly to the needle insertion axis, and (3) steering by means of tissue

manipulation, in which instead of steering the needle toward a stationary target, external forces are applied to the tissue to align the target with the needle trajectory. In the second review [16], a distinction was made between active steering, referring to needles that are steered by means of actuation with no need of tissue interaction, and passive steering, relying on needle-tissue interaction forces that lead to deflection of the needle.

Both reviews follow a bottom-up approach in which existing needles and needle designs are clustered based on their steering strategy. Moreover, both reviews focus on scientific literature only and do not include patent literature. In this review article, we adopted a top-down approach, focusing on the fundamental differences between steering mechanisms of needle-like instruments and on logically derived design solutions, with the goal to create a framework of all mechanically possible solutions for three-dimensional (3D) steering through solid organs. Moreover, we expanded the search in the patent literature, and we applied a systematic search and review methodology, in order to provide a comprehensive overview of the state of the art.

2.2. LITERATURE SEARCH METHODS

A search of the scientific literature and the patent literature for instruments that can be steered through solid organs was conducted using Scopus and the Web of Science Derwent Innovations Index (DII), respectively. In both databases, the search query was a Boolean combination of keywords regarding the following: (1) the instrument type, (2) the target application, and (3) the function of interest, while excluding terms that led to a considerable amount of noise in the search results.

2.2.1. Scientific literature search

We conducted our scientific literature search in Scopus. Scopus offers several advantages compared to both Google Scholar and Web of Science. Google Scholar provides the broadest coverage out of all three search services [17], but one of its limitations is that it does not allow for nested Boolean searches or for exclusively searching in the abstract of papers. Web of Science does allow for complex syntaxes and for searching within specific parts of papers, but it comprises fewer journals and conference proceedings than Scopus. Furthermore, in Web of Science, each paper is classified in only one discipline, meaning that even if a paper is related to both the disciplines of, for example, Engineering and Computer Sciences, it will still be classified in either Engineering or Computer Sciences, and not in both [18].

In our Scopus search, we used the function “LIMIT TO” to limit the search to English language papers and within the subject areas “Engineering” and “Medicine”, which means that all the papers classified in Engineering and Medicine were included (i.e., even those that

were not exclusively classified to these two disciplines but were cross-classified to third disciplines). The entire search query was *TITLE-ABS-KEY((needle OR probe OR cannula OR stylet) AND (tissue OR medic* OR surg*) AND (steer* OR deflect* OR articulat* OR manouv* OR manoeuv* OR “flexible needle”) AND NOT (suture* OR syringe)) AND (LIMIT-TO (SUBJAREA, “MEDI”) OR LIMIT-TO(SUBJAREA, “ENGI”)) AND (LIMIT-TO(LANGUAGE, “English”))*. No limitation to the publication year was applied. Besides the search in Scopus, we checked the references of the papers included in this review for retrieving relevant works that were not captured by the Scopus search.

2.2.2. Patent literature search

We compared the Web of Science DII with Google Patents and Free Patents Online (FPO) and concluded that DII provides several advantages compared to the other two patent databases. Similar to Google Scholar, Google Patents does not support nested Boolean searches, and it only allows for full-text searches and searches in the title rather than exclusively searching in the patent abstract. Patent titles are often not informative, whereas a full-text search, albeit comprehensive, would lead to extensive noise in the form of irrelevant patents which happen to mention the search term(s) in an unrelated context. FPO does provide the option to limit a search exclusively to specific parts of a patent (e.g., abstract) as well as to use a nested Boolean search syntax. However, because patents typically use nonspecific formulations in their abstract, restricting a search to the patent abstract increases the risk of missing relevant patents. Patents in the DII database are complemented with an edited title and abstract that are manually prepared by a human abstractor based on the claims and novelty of the patent. The edited title and abstract also comprise information about the uses and advantages of the technology [19]. A search in the edited title and abstract can be performed using the DII “Topic search” (TS) field.

We restricted our search within the technological field with Derwent Class Code (DC) “P3,” which corresponds to the health section of the engineering area. Section P3 contains several subsections. We focused our search on the following subsections: “P31,” containing results from the group “Diagnosis, surgery”; “P33,” representing “Medical aids, oral administration”; and “P34,” representing “Sterilizing, syringes, electrotherapy.” We further restricted the search regionally using the first two letters of the patent number (PN). Specifically, we searched only for US (US*) and European (EP*) patents, as well as patent applications (WO*). The entire search query was *TS=((needle OR probe OR cannula OR stylet) AND (tissue OR medic* OR surg*) AND (steer* OR deflect* OR articulat* OR manouv* OR manoeuv* OR “flexible needle”) NOT (suture* OR syringe)) AND DC=(P31 OR P33 OR P34) AND PN=(US* OR WO* OR EP*)*. No limitation to the publication year was applied. Patents in which priority date and inventor names were identical were considered to be

potential duplicates. After checking the edited title and abstract of such patents for false positives, duplicate patents were removed.

2.2.3. Eligibility criteria

Our review focuses on steerable needles. We defined a needle as an instrument that is able to puncture a solid tissue and move through it. Instruments that can move (only) through a body lumen, vitreous humor, or the vascular system were excluded. Furthermore, only those instruments that are capable of maneuvering along a curved path, that is, are able to steer, were considered as relevant. If a research group published multiple papers on the same needle design, only the most comprehensive paper, in terms of the description of the mechanical working principle, was included. Papers from different research groups reporting on steerable needles of similar designs were counted as independent designs. Works that focused on needle–tissue interaction, computational modeling, motion planning algorithms, or control of a steerable needle and not on the mechanical design of the needle were excluded. Also, works that only added a feature that does not relate to the steering performance of a needle presented in a different paper or patent were excluded.

2.2.4. Study selection

The title and abstract of the scientific papers were initially screened by the first author (M.S.) based on the above-mentioned eligibility criteria. The references of the two previous reviews [15, 16] were also checked but did not reveal papers that were not already retrieved by our search. Next, the full text of the remaining papers was read. To test the clarity of our eligibility criteria, a sample of 50 scientific papers was chosen by M.S. and independently classified as relevant or not by the last author (D.D.). The blind test resulted in 92% (46 out of the 50 papers) agreement between the two authors.

The patents were also first screened based on the eligibility criteria by reading the title and edited abstract. Next, the selected patents were split between M.S. and T.P.P. and studied in depth by reading the full text. When in doubt (six patents), the two authors discussed the relevance of the work until consensus was reached about whether or not to include the work.

2.3. LITERATURE SEARCH RESULTS

The searches yielded 1292 scientific papers and 1014 patents (last update 15 February 2016). A total of 78 patent duplicates were excluded, leaving 936 unique patents for further inspection. After checking the title and abstract of these papers and patents based on our eligibility criteria, 1102 papers and 857 patents were excluded, leaving 190 scientific papers and 79 patents for full-text inspection. After full-text inspection, 22 papers and 22 patents

were identified fulfilling all criteria. After checking the references of these 44 works, two more relevant papers were found and added, leading to a total of 24 papers (Table 2.1) and 22 patents (Table 2.2) included in this review.

2.4. CLASSIFICATION OF POSSIBLE MECHANICAL SOLUTIONS FOR 3D STEERING

To identify fundamentally distinct steering mechanisms, we first analysed the instrument motions and geometrical features that are responsible for 3D steering. We assumed that every needle can be pushed forward (i.e., translated) and rotated about its longitudinal axis. Note, however, that when the needle interacts with the tissue, these motions can be compromised. Specifically, when a long and thin needle is pushed into the tissue, buckling can occur [64], whereas rotation of a needle as it is advanced in the tissue can generate a torsional stress on the needle body which may result in angular lag between the orientation of the needle base and the needle tip, making the control of the needle trajectory difficult [65]. Moreover, to maneuver a needle in 3D, translation and rotation are not sufficient. To enable 3D steering, the needle (or its tip) should be also able to deflect. The first level of our classification concerns the way in which needle (or tip) deflection is induced. Specifically, we distinguish between needles with a *pre-defined deflection angle* and needles with an *on-demand deflection angle*. Needles with a pre-defined deflection angle have a pre-defined shape that determines the deflection angle of the needle. These needles can have a particular tip shape (e.g., bevel tip) or a particular body shape (e.g., pre-curved needles). Needles with an on-demand deflection angle have one or more means (e.g., wires, a magnetic head, etc.) able to change the deflection angle of the needle upon actuation.

The second level of our classification concerns the number of planes in which a needle can deflect. Needles with a pre-defined shape or an on-demand actuation can deflect in one plane, whereas deflection in a perpendicular plane is achieved by retracting the needle, rotating it about its longitudinal axis, and pushing it again forward. It follows that deflection in one plane (called henceforth *single deflection*) is sufficient for 3D steering. Some needles, however, allow for deflection in two perpendicular planes (called henceforth *double deflection*) without the need of rotation, which increases the number of possible 3D configurations of the needle, thereby improving steerability as compared to needles relying on single deflection.

Table 2.1. Author(s), year of publication, key application(s), affiliation of the first author of the relevant papers, and corresponding category in the classification of the relevant papers.

Author(s)	Publication year	Clinical Application(s)	Affiliation	Classification
Adebar et al. [20]	2016	Liver Biopsy	Stanford University, CA, USA	One on-demand deflection angle
Ayvali et al. [21]	2012	N/A	University of Maryland, MD, USA	One on-demand deflection angle
Burrows et al. [22]	2013	Neurosurgery	Imperial College, London, UK	Two on-demand deflection angles
Chen and Chen [23]	2009	N/A	University of Hong Kong, China	Bevel-tip
Drummond and Scott [24]	1980	Central anaesthesia	University of Edinburgh, UK	Bevel-tip
Hamzavi et al. [25]	2008	Liver biopsy	University of Singapore, Singapore	Two on-demand deflection angles
Ko and Rodriguez y Baena [26]	2014	Neurosurgery	Imperial College, London, UK	One on-demand deflection angle
Konh et al. [27]	2015	N/A	Temple University, PA, USA	One on-demand deflection angle
Kratchman et al. [28]	2011	Lung biopsy	Vanderbilt University, Nashville, USA	One on-demand deflection angle
Losey et al. [29]	2013	N/A	Vanderbilt University, Nashville, USA	Two on-demand deflection angles
Okazawa et al. [12]	2005	N/A	University of British Columbia, Canada	One-plane pre-curved
Ryu et al. [30]	2015	Brachytherapy	Stanford University, CA, USA	One on-demand deflection angle
Sears and Dupont [31]	2006	N/A	Boston University, Boston, USA	Two-plane pre-curved
Swaney et al. [13]	2013	Neurosurgery	Vanderbilt University, Nashville, USA	Bevel-tip
Swaney et al. [32]	2015	Bronchoscopy	Vanderbilt University, Nashville, USA	Two-plane pre-curved
Tang et al. [33]	2008	N/A	University of Hong Kong, China	Two on-demand deflection angles
Terayama et al. [34]	2007	Liver biopsy, Anesthesia	Osaka University, Japan	One-plane pre-curved
Torabi et al. [35]	2014	Brachytherapy	Harvard University, Boston, USA	One-plane pre-curved
Van de Berg et al. [36]	2015	N/A	Delft University of Technology, NL	Two on-demand deflection angles
Wang et al. [37]	2010	N/A	Tianjin University of Technology, China	Bevel-tip

Author(s)	Publication year	Clinical Application(s)*	Affiliation	Classification
Wang et al. [38]	2012	N/A	Tianjin University of Technology, China	One on-demand deflection angle
Webster et al. [39]	2006	N/A	Vanderbilt University, Nashville, USA	Two-plane pre-curved
Yan et al. [40]	2007	N/A	Jefferson University, PA, USA	One on-demand deflection angle
York et al. [41]	2015	Neurosurgery	Vanderbilt University, Nashville, USA	One on-demand deflection angle

N/A is used when no specific application is mentioned

*The clinical applications mentioned in the table do not represent the full scope of possible applications mentioned in the selected paper.

Table 2.2. Inventor(s), priority date, key clinical application(s), affiliation of the first author and category in the classification of the relevant patents.

Inventor(s)	Priority date	Clinical Application(s)*	Affiliation	Classification
Arramon [42]	2003	Vertebroplasty	ArthroCare Corporation, Austin, TX	One-plane pre-curved
Arvanaghi [43]	2006	Biopsies	Independent Inventor	Bevel-tip
Brockman and Harshman [44]	2012	Vertebroplasty	Stryker Corporation, Kalamazoo, MI (US)	One on-demand deflection angle/ Two on-demand deflection angles
Burger et al. [45]	2009	Vertebroplasty/ Kyphoplasty	Osseon Therapeutics, Inc., CA (US)	One on-demand deflection angle
Desai and Ayvali [46]	2012	Biopsies (Breast, Prostate), Brachytherapy	University of Maryland, USA	One on-demand deflection angle/ Two on-demand deflection angles
Eck [47]	2006	Drug delivery	Philips Intellectual Property GmbH & Koninklijke Philips Electronics NV, NL	Two on-demand deflection angles
Germain [48]	2001	Brachytherapy	DFINE, Inc., San Jose, CA, USA	One on-demand deflection angle
Kaplan [49]	2001	Brachytherapy	Microsperix LLC, Atlanta, USA	One plane pre-curved
Kraft and Hole [50]	2002	Biopsies (Bone Marrow, fat, muscle tissue)	Independent Inventor	One plane pre-curved/ One on-demand deflection angle/ Two on-demand deflection angles

Inventor(s)	Priority date	Clinical Application(s)*	Affiliation	Classification
Krueger and Linderman [51]	2005	Vertebroplasty	Allegiance Corp. & Carefusion 2200 Inc.	One-plane pre-curved
Kuhle [52]	2002	Biopsies	Independent Inventor	Bevel-tip
Liu et al. [53]	2007	Vertebroplasty/ Kyphoplasty	Osseon Therapeutics Inc., CA, USA	One-plane pre-curved/ One on-demand deflection angle
Mathis et al. [54]	2004	Biopsies (Lung)	PneumRx Inc., CA, USA	One on-demand deflection angle
Mehta et al. [55]	2010	Tissue repair to shoulder or other joint area	Independent Inventor	One on-demand deflection angle
Melsheimer [56]	2009	Biopsies (Bone, Organs)	Cook Inc. & Cook Medical Technologies LLC, USA	One-plane pre-curved/ Bevel-tip and one-plane pre-curved
Pellegrino et al. [57]	2010	Vertebroplasty/ Kyphoplasty	Relievan Medsystem Inc., CA, USA	One plane pre-curved
Rodriguez Y Baena and Frasson [58]	2009	Brain or liver surgery	Imperial College London, UK	Two on-demand deflection angles
Ryan and Winslow [59]	1991	Discectomy	Surgical Dynamics Inc., CA, USA	One on-demand deflection angle/ Two on demand deflection angle
Salcudean et al. [60]	2002	N/A	University of British Columbia, Canada	One plane pre-curved
Smits et al. [61]	2002	N/A	Medtronic, Minneapolis, USA	One on-demand deflection angle/ Two on-demand deflection angles
Swaney and Webster [62]	2013	Biopsies, Brachytherapy, Drug delivery	Vanderbilt University, Nashville, USA	Bevel-tip
Webster et al. [63]	2005	Bio-sensing	Johns Hopkins University, Baltimore, USA	Two plane pre-curved

N/A is used when no specific application is mentioned

*The clinical applications mentioned in the table do not represent the full scope of possible applications mentioned in the patent.

The third level of our classification depicts eight distinct design solutions derived as combinations of the deflection method (first level of the classification) and the number of deflection planes (second level of the classification):

1. Bevel-tip needles

In this type of needles, the distribution of forces exerted by the tissue on the bevel tip is asymmetric, as a result of which the needle bends in the direction of the bevel.

2. One-plane pre-curved needles

These needles consist of an inner tube which has a pre-set curvature and is fed through an outer straight tube.

3. Double bevel-tip needles

These needles have a tip which is beveled on two sides perpendicular to each other.

4. Two-plane pre-curved needles

These needles consist of at least two segments with a pre-set curvature perpendicular to each other.

5. Bevel-tip and one-plane pre-curved needles

These needles are a combination of solutions (1) and (2).

6. Needles with one on-demand deflection angle

These needles contain at least one actuated part which causes deflection of the needle upon actuation.

7. Needles with two on-demand deflection angles

These needles have at least two parts that lead to deflection in perpendicular planes upon actuation.

8. Needles with one on-demand angle and one predefined deflection angle

These needles are a combination of solution (1) or (2) with solution (6).

We dismissed solution 3 (“Double bevel-tip needle”) as practically meaningless: a “double” bevel tip is in essence not distinct from the bevel tips in solution 1. Therefore, in the remainder of this review, we will consider only seven possible solutions as part of our classification (Figure 2.1).

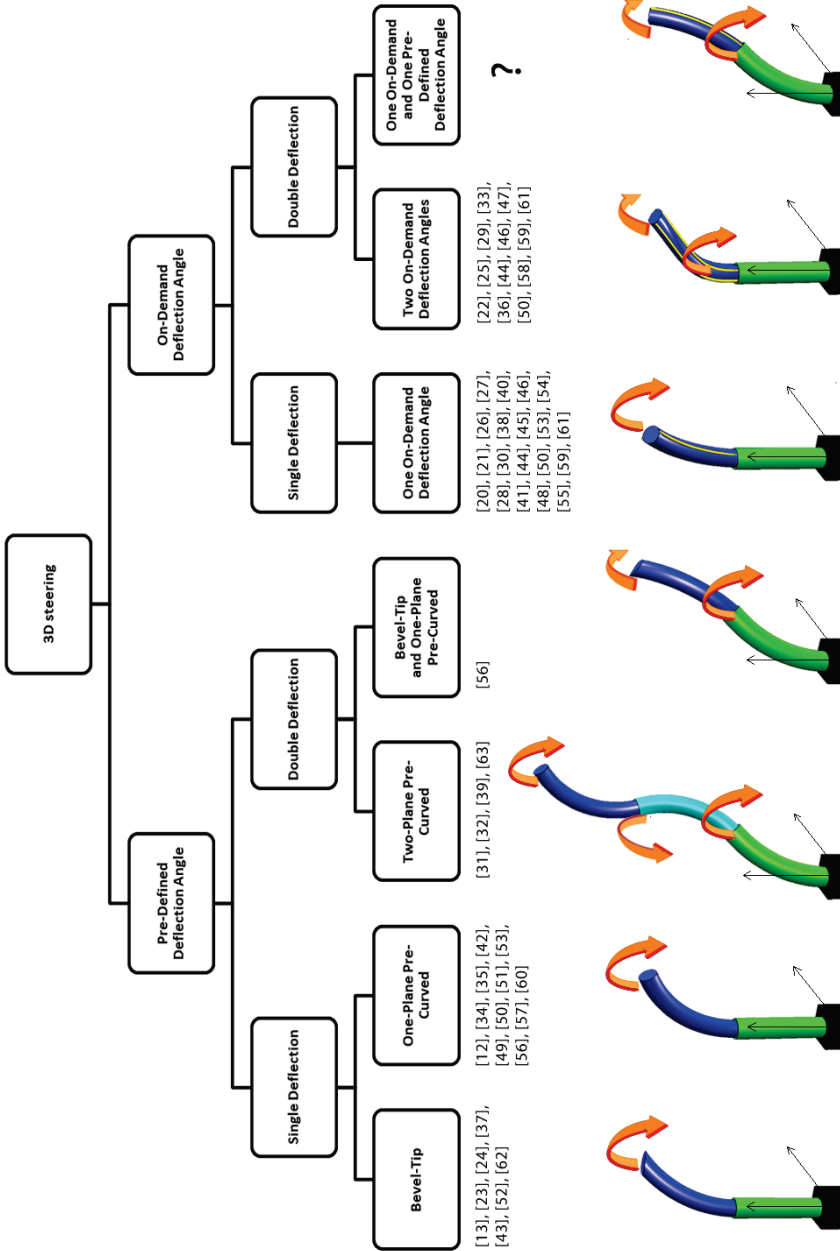


Figure 2.1. Classification of possible mechanical solutions for 3D steering through solid organs. Arrows indicate the planes in which the instrument can deflect. The question mark indicates that no examples of such instruments were found in the literature.

2.5. ALLOCATION OF THE RETRIEVED STEERABLE NEEDLE DESIGNS IN THE CLASSIFICATION SCHEME

The needle designs retrieved from the literature were allocated into the seven possible mechanical solutions of our classification for 3D steering. Below, the working principle of each of these seven solutions is described, papers and patents which apply the respective solution are presented, and the main design variations are highlighted.

2.5.1. Bevel-tip needles

Upon advancement of a needle through a solid tissue, reaction forces are exerted by the tissue on the tip and along the needle surface. Due to the presence of the bevel, the distribution of these forces (so-called “tissue interaction forces”) on the tip is asymmetric. The curvature of the trajectory can be controlled by rotating the needle while pushing it through the tissue. When the needle is pushed forward without rotation, it bends in the direction of the bevel. When the needle is rotated with a rate that is higher than the insertion rate, the needle follows an approximately straight trajectory (or, strictly speaking, a helical trajectory with small pitch). By altering between insertion with and without rotation of the needle, the surgeon can control the curvature and thus the final trajectory of the needle. This control strategy is often referred to as “duty cycling,” where the “duty cycle” is defined as the period in which the needle is inserted while being rotated divided by the period of insertion without rotation. A duty cycle of 100% yields a straight path, whereas the maximum needle deflection is achieved when the needle is not rotated at all (i.e., a duty cycle of 0%) (see previous studies [66–68] for examples of applications of this control strategy).

The bevel tip has been used in needles for percutaneous interventions already in the 1980s [24] and remains one of the most popular designs for steering during such procedures [69]. Several variations of the basic bevel-tip geometry have been presented in literature. The main purpose of these variations is to increase the maximum deflection angle of the needle either by geometric modifications of the shaft (or a segment of the shaft) that lower its bending stiffness [13, 23, 37, 43, 62] or by increasing the surface area that is in contact with the tissue [52]. Swaney et al. [13] Swaney and Webster [62] presented a needle with a flexure joint incorporated in the bevel tip, which creates a so-called “flexure tip” (Figure 2.2). Upon insertion into the tissue, the flexure tip deflects more than the shaft due to the low bending stiffness of the flexure. The configuration of the flexed needle looks similar to a kinked bevel-tip needle and can bend more than a standard bevel-tip needle [70]. The curvature of the needle is adjusted using the “duty cycling” control strategy, where the needle is simultaneously rotated and advanced. When only rotation is applied to the needle body, the flexure at the tip disappears and the needle returns to a configuration similar to a standard

bevel tip. The flexure joint can be replaced with a compliant mechanism, as shown in Chen and Chen [23], in which the needle has a bevel tip and two compliant hinges, that is, flexible members that store energy when they are deformed (input) and transfer this energy to the environment (output). Another way to increase the deflection angle of a bevel-tip needle is presented by Wang et al. [37], who developed an articulated bevel-tip needle made of multiple sections. The head of the needle bends due to asymmetric forces applied at the bevel tip, with the articulations that are distributed along the needle body increasing the deflection angle. Another approach for increasing the deflection angle relatively to a bevel tip is described by Kuhle [52], who patented a needle having a bevel tip with a larger diameter than the diameter of the shaft. The underlying principle of this mechanism is that the larger diameter of the tip creates a larger contact area with the tissue, which leads to greater resistance from the tissue, thereby a larger deflection as compared to a needle with uniform diameter.

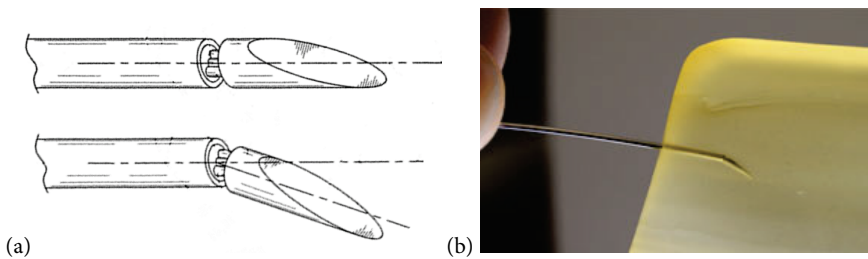


Figure 2.2. Example of a bevel-tip needle. The design presents a flexure joint at the tip, which deflects more than the shaft upon insertion in the tissue: (a) a schematic drawing (adapted from Swaney and Webster [62]) and (b) a photo of the prototype [13] (courtesy of PJ Swaney).

2.5.2. One-plane pre-curved needles

These needles consist of a straight tubular outer part (cannula) and a cylindrical inner part (stylet) with a pre-set curvature. The pre-curved stylet is fed through the cannula which forces the stylet to assume an approximately straight configuration. As the stylet is moved out of the distal end of the cannula, it returns to its initial bent shape, allowing the needle to follow a curved trajectory. Note that there exist nested cannula systems that cannot bend once into the tissue due to their high stiffness. These systems have been excluded from our review.

We found six needles that use this steering mechanism of a pre-curved stylet/straight cannula [12, 34, 35, 51, 53, 57, 60] and four needles with small variations of this mechanism [42, 49, 50, 56]. Okazawa et al. [12] described a pre-curved stylet/straight cannula concept of a steerable needle (for the complete design description of the instrument, see also Salcudean et al. [60]) manually controlled with a joystick (Figure 2.3). Torabi et al. [35] used such a

steerable needle in combination with a robotic system for placing seeds during brachytherapy. Another example of a straight cannula and pre-curved stylet is presented by Terayama et al. [34] in combination with ultrasound imaging that provided information about the position of the needle during the advancement through the tissue.

In one variation of the basic pre-curved stylet/straight cannula design, the shaft has notches of various shapes and dimensions, which increase the flexibility of the instrument and hence achieve a greater deflection angle [50]. An increase in the deflection angle can be also achieved by having a cannula and a stylet that are both pre-curved in such a way that they enable (i.e., reinforce) deflection toward the same direction [57]. In a more substantial design variation, the instrument consists of a cannula with a pre-set curvature and a straight stylet. The instrument is in its straight configuration when the stylet supports the entire cannula length. Steering can be accomplished by retracting the straight stylet (fully or partially) to allow the pre-curved tip of the cannula to deflect [42]. Another variation is a hybrid instrument combining a pre-curved stylet with a bevel tip, both causing deflection in the same plane [49, 56]. Among the pre-curved needles, the one presented by Liu et al. [53] is commercially available under the name of “Osseoflex SN,” used for the treatment of vertebral compression fractures.

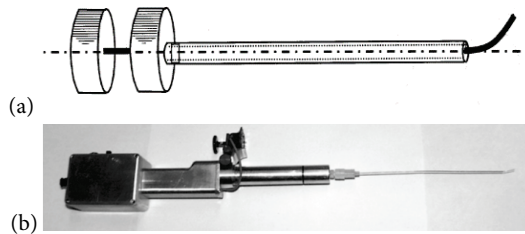


Figure 2.3. Example of a straight cannula and pre-curved stylet. The design shows the deflection of the stylet once it is pushed out of the cannula: (a) a schematic drawing (adapted from Salcudean et al. [60]) and (b) a photo of the prototype (from Okazawa et al. [12]).

2.5.3. Two-plane pre-curved needles

Two-plane pre-curved needles have at least two segments with a pre-set curvature perpendicular to each other. The working mechanism of these needles is the same as that of single pre-curved needles, with the difference that two-plane pre-curved needles can follow a 3D path through the tissue without having to rotate the entire needle. Two-plane pre-curved needles consist of multiple pre-curved concentric tubes arranged in a telescopic way. Each of the tubes can independently be extended and rotated axially with respect to one another. Each section of the shaft follows the trajectory of the tip, in what is called a “follow-the-leader”

concept (see Sears and Dupont [31] for a detailed description of the concept). The overall shape of the needle is determined by the position and orientation of each of the concentric tubes (Figure 2.4). Webster et al. [39] named this design “active cannula” (for the complete design description of the system, see also Webster et al. [63]). Recently, the concentric tube steering mechanism has been combined with the aforementioned flexure bevel-tip needle [13] to steer through lung tissue and reach peripheral lesions (design and application are described in Swaney et al. [32]).

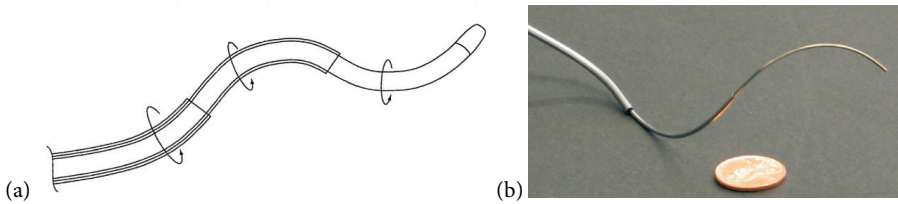


Figure 2.4. Example of a two plane pre-curved needle. The design consists of multiple pre-curved concentric tubes arranged in a telescopic way: (a) a schematic drawing (adapted from Webster et al. [63]) and (b) a photo of the prototype (from Webster et al. [39]).

2.5.4. Bevel-tip and one-plane pre-curved needles

In this type of needles, the working principles of the bevel-tip needles (solution 1) and the pre-curved needles (solution 2) are combined. A needle following this principle would have at least two segments: one segment with a bevel tip that causes the deflection in one plane, and another segment that is pre-curved and allows for deflection in a perpendicular plane. A common practice is to use the two segments where the bevel angle and the pre-curvature allow a deflection in the same plane. This design is used to increase the deflection angle as described in the category of one-plane pre-curved needles. However, in an embodiment of a patent by Melsheimer [56], it is mentioned that the segment with the bevel angle can be used to generate needle deflection in the plane perpendicular to the plane of the pre-curved segment.

2.5.5. Needles with one on-demand deflection angle

Needles with one on-demand deflection angle have at least one actuated part which causes deflection of the needle on demand. The deflection angle of the needle can be locally and actively controlled. Once deflected, the needle can be steered along a curved path. Even though needles of this type seem very diverse due to the wealth of possible actuation means (e.g., mechanical, thermal, and magnetic actuation), they all follow the same working principle of 3D steering.

Tendon-driven needles are examples of mechanically actuated steerable needles in which control wires or rods are used to make the needle deflect [20, 28, 41, 44, 45, 48, 50, 53–55, 59, 61]. Two tendons (wires) run along the length of the needle body, whereas a handle at the needle base is used to pull one of the tendons, increasing the tendon tension. Since the wires are eccentrically attached to the needle tip, the tension in one of the tendons makes the tip deflect. The deflection angle of the tip depends on the force applied on the tendon, with a larger pulling force corresponding to a larger deflection angle. In two examples, Burger et al. [45] and Liu et al. [53], the shaft of the instrument has segments with lower bending stiffness than the bulk of the shaft. Because of the lower bending stiffness, these segments deflect upon actuation more than the rest of the shaft. A series of asymmetric cuts at the needle tip is presented in York et al. [41], creating a compliant region, which bends in one direction by pulling a single wire. In another design of a tendon-driven needle, a flexural conical tip (inspired by the flexure tip in Swaney et al. [13]) is used to create an articulated tip [20]. The tip is actuated by a nitinol pull wire that runs along the needle shaft, in combination with a miniaturized cable pulley. Among the needles that are tendon-driven, the one presented by Mathis et al. [54] is commercially available under the name of “Seeker Steerable Biopsy Needle™” (PneumRX, Mountain View, CA, USA). The needle has a cannula and a stylet. Its trajectory is controlled by a joystick which allows the physician to make fine adjustments intra-operatively. This needle is mainly used for transthoracic lung biopsy [28].

Actuation for 3D steering can be achieved using shape-memory or pseudoelastic materials, which can change their shape in response to a stimulus (e.g., heat). When embedded in the shaft of a needle, these so-called smart materials enable active and local control of the needle deflection without the need of tissue interaction forces. Shape-memory alloy (SMA) wires, for example, are used to connect several deflectable segments in the shaft of the needle described by Ayvali et al. [21] and Desai and Ayvali [46]. The SMA wires are initially deformed with an annealing process to assume an arc shape. They are then straightened and placed between the segments of the needle. By increasing the temperature (e.g., induced electrically by Joule heating), the SMA wires return to their original arc shape (Figure 2.5). Similarly, Ryu et al. [30] presented a needle with a cannula and a stylet locally actuated by magnetic resonance imaging (MRI)-compatible SMA wires integrated at the end of the stylet. The MRI compatibility of this needle is achieved using laser heating instead of electrical current to actuate the SMA wires. Optical fibers run parallel to the body needle axis and conduce laser light over the tip, transmitting optical heating to the SMA wires.

As mentioned in the section on bevel-tip needles, adding a flexure joint near the tip increases the deflection angle of the needle as compared to a needle without a flexure joint. Konh et al. [27] described a needle in which a flexure bevel tip is combined with SMA-wire actuation to control the needle deflection angle. The needle body is made of two hollow tubes

connected by a nylon flexure joint and a nitinol wire which lies on the surface of the needle with one end crimped on the tip and the other end glued along the body of the needle. When the needle bends upon actuation of the SMA wire, the presence of the joint allows for a larger deflection angle than in the case of a jointless needle.

Piezoelectric actuators are also used for controlling the needle deflection [40]. Applying an electric field on a piezoelectric element induces a mechanical effect (e.g., extension or contraction). The actuators are placed on different sides of the surface of the needle, such that their longitudinal strain results in needle deflection.

In the category “bevel-tip needles,” we described the design of an articulated bevel tip presented by Wang et al. [37], where articulations are used to increase the deflection of the needle as compared to needles without articulations. The same authors proposed a variation of this needle composed of the same segments and a magnetic head [38]. An external magnetic field generates magnetic forces, which are used to manipulate the needle trajectory. By changing the direction and magnitude of the magnetic field, the needle can be steered in two perpendicular planes.

Another design of a needle with one on-demand deflection angle consists of two body parts aligned parallel to each other and each movable independently along the needle by means of two linear actuators [26]. The initial configuration of the needle has a conical shape with each of the segments having a bevel tip. Pushing the entire needle forward with the body parts aligned generates a straight path. In order to steer, an offset at the tip needs to be created, which is done by means of actuators that move the needle parts backward and forward. When the entire needle is pushed forward into the tissue, the offset creates an asymmetry that results in deflection in one plane. This design is an example of bevel-tip needle; however, the steering mechanism depends not only on the bevel tip but also on the actuation sequence. Therefore, we decided to include this design in the “one on-demand deflection angle” category.

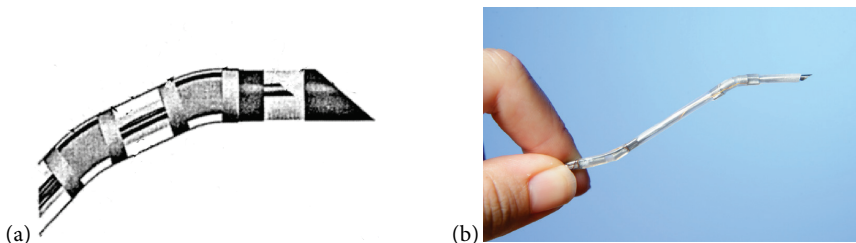


Figure 2.5. Example of a needle with one on-demand deflection angle. The design consists of several deflectable segments connected by SMA wires. The needle deflects upon actuation of the SMA wires: (a) a schematic drawing (adapted from Desai and Ayvali [46]) and (b) a photo of the prototype (from Ayvali et al. [21]).

2.5.6. Needles with two on-demand deflection angles

Needles with two on-demand deflection angles have at least two parts that lead to deflection in perpendicular planes upon actuation. Many of the mechanisms mentioned in solution 5 can be extended toward needles with two on-demand deflection angles. This is the case for the patents [44, 46, 50, 59, 61] which present alterations of the designs of one on-demand deflection needle to allow for deflection in two perpendicular planes.

For a needle with tendon actuation to deflect in two perpendicular planes, at least two wires placed at 90° radially to each other are needed. Pulling one of the wires will cause the needle to deflect in one plane, whereas pulling the other wire will lead to deflection of the needle in a plane perpendicular thereto. Van de Berg et al. [36] presented a tendon-actuated flexible cannula with a conical tip. This needle can deflect in two orthogonal planes by means of four actuation cables that run over a ball joint placed near the tip. Losey et al. [29] used two pairs of Nitinol pull wires to actuate two flexure joints placed in series and rotated 90° with respect to one another. The so-called flexure-based “wrist” design is inspired from the flexure-tip needle described by Swaney et al. [13] (see solution 1). Wires were also used by Hamzavi et al. [25] to actuate three elements, each of them made of three sections and placed at the end of the needle.

In a similar way to the tendon actuation, the design of needles actuated by means of smart materials can be modified to allow for two on-demand deflection angles. Ayvali et al. [21] and Desai and Ayvali [46] proposed a modification of the needle design presented in the previous group by positioning the SMA elements in a configuration that allows deflection in two perpendicular planes. Another example of smart materials used as actuators in steerable instrument is magnetorheological (MR) fluids. In a patent by Eck [47] the body of the needle is filled with an MR fluid that can switch between a fluid and a solid state by the selective activation of an external magnetic field. The transition from a fluid to a solid state increases the stiffness of the needle, thereby generating compression on the surrounding tissue. The needle is able to follow a desired path by means of solidifying the needle body, pushing it further, and then reducing the compression again by switching the state of the MR from solid to fluid.

Another method to introduce deflection in two perpendicular planes is shown in Tang et al. [33], where the needle consists of a magnetized head and a body made of diamagnetic material. The two parts are separated by a compliant hinge, which increases the flexibility of the needle. When an external magnetic field is applied, the head of the needle bends, resulting in a change of the needle trajectory.

Another design of a needle with two on-demand deflection angles consists of at least three body sections aligned parallel to each other and each section being movable independently along the needle [58, 71]. The body of this needle consists of four parts, each part having a

curved outer surface and two inner surfaces that are interlocked to the surfaces of the adjacent body sections with a mechanism that enables a sliding motion (Figure 2.6). The frontal end of each of the body parts has a bevel tip, so that in the aligned configuration, the tip of the needle has a conical shape. When one body section moves forward, it will bend due to interaction forces between the tissue and the bevel tip. The rest of the needle will follow the bent part. The curvature of this multi-part needle can be controlled at any time during the insertion procedure by changing the offset between the body part which is moved forward and the rest of the needle. Burrows et al. [22] developed and tested a prototype with a diameter of 8 mm to demonstrate the 3D steerability of such a needle in an arbitrary 3D path with eight principal directions. This prototype is an improvement of the previous two-body-part prototype presented by Ko and Rodriguez y Baena [26] (solution 5). As explained earlier, because the steering mechanism depends not only on the bevel tip but also on the actuation sequence, we decided to include this design in the “two on-demand deflection angles” category.

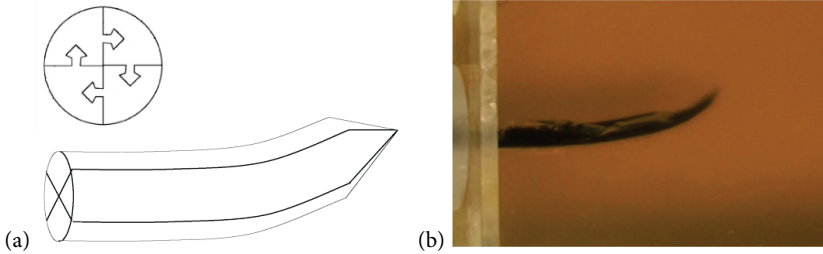


Figure 2.6. Example of a needle with two on-demand deflection angles. The design consists of four parts interlocked with a mechanism that enables a sliding motion: (a) a schematic drawing (adapted from Rodriguez y Baena and Frasson [58]) and (b) a photo of the prototype (from Burrows et al. [22]).

2.5.7. Needles with one on-demand angle and one pre-defined deflection angle

Needles in this category would have at least two segments: one segment bearing an on-demand mechanism of the aforementioned kind (e.g., steering wires, SMA) which causes deflection in one plane and a second segment with a bevel tip or a pre-set curvature for deflection in a perpendicular plane. No examples for needles using a combination of one on-demand deflection angle and one pre-defined deflection angle were found.

2.6. DISCUSSION

In this article, we provided an overview of possible mechanical solutions for 3D steering of a medical needle. First, we distinguished between needles that deflect due to a pre-defined

shape (pre-defined deflection angle) and needles that deflect due to a means of actuation that changes the deflection angle of the needle (on-demand deflection angle). Second, we differentiated between needles that deflect in one plane (single deflection) and needles that deflect in two perpendicular planes (double deflection). Finally, we defined seven mechanical solutions and classified the needle designs retrieved both from the scientific and patent literature into these solutions.

2.6.1. Comparative study

Our review includes a patent search which was not considered in the two previous reviews focusing on the mechanical design of steerable needles [15, 16]. The number of included papers is relatively small (24 design papers) with respect to the total number of papers published on this subject. The reason is that if a research group published multiple papers on the same needle design, only the most comprehensive paper, in terms of the description of the mechanical working principle, was included. Our analysis of the literature indicated that single-deflection needle designs are more popular than double-deflection ones, with only eight papers and nine patents describing double-deflection needles, while 16 papers and 19 patents describe single-deflection needle. This may be due to the fact that single deflection is sufficient for 3D steering and it requires simpler mechanical designs than double deflection. However, double-deflection mechanisms allow steering in two different planes without the need of rotation of the needle body, reducing problems with the control of the trajectory of the needle. The interest in on-demand deflection angle needles seems to be quite recent and diverse (employing SMA, piezoelectric, magnetic field, cables, etc.). Double deflection is more prevalent in combination with an on-demand deflection angle (five papers and seven patents compared to three papers and two patents on pre-defined deflection angle needles).

2.6.2. Tissue interaction

When we advance a needle in the tissue, forces arise on the tip and the body of the needle, the so-called needle–tissue interaction forces. Depending on the design of the needle, these forces may influence the trajectory of the needle (for an overview of experimental needle–tissue interaction forces data, see van Gerwen et al. [72]).

Needles with a bevel tip require tissue interaction forces in order to be steered. The distribution of these forces on the tip is asymmetric due to the presence of the bevel. As a result, the needle bends in the direction of the bevel. The deflection of the needle due to the bevel is a function of several parameters, including needle diameter, bevel angle, insertion velocity, and gel elasticity [73]. Macroscopic and microscopic observations of needle-gel insertion [74] showed that increasing the velocity and the needle diameter results in smaller needle deflections, while increasing the gel elasticity results in larger needle deflections.

Increasing the bevel angle shows a non-monotonic variation in the needle deflection. Needles with three different bevel angles (30°, 60°, and 75°) were inserted in a gel with known stiffness. A bevel angle of 30° and 75° resulted in larger needle deflection compared to the bevel angle of 60°. This behavior is explained by the coupling between the rupture and the compression of gel at the tip in microscopic observations. Specifically, during the insertion of the needle with bevel angle of 30°, a long and narrow gel rupture and low compression of the gel were observed, while using the needle with bevel angle of 75° resulted in a wide and short gel rupture and high compression of the gel. These two combinations (30° and 75°) generated higher needle deflection compared to a needle with bevel angle of 60°. In general, increasing the gel elasticity results in larger needle deflections.

Thanks to their pre-set curvature; pre-curved needles, on the other hand, do not require tissue interaction forces in order to be steered. However, when the needle is inserted in the tissue, needle-tissue interaction forces may affect the needle deflection, with a greater degree of the pre-set curvature leading to a larger needle deflection [70]. Furthermore, increasing the gel elasticity will result in larger needle deflection as observed for the bevel-tip needle.

The on-demand deflection instruments may or may not rely on tissue interaction for steering, depending on their working principle. Specifically, the wire- and SMA-actuated needles [75] can be steered without the need of interaction forces. Designs in which the bevel tip is used to steer and the actuation means is used to change the bevel tip continuously (e.g., the multiple needle part presented by Rodriguez Y Baena and Frasson [58]) can only deflect when needle-tissue interaction forces are present.

2.6.3. Design choices related to the deflection angle of steerable needles

One of the requirements to take into consideration during the design of a steerable needle is the maximum curvature to be achieved. The curvature of a steerable needle depends on the geometrical characteristics of the needle, such as the tip shape and the shaft diameter, and the material properties of the environment, such as tissue stiffness. For example, in our survey, we showed that there are different ways to increase the curvature with respect to a standard bevel-tip needle. Swaney et al. [13] showed how a flexure joint at the needle tip increases the deflection with respect to the standard bevel tip. In the same way, the use of compliant hinges at the tip increases the flexibility of the needle, which in turn results in larger deflection angles [33]. A needle with a pre-curved segment can achieve larger deflection angles than a needle with a bevel tip [70]. A combination of a pre-curved segment with bevel tip [49] or a combination of a pre-curved cannula with a pre-curved stylet [57] will reinforce the deflection in one direction.

The diameter of the shaft is another parameter that can be changed with respect to the tip of the instrument in order to achieve larger deflection angles. A smaller shaft diameter means

higher shaft flexibility, leading to a larger deflection angle once the needle is inserted into the tissue. Kuhle [52] presented a needle in which the diameter of the bevel tip is larger than the diameter of the shaft. In this way, the contact area at the tip is increased, while the diameter of the shaft is kept small. The same design choice can be found in Engh et al. [67], where a stainless steel tip of 16 gauge is attached to a nitinol shaft of 29 gauge. Adding notches of various shapes and dimensions at the tip increases the flexibility of the instrument and facilitates the deflection in one direction [50]. The same happens in the design of the “wrist needle” [41] where asymmetric cuts at the end of the shaft create a compliant region that facilitates needle deflection.

Tissue properties also influence the deflection angle of the needle. For example, Majewicz et al. [76] found a significant difference in performance of the same pre-bent needle in ex vivo experiments versus in vivo experiments (minimum curvature radius achieved: 5.23 and 10.4 cm, respectively). The authors explained this difference as an effect of the increased stiffness and the inhomogeneity of the tissue due to perfused blood vessel in vivo.

2.6.4. Commercially available instruments

We found four commercially available steerable needles: the Osseoflex SN steerable needle (Osseon LLC, Santa Rosa, CA, USA [77]), the Seeker Steerable Biopsy Needle (PneumRx [54]), the Morrison Steerable Needle (AprioMed AB, Uppsala, Sweden [78]), and the Pakter curved needle set (Cook Medical Inc., Bloomington, IN, USA [79]). The patents corresponding to the needles by Osseon and PneumRx were retrieved from our systematic patent search, whereas the AprioMed and Cook needles were not in the list of the 952 retrieved patents. The Osseoflex SN is presented in Liu et al. [53] and categorized as an example of “one-plane pre-curved needle.” It is used mainly for the treatment of vertebral compression fracture (Figure 2.7). The Seeker Steerable Biopsy Needle is presented in Mathis et al. [54] described as an example of a tendon-driven needle in “needles with one on-demand deflection angle.” It is mainly used for transthoracic lung biopsy (Figure 2.8). The Morrison Steerable Needle was only found when searching for commercially available instruments in Google using the query “steerable needle.” The edited title and abstract of the corresponding patent in the DII database used the word “mandrel” to characterize the instrument, which was not included in our selected keywords for specifying instrument type. Adding the word “mandrel” to our patent search query yielded extra 25 patents. Within these works, only the patent from AprioMed was relevant for our study [80]. The AprioMed instrument fits in the “on-demand deflection angle—single deflection” solution of our classification and uses the control wire/rod principle to allow deflection. The needle comprises a tubular stationary outer part with a semi-circumferential slot-like opening and a movable rod-like inner part that is attached to the stationary part only at the side of the opening that is close to the tip. As

the movable part slides in and out of the stationary part, the distal section of the stationary part deflects. The Morrison Steerable Needle is mainly used for musculoskeletal percutaneous injection, aspiration procedure, and tissue sampling (Figure 2.9). The edited title and abstract of the patent of “Pakter curved needle set” do not include any of the words we used for describing the function of the needle, such as “steer” or “deflect.” This needle has a straight cannula in stainless steel (cannula) and a pre-curved stylet in nitinol; therefore, it could fall in the category of the “one-plane pre-curved needles” [81]. Discography is a typical procedure where the Pakter curved needle set is used to inject contrast medium into the center of the disks (Figure 2.10).



Figure 2.7. Osseoflex SN steerable needle (Osseon, Santa Rosa, CA, USA) [77].



Figure 2.8. Seeker Steerable Biopsy Needle™ (PneumRx Inc., Mountain View, CA, USA) [54].



Figure 2.9. Morrison Steerable Needle™ (AprioMed AB, Uppsala, Sweden) [78].

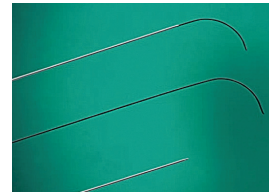


Figure 2.10. Pakter curved needle sets (Cook Medical Inc., Bloomington, IN, USA) [79].

2.6.5. Limitations

This review focuses on the mechanical principles of steerable needles without taking into account additional technologies that can be used to help the physician during the percutaneous intervention (e.g., image guidance). We also did not consider control methods, computational modeling, and motion planning algorithms used in robotic-assisted needle steering [64]. Real-time data from image systems (computed tomography (CT) scan, MRI, fluoroscopy, and ultrasound) give information about the shape and position of the instrument during minimally invasive procedures [82, 83]. Combining these data with computational models that predict needle deflection during insertion in the tissue would result in an accurate planning of the procedure [84, 85]. Several models describing needle

insertion into soft tissue are presented in the literature. Misra et al. [86] divided these models in linear elasticity-based models, nonlinear (hyperelastic) elasticity-based finite element (FE) models, and other models that are not based on FE methods or continuum mechanics (e.g., mass-spring-damper models).

Furthermore, buckling of the instrument was not considered in this review. Since buckling is an important failure mode of long slender instruments [87], an overview of the instrument types in terms of their tendency to buckle would be a useful complement to this study.

2.7. CONCLUSION AND FUTURE WORK

We proposed a systematic classification of possible mechanical solutions for 3D steering through solid organs, which was created with a top-down approach. First, we distinguished between mechanisms in which deflection is induced (needles with pre-defined deflection angle versus needles with on-demand deflection angle). Second, we distinguished between the number of deflection planes (one plane versus two planes). The combination of these two levels led to eight solutions, of which seven were considered meaningful. Accordingly, we allocated steerable needle designs retrieved from a systematic scientific and patent literature search into these seven solutions. This methodological approach allowed us to extend the solution space to all viable designs beyond these already materialized and present in literature. Indeed, we identified one solution (“one on-demand angle and one pre-defined deflection angle”) for which no existing steerable design mechanism was found. This “gap” may function as a source of inspiration for investigating new steerable needle mechanisms. The top-down approach used in this review can also be applied to other research questions and other fields of application. Future scientific and patent studies should also take into account computational modeling, motion planning algorithm, and control of steerable needles.

REFERENCES

1. Phelan S, O'Doherty A, Hill A. Epithelial displacement during breast needle core biopsy causes diagnostic difficulties in subsequent surgical excision specimens. *J Clin Pathol.* 2006; 60(4):373–376.
2. Nath, R, Amols H, Coffey C. Intravascular brachytherapy physics: report of the AAPM Radiation Therapy Committee Task Group no. 60. *Med Phys.* 1999; 26(2):119–152.
3. Horlocker TT, Wedel DJ. Neurologic complications of spinal and epidural anesthesia. *Reg Anesth Pain Med.* 2000; 25(1):83–98.
4. Youk JH, Kim EK, Kim MJ. Analysis of false-negative results after US-guided 14-gauge core needle breast biopsy. *Eur Radiol.* 2010; 20(4):782–789.

5. Volpe A, Kachura JR, Geddie WR. Techniques, safety and accuracy of sampling of renal tumors by fine needle aspiration and core biopsy. *J Urol.* 2007; 178(2):379–386.
6. Wan G, Wei Z, Gardi L. Brachytherapy needle deflection evaluation and correction. *Med Phys.* 2005; 32(4):902–909.
7. Jeng CL, Torrillo TM, Rosenblatt MA. Complications of peripheral nerve blocks. *Br J Anaesth.* 2010; 105(1):97–107.
8. Kohn LT, Corrigan JM, Donaldson MS. *To err is human: building a safer health system.* Washington, DC: National Academies Press, 2000.
9. Carr JJ, Hemler PF, Halford PW. Stereotactic localization of breast lesions: how it works and methods to improve accuracy. *Radiographics* 2001; 21(2):463–473.
10. O’Leary M, Simone C, Washio T. Robotic needle insertion: effects of friction and needle geometry. In: *Proceedings of the IEEE international conference robotics and automation (Cat. No. 03CH37422); 2003 Sept 14–19, p.1774–1780.*
11. Gao D, Lei Y, Zheng H. Needle steering for robot-assisted insertion into soft tissue: a survey. *Chin J Mech Eng.* 2012; 25(4):629–638.
12. Okazawa S, Ebrahimi R, Chuang J. Hand-held steerable needle device. *IEEE/ASME T Mech.* 2005; 10(3):285–296.
13. Swaney PJ, Burgner J, Gilbert HB. A flexure-based steerable needle: high curvature with reduced tissue damage. *IEEE Trans Biomed Eng.* 2013; 60(4):906–909.
14. Abolhassani N, Patel R, Moallem M. Needle insertion into soft tissue: a survey. *Med Eng Phys.* 2007; 29(4):413–431.
15. Cowan NJ, Goldberg K, Chirikjian GS et al.. Robotic needle steering: design, modeling, planning, and image guidance. In: *Rosen, J, Hannaford, B, Satava, RM (eds) Surgical robotics; 2011; Boston, MA: Springer; pp.557–582.*
16. Van de Berg NJ, Van Gerwen DJ, Dankelman J. Design choices in needle steering—A review. *IEEE/ASME T Mech.* 2014; 20(5):2172–2183.
17. De Winter JCF, Zadpoor AA, Dodou D. The expansion of Google Scholar versus Web of Science: a longitudinal study. *Scientometrics* 2014; 98(2):1547–1565.
18. De Winter JCF, Dodou D. A surge of p-values between 0.041 and 0.049 in recent decades (but negative results are increasing rapidly too). *Peer J.* 2015; 3:e733.
19. The Thomson Corporation. *Derwent Innovation IndexSM.* 2007.
20. Adebar TK, Greer JD, Laeseke PF. Methods for improving the curvature of steerable needles in biological tissue. *IEEE T Bio-med Eng.* 2016; 63(6):1167–1177.
21. Ayvali E, Liang CP, Ho M. Towards a discretely actuated steerable cannula for diagnostic and therapeutic procedures. *Int J Rob Res.* 2012; 31(5):588–603.
22. Burrows C, Secoli R, Rodriguez y Baena, FM. Experimental characterisation of a biologically inspired 3D steering needle. In: *Proceedings of the 13th international conference on control, automation and systems; 2013 Oct 20–23; Gwangju, Korea. New York: IEEE; pp.1252–1257.*
23. Chen Z, Chen YH. Analysis of multi-hinge compliant needle insertion. In: *Proceedings of the IEEE international conference virtual environments, human-computer interfaces and measurements systems; 2009 May 11–13; Hong Kong. New York: IEEE; pp.314–318.*
24. Drummond GB, Scott, DH. Deflection of spinal needles by the bevel. *Anaesthesia* 1980; 35(9):854–857.

25. Hamzavi N, Chui CK, Chui CC. Flexible liver needle navigation using fish-like robotic elements. In: Proceedings of the IEEE international conference on systems, man and cybernetics; 2008 Oct 12–15; Singapore. New York: IEEE; pp.3491–3496.
26. Ko S, Rodriguez Y Baena FM. Toward a miniaturized needle steering system with path planning for obstacle avoidance. *IEEE Trans Biomed Eng.* 2013; 6(4):910–917.
27. Konh B, Lee H, Lee HH. Towards the design and development of an active needle for therapeutic procedures. In: Proceedings of the IEEE annual northeast biomedical engineering conference; 2015 Apr 17–19; Troy, NY. New York: IEEE; pp.1–2..
28. Kratchman LB, Rahman MM, Saunders, JR. Toward robotic needle steering in lung biopsy: a tendon-actuated approach. *Proc SPIE.* 2011; 7964.
29. Losey PD, York PA, Swaney, PJ. A flexure-based wrist for needle-sized surgical robots. *SPIE Med Imaging.* 2013; 86711G.
30. Ryu CS, Quek ZF, Koh JS. Design of an optically controlled MR-compatible active needle. *IEEE T Robot.* 2015; 31:1–11.
31. Sears P, Dupont P. A steerable needle technology using curved concentric tubes. In: Proceedings of the 2006 IEEE/RSJ international conference on intelligent robots and systems (IROS); 2006 Oct 9–15; Beijing, China. New York: IEEE; pp.2850–2856.
32. Swaney PJ, Mahoney AW, Ramirez AA. Tendons, concentric tubes, and a bevel tip: three steerable robots in one transoral lung access system. *IEEE Int Conf Robot Autom;* 2015:5378–5383.
33. Tang L, Chen Y, He X. Magnetic force aided compliant needle navigation and needle performance analysis. In: Proceedings of the IEEE international conference on robotics and biomimetics; 2007 15–18 Dec; Sanya, China. New York: IEEE; pp.612–626.
34. Terayama M, Furusho J, Monden M. Curved multi-tube device for path-error correction in a needle-insertion system. *Int J Med Robot.* 2007; 3(2):125–134.
35. Torabi M, Gupta R, Walsh CJ. Compact robotically steerable image guided instrument for multi-adjacent-point (MAP) targeting. *IEEE T Robot.* 2014; 30(4):802–815.
36. Van de Berg NJ, Dankelman J, Van den Dobbelsteen JJ. Design of an actively controlled steerable needle with tendon actuation and FBG-based shape sensing. *Med Eng Phys.* 2015; 37(6):617–622.
37. Wang YZ, Yin QL, Liu CL. Towards an articulated needle. *Appl Mech Mater.* 2012; 152:946–951.
38. Wang YZ, Zhou ZG, Chen YH. Towards a magnetic articulated needle. *Adv Materials Res.* 2012; 393:1060–1063.
39. Webster RJ, Okamura AM, Cowan NJ. Toward active cannulas: miniature snake-like surgical robots. In: Proceedings of the 2006 IEEE/RSJ International Conference on Intelligent Robots and Systems (IROS), 2006 Oct 9–15; Beijing, China. New York: IEEE; pp.2857–2863.
40. Yan K, Podder T, Ng WS. Smart needle for percutaneous surgery: influential factor investigation. In: Proceedings of the 2007 29th annual international conference of the IEEE engineering in medicine and biology society (EMBC); 2007 Aug 22-26; Lyon, France. New York: IEEE; p.461–464.
41. York AP, Swaney PJ, Gilbert HB. A wrist for needle-sized surgical robots. In: Proceedings of the IEEE international conference robotics and automation; 2015 May 26–30; Seattle, WA. New York: IEEE; pp.1776–1781.
42. Arramon YP . Bone access system. Patent 20060064101 A1, USA, 2006.
43. Arvanaghi B . Bendable needle assembly. Patent 20080097347 A1, USA, 2006.
44. Brockman CS, Harshman GJ. Systems and method for off-axis tissue manipulation. Patent 20130345765 A1, USA, 2013.

45. Burger K, Cheatwood J, Chen S. Steerable curvable vertebroplasty drill. Patent 20140316413, USA, 2014.
46. Desai JP, Ayvali E. Actuated steerable probe and system and methods of using same. Patent 20130296885, USA, 2013.
47. Eck K. Surgical needle and methods of guiding surgical needle. Patent 20090177151, USA, 2009.
48. Germain A. System for use in treatment of vertebral fractures. Patent 20100082033 A1, USA, 2010.
49. Kaplan EJ. Deflectable implantation device and method for use. Patent 20080091056, USA, 2008.
50. Kraft D, Hole J. Device and method for rapid aspiration and collection of body tissue from within enclosed body space. Patent 200701544460, USA, 2007.
51. Krueger JA, Linderman ED. Device system and method for delivering a curable material into bone. Patent 200701118142 A1, USA, 2007.
52. Kuhle WG. Biopsy needle with flared tip. Patent 5938635 A, USA, 1999.
53. Liu YK, Lau JR, Threlkeld JE. Closed vertebroplasty bone cement injection system. Patent 20090131945 A1, USA, 2009.
54. Mathis M, Thompson, D Addis B. Steerable device for accessing a target site and methods. Patent 200601674416, USA, 2006.
55. Mehta VM, Lipford BL, Schneider E. Arthroscopic tunnel guide for rotator cuff repair. Patent 20130345711 A1, USA, 2013.
56. Melsheimer JS. Deflectable biopsy device. Patent 20120220894 A1, USA, 2012.
57. Pellegrino R, Smith P, Harold C. System and methods for navigating an instrument through bone. Patent 2011085212 A2, USA, 2011.
58. Rodriguez y Baena, FM, Frasson, L. Steerable probes. Patent 20120279325 A1, USA, 2012.
59. Ryan TJ, Winslow CJ. Percutaneous discectomy system having a bendable discectomy probe and a steerable cannula. Patent 5285795, USA, 1994.
60. Salcudean SE, Rohling RN, Okazawa, SH. Steerable needle. Patent 20040133168, USA, 2004.
61. Smits KFAA, Rutten JJC, Adams PG. Method and apparatus for imparting curves in implantable elongated medical instruments. Patent 20030130712, USA, 2003.
62. Swaney PJ, Webster RJ. Steerable surgical needle. Patent 20140276586 A1, USA, 2014.
63. Webster RJ, Okamura AM, Cowan NJ. Active cannula for bio-sensing and surgical intervention. Patent 20130018303 A1, USA, 2013.
64. Reed KB, Majewicz A, Kallem V. Robot-assisted needle steering. *IEEE Robot Autom Mag.* 2011; 18(4):35–46.
65. Swensen JP, Lin M, Okamura AM. Torsional dynamics of steerable needles: modeling and fluoroscopic guidance. *IEEE Trans Biomed Eng.* 2014; 61(11):2707–2717.
66. Minhas DS, Engh JA, Fenske MM. Modeling of needle steering via duty-cycled spinning. In: *Proceedings of the 2007 29th annual international conference of the IEEE engineering in medicine and biology society (EMBC); 2007 Aug 22-26; Lyon, France.* New York: IEEE; pp.2756–2759.
67. Engh JA, Podnar G, Kondziolka D. Toward effective needle steering in brain tissue. In: *Proceedings of the 2006 28th annual international conference of the IEEE engineering in medicine and biology society (EMBC), 2006 Aug 30 – Sept 3; New York, USA.* New York: IEEE; pp.559–562.
68. Webster RJ, Kim JS, Cowan NJ. Nonholonomic modeling of needle steering. *Int J Robot Res.* 2006; 25(5–6):509–525.
69. Smuck M, Andrew JY, Tang CT. Influence of needle type on the incidence of intravascular injection during transforaminal epidural injections: a comparison of short-bevel and long-bevel needles. *Spine J.* 2010; 10(5):367–371.

70. Wedlick TR, Okamura AM. Characterization of pre-curved needles for steering in tissue. In: Proceedings of the 2007 31th annual international conference of the IEEE engineering in medicine and biology society (EMBC); 2009 Sept 3–6; Minneapolis, MN, USA. New York: IEEE; pp.1200–1203.
71. Frasson L, Ferroni F, Ko SY. Experimental evaluation of a novel steerable probe with a programmable bevel tip inspired by nature. *J Robot Surg.* 2012; 6(3):189–197.
72. Van Gerwen DJ, Dankelman J, Van den Dobbelsteen JJ. Needle–tissue interaction forces—a survey of experimental data. *Med Eng Phys.* 2012; 34(6):665–680.
73. Misra S, Reed KB, Andrew SD. Needle-tissue interaction forces for bevel-tip steerable needles. In: Proceedings of the 2nd IEEE RAS & EMBS international conference on biomedical robotics and biomechatronics (BioRob); 2008 Oct 19–22; Scottsdale, AZ, USA. New York: IEEE; pp.224–231.
74. Van Veen YR, Jahya A, Misra S. Macroscopic and microscopic observations of needle insertion into gels. *Proc Inst Mech Eng H.* 2012; 226(6):441–449.
75. Konh B, Honarvar M, Hutapea P. Design optimization study of a shape memory alloy active needle for biomedical applications. *Med Eng Phys.* 2015; 37(5):469–477.
76. Majewicz A, Marra SP, Van Vledder MG. Behavior of tip-steerable needles in ex vivo and in vivo tissue. *IEEE Trans Biomed Eng.* 2012; 59(10):2705–2715.
77. Osseon, <http://www.osseon.com/osseoflex-sn-steerable-needle/> (accessed 21 July 2016).
78. AprioMed, <http://apriomed.com/products/morrison-steerable-needle/9292/> (accessed 21 July 2016).
79. Cook Medical, https://www.cookmedical.com/products/ir_dchncs_webds/ (accessed 21 July 2016).
80. Morrison WB, Akerfeldt D. Steerable medical puncture instrument. Patent 20120136381 A1, USA, 2012.
81. Pakter RL, Morris EJ. Hollow, curved, superelastic medical needle. Patent 6592559 B1, USA, 2003.
82. Gluzman D, Shoham M. Image-guided robotic flexible needle steering. *IEEE T Robot.* 2007; 23(3):459–467.
83. Neubach Z, Shoham M. Ultrasound-guided robot for flexible needle steering. *IEEE T Bio-med Eng.* 2010; 57(4):799–805.
84. Reed KB, Kallem V, Alterovitz R. Integrated planning and image-guided control for planar needle steering. In: Proceedings of the 2nd IEEE RAS & EMBS international conference on biomedical robotics and biomechatronics (BioRob); 2008 Oct 19–22; Scottsdale, AZ, USA. New York: IEEE; pp.819–824.
85. Alterovitz R, Goldberg K, Okamura A. Planning for steerable bevel-tip needle insertion through 2D soft tissue with obstacles. In: Proceedings of the IEEE international conference on robotics and automation, 2005 Apr 18–22; Barcelona. New York: IEEE; pp.1652–1657.
86. Misra S, Ramesh K, Okamura AM. Modeling of tool-tissue interactions for computer-based surgical simulation: a literature review. *Presence* 2008; 17(5):463–491.
87. Sakes A, Dodou D, Breedveld P. Buckling prevention strategies in nature as inspiration for improving percutaneous instruments: a review. *Bioinspir Biomim.* 2016; 11(12):021001.

Chapter 3

Ovipositor-Inspired Steerable Needle: Design and Preliminary Experimental Evaluation

Published as:

Scali M*, Pusch TP*, Breedveld P, Dodou D. Ovipositor-inspired steerable needle: design and preliminary experimental evaluation, *Bioinspiration & Biomimetics*. 2017; 13(1):016006. <https://doi.org/10.1088/1748-3190/aa92b9>

© IOP Publishing. Reproduced with permission. All rights reserved.

*Authors contributed equally to the realization of this paper

ABSTRACT

Flexible steerable needles have the potential to allow surgeons to reach deep targets inside the human body with higher accuracy than rigid needles do. Furthermore, by maneuvering around critical anatomical structures, steerable needles could limit the risk of tissue damage. However, the design of a thin needle (e.g., diameter under 2 mm) with a multi-direction steering mechanism is challenging. The goal of this paper is to outline the design and experimental evaluation of a biologically inspired needle with a diameter under 2 mm that advances through straight and curved trajectories in a soft substrate without being pushed, without buckling, and without the need of axial rotation. The needle design, inspired by the ovipositor of parasitoid wasps, consisted of seven nickel titanium wires and had a total diameter of 1.2 mm. The motion of the needle was tested in gelatine phantoms. Forward motion of the needle was evaluated based on the lag between the actual and the desired insertion depth of the needle. Steering was evaluated based on the radius of curvature of a circle fitted to the needle centerline and on the ratio of the needle deflection from the straight path to the insertion depth. The needle moved forward inside the gelatine with a lag of 0.21 (single wire actuation) and 0.34 (double wire actuation) and achieved a maximum curvature of 0.0184 cm^{-1} and a deflection-to-insertion ratio of 0.0778. The proposed biologically inspired needle design is a relevant step towards the development of thin needles for percutaneous interventions.

3.1. INTRODUCTION

Medical needles are commonly used in percutaneous procedures, where accurate and precise tissue targeting is required to obtain diagnostic samples [1, 2], position radioactive seeds [3, 4], and deliver drugs [5, 6]. Needle placement can be affected by several factors, such as needle deflection due to needle-tissue interaction, organ movement due to physiological processes (e.g., breathing), and human error [7]. If the needle is misplaced, intraoperative adjustment of the needle path or reinsertion of the needle is necessary, which could increase the risk and extent of tissue damage and the intervention time.

While rigid needles allow for small adjustments around a straight path, flexible steerable needles can follow curved trajectories, which might improve accuracy and precision in reaching target tissues [8]. Moreover, flexible steerable needles are likely to limit the risk of tissue damage by maneuvering around critical anatomical structures (e.g., blood vessels) that are laid along the needle trajectory towards the target.

3.1.1. Steerable needle mechanism

Several steerable needle designs and mechanisms have been described in the literature (for a review see [9]). Two main methods for steering can be distinguished: steering due to a pre-defined needle shape and due to a means of actuation.

Bevel-tip needles [10–13] and pre-curved needles [14, 15] are examples of needles with a pre-defined shape. When a bevel-tip needle is inserted into the tissue, off-axis reaction forces at the tip bend the needle in the direction of the bevel [16, 17]. The curvature of the needle is usually controlled by rotating the needle while it is advanced through the tissue [18]. Several variations of bevel-tip needles have been proposed in order to increase the maximum curvature of the needle. For example, Swaney et al. [10] presented a bevel-tip needle with a flexure joint that is thinner than the needle body, and Wang et al. [12] added articulations along the body of a bevel-tip needle, with both modifications allowing for a larger deflection of the needle upon insertion in the tissue than a standard bevel-tip needle. Another way to increase the steering curvature is by increasing the diameter of the tip with respect to the diameter of the body which leads to a larger contact area with the tissue compared to a standard bevel-tip needle [13]. Also in pre-curved needles off-axis reaction forces are generated at the tip by the surrounded tissue, causing the needle to bend upon insertion into the tissue. Pre-curved needles commonly consist of a pre-curved stylet (internal tube) and a straight cannula (external tube) [14]. The needle follows a straight direction when the stylet is fed through the cannula and curves once the stylet is pushed forward. Notches of different shapes and dimensions have been added to the pre-curved stylet in order to increase the flexibility and hence the steering curvature [19]. Needle designs with both the stylet and the

cannula pre-curved [20] or with a pre-curved stylet bearing a bevel-tip [21] are two other variations used to achieve a high curvature. Steering in multiple directions is achieved by rotating the needle shaft around its axis. Multiple pre-curved tubes can be also arranged in a telescopic way, creating a so-called “active cannula” [22], where the final curvature is a result of the amount of rotation and extension provided by each of the tubes. A hybrid approach was presented by Bui et al. [23], where the needle consists of a straight cannula and a straight stylet with a bevel-tip. In this case, the amount of steering is a function of the offset between the bevel-tip and the cannula.

3 An example of needles that steer due to a means of actuation are tendon-driven needles [24–26]. Tendon-driven needles use a mechanical actuation means (e.g., cables) to deflect the tip and draw a curved path. Van de Berg et al. [24] presented a tendon-actuated flexible needle that steers by means of four cables running over a ball joint placed near the tip. Adebar et al. [26] used Nitinol pull wires and a miniaturized cable pulley to actuate a flexural conical tip. Shape-memory or pseudoelastic materials have also been used as actuation means for needle steering [27, 28]. For example, Ayvali et al. [27] described a needle made out of segments interconnected by shape memory alloy wires that deflect in response to Joule heating. Konh et al. [28] used an SMA-wire to connect the body of the needle with a bevel-tip. The wire is used to control the deflection angle of the needle. In the design of Yan et al. [29] the deflection of the needle is controlled by piezoelectric actuators. These are placed on the external surface of the needle, and by applying an electrical field a longitudinal strain is induced, resulting in deflection of the needle.

Despite the potential of flexible steerable needles, some functional limitations can also be identified. Needles with a predefined shape mostly steer in 2D with a constant radius, meaning that for steering in 3D with a variable radius, axial rotation of the needle is needed. Rotating a needle while it is being advanced through the tissue can generate a torsional stress on the needle body. This may in turn result in angular lag between the orientation of the needle base and the needle tip, making the control of the needle trajectory difficult [30, 31]. Actuated needles do allow for steering in 3D without axial rotation, but actuating elements requires space, inhibiting the miniaturization of this type of needles. Moreover, both in needles with predefined shape and actuated needles, buckling can occur when they are pushed deep into the tissue, which compromises their structural integrity and the safety of the medical procedure [32].

3.1.2. Biological inspiration for steerable needles

In nature, several species of parasitoid wasps possess a thin and flexible needle-like structure, called ovipositor, which is used to deposit eggs in a host (e.g., a larva) hidden into tree trunks (e.g., the wasp species *Megarhyssa atrata* [33]) or fruits (e.g., the wasp species *Apocrypta*

westwoodi [34]) (Figure 3.1a). The wasp ovipositor holds promise as a biological paradigm for medical needles, as it avoids buckling despite the fact that it is long and thin (with an aspect ratio higher than 200 in some species [35]) and is presumably able to steer in 3D without axial rotation.

The wasp ovipositor consists of three longitudinal segments called valves: two ventral valves and one dorsal valve. The valves are mechanically interlocked by means of a jigsaw-puzzle-like mechanism, called olistheter, but can still slide along each other, actuated by abdominal musculature (Figure 3.1c) [36]. The wasp advances the ovipositor through the substrate by moving the valves antagonistically: one ventral valve is advanced forward at a time, while the other ventral valve and the dorsal valve are standing still or pulled backwards. Directional serrations at the ovipositor tip allow the stationary/pulled backwards valves to anchor against the substrate [37] (Figure 3.1b). The created pretension in the ovipositor and friction against the substrate compensates for the dynamic friction force along the advancing valve and the forces at the tip of the valve, thereby preventing buckling of the ovipositor [35].

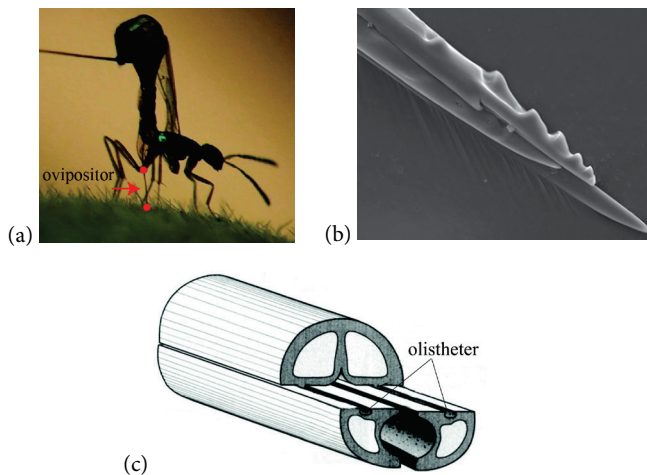


Figure 3.1. (a) Parasitoid wasp (*Apocrypta westwoodi*) ovipositing in a fig. Adapted with permission from [34]. (b) Scanning electron micrograph (SEM) showing the morphology of the ovipositor tip, with visible serrations on the surface. Adapted with permission from [34]. (c) Schematic representation of the ovipositor, with valves differentially protruding, held together by jigsaw-puzzle-like olistheter. Adapted with permission from [36].

Next to buckling prevention and advancement of the ovipositor along a straight path, the wasp is presumably also able to steer the ovipositor along 3D-curved trajectories. Several hypotheses aiming to explain the steering mechanism of the wasp ovipositor have been proposed [38–40]. According to one prevailing hypothesis, steering motion is achieved by

selectively advancing the valves, thereby creating an offset at the tip, which, due to its beveled shape and off-axis reaction forces applied on it by the surrounding substrate, deflects [40].

The mechanism used by the wasp for advancing and steering inside solid substrates has inspired the design of a variety of devices, ranging from planetary and earth drills [41] to medical needles and probes [42]. Over the last decade, Rodriguez y Baena and coworkers have developed and tested a series of medical needles and probes inspired by the wasp ovipositor. Specifically, the steerable probe described by Frasson et al. [42] consists of four segments connected with a jigsaw-puzzle interlocking mechanism similar to the olistheter in the wasp ovipositor. Each of the segments has a bevel-tip, so that when the segments are aligned, the needle tip has a conical shape. The segments are actuated independently from each other. First, one of the segments is moved forward, and due to off-axis reaction forces at the segment tip from the substrate, the segment deflects in the direction of the bevel. Then, the other segments are advanced, following the curved trajectory laid out by the first segment. The curvature of the probe can be controlled by changing the offset between the segment that is protruded and the rest of the probe, a steering principle called “programmable bevel-tip” [43, 44]. Frasson et al. [44] experimentally demonstrated that there is a linear relationship between the offset and the steering curvature, and that for a probe with a larger diameter a larger offset is needed in order to achieve the same curvature as with a smaller probe. Extensive work has been also done on the optimization of the probe in terms of the geometry of the interlocking mechanism [45–47] and the surface topography of the probe [48–51]. Specifically, it was found that a small fin- or tooth-like outer-surface topography make the needle insertion easier compared to the use of smooth surfaces, while providing large gripping forces when the needle is retracted [48, 49]. The insertion into tissue by reciprocal motion of the segments has been tested [52–54], the probe-tissue interaction has been simulated with finite element methods [55], and control strategies for steering in three dimensions have been investigated [56]. A series of prototypes have been presented, with diameters of 12 mm [57], 8 mm [58], and 4 mm [59]. It was found that forward motion through soft substrates by means of reciprocal motion of the segments of the probe is possible, albeit limited to certain types of substrate materials, such as muscle and agar gel. In this case, teeth on the probe surface have been used to enable forward motion [52]. It has been further shown that reciprocal insertion could result in less tissue disruption and less target displacement than direct pushing of probe would cause [54, 60].

Sprang et al. [61] presented an ovipositor-inspired needle consisting of four rigid longitudinal square segments and a total thickness of 2 mm that was advanced through gelatine with zero external pushing force. Sprang et al.’s prototype did not bear serrations; instead, the dynamic friction force along the advancing segment and the force at the segment tip was compensated by the difference in contact area between the stationary and advancing

segments. Only forward motion was investigated; the prototype was not designed for steering. Moreover, Sprang's needle did not contain an interlocking mechanism to hold the segments together; this design choice was due to difficult miniaturization of the required jigsaw-puzzle profiles. The lack of interlocking led to bifurcation of the four segments during propagation of the needle through the gel.

3.1.3. Aim

This work builds upon the existing studies on ovipositor-inspired steerable needles and probes and proposes a new design approach in order to develop a needle that uses a push-pull mechanism during both forward motion and steering. The needle steers without the need for axial rotation and has a diameter suitable for core needle biopsy and brachytherapy treatments. Specifically, we aimed for a needle diameter under 2 mm, that is, approximately 14 Gauge (G), considering that needles commonly used in core needle biopsy and brachytherapy have diameters of 14–19 G [62] and 17–18 G [63], respectively. We first present the design of the needle, followed by an experimental evaluation of the forward motion and steering performance of the needle. A preliminary version of this work has been briefly reported in [64].

3.2. NEEDLE DESIGN

3.2.1. Conceptual design

Shape of longitudinal segments

A direct technical analogue of the wasp ovipositor would be a needle consisting of four wedge-shaped sections arranged in such a way that altogether they form a circle. However, manufacturing long and well aligned wedge-shaped sections in small dimensions is technically challenging [46]. One way to bypass this issue is by reasoning that the wedge-shaped sections can be approximated by a set of cylindrical sections arranged in such a way that altogether they approximate a circle. Following this line of reasoning, we decided to use off-the-shelf round flexible metal wires as longitudinal segments (Figure 3.2).

Number of longitudinal segments

Choosing the number of wires is an optimization process between the number of steering directions, slip during forward motion, total diameter of the needle, and bending stiffness. Steering can be induced by selectively moving one or more of the wires forward, thereby creating radial asymmetry at the needle tip. The steering direction and angle can be varied by choosing different combinations of wires to protrude and different offsets. Theoretically,

omnidirectional steering is possible with a minimum of four wires; however, increasing the number of wires allows for a larger number of steering directions. With respect to slip during forward motion, it has been previously shown that the higher the ratio between the number of stationary and moving longitudinal segments, the lower the slip [61], thereby the smaller the lag between the actual and desired insertion depth. In other words, a larger number of wires allows for a larger number of steering directions and for lower slip in forward motion. On the other hand, for a constant diameter of the wires, the diameter and bending stiffness of the needle increases with the number of wires. Moreover, a larger diameter implies greater invasiveness of the medical procedure and more tissue damage.

In our study, we selected the number of wires that would allow us to investigate whether forward motion and steering of a needle consisting of multiple untreated wires (i.e., no bevel-tip or microtextured surface) is viable. A total of five wires would have been enough to create an asymmetry between advancing wires while maintaining a ratio of stationary to advancing wires greater than one. However, in order to allow steering in two perpendicular planes, we opted for six wires, concentrically arranged around a seventh central stabilizing wire (Figure 3.2).

Interlocking mechanism

As mentioned in Section 3.1.2, the ovipositor valves are interlocked by the olistheter, a jigsaw-puzzle like structure, which allows the valves to slide along each other, avoiding their separation. Frasson et al. [46] and Burrows et al. [59] used a similar structure in their $\text{\O}12$ mm and $\text{\O}4$ mm prototypes. However, miniaturization of such a complex interlocking mechanism is challenging from a manufacturing perspective. To develop a needle with a diameter under 2 mm, we decided to step away from nature and to interlock the wires externally using an interlocking ring with seven holes through which the wires are fed. We adjusted the ring shape to a flower-shape to reduce the resistance with the substrate (Figure 3.2).

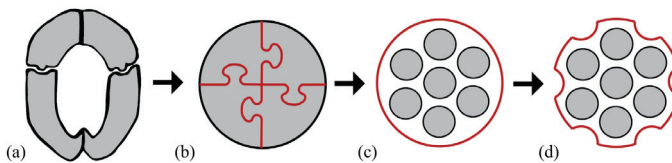


Figure 3.2. Conceptual design process. (a) Cross-section of the ovipositor with two ventral valves and one dorsal valve. Adapted with permission from [65]. (b) Four wedge-shaped sections (gray) that approximate the ovipositor valves interlocked by means of jigsaw-puzzle profiles (red) mimicking the olistheter. Based on [46]. (c) Simplified mechanism with seven flexible wires (gray) with a round-shape interlocking ring (red). (d) Seven flexible wires (gray) with a flower-shaped ring around them (red).

3.2.2. Needle prototype

The ovipositor-inspired needle prototype consists of seven superelastic nickel titanium (NiTi) wires with a diameter of 0.25 mm and a length of 160 mm. The diameter of 0.25 mm was chosen as it was the smallest available for the material characteristics required (i.e., straightened NiTi wires). Six wires can slide independently from each other along the length of the needle and are concentrically arranged around the seventh wire, which is fixed at the needle base. The wires are straight at room temperature and have a smooth surface.

Two types of rings are used to hold the wires together: the flower-shaped interlocking ring and five standard rings (Figure 3.3). The flower-shaped interlocking ring (aluminum, $\text{Ø}1.2$ mm, 2.0 mm long) aligns the wires and keeps them together. The ring has seven holes through which the wires are fed: one central hole and six outer holes arranged in a circle with a radius of 0.38 mm. The central wire is glued to the central hole, whereas the six outer wires can slide through the outer holes. The diameter of the holes is 0.3 mm, letting the 0.25-mm wires move freely inside the ring.

In order to avoid buckling of individual wires during the actuation and to keep all the wires together along the full length of the needle, five stainless steel rings ($\text{Ø}_{\text{in}} 0.9$ mm, $\text{Ø}_{\text{out}} 1.0$ mm, 2.0 mm long), uniformly spaced between the base of the needle, are used. The total diameter of the needle is 1.2 mm at the tip, which corresponds to the outer diameter of the interlocking ring. The body of the needle has a diameter of 0.75 mm.

Each of the six movable wires is connected to a slider that is moved backward and forward by a bipolar stepper motor AM0820 with step angle 18° (Faulhaber, Germany) in conjunction with a leadscrew (M2, 28 mm long). The stepper motors and leadscrews are placed in an aluminium housing. A stepper motor combined with a leadscrew-slider mechanism was chosen, in order to achieve a linear motion of the wires. Linear motion could have also been achieved by means of linear actuators, but those are usually bulky. The maximum travel distance of each slider and thus of the needle wires is 20 mm. The six stepper motors are actuated using six stepper drivers DRV8834 (Texas Instruments, TX) and an Arduino MEGA 2560 micro-controller.

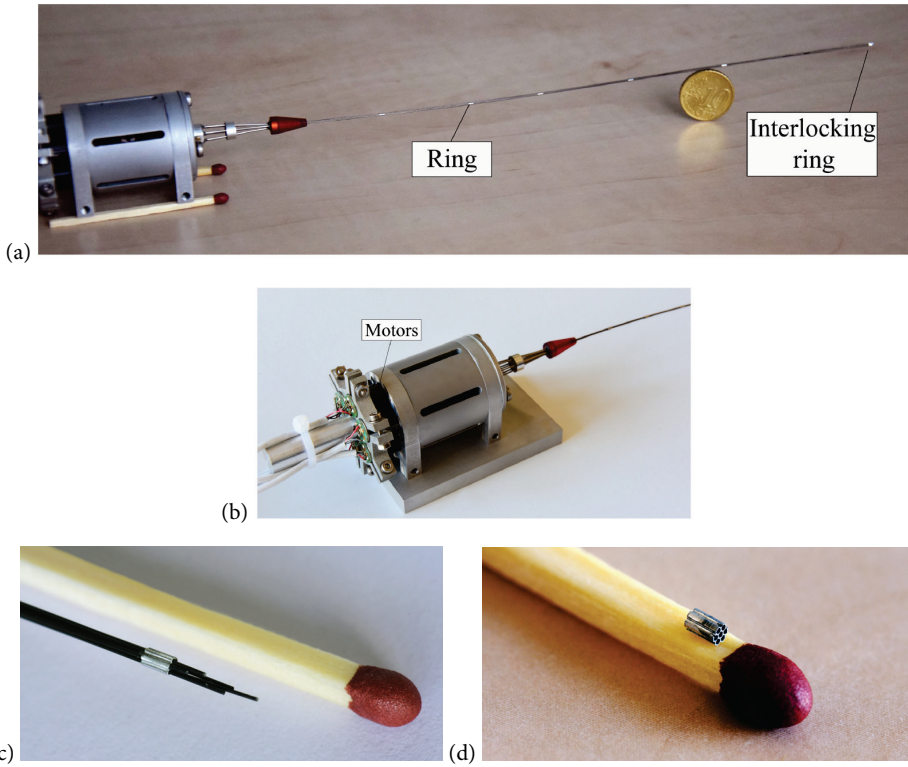


Figure 3.3. (a) Ovipositor-needle prototype with the actuation unit, wires, five rings, and a flower-shaped interlocking ring at the tip. (b) Close-up of the actuation unit. (c) Close-up of the tip of the needle with the flower-shaped ring and some of the wires moved forward. (d) Close-up of the flower-shaped interlocking ring ($\text{Ø}1.2 \text{ mm}$).

3.2.3. Forward motion and steering of the needle

Forward motion

The needle is moved forward through the substrate by first pushing the six wires one-by-one or two-by-two, followed by pulling on all six wires simultaneously, which advances the interlocking ring and the central wire into the substrate. This two-phase motion sequence will henceforth be referred to as a “cycle”.

Figure 3.4 shows the forces acting on the needle prototype during the forward motion. Assume the general case in which m wires move forward and n wires are stationary. The motion of a single wire can be expressed as the sum of the external force \mathbf{F}_{ext} (i.e., pushing), the friction force along the length of the wire in contact with the substrate $\mathbf{F}_{\text{wire,fric}}$, the cutting force acting at the tip $\mathbf{F}_{\text{wire,cut}}$, and the static friction between the interlocking ring and the substrate $\mathbf{F}_{\text{ring,stat}}$.

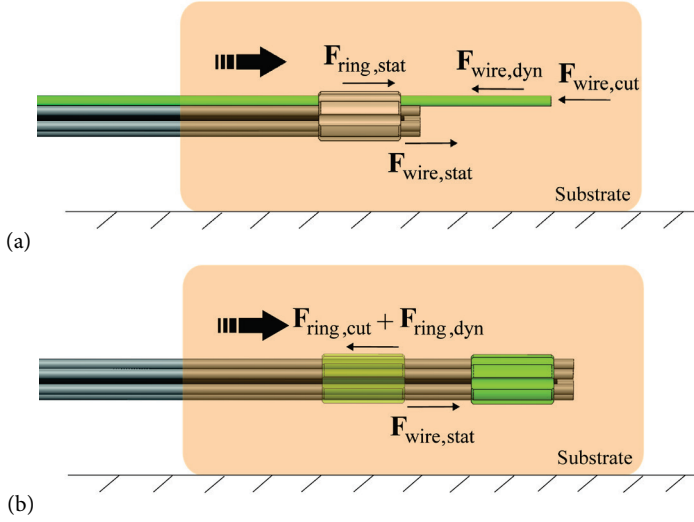


Figure 3.4. Schematic representation of the forward motion mechanism of a needle with six peripheral wires and one central wire. (a) First, one wire is pushed forward at the time (green). (b) After all six peripheral wires have been moved forward one-by-one, they are pulled back simultaneously, resulting in advancement of the ring and the central wire inside the substrate. The thick arrow represents the motion of the wires and the ring.

If we consider a total of $m + n$ wires, using the Newton's second law we get:

$$\sum_{i=1}^{m+n} (\mathbf{F}_{ext,i} + \mathbf{F}_{wire,fric,i} + \mathbf{F}_{wire,cut,i}) + \mathbf{F}_{ring,stat} = \sum_{i=1}^{m+n} m_{wire,i} \mathbf{a}_{wire,i} \quad (3.1)$$

Where m_{wire} is the mass of the wire and \mathbf{a}_{wire} is its acceleration. As shown in previous studies [53, 61] the needle can move forward with a zero net external force ($\sum \mathbf{F}_{ext} = 0$) or (even) a net pulling force ($\sum \mathbf{F}_{ext} < 0$):

$$\begin{aligned} \sum_{i=1}^{m+n} \mathbf{F}_{ext,i} = & - \sum_{i=1}^m (\mathbf{F}_{wire,dyn,i} + \mathbf{F}_{wire,cut,i}) - \sum_{i=1}^n \mathbf{F}_{wire,stat,i} - \mathbf{F}_{ring,stat} \\ & + \sum_{i=1}^{m+n} m_{wire,i} \mathbf{a}_{wire,i} \leq 0 \end{aligned} \quad (3.2)$$

Where $\mathbf{F}_{wire,dyn}$ is the dynamic friction force acting on the moving wire, and $\mathbf{F}_{wire,stat}$ is the static friction force acting on the static wires; there are no forces acting at the tip of the static wires. Assuming that the inertia term is negligibly small, and in order for the m wires to move forward, the sum of the dynamic friction force and the cutting force of the wires moving forward should be smaller than the static friction force of the n stationary wires and the interlocking ring, that is:

$$-\sum_{i=1}^m (\mathbf{F}_{\text{wire,dyn},i} + \mathbf{F}_{\text{wire,cut},i}) \leq \sum_{i=1}^n \mathbf{F}_{\text{wire,stat},i} + \mathbf{F}_{\text{ring,stat}} \quad (3.3)$$

In the second phase of the actuation cycle, in which all $m + n$ wires are pulled simultaneously, the cutting and dynamic friction force of the advancing interlocking ring should be compensated by the static friction force between the wires and the substrate, that is:

$$\mathbf{F}_{\text{ring,cut}} + \mathbf{F}_{\text{ring,dyn}} \leq \sum_i^{m+n} \mathbf{F}_{\text{wire,stat},i} \quad (3.4)$$

where $\mathbf{F}_{\text{ring,cut}}$ and $\mathbf{F}_{\text{ring,dyn}}$ are the cutting force and the dynamic friction force of the interlocking ring, respectively. By repeating this actuation cycle, the needle advances inside the substrate. If any of the two inequalities is not satisfied, the needle slips.

Steering

Each needle wire has a flat (rather than bevel) tip, therefore the first step for steering is to generate an asymmetry at the needle tip. This is done by inducing an offset (henceforth called bevel offset, BO) between a pair of adjacent needle wires. We call this configuration “discrete bevel-tip”, since it is a tip made out of multiple single segments that approximate a bevel-tip (Figure 3.5c). With a discrete bevel-tip it is possible to create various bevel angles. For example, by moving a wire forward over an offset BO_1 a bevel angle a_1 is generated (Figure 3.5h), whereas by moving a wire over an offset $BO_2 > BO_1$ a bevel angle $a_2 < a_1$ is generated (Figure 3.5i). Steering could be achieved with the following actuation scheme. First, a BO is set between two adjacent wires, and this discrete bevel-tip is advanced to a predefined distance (henceforth called stroke, S), deflecting and laying a curved path in the substrate. Next, a BO is set between the two adjacent wires that are consecutive to the first pair of wires, and this second discrete bevel-tip is advanced for S , reinforcing the curved path laid by the first pair. Then, the remaining two wires are advanced over S , following the curved path laid by the other two pairs (Figure 3.5). Finally, all six wires are pulled simultaneously backwards, so that the seventh (central) wire and the interlocking ring move forward along the curved trajectory. The steering direction is determined by the pair of wires used to form the discrete bevel-tips. For example, steering to the left is achieved by creating a discrete bevel-tip between wires 1 and 6 (with wire 6 protruding by a distance BO with respect to wire 1) and a second discrete bevel between wires 4 and 5 (with wire 5 protruding by a distance BO with respect to wire 4) (Figure 3.5). Similarly, steering to the right is achieved by creating a discrete bevel-tip between wires 1 and 2 and a second bevel-tip between wires 3 and 4.

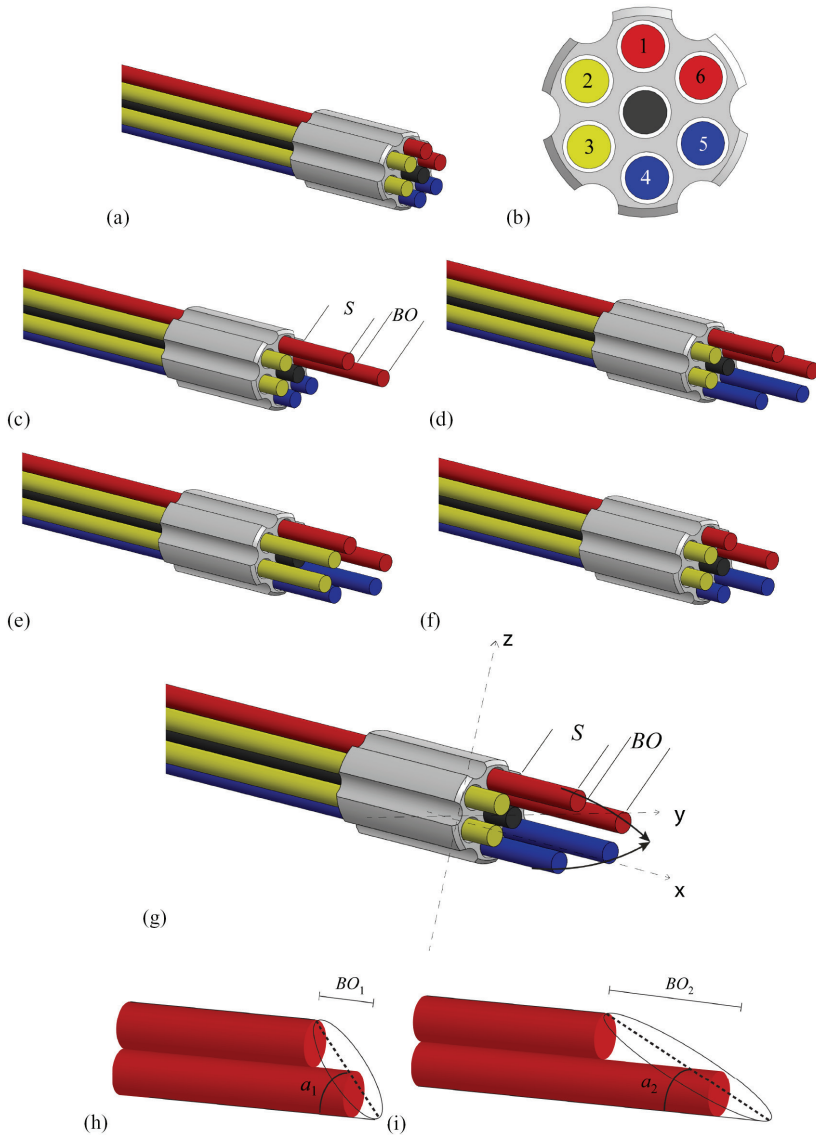


Figure 3.5. (a) Initial position of the wires. (b) Cross-section of the needle. (c)–(f) Steps of the actuation cycle. Steering to the left is achieved by creating a first discrete bevel between wires 1–6 (red), with wire 6 protruding by bevel offset (BO) with respect to wire 1. (c) The two wires are then advanced to the desired stroke (S). (d) A second discrete bevel is created between wires 5–4 (blue), with wire 5 protruding with the same BO and moves for S . (e) Wires 3–2 are then pushed forward for S (yellow). (f) Lastly, all six wires are pulled to let the ring advanced. (g) Schematic representation of the needle tip showing the steering mechanism. (h) Discrete bevel-tip with angle a_1 and BO_1 . (i) Discrete bevel-tip with angle a_2 and BO_2 . In this example, $BO_2 > BO_1$. A large BO corresponds to a small angle, that is, $a_2 < a_1$.

3.3. MATERIALS AND METHODS

The performance of the needle prototype was evaluated in two experiments. In experiment 1 we evaluated the performance of the prototype in forward motion, and in experiment 2 we evaluated the steering performance. The experimental setup was the same for both experiments.

3.3.1. Experimental setup

The experimental setup consisted of the actuation unit as described in Section 3.2, a test rig, and data acquisition systems (Figure 3.6a). The actuation unit was mounted on an aluminum base plate using four bolts. A lightweight aluminum cart (210 × 50 mm, 28 g) mounted to four wheels was designed to carry a gelatine phantom (Dr. Oetker).

The gelatine phantoms were prepared by mixing gelatine powder with water heated at 70–80 °C. The liquid gelatine was poured into containers and stored overnight at 5 °C. A new batch of gelatine was prepared for each day of the experiments. A gelatine block of 50 × 170 × 30 mm (width × length × height) was cut and placed on the cart for each experimental trial.

An alignment ring (aluminum, Ø 3.0 mm, 2.0 mm long) was added to the body of the needle and fixed to the cart (Figure 3.6b). The alignment ring contained seven holes and had an asymmetric cross-section to ensure that the needle was radially aligned along its length. The wires could freely slide through the seven holes of the alignment ring.

In our experiments, instead of moving the needle and its actuation unit toward the gelatine cart, the actuation unit was fixed; actuating the needle resulted in moving the gelatine cart toward the actuation unit. The rolling motion of the four wheels was laterally constrained by a groove in the base plate, and the rolling friction of the wheels was negligible. A millimeter graph paper was placed at the bottom surface of the cart to give a reference to the needle deflection during the experiments. A laser proximity sensor (MicroEpsilon optoNCDT1302-200, range: 200 mm, resolution: 0.1 mm) was used to record the position of the cart. The laser sensor data were collected using a data acquisition unit (NI USB-6211, 16-bit) in conjunction with LabVIEW 2013 at a sampling frequency of 5 Hz.

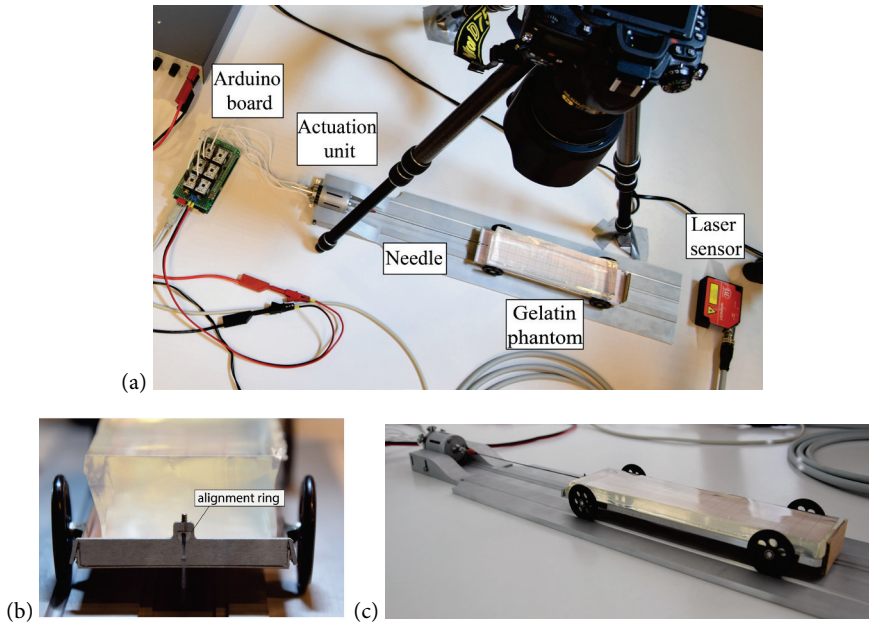


Figure 3.6. (a) Experimental setup for the evaluation of the needle prototype performance. The actuation unit is mounted on an aluminum base plate. The needle moved forward and steered into a gelatine phantom carried by a lightweight aluminum cart. A laser proximity sensor was used to record the position of the cart. (b) Side view of the cart loaded with gelatine. (c) Close-up of the point of entrance of the needle in the gelatine phantom, showing the alignment ring fixed to the cart.

Next to the recording of the position of the cart, in experiment 2 the experimental trials were recorded using a video camera (HC-V250, Panasonic, Osaka, Japan). Moreover, at the end of each experimental trial of experiment 2 a top-down view photograph of the needle inside the gelatine phantom was taken with a camera (Nikon D750, Tokyo, Japan) mounted on a tripod, in order to define the final curvature of the needle. The position of the camera was calibrated with a spirit level to ensure that it was orthogonal to the table where the needle and the cart were placed.

For all experimental trials of both experiments, 4% weight of gelatine powder in water was used. A Young's modulus of 4.65 kPa was measured for this gelatine phantom by means of dynamic mechanical analysis (PerkinElmer Instruments, amplitude = 40 μm , frequency = 1 Hz, parallel plate geometry with 20 mm diameter), which corresponds to brain tissue elasticity (2.7–5 kPa [66]). The combined weight of the cart and gelatine phantom was kept constant for all trials (mean = 214.66 g, standard deviation = 1.69 g). The needle segments were actuated at a speed of 2 mm s^{-1} . The total number of cycles executed by the Arduino software was chosen to result in a theoretical needle insertion depth of 120 mm in

all experimental trials of both experiments. Each trial was conducted with a specific stroke (see Section 3.3.2 and Section 3.3.3), and during each actuation cycle the wires were moved forward over that stroke. The number of cycles equaled the ratio of 120 mm over the stroke.

3.3.2. Experiment 1—forward motion

Hypothesis

We expected the slip of the needle during forward motion to be inversely proportional to the ratio of the number of stationary to moving needle wires. That is, the slip is expected to increase with the number of simultaneously actuated wires, in line with Sprang et al. [61].

Dependent and independent variables

The dependent variable in experiment 1 was the slip between the needle and the gelatine. We define slip as the ratio of the measured insertion depth to the theoretical insertion depth of the needle. The independent variable was the number of wires that were actuated simultaneously, either one (single actuation) or two (paired actuation). Stroke S was set to 4.0 mm for both single and paired actuation trials.

Experimental procedure

A gelatine block was placed on the cart, and the needle was manually inserted about 25 mm into the gelatine (starting position) to reduce the effects of cutting and friction forces acting on the tip during punching of the substrate. The desired actuation setting (single or paired actuation) was entered in the Arduino software, the laser sensor was switched on, and the needle wires were actuated. The needle wires were actuated counterclockwise, starting with wire 1 in single actuation and with wires 1–2 in paired actuation. At the end of each trial the needle was removed from the phantom and cleaned with warm water. A new gelatine phantom was used for each trial. Six trials were conducted for each actuation condition (single versus paired), in a randomized order. All measurements were conducted over the course of one day.

Data analysis

The raw data of the cart position collected by the laser sensor were imported and processed in MATLAB (version 2014b). The slip ratio *slip* was calculated as:

$$slip = 1 - \frac{d_{\text{meas}}}{d_{\text{theor}}} \quad (3.5)$$

where d_{theor} is the theoretical insertion depth for each cycle and d_{meas} is the measured insertion depth for each cycle, calculated by the difference between the position of the cart at the starting point of two consequential actuation cycles:

$$d_{\text{meas}} = p_{a+1} - p_a \quad (3.6)$$

Where a is the number of an actuation cycle, and p is the position of the cart. For estimating *slip*, we assumed that the advancing needle did not deviate from the straight path.

3.3.3. Experiment 2—steering

Hypothesis

We hypothesized that the steering curvature of the needle is proportional to the bevel offset BO , consistent with experimental and analytical studies on bevel-tip needles showing that smaller bevel angles lead to larger steering curvatures [67, 68]. For a given BO we further expected a proportional relationship between steering curvature and stroke S , as S can be compared to the length of a cantilever beam subjected to a load at its tip.

Dependent and independent variables

The dependent variable was the steering curvature of the needle. The independent variables were BO , S , and the steering direction. BO was varied between 0.9, 1.8, and 3.6 mm, resulting in bevel angles of about 20, 10, and 5 degrees respectively. S was varied between 2.0, 4.0, and 6.0 mm. The steering direction was varied either left or right.

Experimental procedure

From the 18 possible combinations ($3 BO \times 3 S \times 2$ steering directions), a set of 10 conditions was chosen, so that BO was varied for a constant $S = 4.0$ mm, and S was varied for a constant $BO = 3.6$ mm, for both steering directions. The stroke value of 4.0 mm was chosen because it was expected that it would result in higher steering curvatures than a stroke of 2.0 mm, while keeping the needle wires closer to each other than a stroke of 6 mm. The bevel offset value of 3.6 mm, which corresponds to the smallest bevel angle, was chosen because it was expected that the curvature increases with small bevel angles [69]. For steering to the left, the wire pairs were actuated clockwise, starting with the wire pair 6–5. For steering to the right, the wire pairs were actuated counterclockwise, starting with the wire pair 1–2. The same experimental procedure was followed as in experiment 1. Each condition was repeated five times, resulting in a total of 50 trials. All trials were conducted in a randomized order over the course of eight days.

Data analysis

The photographs of the final position of the needle inside the gelatine were cropped to exclude the 25 mm of the initial manual insertion. Then the MATLAB image processing toolbox was used to convert the photographs into binary images, after which the needle shape

and centerline were extracted. Next, a circle was fitted to the needle centerline based on the circle equation in one plane

$$x^T \cdot x + b^T \cdot x + c = 0 \quad (3.7)$$

where $x, b \in R^2$. Using the extracted needle data points (x), the fitted circle radius r_{fit} was obtained for each experimental trial, and the curvature k was calculated as

$$k = (r_{\text{fit}})^{-1} \quad (3.8)$$

where k was obtained assuming that the needle moved only in one plane. For the trials in which steering was not achieved, we set k to 0.

In addition, the deflection-to-insertion ratio d/i was estimated by extracting the initial and end distance from the centerline to calculate the deflection d of the needle from the straight path and by dividing d with the insertion depth i .

3.4. RESULTS

3.4.1. Experiment 1—forward motion

One dataset of the single actuation trials was removed because the laser sensor data were erroneous. The mean value of *slip* was 0.21 for single actuation ($n = 5$) and 0.34 for paired actuation ($n = 6$) (Figure 3.7). In Figure 3.7 it can be seen that the variability in slip across trials was greater in the paired actuation than in the single actuation. In both single and paired actuation, *slip* was highest in the first cycles and stabilized after about nine cycles. The mean total insertion depth of the needle in the single actuation trials was 94.6 mm ($n = 5$) and 79.4 mm in paired actuation ($n = 6$).

3.4.2. Experiment 2—steering

Steering to the left was unsuccessful (i.e., steering in the opposite direction or not steering at all) in 10 out of the 25 trials. Eight of the ten failed tests occurred while steering with a high *BO* and *S*. Specifically, in both Conditions 7 ($BO = 3.6$ mm, $S = 4.0$ mm) and 9 ($BO = 3.6$ mm, $S = 6.0$ mm), four out of the five trials showed steering in the opposite direction; these two conditions were excluded from further analysis. In each of Conditions 3 ($BO = 1.8$ mm, $S = 4.0$ mm) and 5 ($BO = 0.9$ mm, $S = 4.0$ mm), one trial showed no steering; the curvature for these two trials was set to 0. Steering to the right was successful (i.e., steering to the right direction) in all trials.

Steering curvatures were larger for steering to the right than for steering to the left (Figure 3.8). The standard deviation across trials of the same condition increased with increasing *BO*

and S when steering to the right. The largest mean curvature ($k = 0.0184 \text{ cm}^{-1}$) was achieved for Condition 2 ($BO = 3.6 \text{ mm}$, $S = 2.0 \text{ mm}$, steering direction = right). Figure 3.9 shows the deflection-to-insertion ratio for each condition. Ratios were higher for steering to the right than for steering to the left. The highest deflection-to-insertion ratio (0.0778; mean across 5 trials) was achieved for Condition 10 ($BO = 3.6 \text{ mm}$, $S = 6 \text{ mm}$, steering direction right). Table 3.1 shows the mean curvature values and corresponding standard deviations for each condition (for a video of the needle steering inside the gelatine phantom see supplementary material).

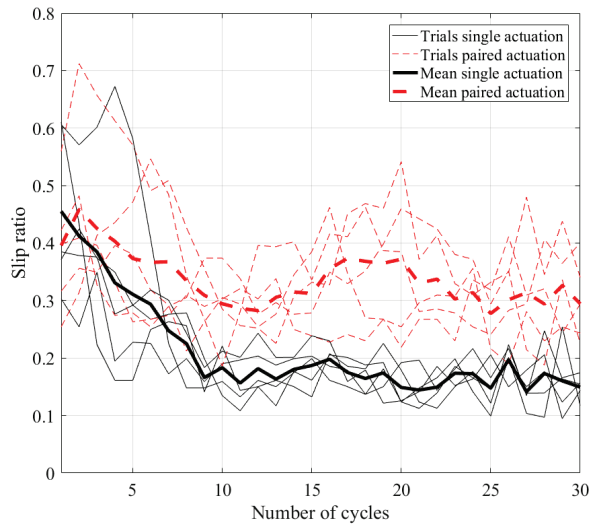


Figure 3.7. Results of experiment 1, showing the slip ratio of the needle in single (solid line) and paired (dashed line) actuation. Thick lines depict the mean values, and thin lines depict the individual trials.

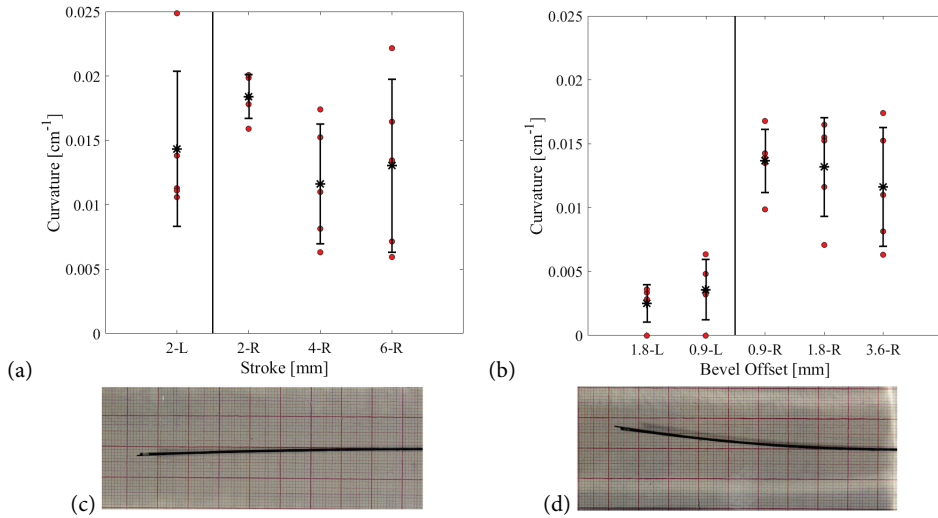


Figure 3.8. Curvature (cm^{-1}) for different conditions. (a) Results of the conditions with constant bevel offset (3.6 mm). Condition 9 ($BO = 3.6$ mm, $S = 6.0$ mm, left) and Condition 7 ($BO = 3.6$ mm, $S = 4.0$ mm, left) have been excluded. (b) Results of the conditions with constant stroke (4.0 mm). Condition 7 ($BO = 3.6$ mm, $S = 4.0$ mm, left) has been excluded. The dots indicate single trials, the asterisks the mean value, and the error bars the standard deviation (± 1 SD). L = left, R = right; the vertical line separates the conditions for left direction from the conditions for right direction. (c) Example of the needle steering on the left ($BO = 0.9$, $S = 4.0$ mm) inside the gelatine. (d) Example of the needle steering on the right ($BO = 1.8$ mm, $S = 4.0$ mm) inside the gelatine.

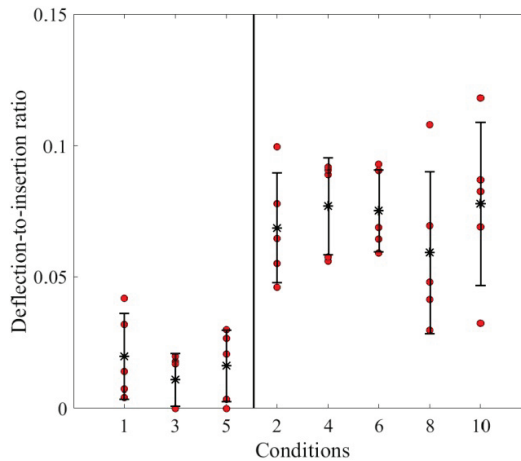


Figure 3.9. Deflection-to-insertion ratio for different conditions. The dots indicate single trials, the asterisks the mean value, and the error bars the standard deviation (± 1 SD). The vertical line separates the conditions for left direction from the conditions for right direction.

Table 3.1. Experimental conditions and curvature mean values for experiment 2.

Condition	BO (mm)	S (mm)	Steering direction	k (cm ⁻¹) (mean±std)	d/i (no unit) (mean±std)
1	3.6	2.0	Left	0.0143±0.0060	0.0198±0.0163
2	3.6	2.0	Right	0.0184±0.0017	0.0686±0.0209
3	1.8	4.0	Left	0.0025±0.0014	0.0108±0.0099
4	1.8	4.0	Right	0.0132±0.0039	0.0769±0.0185
5	0.9	4.0	Left	0.0036±0.0024	0.0161±0.0136
6	0.9	4.0	Right	0.0137±0.0025	0.0751±0.0155
7	3.6	4.0	Left	N/A	N/A
8	3.6	4.0	Right	0.0116±0.0047	0.0592±0.0308
9	3.6	6.0	Left	N/A	N/A
10	3.6	6.0	Right	0.0130±0.0067	0.0778±0.0310

Note. BO = bevel offset; S = stroke; k = curvature; d/i = deflection-to-insertion ratio; N/A = condition excluded from the analysis because four out of five trials showed steering in the opposite direction.

3.5. DISCUSSION

In this study, we presented a novel design of a steerable needle inspired by the ovipositor of parasitoid wasps. Preventing buckling through zero external pushing force and steering by means of a reconfigurable tip are two features of the wasp ovipositor that have already been incorporated in earlier steerable needle designs showing promising results [53, 61]. While previous work has mainly been directed toward probes for neurosurgery with a minimum diameter of 4 mm [59], the goal of our study was to develop a needle that utilizes the ovipositor mechanism while having a diameter under 2 mm, so that it can be used in percutaneous procedures, such as brachytherapy and core needle biopsy.

3.5.1. Needle design

With a diameter of 1.2 mm, the prototype presented here is thinner than other ovipositor-inspired needles and probes in the literature, which range between 4 and 12 mm [57–59]. This small diameter was achieved by using flexible wires as needle segments instead of wedge-shaped sections. The use of wires allows for a circular needle without the manufacturability challenges of creating cylindrical sections. We used an external interlocking mechanism placed at the tip, instead of internal interlocking of the segments [45], as the latter is difficult to manufacture in small dimensions. We showed that a push-pull mechanism, previously only tested in forward motion [61], can also be exploited during steering, preventing buckling while moving in a curved trajectory and thus improving the controllability of the needle

motion. Moreover, instead of a bevel-tip, we proposed a steering mechanism that relies on the creation of a “discrete” bevel between adjacent segments; such a configuration-based asymmetry allows to overcome manufacturability challenges in creating a bevel in small dimensions. Moreover, a discrete bevel-tip is dynamically variable, which might allow for more accurate control of the steering direction of the needle as compared to a needle with a fixed bevel. Changing the direction of steering without the need of axial rotation prevents the generation of torsional stress on the needle body and therefore prevent angular lag between the orientation of the needle base and the needle tip [70]. This way of steering can facilitate the control of the needle tip and decrease the risk of tissue damage [23].

In summary, in this prototype, a series of novel aspects has been introduced and tested: (1) the use of flexible Nitinol wires, which allows for developing a needle with a small diameter without the need of manufacturing cylindrical sectors; (2) the use of external interlocking, which is arguably simpler to fabricate than an internal interlocking mechanism; (3) a new method of steering, in which beveled components are not needed; instead, a type of “discrete” bevel is created by the configuration of the wires; (4) push-pull advancement during steering, which prevents buckling while in a curved trajectory.

3.5.2. Experiment 1—forward motion

Experiment 1 showed that needle slip was lower in single than paired actuation (0.21 versus 0.33), consistent with our hypothesis and previous work [61]. The slip values in our work are considerably lower than the mean slip of 0.7 reported in Sprang et al. [61]. The difference in slip between the two studies might be attributed to the fact that Sprang et al. used a stiffer gel (8 versus 4wt%) and needle segments with larger diameter (0.5 versus 0.25 mm) than we did. A stiffer gel and a thicker needle both increase the forces at the tip of the needle, resulting to higher slip. Previous work has indeed shown that peak axial needle insertion force increases with needle size [71].

The slip ratio was higher at the beginning of the trial and stabilized after about nine cycles, which indicates that a certain initial insertion depth (of about 25 mm) is needed for the needle to move forward with constant slip. We conducted an additional experiment with five trials in which the initial needle insertion was 50 mm and found that for this initial insertion depth, the slip ratio was constant throughout the measurement. This result is consistent with previous studies having shown that during needle insertion, the friction force on the needle increases with insertion depth while the approximate cutting force stays constant [72]. We can expect that an equilibrium is reached at a certain depth between the static friction of the stationary wires and interlocking ring and the dynamic friction and cutting forces of the advancing wires, see also Equation (3.3).

The greater variability in slip between trials observed in the paired actuation as compared to the single actuation can be due to the random deflection of the wires once they are advanced inside the gelatine. In paired actuation, the two wires that are moved forward simultaneously can either stay close to each other or separate from each other (i.e., bifurcate) as they move out of the flower shaped interlocking ring. Bifurcating wires are likely to result in higher friction as compared to trials in which the two wires stay together. Bifurcation was also observed in Sprang et al. [61], in which the needle parts were not interlocked.

3.5.3. Experiment 2—steering

Needle steering is achieved by creating an offset between a pair of adjacent needle wires, which we call a “discrete bevel-tip”. This concept is similar to the “programmable bevel” concept shown in Ko et al. [57], where steering was achieved by creating an offset between the needle part and pushing the needle inside a gelatine phantom. A difference between the concepts of a discrete bevel-tip and a programmable bevel is that in the former, the needle is not directly pushed inside the gelatine; instead the insertion is achieved by a push and pull actuation sequence that, combined with the tip asymmetry, results in a curved path. A second difference is that the programmable bevel needle design presented by Ko et al. [57] consists of needle parts with a fixed bevel-tip, whereas in our design the needle parts have a flat tip and the bevel is created by making an offset between them, which means that the bevel angle can be altered.

From the results of experiment 2 we did not find a systematic effect of BO on curvature. It is known that needle deflection increases when the bevel angle decreases [69]. However, when the bevel angle is lower than 30° , as in our case, the changes in needle deflection as a function of the bevel angle are barely noticeable. Similarly, Jiang et al. [73] found no significant differences in curvature values for needles with a bevel angle of 30° and 10° . In Figures 3.8b and 3.9 we saw that the needle curvature in the right direction was lower for a larger bevel offset BO . This is opposite to our hypothesis. A similar result was also reported in Frasson et al. [44], who suggested that this unexpected result could have been due to the diameter of the probe, which was larger than regular needles (i.e., 9 mm). A possible explanation of our results could be that the wires tend to bifurcate more for larger BO and S . If the first pair of advancing wires bifurcates (i.e., first discrete bevel), the second pair of advancing wires may not follow the path laid by the first discrete bevel but lay a new path instead. As a result, the needle would lose the discrete bevel configuration and not deflect towards the desired direction. 3D microscopic observations of bevel-tip needles conducted by Van Veen et al. [74] showed indeed that the gel rupture at the needle tip is wider and shorter for large bevel angles. A wider and shorter rupture profile provides a larger clearance for the tip to move out of plane. Therefore, it is possible that in the case of a smaller BO (i.e.,

larger bevel angle) the wires had more tendency to move towards the steering direction. The irregular deflection of the wires can also explain the greater variability observed in the results for conditions with large BO and S .

The value of curvature achieved with this needle design is smaller than the values presented in the state-of-the-art [57, 75]. In future prototypes the resulting steering curvature can be increased in different ways [75]. Designing a needle with a smaller diameter will decrease the bending resistance and therefore increase the curvature [74]; the same result can be obtained by using a material with lower stiffness than Nitinol. It has been also shown that pre-bending a needle can have positive effects on the resulting curvature [26]. It should be noted here that the amount of needle steering needed depends on the medical application. For example, in some cases the steering is used to compensate for tissue or target motion [76–78], and only a small deflection of the needle from the straight path is required (range between 2 mm and 6 mm [77]). The needle presented in this paper can reach deflections up to 7.8 mm (maximum mean value), making it suitable for these types of procedures.

To test whether the needle can change direction of steering without the need of axial rotation, we performed three extra trials, in which the wires were actuated clockwise for the first half of the actuation cycles (to steer to the left) and anticlockwise for the second half of the actuation cycles (to steer to the right). These three trials were conducted for $BO = 0.9$ mm and $S = 2.0$ mm, which was the combination of BO and S that resulted in the least incidences of bifurcation in experiment 2. Besides the limited steering of the needle to the left (see results of experiment 2), a change in direction in the middle of the laid trajectory was noticeable (Figure 3.10).

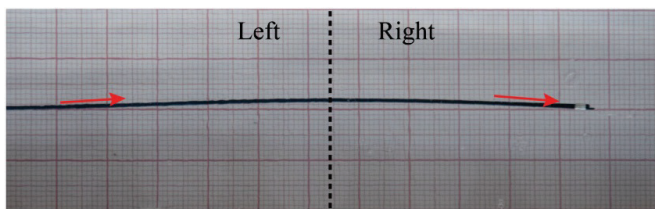


Figure 3.10. Final position of the needle inside the gelatine during the trial in which the steering direction was changed from left to right ($BO = 0.9$ mm, $S = 2.0$ mm). Arrows showing the direction of steering and the middle-dashed line point when direction changed.

3.5.4. Limitations

In experiment 2, higher curvatures were achieved when steering to the right than when steering to the left. This directional preference might have been caused by a tendency of the

needle wires to pre-curve. Indeed, after having assembled the needle we observed that the wires at their relaxed state curved slightly to the right.

In our data analysis we assumed that the needle deflection occurs only in the steering plane. However, visual observations showed that the needle also tended to deflect upwards. This upward deflection was not quantified but was present in all our trials and is likely to have been caused by pre-curve in the wires and/or vertical misalignment of the gelatine cart and the actuation unit. Jahya et al. [79] also reported such “out of plane” deflection and further observed that this deflection increases with the bevel angle of the needle tip. For this reason, the absolute values of slip and steering curvature results of experiments 1 and 2 should be interpreted with caution.

In both experiments, the inertia of the gelatine cart and bearing friction might have influenced the slip results. A large mass of gelatine tends to reduce slip in the pushing phase, while the contrary holds during the pulling phase. The friction between the cart which is moving and the base has to be minimal. Parittotokkaporn et al. [53] used a linear air bearing (aerostatic) with a friction coefficient around 0.0001. This value is lower than a typical friction coefficient of a lubricated ball bearing. In our design we opted for ball bearings, because these have a low friction coefficient (0.001–0.005 [80]) as well as lower costs and maintenance than the air bearings.

3.5.5. Future work

In future prototypes, we plan to eliminate the pre-curvature in the steering direction by selecting straight annealed Nitinol wires. Different tip designs will be investigated to limit the bifurcation of the wires once they are moved away from the interlocking ring.

A better understanding of the interaction between wires and gelatine could help in explaining the behavior of the needle as a function of BO and S . Measurements of friction forces along the needle and forces at the needle tip can be done and used as reference for future design choices, in term of number of wires and actuation method. Furthermore, a stress–strain analyses in the gelatine at the needle tip could give us information on tissue damage during the reciprocal actuation of the wires. Moreover, *ex vivo* experiments are needed for a better understanding of the phenomena in real tissue.

The needle design presented in this paper represents only one of the many possible designs that can originate from our steerable needle concept. The number as well as the diameter of the wires can be changed so that the needle has suitable dimensions for specific applications. A possible application is brachytherapy, where multiple seeds have to be implanted in the prostate; this is usually done with 20–30 needle insertions [81]. Using a needle with enhanced steerability, it would be possible to use only one needle and change the

direction of the needle “on-the-spot” without the need of multiple punctures, reducing pain and tissue damage.

3.6. CONCLUSION

This paper presents the design and experimental evaluation of a wasp ovipositor-inspired needle with a diameter of 1.2 mm. We showed that the needle can penetrate a gelatine phantom of 4wt% with zero external push force, and that it steers by means of a “discrete” bevel-tip. The proposed biologically inspired needle design is an important step towards the development of ultra-thin steerable needles for percutaneous interventions.

SUPPLEMENTARY MATERIAL

Supplementary information is available at: stacks.iop.org/BB/13/016006/mmedia.

REFERENCES

- 1 Phelan S, O’Doherty A, Hill A and Quinn CM. Epithelial displacement during breast needle core biopsy causes diagnostic difficulties in subsequent surgical excision specimens. *J Clin Pathol.* 2006; 60:373–6.
- 2 Volpe A, Kachura J R, Geddie WR, Evans AJ, Gharajeh A, Saravanan A and Jewett MA. Techniques, safety and accuracy of sampling of renal tumors by fine needle aspiration and core biopsy. *J Urol.* 2007; 178:379–86.
- 3 Podder TK, Dicker A P, Hutapea P, Darvish K and Yu Y. A novel curvilinear approach for prostate seed implantation. *Med Phys.* 2012; 30:1887–92.
- 4 Wan G, Wei Z, Gardi L, Downey D B and Fenster A. Brachytherapy needle deflection evaluation and correction. *Med Phys.* 2005; 32:902–9.
- 5 Jeng CL, Torrillo TM and Rosenblatt MA. Complications of peripheral nerve blocks. *Br J Anaesth.* 2010; 105:97–107.
- 6 Maddali P, Moisi M, Page J, Chamiraju P, Fisahn C, Oskouian R and Tubbs RS. Anatomical complications of epidural anesthesia: a comprehensive review. *Clin Anat.* 2017; 30:342–6.
- 7 Kohn LT, Corrigan JM and Donaldson MS. 2000 To Err is Human: Building a Safer Health System (Washington, DC: National Academy of Science).
- 8 Palisch A, Patel R G, Gutowski C, Zoga A C, Colucci P, O’Hara B J, Roberts C C and Abraham J. Analysis of needle type for musculoskeletal lesion biopsy: results of a novel steerable needle. *Curr Orthop Pract.* 2016; 27:393–9.
- 9 Scali M, Pusch TP, Breedveld P and Dodou D. Needle-like instrument for steering through solid organs: a review of the scientific and patent literature. *Proc Inst Mech Eng H.* 2016; 231(3):250–65.
- 10 Swaney PJ, Burgner J, Gilbert HB and Webster RJ. A flexure-based steerable needle: High curvature with reduced tissue damage. *IEEE Trans Biomed Eng.* 2013; 60:906–9.
- 11 Drummond GB and Scott DH. Deflection of spinal needles by the bevel. *Anaesthesia.* 1980; 35:854–7.

- 12 Wang YZ, Yin QL, Liu CJ and Chen YH. Towards an articulated needle. *Appl Mech Mater.* 2012; 152:946–51.
- 13 Kuhle WG. Biopsy needle with flared tip. US Patent 5938635. 1999.
- 14 Okazawa S, Ebrahimi R, Chuang J, Salcudean SE and Rohling R. Hand-held steerable needle device. *IEEE/ASME Trans Mechatronics.* 2005; 10:285–96.
- 15 Torabi M, Gupta R and Walsh CJ. Compact robotically steerable image guided instrument for multi-adjacent-point (MAP) targeting. *IEEE Trans Robot.* 2014; 30:802–15.
- 16 Misra S, Reed KB, Douglas AS, Ramesh KT and Okamura AM. Needle-tissue interaction forces for bevel-tip steerable needles. 2nd IEEE RAS EMBS Int Conf on Biomedical Robotics and Biomechatronics; 2008 Oct 19–22; Scottsdale, AZ, USA. IEEE; 2008 p. 224–31.
- 17 Webster RJ, Kim JS, Cowan NJ, Chirikjian GS and Okamura AM. Nonholonomic modeling of needle steering. *Int J Robotics Res.* 2006; 25:509–25.
- 18 Minhas DS, Engh JA, Fenske MM and Riviere CN. Modeling of needle steering via duty cycled spinning. 29th Annual Int Conf of the IEEE Engineering in Medicine and Biology Society; 2007 Aug 22–26; Lyon, France. IEEE; 2007 p. 2756–9.
- 19 Kraft D and Hole J. Device and method for rapid aspiration and collection of body tissue from within an enclosed body space. US Patent 9131925. 2008.
- 20 Pellegrino R, Patel S and Carrison H. Systems and methods for navigating an instrument through bone WO Patent 2011085212. 2013.
- 21 Kaplan EJ. Deflectable implantation device and method of use US Patent 7282020. 2007.
- 22 Webster RJ, Okamura AM and Cowan NJ. Toward active cannulas: miniature snake-like surgical robots. *IEEE/RSJ Int Conf on Intelligent Robots and Systems (IROS)*; 2006 Oct 9–15; Beijing, China. IEEE; 2006 p. 2857–63.
- 23 Bui VK, Park S, Park JO and Ko SY. A novel curvature-controllable steerable needle for percutaneous intervention. *Proc Inst Mech Eng H.* 2016; 230:727–38.
- 24 Van de Berg NJ, Dankelman J and van den Dobbelsteen JJ. Design of an actively controlled steerable needle with tendon actuation and FBG-based shape sensing. *Med Eng Phys.* 2015; 37:617–22.
- 25 Losey DP, York PA, Swaney PJ, Burgner J and Webster RJ III. A flexure-based wrist for needle-sized surgical robots. *Proc. SPIE 8671, Medical Imaging: Image-Guided Procedures, Robotic Interventions, and Modeling*; 2013 Mar 14; Lake Buena Vista (Orlando Area), Florida, US. SPIE; 2013 p.8671.
- 26 Adebar TK, Greer JD, Laeseke PF, Hwang GL and Okamura AM. Methods for improving the curvature of steerable needles in biological tissue. *IEEE Trans Biomed Eng.* 2016; 63:1167–77.
- 27 Ayvali E, Ho M and Desai JP. A novel discretely actuated steerable probe for percutaneous procedures. In *Exp Robot*; 2014. Berlin: Springer; p. 115–23.
- 28 Konh B, Lee H, Lee HH, Zhao V, Martin VP and Hutapea P. Towards the design and development of an active needle for therapeutic procedures. 41st IEEE Annual Northeast Biomedical Engineering Conf. (NEBEC); 2015 Apr 17–19; Troy, NY. IEEE; 2015 p. 1-2.
- 29 Yan K, Podder T, Ng W S and Yu Y 2007 Smart needle for percutaneous surgery: Influential factor investigation 29th Annual Int Conf of the IEEE Engineering in Medicine and Biology Society; 2007 Aug 22–26; Lyon, France. IEEE; 2007 p. 461–4.
- 30 Swensen JP, Lin M, Okamura AM and Cowan NJ. Torsional dynamics of steerable needles: modeling and fluoroscopic guidance. *IEEE Trans Biomed Eng.* 2014; 61:2707–17.

- 31 Reed KB, Okamura AM and Cowan NJ. Modeling and control of needles with torsional friction *IEEE Trans Biomed Eng.* 2009; 56: 2905–16.
- 32 Reed KB, Majewicz A, Kalleem V, Alterovitz R, Goldberg K, Cowan NJ and Okamura AM. Robot-assisted needle steering. *IEEE Robot Autom Mag.* 2011; 18:35–46.
- 33 Le Lannic J and Nénon JP. Functional morphology of the ovipositor in *Megarhyssa atrata* (Hymenoptera, Ichneumonidae) and its penetration into wood. *Zoomorphology.* 1999; 119:73–9.
- 34 Kundanati L and Gundiah N. Biomechanics of substrate boring by fig wasps. *J Exp Biol* 2014; 217:1946–54.
- 35 Vincent JF and King MJ. The mechanism of drilling by wood wasp ovipositors *Biomimetics.* 1995; 3:187–201.
- 36 Rahman MH, Fitton MG and Quicke DL. Ovipositor internal microsculpture in the Braconidae (Insecta, Hymenoptera). *Zool Scr.* 1998; 27:319–32.
- 37 Quicke DL, Wyeth P, Fawke JD, Basibuyuk HH and Vincent JF. Manganese and zinc in the ovipositors and mandibles of hymenopterous insects. *Zool J Linnean Soc.* 1998; 24:387–96.
- 38 Quicke DL, Fitton MG and Harris J. Ovipositor steering mechanisms in braconid wasps. *J Hymenopt Res.* 1995; 4:110–20.
- 39 Quicke DL and Fitton MG. Ovipositor steering mechanisms in parasitic wasps of the families Gasteruptionidae and Aulacidae (Hymenoptera). *Proc R Soc B.* 1995; 261:99–103.
- 40 Pollard D. Directional control of the stylets in phytophagous Hemiptera *Physiol Entomol.* 1969; 44:173–85.
- 41 Gao Y, Ellery A, Jaddou M and Vincent J. Deployable wood wasp drill for planetary subsurface sampling. *IEEE Aerospace Conf*; 2006 Mar 4–11; Big Sky, MT, USA. *IEEE*; 2006 p. 8.
- 42 Frasson L, Ko SY, Turner A, Parittotokkaporn T, Vincent JF and Rodriguez y Baena F. STING: a soft-tissue intervention and neurosurgical guide to access deep brain lesions through curved trajectories. *Proc Inst Mech Eng H.* 2010; 224: 775–88.
- 43 Ko SY, Davies BL and Rodriguez y Baena F. Two-dimensional needle steering with a ‘programmable bevel’ inspired by nature: modeling preliminaries. *IEEE Int Conf on Intelligent Robots*; 2010 Oct 18–22; Taipei, Taiwan. *IEEE*; 2010 p. 2319–24.
- 44 Frasson L, Ferroni F, Ko S Y, Dogangil G and Rodriguez y Baena F. Experimental evaluation of a novel steerable probe with a programmable bevel tip inspired by nature. *J Robot Surg.* 2012; 6:189–97.
- 45 Frasson L, Reina S, Davies BL and Rodriguez y Baena F. Design optimisation of a biologically inspired multi-part probe for soft tissue surgery. In: Dössel O., Schlegel W.C. (eds) *World Congress on Medical Physics and Biomedical Engineering IFMBE Proceedings*, 2009 Sept 7–12; Munich, Germany. Berlin: Springer; 2009 p. 307–10.
- 46 Frasson L, Neubert J, Reina S, Oldfield M, Davies BL and Rodriguez y Baena F. Development and validation of a numerical model for cross-section optimization of a multi-part probe for soft tissue intervention. *Annual Int Conf of the IEEE Engineering in Medicine and Biology Society*; 2010 Aug 31–Sept 4; Buenos Aires, Argentina. *IEEE*; 2010 p. 3202–5.
- 47 Leibinger A, Oldfield M and Rodriguez y Baena F. Multi-objective design optimization for a steerable needle for soft tissue surgery. In J Goh (eds) *The 15th Int Conf on Biomedical Engineering. IFBME Proceedings*; 2014. Cham: Springer; 2014 p. 420–3.
- 48 Frasson L, Parittotokkaporn T, Schneider A, Davies BL, Vincent JFV, Hup SE et al. Biologically inspired microtexturing: investigation into the surface topography of next-generation

- neurosurgical probes. 30th Int. Conf. of the IEEE Engineering in Medicine and Biology Society; 2008 Aug 20–25; Vancouver, BC, Canada. IEEE; 2008 p. 5611–4.
- 49 Schneider A, Frasson L, Parittotokkaporn T, Rodriguez y Baena F, Davies BL and Huq SE. Biomimetic microtexturing for neurosurgical probe surfaces to influence tribological characteristics during tissue penetration. *Microelectron Eng.* 2009; 86:1515–7.
- 50 Schneider A, Frasson L, Parittotokkaporn T, Rodriguez y Baena F, Davies BL and Huq S. Microfabrication of components for a novel biomimetic neurological endoscope. 4th Int. Conf. on Multi-Material Micro Manufacture; 2008:p. 9–11.
- 51 Parittotokkaporn T, Thomas DGT, Huq E, Davies BL, Degenaar P and Rodriguez y Baena F. Microtextured surfaces for deep-brain stimulation electrodes: a biologically inspired design to reduce lead migration. *World Neurosurg.* 2012; 77:569–76.
- 52 Frasson L, Parittotokkaporn T, Davies BL and Rodriguez y Baena F. Early developments of a novel smart actuator inspired by nature. *Int J Intell Syst Technol Appl.* 2009; 8:409–22.
- 53 Parittotokkaporn T, Frasson L, Schneider A, Huq SE, Davies BL, Degenaar P et al. Soft tissue traversal with zero net force: feasibility study of a biologically inspired design based on reciprocal motion. *IEEE Int Conf on Robotics and Biomimetics*; 2009 Feb 22–25; Bangkok, Thailand. IEEE; 2009 p. 80–5.
- 54 Parittotokkaporn T, Frasson L, Schneider A, Davies BL, Degenaar P and Rodriguez y Baena F. Insertion experiments of a biologically inspired microtextured and multi-part probe based on reciprocal motion. *Annual Int Conf of the IEEE Engineering in Medicine and Biology Society*; 2010 Aug 1-Sept 4; Buenos Aires, Argentina. IEEE; 2010 p. 3190–3.
- 55 Oldfield M, Dini D, Giordano G and Rodriguez y Baena F. Detailed finite element modelling of deep needle insertions into a soft tissue phantom using a cohesive approach. *Comput Methods Biomech Biomed Eng.* 2013; 16:530–43.
- 56 Secoli R and Rodriguez y Baena F. Closed-loop 3D motion modeling and control of a steerable needle for soft tissue surgery *IEEE Int. Conf. on Robotics and Automation*; 2013 May 6–10; Karlsruhe, Germany. IEEE; 2013 p. 5831–6.
- 57 Ko S Y, Frasson L and Rodriguez y Baena F. Closed-loop planar motion control of a steerable probe with a ‘programmable bevel’ inspired by nature. *IEEE Trans Robot.* 2011; 27:970–83.
- 58 Burrows C, Secoli R and Rodriguez y Baena F. Experimental characterisation of a biologically inspired 3D steering needle. *13th Int Conf on Control, Automation and Systems*; 2013 Oct 20–23; Gwangju, South Korea. IEEE; 2013 p. 1252–7.
- 59 Burrows C, Liu F, Leibinger A, Secoli R and Rodriguez y Baena F. Multi-target planar needle steering with a bio-inspired needle design. In: Boschetti G., Gasparetto A. (eds) *Advances in Italian Mechanism Science. Mechanisms and Machine Science*, vol 47. 2017; Springer, Cham; p. 51–60.
- 60 Leibinger A, Oldfield MJ and Rodriguez y Baena F. Minimally disruptive needle insertion: a biologically inspired solution. *Interface Focus* 2016; 6:20150107.
- 61 Sprang T, Breedveld P and Dodou D. Wasp-inspired needle insertion with low net push force. In: Lepora N, Mura A, Mangan M, Verschure P, Desmulliez M, Prescott T (eds) *Biomimetic and Biohybrid Systems. Living Machines 2016. Lecture Notes in Computer Science*, vol 9793. 2016; Springer, Cham; p. 307–18.
- 62 Gherardi G. *Fine-Needle Biopsy of Superficial and Deep Masses: Interventional Approach and Interpretation Methodology by Pattern Recognition.* 2009; Verlag: Springer.
- 63 Podder T et al. In vivo motion and force measurement of surgical needle intervention during prostate brachytherapy. *Med Phys* 2006; 33:2915–22.

- 64 Scali M, Pusch TP, Breedveld P and Dodou D. Design and preliminary evaluation of a bio-inspired steerable needle 28th Int. Conf. Society for Medical Innovation and Technology (SMIT); 2016; Delft, the Netherlands.
- 65 Rogers D. The ichneumon wasp *Venturia canescens*: oviposition and avoidance of superparasitism. *Entomol Exp Appl.* 1972; 15:190–4.
- 66 Chatelin S, Constantinesco A and Willinger R. Fifty years of brain tissue mechanical testing: from in vitro to in vivo investigations. *Biorheology.* 2010; 47:255–76.
- 67 Webster RJ, Memisevic J and Okamura AM. Design considerations for robotic needle steering. *IEEE Int Conf on Robotics and Automation*; 2005 Apr 18–22; Barcelona, Spain. IEEE; 2005 p. 3588–94.
- 68 Misra S, Reed KB, Schafer BW, Ramesh KT and Okamura AM. Mechanics of flexible needles robotically steered through soft tissue. *Int J Robot Res.* 2010; 29:1640–60.
- 69 Konh B, Honarvar M, Darvish K and Hutapea P. Simulation and experimental studies in needle-tissue interactions. *J Clin Monit Comput.* 2016; 31:1–12.
- 70 Swensen JP and Cowan NJ. Torsional dynamics compensation enhances robotic control of tip-steerable needles *IEEE Int. Conf. on Robotics and Automation*; 2012 May 14–18; Saint Paul, MN, USA. IEEE; 2012 p. 1601–6.
- 71 Van Gerwen DJ, Dankelman J and van den Dobbelsteen JJ. Needle-tissue interaction forces—A survey of experimental data. *Med Eng Phys.* 2012; 34:665–80.
- 72 Hing JT, Brooks AD and Desai JP. Reality-based needle insertion simulation for haptic feedback in prostate brachytherapy. *IEEE Int Conf on Robotics and Automation*; 2006 May 15–19 Orlando, FL, USA. IEEE; 2006 p. 619–24.
- 73 Jiang S and Wang X. Mechanics-based interactive modeling for medical flexible needle insertion in consideration of nonlinear factors. *J Comput Nonlin Dyn* 2016; 11:011004.
- 74 van Veen YR, Jahya A and Misra S. Macroscopic and microscopic observations of needle insertion into gels. *Proc Inst Mech Eng H.* 2012; 226:441–9.
- 75 Scali M, Kreeft D, Breedveld P and Dodou D. Design and evaluation of a wasp-inspired steerable needle. *Proc. SPIE 10162, Bioinspiration, Biomimetics, and Bioreplication*; 2017 Apr 17; p. 1016207–13.
- 76 Abolhassani N, Patel RV and Ayazi F. Minimization of needle deflection in robot-assisted percutaneous therapy. *Int J Med Robot.* 2007; 3:140–8.
- 77 Stone NN, Roy J, Hong S, Lo Y C and Stock RG. Prostate gland motion and deformation caused by needle placement during brachytherapy. *Brachytherapy* 2002; 1:154–60.
- 78 Sadjadi H, Hastrudi ZK and Fichtinger G. Needle deflection estimation: prostate brachytherapy phantom experiments. *Int J Comput Assist Radiol Surg.* 2014; 9:921–9.
- 79 Jahya A, van der Heijden F and Misra S. Observations of three-dimensional needle deflection during insertion into soft tissue. *4th IEEE RAS EMBS Int Conf on Biomedical Robotics and Biomechatronics*; 2012 Jun 24–27; Rome, Italy. IEEE; 2012 p. 1205–10.
- 80 Powell JW. *Design of Aerostatic Bearings.* Brighton: Machinery Publishing; 1970.
- 81 Alterovitz R, Pouliot J, Taschereau R, Hsu IC and Goldberg K. Simulating needle insertion and radioactive seed implantation for prostate brachytherapy. *Stud Health Technol Inform.* 2003; 94:19–25.

Chapter **4**

Design and Evaluation of a Wasp- Inspired Steerable Needle

Published as:

Scali M, Kreeft D, Breedveld P, Dodou D. Design and evaluation of a wasp-inspired steerable needle. Proceedings Volume 10162, Bioinspiration, Biomimetics, and Bioreplication. 2017: 1016207.

© (2017) Society of Photo-Optical Instrumentation Engineers (SPIE).

ABSTRACT

Flexible steerable needles can follow complex curved paths inside the human body. In a previous work, we developed a multiple-part steerable needle prototype with a diameter of 1.2 mm, inspired by the ovipositor of parasitoid wasps. The needle consisted of seven nickel-titanium longitudinally aligned wires held together at the tip by a cylindrical ring with seven holes. The steerability of the needle was evaluated in a gelatine phantom and was found to be lower than that of other steerable needles in the literature. One possible cause of this limited steerability is that during motion the wires tend to separate from each other (i.e., bifurcate). Our aim here was to reduce bifurcation in order to increase the steering curvature of the needle, while keeping the diameter around 1.5 mm, and thus compatible with needles used in medical practice. To achieve that, we changed the shape of the ring from cylindrical to conical. We evaluated the steering performance in gelatine, using the conical ring in two configurations: (1) with the apex of the cone towards the needle tip, so that the wires converge, thus expected to reduce bifurcation, (2) with the apex of the cone placed towards the needle base, so that the wires diverge, thus expected to magnify bifurcation. Results showed that the diverging ring generated larger steering curvatures. We can conclude that reducing the bifurcation of the wires is not enough for increasing the steering curvature and that inducing this same phenomenon instead could actually lead to higher curvatures.

4.1. INTRODUCTION

In percutaneous interventions, when a target area inside the human body can be reached via a straight line, rigid needles are typically used. However, when the target is difficult to reach and avoiding organs or vessels along the path becomes essential, the physician might decide to proceed with open surgery or to not perform the procedure, with obvious consequences for the patient's health. Over the last decades, researchers have been developing flexible steerable needles (see [1] for a review), which allow to follow complex curved paths. The steering curvature required to reach a target depends on the specific medical procedure. In some cases, such as in brachytherapy, the needle has only to compensate for the movement of tissues and organs in the environment, and so the maximum deviation from a straight path (i.e., deflection) required is relatively small (e.g., between 2 mm and 6 mm) [2]. In cases in which the target is blocked by sensitive structures (e.g., vessels), much higher needle deflections are required (e.g., 30 mm) over a relatively short distance from the insertion point (e.g., 80 mm) [3].

4.1.1. Needle steering curvature

Curvature is a quantitative measure of the amount by which a curve deviates from a straight line. In the case of a circle, the curvature equals the reciprocal of the circle radius at every point. In the case of a general curve, the curvature equals the curvature of the osculating circle, which is the tangent circle that approximates the curve the best. The steerability of a needle is often expressed as the minimum achievable radius of curvature, that is, the reciprocal of the curvature. Alternatively, steerability can be expressed as the ratio of the maximum deviation of the needle from a straight path to the distance between the position from which the needle starts to deflect and the position of maximum deviation [4], called henceforth “deflection-to-insertion ratio”. The steering curvature is high when the radius of curvature is low and/or the deflection-to-insertion ratio is high. The steering curvature depends on the needle design characteristics, namely the needle diameter, the type and degree of asymmetry of the needle tip, and the needle material. Decreasing the needle diameter lowers the second moment of inertia, resulting in lower bending resistance, thereby increasing the steering curvature [5]. Asymmetry at the needle tip can be induced with a bevel-tip, a pre-bent segment, or a combination of both [6]. The smaller the bevel angle, the higher the curvature. Simulations by Konh et al. [7] indicated that a decrease of the bevel angle from 60° to 20° corresponds to an increase in needle deflection from 7.3 mm to 25.5 mm for an insertion depth of 150 mm and a needle diameter of 0.64 mm. It has further been shown that the effect of the bevel angle on the steering curvature decreases for small bevel angles, with differences in deflection being barely noticeable between needles ($\varnothing 1.27$ mm)

with a bevel angle of 30° and 10° [8]. Asymmetry at the needle tip can be also induced by bending the tip. The bend can be permanent and activated by tissue interaction, or temporary and activated by cables [9] or other means [10]. Increasing the tip angle of a pre-bent needle also increases the steering curvature [11]. Moreover, adding a bend to a conical [3] or bevel-tip needle [12] increases the steering curvature compared to a needle without a bend. Pre-bending bevel-tip needles can considerably improve the steering curvature, with minimum radii of curvature of 16.45 cm versus 5.62 cm reported for bevel-tip versus pre-bent bevel-tip needles, respectively [6]. Another way of lowering the bending resistance of the needle is by carving one or more sets of notches on the needle shaft. In Khadem et al. [13], adding four sets of notches to an 18G standard needle increased deflection from 25 mm to 33 mm. The steering curvature further depends on the needle material. With stiffness approximately 1/3 of that of standard stainless steel, Nitinol, for example, has been used in needles to increase the steering curvature [14]. Table 4.1 presents an overview of the minimum radius of curvature and/or maximum needle tip deflection-to-insertion ratio for various needle designs reported in the literature.

4.1.2. Aim

In previous work [15], we developed a multiple-part needle prototype inspired by the ovipositor of parasitoid wasps and evaluated its steerability in a gelatine phantom. The needle consists of seven Nitinol wires, each with a diameter of 0.25 mm and a length of 160 mm. Six of the wires are arranged circularly around the seventh wire. An interlocking ring (aluminum, $\text{Ø}1.2$ mm, 2.0 mm long) with seven holes ($\text{Ø}0.3$ mm) keeps the wires together at the tip of the needle. The total diameter of the needle is 1.2 mm at the tip (i.e., equal to the diameter of the ring) and 0.75 mm along the body. The needle is able to advance through a gelatine phantom with zero external push force and to follow a curved path. Specifically, by actuating one or two wires simultaneously, the needle can advance forward within the substrate, as the remaining four or five stationary wires generate sufficient friction force to compensate for the friction and cutting force of the advancing wires. Steering is achieved by creating an offset between adjacent wires, a configuration which we call a “discrete bevel-tip”, and by moving each pair of offset adjacent wires over a pre-defined distance (stroke). Depending on the actuation sequence of the wires, the needle steers to the left or to the right.

We tested several combinations of offset (i.e., 3.6 mm, 1.8 mm, and 0.9 mm) and stroke (i.e., 2 mm, 4 mm, and 6 mm) and found a maximum steering curvature of 0.018 cm^{-1} (average across 5 trials), achieved with an offset of 3.6 mm and a stroke of 2 mm, and a maximum deflection-to-insertion ratio of 0.078 (average across 5 trials), achieved with an offset of 3.6 mm and a stroke of 6 mm. These values are lower than values reported for other needle designs (see Table 4.1). One possible cause of this limited steerability is that during motion

the wires tend to separate from each other (i.e., bifurcate), because of which the discrete bevel loses its definition and the steering motion becomes compromised.

The aim of the present work was to reduce the bifurcation of the wires in order to increase the steering curvature of the needle, while keeping the final diameter smaller than 2 mm, and thus compatible with the diameter of the needles used, for example, in core needle biopsy (14–19G) [16] and brachytherapy (17–18G) [17]. We first present the conceptual design of the needle prototype and the steering method used, followed by an experimental evaluation of the steering performance of the needle.

4.2. NEEDLE DESIGN

4.2.1. Conceptual design for reducing wire bifurcation

One possible origin of the bifurcation of the wires observed in the previous prototype is the tolerance between the holes of the interlocking ring and the wires (0.025 mm). This space could cause the wires to exhibit play while they move through the holes and to bend towards a direction different from the steering direction. A possible solution could be to increase the length of the interlocking ring, which would limit the bending angle of the wires inside the holes. Accordingly, we increased the length of the interlocking ring of the prototype from 2 mm to 5 mm.

Bifurcation could be further reduced by guiding the wires towards the central wire. To achieve that, we changed the shape of the interlocking ring from cylindrical to conical. By creating an angle with respect to the longitudinal axis of the needle, the wires would mimic a pre-bent needle, converging towards the central wire. This ring will be henceforth referred to as “converging ring” (Figure 4.1). The angle β of the conical ring with respect to the longitudinal axis of the ring can be defined as a function of the minimum and maximum diameter d_1 and d_2 of the ring and its length l :

$$d_2 = 2l \tan \beta + d_1 \quad (4.1)$$

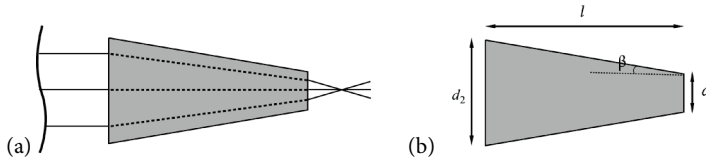


Figure 4.1. (a) Schematic representation of the converging ring with the wires guided towards the center. The vertical curved line on the left indicates the continuation of the needle body towards the needle base. The needle tip is depicted at the rightmost side of the drawing. (b) Design parameters of the conical ring. d_1 and d_2 are the minimum and maximum diameters, respectively, l is the length of the ring, and β is the angle with respect to the longitudinal axis of the ring.

Assuming $l = 5$ mm, $d_1 = 1.2$ mm, and $\beta = 2^\circ$, it can be derived from Equation 4.1 that $d_2 = 1.55$ mm. The total diameter of the prototype coincides with the ring diameter, which is 1.55 mm (i.e., lower than 2 mm).

To test our hypothesis that the bifurcation of the wires was the main cause of limited steering in our previous prototype, we also created a ring that intentionally induces bifurcation of the wires and observed the effect of such a ring on the steering curvature. This ring is identical to the converging ring described above, but with its apex placed towards the base of the needle, so that the wires are moved away from the central wire, therefore magnifying the bifurcation (Figure 4.2). This ring will be henceforth referred to as “diverging ring”.

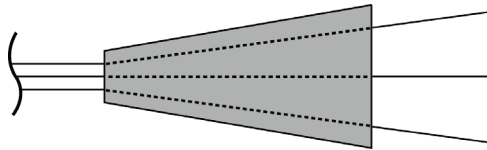


Figure 4.2. Schematic representation of the diverging ring. The vertical curved line on the left indicates the continuation of the needle body towards the needle base. The needle tip is depicted at the rightmost side of the drawing.

Table 4.1. State-of-the-art on steering curvatures.

Reference	Needle design	Material	Outer diameter [mm]	Smallest radius of curvature [mm]	Deflection-to-insertion ratio [mm/mm]	Insertion speed [mm/s]	Medium
Adebar et al. [3]	Articulated tip (45°, length 9 mm)	Nitinol	0.8 (body), 2.0 (hinge), 1.0 (tip)	82.7	0.42* (27.7/65)	ca. 1.6	Ex vivo porcine liver
Bui et al. [18]	Cannula and stylet with bevel-tip (12°)	Nitinol	0.46 (cannula), 0.24 (stylet)	71.8 265.6 (ex vivo)	N/A	3	Gelatine 10%wt Ex vivo cow liver
Dalia et al. [19]	Shape-memory alloy (SMA) actuated needle with conical tip	Nitinol (body), stainless steel (tip)	2.20	N/A	0.2* (30/150)	2.55	Plastisol (3:1 ratio plastic to softener)
Khadem et al. [13]	Needle with 4 set of notches	Stainless steel	1.02	198	0.24* (34.29/140)	5	80% liquid plastic and 20% plastic softener ($E = 35$ kPa)
Ko et al. [20]	Two-segment with bevel-tip	Soft material, Digital Material™ DM_9885 and DM_9895 (body), Rigid material, VeroWhite (tip)	4	ca. 70	N/A	0.5	Gelatine 6%wt ($E = 7$ kPa)
Ko et al. [21]	Four-segment with bevel tip	Rubber-like material	12	178.6	N/A	1	Gelatine 6%wt ($E = 7$ kPa)
Konh et al. [7]	Bevel-tip (30°)	Steel	0.38	N/A	0.24* (36/150)	2.5	Plastisol gel (3:1, plastic: softener)
Majewicz et al. [22]	Bevel-tip (30°)	Nitinol	0.58	164.5 (ex vivo)	N/A	5	Kidney (canine)

Reference	Needle design	Material	Outer diameter [mm]	Smallest radius of curvature [mm]	Deflection-to-insertion ratio [mm/mm]	Insertion speed [mm/s]	Medium
	Pre-bent (15°) with bevel-tip (30°)	Nitinol	0.58	52.3 (ex vivo) 104 (in vivo)	N/A	5	Kidney (canine)
Majewicz et al. [6]	Pre-bent (45°)	Nitinol	0.58	34	N/A	15	Ex vivo goat liver
Minhas et al. [23]	Pre-bent (15°) with bevel-tip (10°)	Nitinol (body), stainless steel (bevel-tip)	1.27 (tip) 0.28 (body)	52*	N/A		Gelatine 6.5%wt
Misra et al. [24]	Bevel-tip (38°)	Nitinol	0.4	179.4	0.78° (98/125)	2.5	Plastisol (4:1 ratio pastic to softner)
Okazawa et al. [25]	Straight cannula and pre-bent stylet	Nitinol	0.81	N/A	0.35° (35/100)	5	Polyvinyl chloride compound ($E = 157$ kPa)
Ryu et al. [26]	SMA actuation needle with symmetric tip	Nitinol and PTFE	1.67	N/A	0.12° (7.2/60)	0.5	Plastisol (4:1 ratio plastic to softner, $E = 40$ kPa)
Rucker et al. [27]	Bevel-tip (35°)	Nitinol	0.86	128 400 (ex vivo)	N/A	N/A	Simulated Muscle Tissue Ballistic Test Media (Sim-Test)
Swaney et al. [12]	Bevel-tip (10° bevel angle) with flexure (max angle 22°)	Stainless steel (body), Nitinol (flexure)	0.91	121 (gelatine) 176 (ex vivo)	N/A	5	Ex vivo bovine liver Gelatine 10%wt Ex vivo pork loin
Patil et al. [14]	Pre-bent with bevel-tip	Nitinol	0.88	67* 137* (ex vivo)	N/A	N/A	Simulated Muscle Tissue Ballistic Test Media (Sim-Test), Corbin, Inc (5:1 ratio with water)

Reference	Needle design	Material	Outer diameter [mm]	Smallest radius of curvature [mm]	Deflection-to-insertion ratio [mm/mm]	Insertion speed [mm/s]	Medium
Wellborn et al. [4]	Flexure needle tip, bevel-tip (10°) with notched wall sheath	Nitinol	0.91 (stylet)	N/A	1.1 (gelatine) 0.21 (ex vivo)	N/A	Knox gelatine phantom 10%wt
Wood et al. [28]	Bevel-tip (7°)	Nitinol	0.52	333*	N/A	N/A	Ex vivo bovine liver Kidney phantom (medical training model, Limbs & Things, Inc., Savannah, Ga.)

*The value has been calculated by us based on numerical data given in the original paper. When not provided, the numbers have been extracted from graphs shown in the original paper.

N/A: Information not available.

4.2.2. Needle prototype

The needle prototype consists of a needle body and an actuation unit. The needle body consists of seven longitudinally aligned wires of Nitinol (straight annealed, activation temperature 20°C), each wire with a diameter of 0.25 mm and a length of 250 mm. The wires are held together at the needle tip by the converging/diverging ring described in Section 4.2.1. The ring has one central 0.3-mm hole and six 0.3-mm circumferential holes through which the wires are fed. The central wire is glued to the central hole, while the other six wires can slide back and forth through the circumferential holes. Six stainless steel rings (\O_{in} : 0.9 mm, \O_{out} : 1.0 mm, 2.0 mm long) are located along the length of the needle, to keep the Nitinol wires together (Figure 4.3).

The actuation unit consists of six stepper motors AM0820 with step angle 18° (Faulhaber, Germany), each motor actuating one of the six wires. The transmission consists of a leadscrew (M2, 28 mm long) and a slider to convert rotational motion of the stepper motors into a linear motion of the wires. Seven stainless steel tubes are attached to the housing to guide the seven wires outside of the actuation unit. The six stepper motors are actuated using six stepper drivers DRV8834 (Texas Instruments, TX) and an Arduino MEGA 2560 microcontroller.

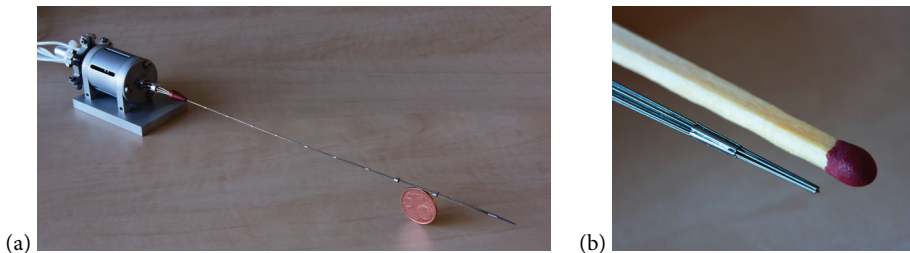


Figure 4.3. (a) Needle prototype with the actuation unit at the leftmost side of the photo. (b) Close-up of the needle tip with the converging ring.

4.2.3. Steering motion

We expect that the steering curvature is higher when using the converging ring as compared to the diverging ring, because in the former case the wires have the tendency to move towards the center, thereby averting bifurcation, whereas in the latter case the wires are forced to bifurcate and the definition of the discrete bevel-tip is lost. Additionally, in the case of the converging ring, the wires mimic the behavior of pre-bent wires, which increases the lateral forces acting at the end side and is thus expected to result in higher steering curvature.

In order to lay a curved path, first an offset (O) is created by moving two pairs of adjacent wire forward, one at the time, while the third pair remains stationary. Then, each of the three pairs is moved forward, one at the time, over a pre-defined distance called stroke (S). Because of the asymmetry created at the tip by the offset and stroke, the needle deflects. Finally, all six wires are moved backwards, causing the interlocking mechanism that is glued to the central wire to advance within the substrate. By repeating these steps, the needle follows a curved path inside the substrate. Depending on the desired steering direction (left or right) different pairs of wires are actuated. Steering to the left is achieved by moving over a pre-defined O the wire pairs 1-2 and 3-4 for the converging ring and 1-6 and 5-4 for the diverging ring. For steering to the right, wire pairs 1-6 and 5-4 are moved for the converging ring and 1-2 and 3-4 for the diverging ring (Figure 4.4).

4.3. MATERIALS AND METHODS

The steerability of the two variations of the prototype (i.e., with the converging and the diverging ring) was experimentally evaluated in a gelatine phantom.

4.3.1. Experimental setup

The experimental setup consisted of an actuation unit mounted on an aluminum platform and data acquisition systems. The base plate of the platform (ca. 405 x 101 mm) had a duct to guide a lightweight aluminum cross-shaped cart (dimensions: 210 x 100 mm, mass = 39 g) mounted to four wheels in order to move along a straight path with low friction. The cart was used to carry a gelatine phantom, in which the needle was inserted (Figure 4.5). To align the needle along its length, we added two rings with an asymmetric cross-section (aluminum, \emptyset 3.0 mm, 2.0 mm long) to the body of the needle and fixed them to the cart. The alignment rings had seven holes through which the wires could freely slide. A camera (Nikon D610 with AF-S NIKKOR 24-70 mm) was positioned above the cart to take a photo of the initial insertion and final position of the needle during the trials.

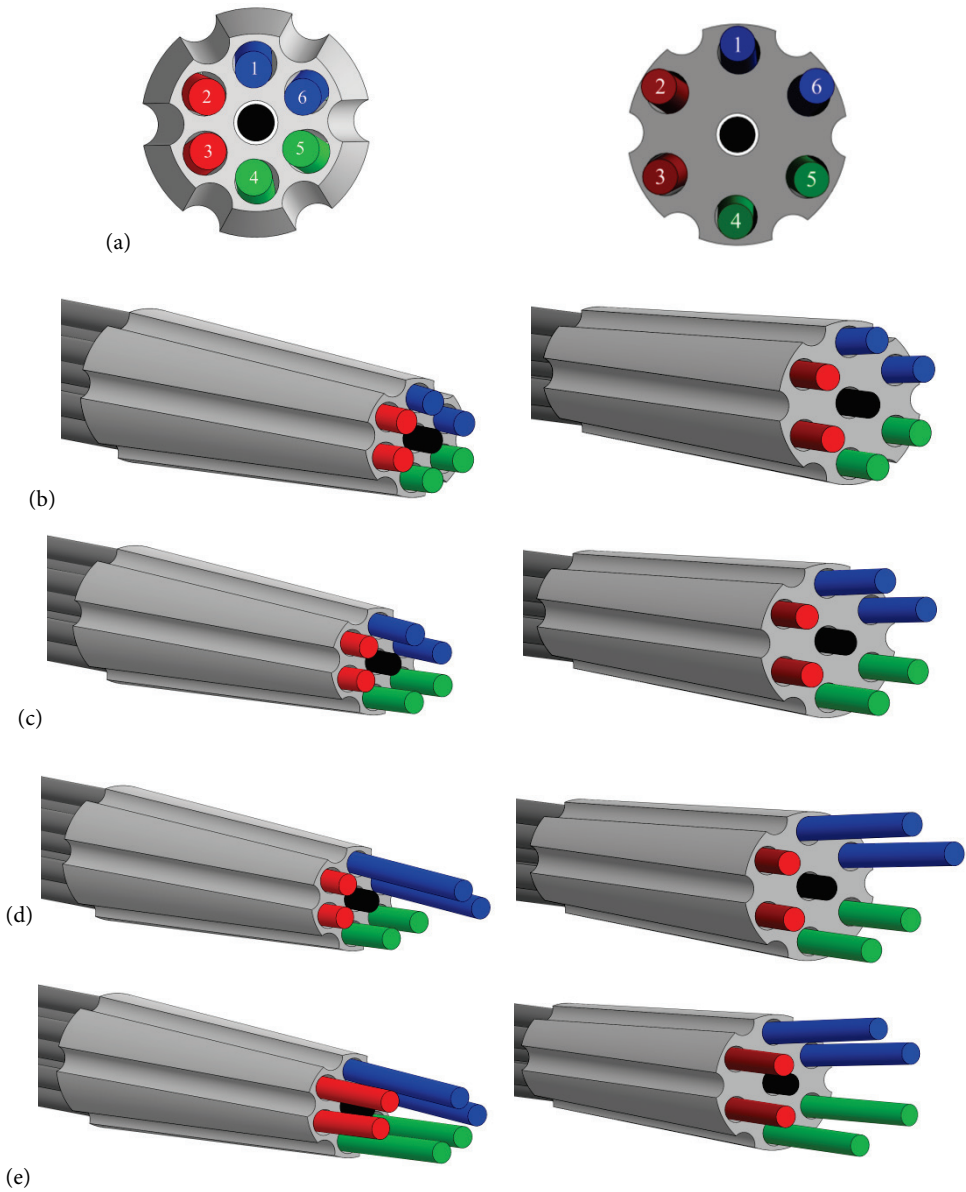


Figure 4.4. The steps of the actuation of the wires used for steering the needle through a substrate with the converging tip (left) and the diverging tip (right). (a) Cross-section of the rings, (b) Initial position of the wires, (c) An offset (O) is created by moving two pairs of wires forward over a pre-defined distance called offset (O), (d) The first pair of wires is moved over a second pre-defined distance, called stroke (S), (e) The other pairs are moved over the same distance S .

The gelatine phantoms were prepared by mixing hot tap water (ca. 70°C) and gelatine powder (Dr. Oetker Professional, the Netherlands). The solution was poured into containers (ca. 230 x 150 x 60 mm) and stored overnight at 5°C. Before each trial, a gelatine block of 48 x 165 x 30 mm (width x length x height, 200.0 ± 0.2 g) was cut and placed on the cart. The gelatine phantoms had a concentration of 5% weight (wt) powder in water, corresponding to a stiffness of 4.6 kPa, which was measured using a universal testing machine (Zwick/Roell Z005, Germany). This value roughly corresponds to the stiffness of brain tissue (0.5-6.0 kPa) [29]. For all experimental trials, we selected a constant forward speed of 1 mm/s and a theoretical travel distance equal to 120 mm.

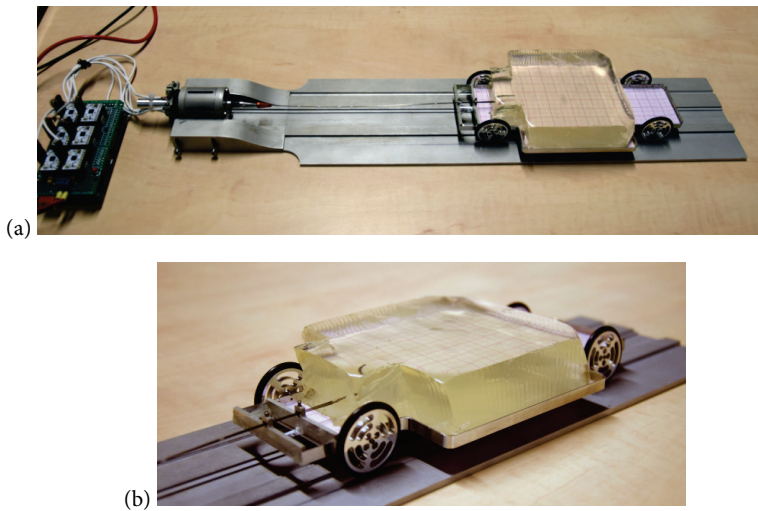


Figure 4.5. (a) Experimental setup showing the actuation unit mounted on an aluminum platform and the gelatine phantom on the cart. (b) Close-up of the needle entering the gelatine.

4.3.2. Experimental design

Hypotheses

Three hypotheses were formulated: a) The higher the offset of the wires, the higher the curvature achieved (i.e., lower radius of curvature), as the asymmetry at the tip increases, causing the needle to bend more. b) The higher the stroke, the higher the curvature achieved (i.e., lower radius of curvature), as the asymmetry at the tip increases, causing the needle to bend more. c) The converging ring reduces the bifurcation of the wires, resulting in higher curvatures than the diverging ring.

Dependent and independent variables

The dependent variable was the deflection-to-insertion ratio of the needle. The independent variables were the initial offset (O) of the wires, the stroke (S), the steering direction, and the type of ring. The offset was varied between 2.0, 4.0, and 6.0 mm. The stroke was varied between 4.0 and 6.0 mm. Two steering directions, left and right, were tested, and two interlocking rings, converging and diverging. Table 4.2 shows the eight experimental conditions tested for each interlocking ring.

Table 4.2. Experimental conditions for each of the interlocking rings.

Condition	Offset [mm]	Stroke [mm]	Direction
1	4.0	4.0	Left
2	6.0	4.0	Left
3	2.0	6.0	Left
4	6.0	6.0	Left
5	4.0	4.0	Right
6	6.0	4.0	Right
7	2.0	6.0	Right
8	6.0	6.0	Right

Experimental procedure

All eight conditions were repeated eight times in a randomized order, first with the converging ring and then with diverging ring. With the help of the actuation unit, the needle was inserted inside the gelatine to a starting position of approximately 35 mm when using the converging ring, and of 45 mm when using the diverging ring; the initial insertion depth was smaller for the converging ring because this ring had a lower drag than the diverging ring. Once the needle was in place, the chosen settings for steering (i.e., O , S , and direction) were uploaded in Arduino and used for the actuation of the wires. At the end of each trial a photo of the final position was taken, the gelatine was removed from the cart, and the wires were cleaned with oil and water. Measurements that were not successful due to, for example, a failure of the motors, were repeated following a randomized order.

Data analysis

The photographs of the final position of the needle inside the gelatine were cropped to exclude the initial insertion of 35 mm and 45 mm for the converging and the diverging ring, respectively. Then, the MATLAB image processing toolbox was used to convert the photographs into binary images, after which the needle shape and centerline were extracted. Next, the initial and end points were extracted and used to calculate the deflection d of the

needle from a straight path and the insertion depth i (Figure 4.6). The deflection-to-insertion ratio d/i was then calculated as a measure of needle curvature.

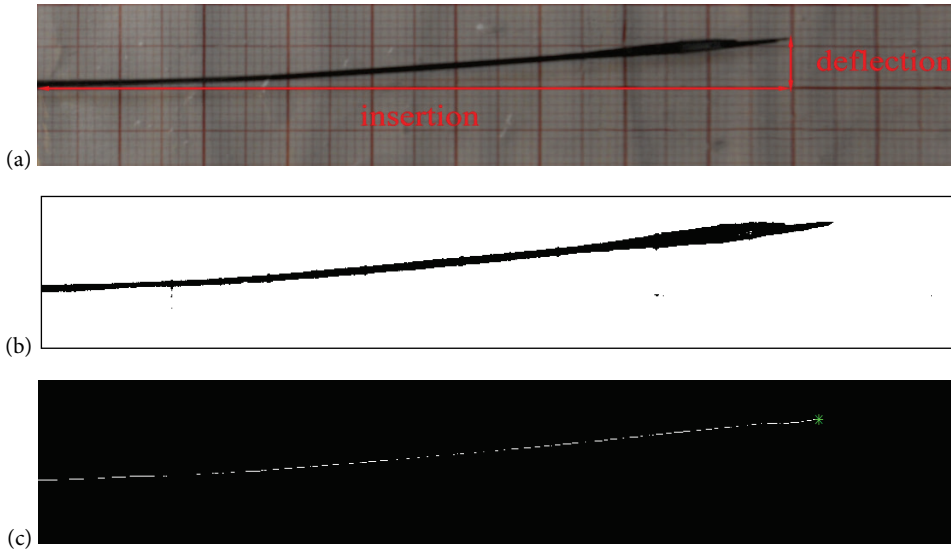


Figure 4.6. Image processing of experimental data. (a) Original image of the final position of the needle. (b) Binary image. (c) Skeleton with end points. This image corresponds to a measurement for Condition 2 (offset 6 mm, stroke 4 mm, left) with the converging ring.

4.4. RESULTS

4.4.1. Converging ring

The measurements for the converging interlocking ring were initially completed successfully 61 out of 64 times. The three failed measurements were caused by motors not actuating the wires correctly and were repeated. The needle steered to a direction opposite to the one expected two times in Condition 6 and two times in Condition 8; these four measurements were excluded from the analysis. Another three measurements (one measurement for each of Conditions 4, 5, and 6) were excluded, because the needle touched the bottom of the cart. The results are summarized in Table 4.3 and Figure 4.7. The highest mean deflection-to-insertion depth ratio was 0.069, achieved for Condition 4 (i.e., offset 6 mm, stroke 6 mm, and direction left), with a standard deviation of 0.027. Among the conditions with high deflection-to-insertion ratio (i.e., > 0.050), Condition 1 showed the lowest variability (i.e., standard deviation of 0.019).

4.4.2. Diverging ring

The measurements for the diverging ring were initially completed successfully 55 out of 64 times. The nine failed measurements were caused by motors not actuating the wires correctly and were repeated. The needle steered in a direction opposite to the one expected in one measurement for Condition 2 and in one measurement for Condition 4; these measurements were excluded from the analysis. The results are summarized in Table 4.3 and Figure 4.7. Condition 7 exhibited the highest mean deflection-to-insertion ratio: 0.097, with standard deviation of 0.033. Steering to the right led to higher deflection-to-insertion ratios than steering to the left.

For the same steering direction (left or right), no significant differences in the deflection-to-insertion ratio were found between any of the offset or stroke conditions for either interlocking mechanism. For the converging ring, steering to the left resulted in a significantly higher deflection-to-insertion ratio than steering to the right for Conditions 3 (Mann-Whitney $U = 7$, $p = 0.007$, $r = 0.65$) and 4 ($U = 7$, $p = 0.026$, $r = 0.60$). For the diverging ring, steering to the right resulted in a significantly higher deflection-to-insertion ratio than steering to the left for Conditions 6 ($U = 9$, $p = 0.029$, $r = 0.57$) and 7 ($U = 9$, $p = 0.015$, $r = 0.60$). The diverging ring led to significantly larger curvatures than the converging ring in Conditions 5 ($U = 1$, $p = 0.001$, $r = 0.80$), 6 ($U = 3$, $p = 0.011$, $r = 0.69$), and 7 ($U = 0$, $p = 0.00016$, $r = 0.84$).

Table 4.3. Results for steering with the converging ring and the diverging ring.

Condition	Converging ring		Diverging ring	
	Sample size	Deflection-to-insertion ratio (mean \pm standard deviation)	Sample size	Deflection-to-insertion ratio (mean \pm standard deviation)
1 (O4-S4-L)	8	0.065 \pm 0.019	8	0.054 \pm 0.034
2 (O6-S4-L)	8	0.063 \pm 0.033	7	0.060 \pm 0.022
3 (O2-S6-L)	8	0.047 \pm 0.022	8	0.054 \pm 0.029
4 (O6-S6-L)	7	0.069 \pm 0.027	7	0.080 \pm 0.042
5 (O4-S4-R)	7	0.033 \pm 0.019	8	0.093 \pm 0.022
6 (O6-S4-R)	5	0.048 \pm 0.024	8	0.096 \pm 0.025
7 (O2-S6-R)	8	0.019 \pm 0.013	8	0.097 \pm 0.033
8 (O6-S6-R)	6	0.049 \pm 0.033	8	0.094 \pm 0.059

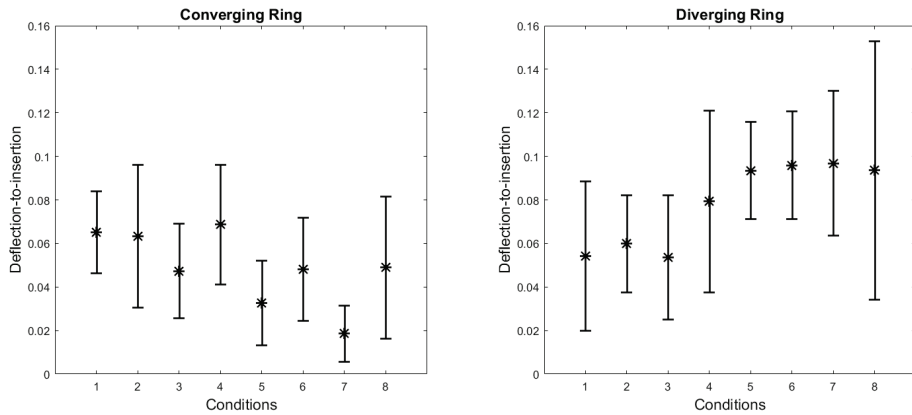


Figure 4.7. Deflection-to-insertion ratio when using the converging ring and diverging ring. The asterisk represents the mean value and the error bars represent the standard deviation.

4.5. DISCUSSION

In this study we have presented a prototype of an ovipositor-inspired needle composed of seven Nitinol wires kept together at the needle tip with a conical interlocking ring. Our goal was to prevent the bifurcation of the wires, a phenomenon observed in a previous version of the prototype [15], and consequently to increase the steering curvature. The conical ring was used in two different configurations: (1) as a “converging ring”, where the wires tend to move toward the center, (2) as a “diverging ring”, where the wires tend to move away from the center. The performance of the needle with both rings has been investigated in a 5%wt gelatine phantom.

In a previous version of the prototype [15] we were creating first an asymmetry between two wires and then reinforcing it by advancing two other wires with the same offset. In the current prototype the offset is created between four wires (i.e., two pairs) and the other two wires (i.e., one pair). The goal of the asymmetry in the first prototype was to create a “discrete bevel tip” which would then make the needle curve in the direction of the bevel. In the current prototype, we use the offset and the stroke to create an asymmetry that mimics a pre-bent tip. Using a pre-bent tip allows for higher curvatures than a normal bevel-tip needle (see Section 4.1.1).

The results showed that for three out of the eight tested conditions (Conditions 5, 6, and 7), the diverging ring led to statistically higher steering curvatures than the converging ring, which is against our hypothesis. A possible reason why the converging ring led to lower steering curvatures than the diverging ring is the interaction between the wires, which is present when using the converging ring and not with the diverging ring. Specifically, during

the actuation sequence, some of the wires are protruding because of the offset created between them (see Figure 4.4c). When the wires are moved over a distance equal to the stroke, the pair of wires that lies behind pushes the protruded wires towards the opposite direction, reducing the final curvature. Another possible explanation for the unexpected steering performance of the diverging ring is the following: with the converging ring, the wires are directed first outwards when entering the holes, and then inwards when exiting the holes, as the diameter of the ring decreases over the ring length (Figure 4.1a). With the diverging ring, on the other hand, the wires are directed only outwards. In other words, in the converging ring the wires are bent twice, whereas in the diverging ring, they are bent only once. This might have affected their local stiffness, which could explain why the steering curvatures obtained with the converging ring were smaller than the curvatures obtained with the diverging ring.

4

In the previous prototype, the steering direction was opposite to the expected one (i.e., needle steering to the left while it was expected to steer to the right and vice versa) in 8 out of 50 trials (16%), whereas in the current prototype, this phenomenon was observed in 6 out of 128 trials (4.69%; 2 of which with the diverging ring). The reduced incidences of “wrong” steering could be explained by the fact that, whereas the tolerance of the interlocking ring in the previous prototype made the wires occasionally follow random directions, in the current prototype the motion of the wires was better controllable and therefore the final direction was more predictable.

The highest mean value (0.097, Condition 7) of deflection-to-insertion ratio obtained with the diverging ring is comparable to those reported by Ryu et al. [25], that is, 0.12 for a needle diameter of 1.67 mm. The ratio corresponds to deflections of around 10 mm over a distance of 90 mm. Such a needle can be used to compensate for motion of tissues and organs in the environment and/or the targets in brachytherapy [2].

The total length of the offset and stroke created between the wires can be seen as the length of a pre-bent segment. Adebar et al. [3] showed that an increase in the length of the bent-tip leads to higher curvatures. In our case the values of this length (i.e., offset + stroke) are 8, 10, and 12 mm (see Table 4.2). With the converging ring, the deflection-to-insertion ratio is indeed higher when the sum of the offset and stroke is higher (i.e., $6 + 6 = 12$ mm); this difference is less visible for the diverging ring. The reason of this might be that with the diverging ring the wires need just a small offset to bend, and the effect of the additional stroke does not change the amount of steering; moreover, the wires in the case of the diverging ring are already pre-directed towards a certain direction (i.e., controllably bifurcated), and since there is no interaction between the wires, the offset might not be contributing to steering.

One limitation of this work was that the transmissions of individual wires occasionally jammed and the motors got stuck. A different design of the housing of the motors could solve

this problem. For example, a larger actuation unit could be used, where the motors with their relative spindles are not constrained, so that they do not get stuck against the wall of the case. Second, we observed that the deflection-to-insertion ratio differed between the two steering direction, left and right. Specifically, the needle steered more to the right than to the left in the case of the diverging ring, and vice versa in the case of the converging ring. This could have been caused by a bias in the wires or by an axial rotation of the ring, making the wires twist, thereby affecting their movement and bending curvature. Third, during our tests we have assumed that the needle deflection occurs only in the steering plane. However, during the experiments we observed that the needle also tended to deflect downwards. This phenomenon is likely to have been caused by the weight of the interlocking ring. Jahya et al. [30] also reported such an “out of plane” deflection and showed that this phenomenon increases with the degree of bevel angle. Fourth, real-time control of the motors actuation was not possible, since the settings were chosen and loaded every time before the start of each test. A continuous instead of stepwise motion would be preferred, in order to limit any effects of the inertia of the gelatine cart on the motion of the needle.

In future work, the steering curvature of the ovipositor-inspired needle can be increased by decreasing the diameter of the needle [5]. This can be done by using fewer wires and/or wires with a smaller diameter. The wires can also be treated, in order to create a fixed asymmetry at the tip; for example, heat treatment can be used to curve the distal end [31]. A flexible or compliant structure to keep the wires together instead of a rigid interlocking ring could also assist in increasing steerability. Finally, the needle should be tested in substrates with different degrees of stiffness and heterogeneity.

4.6. CONCLUSION

This paper presents a design solution to increase the steering curvature of a wasp ovipositor-inspired needle with a diameter of 1.55 mm. We showed that the needle can steer through a 5%wt gelatine phantom by generating an asymmetry at the tip and two configurations of a conical interlocking mechanism (converging and diverging) that mimics a pre-bent needle. The highest mean deflection-to-insertion ratio achieved was 0.097 (standard deviation of 0.033), which is higher than the corresponding ratio of 0.078 achieved by a previous version of the prototype with a straight interlocking ring. This higher ratio was achieved, however, when using the diverging rather than the converging conical ring, which runs opposite to our hypothesis. We can conclude that reducing the bifurcation of the wires is not enough for increasing the steering curvature and that inducing this same phenomenon instead could lead to higher curvatures.

REFERENCES

- 1 Scali M, Pusch TP, Breedveld P and Dodou D. Needle-like instrument for steering through solid organs: a review of the scientific and patent literature. *Proc Inst Mech Eng. H J Eng Med.* 2016; 231(3):250–65.
- 2 Stone NN, Roy J, Hong S, Lo YC and Stock RG. Prostate gland motion and deformation caused by needle placement during brachytherapy. *Brachytherapy* 2002; 1:154–60.
- 3 Adebar TK, Greer JD, Laeseke PF, Hwang GL, Okamura AM. Methods for improving the curvature of steerable needles in biological tissue. *IEEE Trans Biomed Eng.* 2016; 63(6):1167–77.
- 4 Wellborn PS, Swaney PJ. and Webster RJ. Curving clinical biopsy needles: can we steer needles and still obtain core biopsy samples? *J Med Devices.* 2016; 10(3):030904.
- 5 Van Veen YR, Jahya A, Misra S. Macroscopic and microscopic observations of needle insertion into gels. *Proc Inst Mech Eng H.* 2012; 226(6):441–9.
- 6 Majewicz A, Wedlick TR, Reed KB, Okamura AM. Evaluation of robotic needle steering in ex vivo tissue. *Proceedings of the 2010 IEEE International Conference on Robotics and Automation*; 2010 May 3-7; Anchorage, AK, USA. IEEE; 2010 p. 2068–73.
- 7 Konh B, Honarvar M, Darvish K, Hutapea P. Simulation and experimental studies in needle–tissue interactions. *J Clin Monit Comput.* 2017;31(4):861–72.
- 8 Jiang S and Wang X. Mechanics-based interactive modeling for medical flexible needle insertion in consideration of nonlinear factors. *J Comput Nonlin Dyn.* 2016; 11(1):011004.
- 9 Van de Berg NJ, Dankelman J and van den Dobbelsteen JJ. Design of an actively controlled steerable needle with tendon actuation and FBG-based shape sensing. *Med Eng Phys.* 2015; 37(6):617–22.
- 10 Ayvali E, Ho M and Desai JP. A novel discretely actuated steerable probe for percutaneous procedures. In *Experimental Robotics*, Springer, 2014: 115–23.
- 11 Wedlick TR and Okamura AM. Characterization of pre-curved needles for steering in tissue. *Proc IEEE Eng Med Biol Soc.* 2009: 1200–03.
- 12 Swaney PJ, Burgner J, Gilbert HB and Webster RJ. A flexure-based steerable needle: high curvature with reduced tissue damage. *IEEE Trans Biom Eng.* 2013; 60(4):906–9.
- 13 Khadem M, Rossa C, Usmani N, Sloboda RS and Tavakoli M. Introducing notched flexible needles with increased deflection curvature in soft tissue. *IEEE Int Conf on Advanced Intelligent Mechatronics (AIM)*; 2016 Jul 12–15; Banff, AB, Canada. IEEE; 2016 p.1186–91.
- 14 Patil S, Burgner J, Webster RJ, Alterovitz R. Needle steering in 3-D via rapid replanning. *IEEE Trans Rob.* 2014; 30(4):853–64.
- 15 Scali M, Pusch TP., Breedveld P, Dodou D. Ovipositor-inspired steerable needle: design and preliminary experimental evaluation. *Bioinspir Biomim.* 2017; 13(1):016006.
- 16 Gherardi G. *Fine-needle Biopsy of Superficial and Deep Masses: Interventional Approach and Interpretation Methodology by Pattern Recognition* Springer Science & Business Media (2010).
- 17 Podder T, Clark D, Sherman J, Fuller D, Messing E, Rubens D et al. In vivo motion and force measurement of surgical needle intervention during prostate brachytherapy. *Med Phys.* 2006; 33(8):2915–22.
- 18 Bui VK, Sukho P, Park JO and Ko SY. A novel curvature-controllable steerable needle for percutaneous intervention. *Proc Inst Mech Eng H J Eng Med.* 2016; 230(8):727–38.
- 19 Datla NV, Konh B and Hutapea P. Studies with SMA actuated needle for steering within tissue. *ASME Conf. on Smart Material Adaptive Structures and Intelligent Systems (SMASIS)*, 2014.

- 20 Ko SY and y Baena FR. Toward a miniaturized needle steering system with path planning for obstacle avoidance. *IEEE Trans. Biom. Eng.* 2013; 60(4): 910–7.
- 21 Ko SY, Frasson L, and y Baena FR. Closed-loop planar motion control of a steerable probe with a “programmable bevel” inspired by nature. *IEEE Trans Robot.* 2011; 27(5): 970–83.
- 22 Majewicz A, Marra SP, van Vledder MG, Lin M, Choti MA, Song DY et al. Behavior of tip-steerable needles in ex vivo and in vivo tissue. *IEEE Trans Biomed Eng.* 2012; 59(10):2705–15.
- 23 Minhas DS, Engh JA, Fenske MM, Riviere CN. Modeling of needle steering via duty-cycled spinning. *Proc IEEE Eng Med Biol Soc 29th Annu Int Conf; 2007 Aug 22-26; Lyon, France. IEEE;* 2007 p.2756-59.
- 24 Misra S, Reed KB, Schafer BW, Ramesh KT and Okamura A M. Observations and models for needle-tissue interactions. *IEEE Int Conf Robot Autom; 2009 Sept 3–6; Minneapolis, MN, USA. IEEE;* 2009 p.2687–92.
- 25 Okazawa S, Ebrahimi R, Chuang J, Salcudean SE and Rohling R. Hand-held steerable needle device. *IEEE/ASME Trans Mechatron.* 2005; 10(3):285–96.
- 26 Ryu SC, Quek ZF, Koh JS, Renaud P, Black RJ, Moslehi B, Daniel BL, Cho KJ and Cutkosky MR. Design of an optically controlled MR-compatible active needle. *IEEE Trans Robot.* 2015; 31(1):1–11.
- 27 Rucker DC, Das J, Gilbert HB, Swaney PJ, Miga MI, Sarkar N. and Webster RJ. Sliding mode control of steerable needles. *IEEE Trans Robot.* 2013; 29(5):1289–99.
- 28 Wood NA, Shahrouh K, Ost MC and Riviere CN. Needle steering system using duty-cycled rotation for percutaneous kidney access. *Proc IEEE Eng Med Biol Soc Int Conf.* 2010: 5432–35.
- 29 Farrer AI, Odéen H, de Bever J, Coats B, Parker DL, Payne A and Christensen DA. Characterization and evaluation of tissue-mimicking gelatin phantoms for use with MRgFUS. *J Ther Ultrasound.* 2015; 3(9).
- 30 Jahya A, van der Heijden F and Misra S. Observations of three-dimensional needle deflection during insertion into soft tissue. *Proc IEEE/EMBS Int Conf Biomed Robot Biomechatron.* 2012: 1205–10.
- 31 Gilbert HB and Webster RJ. Rapid, reliable shape setting of superelastic nitinol for prototyping robots. *IEEE Robot Autom Lett.* 2016; 1(1):98–105.

Chapter 5

Experimental Evaluation of a Self-Propelling Bio-Inspired Needle in Single- and Multi-Layered Phantoms

Published as:

Scali M, Breedveld P and Dodou D. Experimental evaluation of a self-propelling bio-inspired needle in single- and multi-layered phantoms. *Scientific Reports*. 2019; 9:19988. <https://doi.org/10.1038/s41598-019-56403-0>.

Licensed under CC BY 4.0.

ABSTRACT

In percutaneous interventions, reaching targets located deep inside the body with minimal tissue damage and patient pain requires the use of long and thin needles. However, when pushed through a solid substrate, a structure with a high aspect ratio is prone to buckle. We developed a series of multi-element needles with a diameter smaller than 1 mm and a length larger than 200 mm, and we experimentally evaluated the performance of a bio-inspired insertion mechanism that prevents needle buckling of such slender structures. The needles consisted of Nitinol wires and advance into a substrate by pushing the wires forward one after the other, followed by pulling all the wires simultaneously backward. The resulting net push force is low, allowing the needles to self-propel through the substrate. We investigated the effect of the needle design parameters (number of wires and their diameter) and substrate characteristics (stiffness and number of layers) on the needle motion. Three needle prototypes (consisting of six 0.25-mm wires, six 0.125-mm wires, and three 0.25-mm wires, respectively) were inserted into single- and multi-layered tissue-mimicking phantoms. The prototypes were able to move forward in all phantoms without buckling. The amount of needle slip with respect to the phantom was used to assess the performance of the prototypes. The six-wire 0.25-mm prototype exhibited the least slip among the three prototypes. Summarizing, we showed that a bio-inspired motion mechanism prevents buckling in very thin (diameter <1 mm), long (length >200 mm) needles, allowing deep insertion into tissue-mimicking phantoms.

5.1. INTRODUCTION

Percutaneous procedures, such as biopsy sampling [1, 2], anaesthesia [3, 4], and brachytherapy [5, 6], are minimally invasive interventions where a needle is advanced through soft tissue in order to collect samples, inject drugs, or place radioactive seeds. When a needle is advanced through tissue, forces arise at the needle tip and along the needle body. The force acting on the needle by the surrounding tissue has been described by Okamura et al. [7] as the sum of three components: surface stiffness force ($\mathbf{F}_{\text{stiff}}$), cutting force (\mathbf{F}_{cut}), and friction force (\mathbf{F}_{fric}). In order for the needle to move forward into the tissue, the insertion force (\mathbf{F}_{in}) applied by the operator has to overcome the sum of these components, that is:

$$\mathbf{F}_{\text{in}} = -\mathbf{F}_{\text{stiff}} - \mathbf{F}_{\text{cut}} - \mathbf{F}_{\text{fric}} \quad (5.1)$$

$$\mathbf{F}_{\text{in}} = \begin{cases} -\mathbf{F}_{\text{stiff}}, & x = 0 \\ -\mathbf{F}_{\text{cut}} - \mathbf{F}_{\text{fric}}, & 0 < x < d_1 \end{cases} \quad (5.2)$$

where x is the depth of the needle into the tissue, and d_1 is the end of the tissue layer (Figure 5.1a).

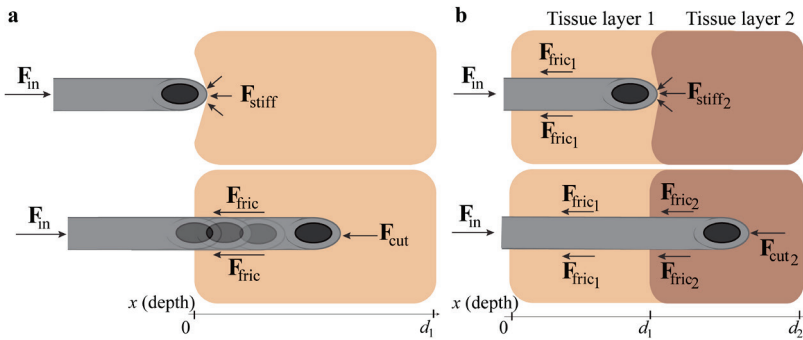


Figure 5.1. Needle insertion into a body tissue. (a) Insertion through a single tissue layer \mathbf{F}_{in} = insertion force, $\mathbf{F}_{\text{stiff}}$ = surface stiffness force, \mathbf{F}_{fric} = friction force and \mathbf{F}_{cut} = cutting force. (b) Insertion through two tissue layers. $\mathbf{F}_{\text{fric}_1}$ is the friction force of the tissue layer 1, $\mathbf{F}_{\text{stiff}_2}$, $\mathbf{F}_{\text{fric}_2}$ and $\mathbf{F}_{\text{cut}_2}$ are the surface stiffness force, the friction force, and the cutting force of the tissue layer 2, respectively. The axis (x) represents the depth of the needle inside the tissue. $x = 0$ is the start of the (first) tissue layer, $x = d_1$ is the end of the (first) tissue layer and the start of the second tissue layer, and $x = d_2$ is the end of the second tissue layer.

The surface stiffness force is due to the elasticity of the tissue and occurs when puncturing the skin or membrane surrounding an organ. The cutting force is generated at the tip of the needle when slicing through the tissue and includes the tissue stiffness force [8]. Assuming that the inner structure of the tissue is homogeneous, the cutting force is independent from

the insertion depth. The friction force acts along the length of the needle and is a combination of Coulomb friction, adhesive friction, and viscous friction (i.e., damping) [7]. The Coulomb friction force is linearly dependent on the normal force acting on the needle body as a reaction to the compression applied to the tissue by the needle (also called clamping force [9]). The adhesive friction force is caused by the tendency of the tissue to stick on the needle surface during insertion [10]. The viscous friction force depends on the needle-tissue interaction damping coefficient and the velocity of the needle insertion. In literature, several friction force models for needle-tissue interaction study exist [11], some of which are simplified, considering only the Coulomb friction force (e.g., Winkler's foundation model [12]), and others being more complex, also including the adhesive and viscous friction elements (e.g., Karnopp model [7], Dahl model [13]). Carra et al. [13] presented a model that takes into account the needle passing through different tissue layers, such as skin, fat, muscle, and connective tissue. Each of these layers contributes with its own cutting, stiffness, and friction forces [13, 14]. To illustrate, for a substrate consisting of two layers, the insertion force has to overcome the resistance of both layers, that is:

$$\mathbf{F}_{in} = \begin{cases} -\mathbf{F}_{fric_1} - \mathbf{F}_{stiff_2}, & x = d_1 \\ -\mathbf{F}_{fric_1} - \mathbf{F}_{cut_2} - \mathbf{F}_{fric_2}, & d_1 < x < d_2 \end{cases} \quad (5.3)$$

Where \mathbf{F}_{in} is the insertion force, \mathbf{F}_{fric_1} is the friction force within tissue layer 1, \mathbf{F}_{fric_2} is the friction force within tissue layer 2, \mathbf{F}_{stiff_2} is the surface stiffness force of tissue layer 2, \mathbf{F}_{cut_2} is the cutting force of tissue layer 2, and d_1 and d_2 are the positions of the needle when it reaches the end of tissue layer 1 (i.e., the start of tissue layer 2) and the end of tissue layer 2, respectively (Figure 5.1b).

When the surface stiffness of the tissue to be penetrated and/or the friction force is high, the \mathbf{F}_{in} needs to increase to compensate for these forces. If \mathbf{F}_{in} reaches the critical load of the needle, buckling occurs [15]. Buckling is expressed as a lateral bending of the needle body along its length. Sudden bending of the needle as a result of buckling can damage the surrounding tissue and reduce the accuracy of needle positioning during the procedure [16].

During puncturing, the critical load (or Euler load) of a slender structure, such as a needle, can be calculated as $F_{load} = \frac{\pi^2 EI}{(KL)^2}$, where E is the Young's modulus of the needle, I is the second moment of area of the cross section of the needle, K the effective factor which takes into account the end-condition of the needle (e.g., if both ends are fixed, $K=0.5$, if both ends are pinned, $K=1$), and L is the unsupported length of the needle. The critical load for a needle being pushed through the tissue is defined by an extended Euler's load equation

$$F_{load} = \frac{\pi^2 EI}{(KL)^2} + \frac{\mu L^2}{\pi^2}, \text{ where } \mu \text{ is the spring stiffness of the tissue [17].}$$

From Euler's equation, it can be seen that increasing the aspect ratio of the needle decreases the critical buckling load. Long and thin (<1 mm) needles are necessary to be able to reach deep targets in a minimally invasive way. Long and thin needles are, however, by default too flexible to be pushed deeply inside solid structures without buckling, and strategies need to be employed in order to increase the critical buckling load of such needles.

In general, buckling of a slender structure can be prevented by increasing the critical buckling load of the structure or by reducing the axial load applied to the structure [18]. In nature, some species of parasitic wasps are able to insert their slender needle-like structure (aspect ratio up to 260 [19]), called ovipositor, without buckling into solid substrates and deposit eggs inside host larvae [19, 20]. The ovipositor consists of multiple slender elements, called valves that are interconnected along their length with a tongue-and-groove mechanism and are able to slide along each other. The wasp supports the part of the ovipositor that is outside the substrate with a sheath. The sheath prevents buckling by increasing the cross-section area and by decreasing the unsupported length (see Euler's equation). For the part of the ovipositor that advances through the solid substrate, the wasp prevents buckling by employing a so-called push-pull mechanism, according to which one valve at the time is pushed forward, while the other valves are pulled backwards. The advantage of this push-pull mechanism compared to pushing of the entire structure at once is that, in the former mechanism, the unsupported length of the valve that is pushed forward (i.e., L in Euler's equation) is decreased, which means that the critical buckling load increases. Additionally, the pushing force of the moving valve is counterbalanced by the pulling force on the other ones, which limits the total axial load applied to the structure (i.e., pushing force), keeping it under the value of the critical buckling load. The presence of directional serrations at the tip allows the valves that are pulled to anchor to the tissue and remain stationary, thereby providing support to the valve that is being pushed [21, 22]. As long as the force acting on the stationary valves is higher than the force acting on the pushed valves, the wasp can insert the ovipositor into the substrate while preventing buckling [22].

Over the past decade, the ovipositor mechanism has inspired researchers to develop novel needle prototypes to overcome buckling during needle insertion [23, 24]. Rodriguez y Baena and co-workers presented a series of ovipositor-inspired prototypes with diameters ranging between 12 mm [25] and 2.5 mm [26]. The probes were made out of four elements, each of them with a bevel-tip and interlocked along their length similar to the wasp ovipositor. One segment at the time was pushed forward while the other three elements were kept stationary. The authors showed that inserting a probe into a substrate using this push-pull motion resulted in less tissue damage than a single-element probe pushed through the tissue [27].

In previous work [24], we developed an ovipositor-inspired self-propelling needle with a diameter of 1.2 mm and a length of 160 mm, consisting of seven Nitinol wires

(diameter = 0.25 mm) that were connected at the tip and actuated independently. The wires were pushed forward one after the other, while the other wires remained stationary. At the end, by pulling all the wires simultaneously, the needle was able to advance without buckling on a straight path as well as curved paths inside a gelatine phantom.

Currently, thin needles used in clinical practice are short to prevent buckling during insertion, therefore they can only reach superficial targets [28]. Examples of thin, short needles commonly used are needles for vaccinations (22–25 G), which are 16–38 mm long [29], and for insulin delivery (29–31 G), which are 6–13 mm long [30]. To our knowledge, needles with diameter smaller than 1 mm and length larger than 200 mm (length-to-diameter ratio >200) have not been developed yet. One reason of this might be that increasing the length-to-diameter ratio of the needle increases the risk of buckling (cf. Euler's load equation: if the diameter decreases, then I decreases and so does the critical load F_{load}), making the insertion of such needle into the tissue very challenging. It is thus relevant to investigate whether the ovipositor-inspired buckling prevention mechanism is functional for ultra-thin long needles.

As mentioned previously, the unsupported length (L) has a large impact on the value of the critical buckling load. If the length is decreased by a scale factor 2, the F_{load} will increase by a scale factor 4. When using a multiple-element needle with a push-pull mechanism, the diameter of the moving element is smaller than the total needle diameter (e.g., 0.25 mm vs. 1.2 mm), but at the same time the unsupported length is kept very small, by moving the wires forward only for a short distance. The result of this is an increase of the F_{load} compared to when the entire needle is pushed forward at once.

Additionally, there is no study that shows how an ovipositor-inspired needle behaves in multi-layered tissue-mimicking phantoms. This type of experiment is useful to understand the needle behaviour in environments that are well-controlled, yet closer than homogeneous phantoms to biological organs, where the needle has to move through several tissue layers with different degrees of stiffness.

In this study, we present three ovipositor-inspired self-propelling needle prototypes with diameters of 0.8, 0.6, and 0.4 mm, and a length of 300 mm. The three prototypes consisted of six Nitinol wires with diameter 0.25 mm, three Nitinol wires with diameter 0.25 mm, and six Nitinol wires with diameter 0.125 mm, respectively. Our aim was to investigate the effect of the substrate properties (i.e., stiffness and number of layers) and the needle design parameters (i.e., number of wires and diameters) on the self-propelling motion. To assess that, the performance of the three needle prototypes was evaluated in single- and multi-layered tissue-mimicking phantoms.

Compared to previous studies, this work presents the following new components: (1) decreasing the diameter of the needle prototype to less than 1 mm and increasing the length

to more than 200 mm (i.e., increasing the length-to-diameter ratio to a value > 200), (2) testing a continuous motion, where the elements are pushed and pulled simultaneously to achieve the self-propelling motion, (3) providing a systematic evaluation of various diameters and numbers of wires on substrates of various stiffness degrees in order to gain insight into the functional principles and working envelope of ovipositor-inspired needle systems, and (4) investigating the behaviour of the needle in multi-layer tissue-mimicking phantoms.

5.2. MATERIALS AND METHODS

5.2.1. Needle tip design and prototype

Our previous ovipositor-inspired prototypes [24, 31] consisted of seven Nitinol wires connected at the tip with an interlocking ring with seven individual holes through which the wires were fed. One wire was glued to the central hole, whereas the other six wires could slide freely through the six holes arranged in a circle around the central hole. The use of an interlocking ring had two limitations: (1) the use of individual holes left gaps in between the wires, permitting gelatine residues to enter the gaps and push the wires apart, making the trajectory into the substrate less predictable. (2) The presence of the ring at the tip increased the diameter of the needle locally from 0.8 mm (body) to 1.2 mm (tip). In order to solve these two problems, in the prototypes presented here, the interlocking ring was replaced with a thin-walled shrinking tube placed around the wires at the tip and fixated to one of the wires, leaving the rest of the wires free to move back and forth.

Three needle prototypes with diameters of 0.8, 0.6, and 0.4 mm were developed. The first prototype consisted of six Nitinol wires (W) with a diameter (D) of 0.25-mm (called henceforth $W6-D0.25$), kept together at the tip by a 10-mm long shrinking tube (Vention Medical) with an expanded inner diameter (EID) = 0.813 mm and a wall thickness (W) = 0.013 mm. The second prototype consisted of three Nitinol wires with a diameter of 0.25 mm ($W3-D0.25$), connected with a 10-mm long shrinking tube with a EID = 0.58 mm and W = 0.006 mm. Finally, the third prototype consisted of six Nitinol wires with a diameter of 0.125 mm ($W6-D0.125$), connected by a 10-mm long shrinking tube with EID = 0.406 mm and W = 0.006 mm. The wires had a total length of 390 mm, of which 90 mm were placed inside an actuation unit and 300 mm outside.

The shrinking tube was attached to one of the Nitinol wires in three steps. First, two cuts were made close to each other in the shrinking tube. Second, the wire was passed from the inside of the tube to the outside via the first cut and then re-entered into the tube via the second cut (Figure 5.2). Third, the wire was glued (Pattex instant glue, Gold original) to the

outside of the shrinking tube in between the two cuts. The other wires were fed through the tube one by one and were able to move freely back and forth relative to the tube.

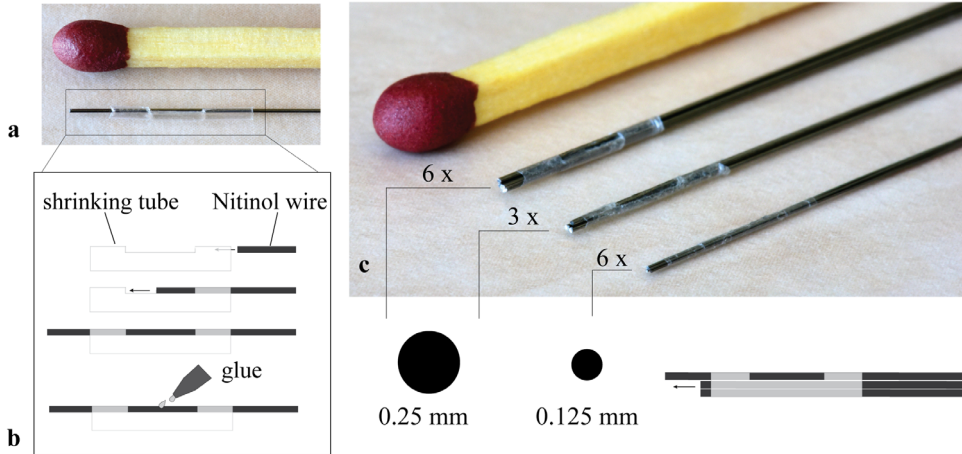


Figure 5.2. Needle tip design and prototypes. (a) Photo of a Nitinol wire connected to a shrinking tube (Venton Medical). (b) Stepwise process to fix a Nitinol wire to the tube (c) Photos of the tip of the six-wire 0.25-mm prototype ($\text{Ø} = 0.8\text{mm}$), three-wire 0.25-mm prototype ($\text{Ø} = 0.6\text{ mm}$), and six-wire 0.125-mm prototype ($\text{Ø} = 0.4\text{ mm}$).

5.2.2. Actuation unit

The actuation unit (Figure 5.3a-b) consisted of six linear stepper motors (RobotDigg Equip Makers) which were able to move each individual wire back and forth. Each wire was clamped to a slider and fed through a telescopic tube system in order to prevent buckling. Bent capillary tubes guided the wires towards the central axis of the system. Universal joints transmitted the motion from the leadscrew of the stepper motors to the sliders. A printed circuit board (PCB) for the control of the stepper motors was developed in-house. The control unit contained an Arduino board (MEGA 2560), stepper motor driver (A4988, Pololu), and LEDs that lit up when the connected motor was running. A set of six optical sensors, placed on a plate behind each of the linear stepper motor, automatically reset the motors to their initial position.

5.2.3. Experimental setup

The experimental setup (Figure 5.3d) consisted of the needle connected to the actuation unit, an aluminium base, an aluminium cart, a gelatine phantom in a customized box, and a data acquisition system. The actuation unit was fixed to the table and aligned to the aluminium

base (550 × 100 mm). The aluminium cart (220 × 90 mm) with the box (200 × 50 × 25 mm) was mounted to four ball bearings from which the oil was removed to minimize rolling friction while carrying the gelatine phantom along the aluminium base. A millimetre paper was attached at the bottom of the box and used as reference during needle insertion. Between the actuation unit and the gelatine phantom, the needle was fed through three capillary tubes (T_1 , T_2 , and T_3) arranged in a telescopic manner to avoid buckling during the experiment (Figure 5.3c). Two sets of tubes were used. For the 0.8- and 0.6-mm prototypes, the tube diameters were $T_1 = 2.5$ mm, $T_2 = 1.9$ mm, and $T_3 = 1.3$ mm, and for the 0.4-mm prototype the tube diameters were $T_1 = 1.9$ mm, $T_2 = 1.3$ mm, and $T_3 = 0.9$ mm. The lengths of the tubes were $T_1 = 10$ mm, $T_2 = 10$ mm, and $T_3 = 11$ mm. A laser proximity sensor (MicroEpsilon optoNCDT ILD1420–200, range: 200 mm) was used to record the position of the cart during the experiments. A data acquisition unit (NI USB-6211, 16-bit) in conjunction with LabVIEW 2013 was used to collect the laser sensor data at a sampling frequency of 5 Hz.

5.2.4. Actuation mode

The wires were actuated following two actuation modes. In the first actuation mode, called *step-by step motion*, the wires were moved forward one by one over a pre-defined distance, called *stroke*. Once all the wires reached that distance, they were simultaneously pulled backwards over the same stroke. We will call henceforth each sequence of a forward and backward motion a *cycle*. In the second phase of each cycle, when the wires had all been pulled backwards, the needle pulled itself forward inside the substrate at a distance equal to the stroke.

5.2.5. Gelatine phantoms

Gelatine powder (Dr. Oetker Professional, the Netherlands) was mixed with heated tap water (ca. 100 °C) to create gelatine phantoms. For the experiments, 5% and 10% weight of gelatine powder in water (wt) was used. These concentrations correspond to Young's moduli of, respectively, 5.3 kPa and 17 kPa, measured using a AR-G2 rheometer with parallel plates of 25 mm in diameter as in Scali et al. [32] (see Supplementary Material for more details). Soft tissues in the human body exhibit a wide range of stiffness degrees, from 0.1 kPa for the brain to 100 kPa for soft cartilage [33]. Indicatively, the 5%wt gelatine approximates healthy liver tissue (<6 kPa), and the 10%wt gelatine approximates cirrhotic liver (>12 kPa) [34].

Customized containers with 190 × 47 × 30 mm boxes were used for the liquid mixture of gelatine and water. The layers of the gelatine phantoms were created in two steps. First, 5%

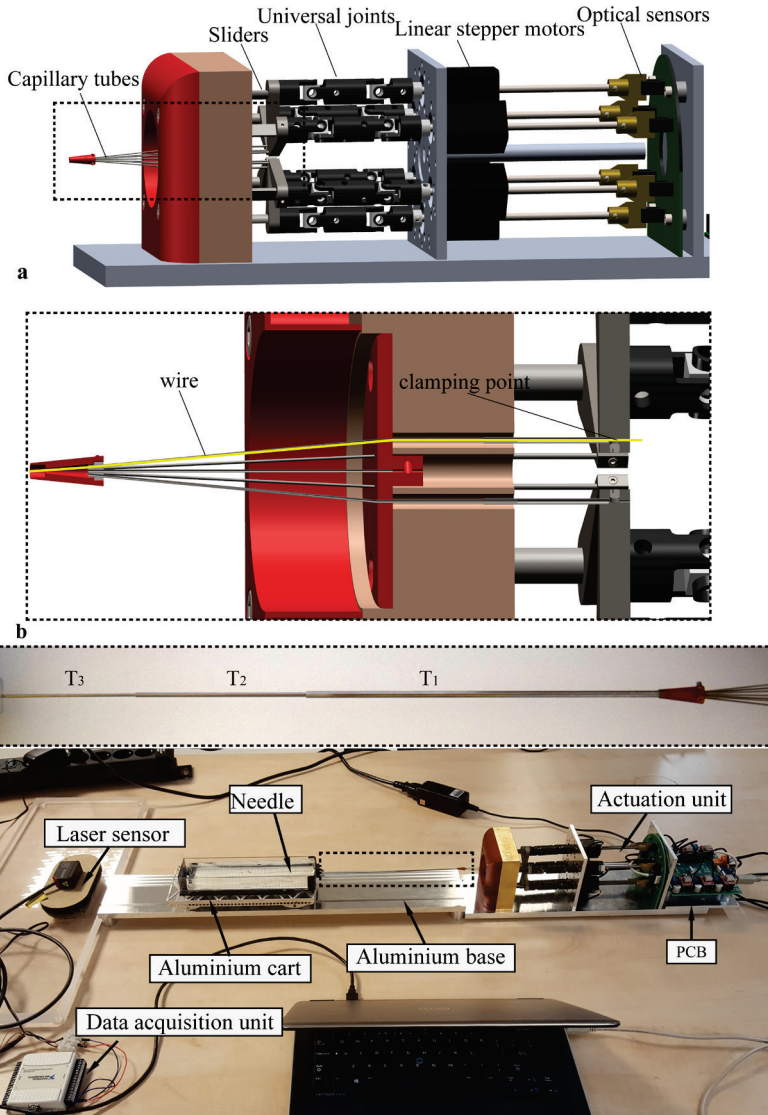


Figure 5.3. Experimental setup. (a) Actuation unit with, from left to right, capillary tubes through which the Nitinol wires are fed, telescopic sliders connected to universal joints, linear stepper motors, and optical sensors (drawing in SolidWorks 2018 by Menno Lageweg/ CC by 4.0). (b) Section view of the frontal part of the actuation unit showing the clamping point of the wire and the telescopic system serving as a buckling prevention mechanism for the wire (drawing in SolidWorks 2018 by Menno Lageweg/ CC by 4.0). (c) Telescopic tube system consisted of three capillary tubes (T₁, T₂, and T₃). (d) Photo of the experimental setup used during the needle insertion experiments.

and 10%wt gelatine phantoms were prepared separately and stored overnight at 4 °C. Then, they were cut in half and the 5%wt layer was placed next to the 10%wt layer. To ensure that the layers are attached, the cut surface of each part was covered with a layer of liquid mixture of 5%wt before putting the layers back into the box. Finally, extra liquid mixture of 5%wt was poured to fill any gap on the contact surface between the two layers. After this process, the boxes were stored for 2 hours at 4 °C in order to solidify the connective part between the gelatine layers.

In total, three gelatine phantom types were used: (1) single-layered phantom consisting of 5%wt gelatine (called henceforth G5) with a total length of 190 mm; (2) multi-layered phantom consisting of one layer 5%wt and a second layer 10%wt gelatine (G5-10), each layer being 95 mm long; and (3) multi-layered phantom consisting of two layers 5%wt separated by a 10-mm layer of 10%wt gelatine (G5-10-5), the first layer 5%wt being 95 mm long and the second 85 mm.

5.2.6. Self-propelling motion

In the case of a needle made out of multiple wires, Equation (5.2) becomes:

$$\sum_{i=1}^N \mathbf{F}_{in,i} = - \sum_{i=1}^N (\mathbf{F}_{fric,i} + \mathbf{F}_{cut,i}) = - \sum_{j=1}^p (\mathbf{F}_{fric,j} + \mathbf{F}_{cut,j}) - \sum_{k=1}^{np} \mathbf{F}_{fric,k} \quad (5.4)$$

where N is the total number of wires, p is the number of protruding wires, and np is the number of non-protruding wires, assuming that no cutting force acts on the non-protruding wires ($\sum_{j=1}^{np} \mathbf{F}_{cut,j} = 0$) (Figure 5.4).

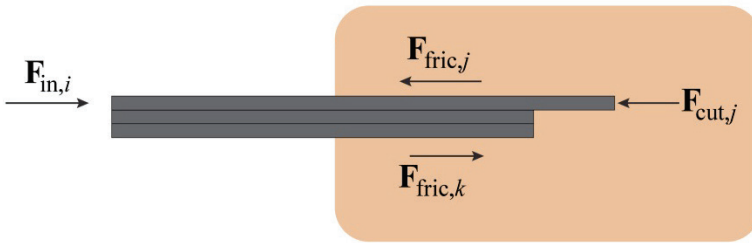


Figure 5.4. Bio-inspired needle insertion into a substrate. $\mathbf{F}_{in,i}$ = total insertion force acting on the needle. $\mathbf{F}_{fric,j}$ = friction force on the protruding wires. $\mathbf{F}_{cut,j}$ = cutting force acting at the tip of the protruding wires. $\mathbf{F}_{fric,k}$ = friction force on the non-protruding wires.

As shown in previous works [24, 35], the needle is able to propel forward through the substrate with a zero net insertion force ($\sum_{i=1}^N \mathbf{F}_{in,i} = 0$) or even net pulling force ($\sum_{i=1}^N \mathbf{F}_{in,i} < 0$) if:

$$-\sum_{j=1}^p (\mathbf{F}_{\text{fric},j} + \mathbf{F}_{\text{cut},j}) - \sum_{k=1}^{np} \mathbf{F}_{\text{fric},k} \leq 0 \quad (5.5)$$

To achieve this, the sum of the friction force and the cutting force of the protruding wires should be smaller than the friction force acting on the non-protruding wires.

$$-\sum_{j=1}^p (\mathbf{F}_{\text{fric},j} + \mathbf{F}_{\text{cut},j}) \leq \sum_{k=1}^{np} \mathbf{F}_{\text{fric},k} \quad (5.6)$$

Once the tissue has been cut (i.e., rupture event), the value of cutting force decreases while the friction force increases with the insertion depth [36, 37]. Equation (5.6) can be satisfied by keeping the number of protruding wires smaller than the number of non-protruding wires ($p < np$), so that the difference between the forces acting on the two groups of wires increases. In the same way, if the contact area between the protruding wires and the substrate is smaller than that of the stationary wires, the friction force on the body of the protruding wires will be lower than the force on the stationary wires. At a certain depth, an equilibrium between the forces acting on the stationary and protruding wires is reached,

$$\sum_{j=1}^p (\mathbf{F}_{\text{fric},j} + \mathbf{F}_{\text{cut},j}) = \sum_{k=1}^{np} \mathbf{F}_{\text{fric},k} \quad (5.7)$$

After that, needle advancement with low net push force is possible, that is, the needle can self-propel through the substrate.

5.2.7. Hypotheses

The slip of the needle per cycle with respect to the gelatine and the number of cycles needed for the needle to travel until a predefined depth were used to assess the effectiveness of the self-propelling of the needle. Assuming that all wires have the same tribological characteristics, that the tips of all wires are identical, that there is perfect contact between the wire and the gelatine, and that the cutting force is negligible, the following hypotheses with respect to the slip of the needle during forward motion through the gelatine were investigated:

1. For a constant number of wires, slip is independent from the wire diameter, because the self-propelling motion relies on the relative friction between the protruding and non-protruding wires.
2. For a constant wire diameter, slip decreases with an increasing number of wires, because the difference between non-protruding and protruding wires is larger in the former case than in the latter.
3. Slip is constant throughout a substrate with constant stiffness.

4. Slip increases when the needle transits from a softer to a stiffer substrate, because the needle encounters more resistance to cut through the stiffer substrate.

5.2.8. Experimental procedure

The procedure for each measurement was as follows:

1. A gelatine phantom (mean \pm standard deviation = 170 ± 0.6 g) was placed inside the box on the cart.
2. The smallest tube of the telescopic system was inserted manually through a hole at the front side of the box for 40 mm inside the gelatine, to ensure that the prototype was inserted in a straight direction. After that, the tube was retracted by 30 mm and fixed at this position so that it does not move during the experiments.
3. The laser sensor was turned on and the needle actuation started. Every measurement was performed with a speed of 2 mm/s and a stroke of 4 mm.
4. The actuation of the needle was let run for 30 cycles or stopped manually once the needle reached an insertion depth of 85 mm.

The needle was cleaned with water after each measurement. A new gelatine phantom was used for each measurement, except when the measurement had to be repeated because of mispositioning of the needle or of the cart. To avoid systematic errors due to the assembly and disassembly of the needles in the actuation unit, the three prototypes were tested one after the other. First the W6-D0.25 was tested in G5, G5-10, and G5-10-5, then the W6-D0.125 was tested in the same three gelatine phantoms, and finally the W3-D0.25 was tested in G5-10. Each prototype-gelatine phantom combination was tested ten times in a randomized order.

During the experiments with the six-wire 0.125-mm prototype, we noticed that, after a certain depth, one or more wires started to buckle in about 50% of the measurements, in particular when the needle was puncturing the 10% layer or was inside the 10% layer. When this happened, the test was stopped and the measurement was repeated.

5.2.9. Data analysis

The raw data recorded by the laser sensor during the tests were imported in MATLAB 2016b. The data included the time and the position of the cart during the test. A Savitzky-Golay filter was used for smoothing the data. The local maxima *peaks* in the plot represent the position of the cart after pulling backwards the six wires, and the local minima *valleys* depict the position of the cart after the six wires have been pushed forward one by one. The distance between two peaks defines a cycle. The peaks and the valleys were detected by applying the function *findpeaks* to the data. We calculated the slip ratio (S_{ratio}) per each cycle as

$$S_{\text{ratio}} = 1 - \frac{d_{\text{meas}}}{d_{\text{theor}}} \quad (5.8)$$

where d_{meas} is the measured distance (i.e., difference between two peaks) and d_{theor} is the theoretical distance travelled (i.e., 4 mm per cycle).

We evaluated the number of cycles at three depths, 55 mm (d_1), 65 mm (d_2), and 85 mm (d_3), where d_1 is the depth at which the needle reaches the 10%wt layer in the phantoms G5-10 and G5-10-5, d_2 is the depth at which the needle transits from the 10%wt layer to the 5%wt layer in G5-10-5, and d_3 is the final depth chosen for all measurements. The number of cycles needed to reach each of the three depths was calculated per phantom. Theoretically, with no slip, the needle should reach d_1 in 14 cycles, d_2 in 16 cycles, and d_3 in 21 cycles. Quantitative data were expressed as mean \pm standard deviation (*SD*).

5.2.10. Statistical analysis

We investigated the performance of the three prototypes during three ranges of cycles, each consisting of 5 cycles: the first 5 cycles (Range 1), from the depth of 55 mm up to the 55 mm + 5 cycles (Range 2), and the 5 cycles preceding the final depth of 85 mm (Range 3). These ranges represent the start, middle, and end of the needle motion inside the gelatine phantom. Independent two-tailed *t*-tests were used to compare the two prototypes with different wire diameter (W6-D0.25 vs. W6-D0.125) and the two prototypes with different number of wires (W6-0.25 vs. W3-0.25) at each of the three ranges. One-way ANOVA and Tukey's post-hoc tests were used to compare the slip ratio between the three gelatine phantoms for the W6-D0.25 prototype and the W6-D0.125 prototype. We conducted one ANOVA test per range (Range 1, Range 2, and Range 3), which led to a total of six statistical comparisons. The significance level was set at $p < 0.001$. The analysis was done in MATLAB 2016b.

5.3. RESULTS

5.3.1. Six-wire 0.25-mm prototype, step-by-step motion, three gelatine phantoms (5%, 5-10%, 5-10-5%)

Figure 5.5a shows the slip ratio over the number of cycles for each gelatine phantom. The mean slip ratio when the needle moved through 5%wt gelatine was about 0.2 and increased to 0.3 once the needle entered the 10%wt layer (in G5-10 and G5-10-5). In G5-10-5, the slip ratio returned to the value of 0.2 once the needle transited from the 10% to the 5%wt layer. The variability of the slip ratio was lower in 5%wt than in 10%wt.

Between cycles 1 and 5, the slip ratio was higher in G5 and G5-10-5 than G5-10. For cycle 6 and higher, the slip ratio remained relatively constant. The depth of 55 mm was reached after 17 cycles in 60% of the measurements in G5 and in 50% of the measurements in G5-10 and G5-10-5. After 20 cycles, the second depth (65 mm) was reached in 50% of the measurements in G5 and in 40% of the measurements in G5-10 and G5-10-5. The final depth (85 mm) was reached after 25 cycles in 40% of the measurements in G5 and G5-10-5, and in 20% of the measurements in G5-10 (see Supplementary Material Fig. S1).

5.3.2. Six-wire 0.125-mm prototype, step-by-step motion, three gelatine phantoms (5%, 5–10%, 5-10-5%)

We excluded two measurements in each of G5 and G5-10-5 and one measurement in G5-10, because of sensor data failure or failure in reaching the final reference distance of 85 mm. The final number of measurements included in the analysis is eight for G5, nine for G5-10, and eight for G5-10-5.

The mean slip ratio when the needle moved through 5%wt gelatine was about 0.3 and increased to 0.5 once the needle entered the 10%wt layer (in G5-10 and G5-10-5). The variability of the slip ratio was lower in 5%wt than in 10%wt. In G5-10-5, the slip ratio decreased again once the 10%wt layer was passed (Figure 5.5b).

The depth of 55 mm was reached after 17 cycles by one measurement in G5-10 and G5-10-5, while the majority (90%) of the measurements needed between 19 and 21 cycles. After 24 cycles, the second depth (65 mm) was reached in 75% of the measurements in G5, in 65% of the measurements in G5-10, and in 50% of the measurements in G5-10-5. The final depth (85 mm) was reached after 30 cycles in 89% of the measurements in G5-10 (see Supplementary Material Fig. S2).

5.3.3. Three-wire 0.25-mm prototype, step-by-step motion, one gelatine phantom (5–10%)

One out of the ten measurements was excluded, because of incorrect data registered by the sensor. The mean slip ratio was approximately 0.3 during the motion of the needle inside 5%wt layer (Figure 5.5c). At the entrance of 10%wt, the median slip ratio increased up to 0.8. Between cycles 1 and 5, the value of the mean slip ratio was higher than in between cycles 5–15 (0.4 vs 0.2). The variability of the slip ratio was lower in 5%wt than in 10%wt.

The depth 55 mm was reached within 20 cycles in 44% of the measurements, the rest of measurements needed between 20 and 25 cycles. Within 30 cycles, the second depth (65 mm) was reached in 55% of the measurements. The final depth (85 mm) was reached in more than 50 cycles in 66% of the measurements (see Supplementary Material Fig. S3).

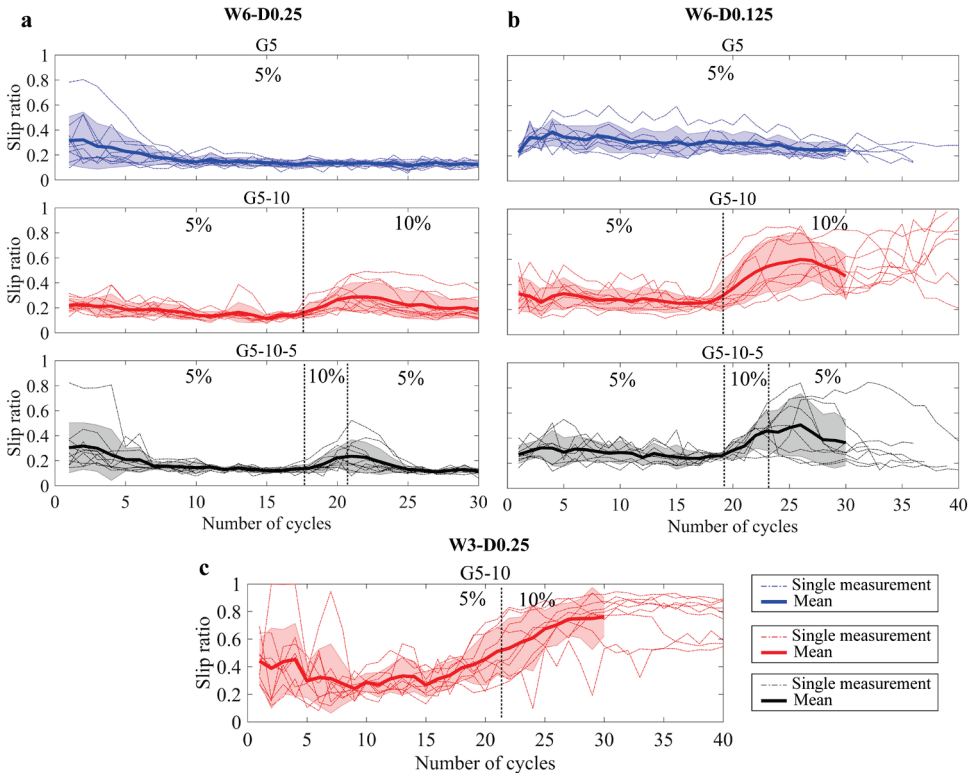


Figure 5.5. Slip ratio per number of cycles during the experiments into phantoms 5%wt (G5), 5%-10%wt (G5-10), and 5%-10%-5% (G5-10-5). (a) Six-wire 0.25-mm prototype (W6-D0.25) actuated with step-by-step motion. (b) Six-wire 0.125-mm (W6-D0.125) prototype actuated with step-by-step motion. (c) Three-wire 0.125-mm (W3-D0.25) prototype actuated with step-by-step motion. The dashed thin lines represent the single measurements, the thick line is the mean value. The area around the mean value represents the standard deviation. Dashed lines indicate the mean number of cycles for the prototypes to reach the different gelatine layers.

5.3.4. Statistical analysis

The slip ratio was significantly lower for the prototypes with the larger wire diameter in Ranges 2 and 3 for each gelatine phantom. The slip ratio was also significantly lower for the prototypes with the larger number of wires (i.e., six wires) in Ranges 2 and 3 (see Table 5.1 and Figure 5.6 for the complete analysis). A significant difference was found between the slip ratio values in the three gelatine phantoms in Range 3 for the six-wire 0.25-mm prototypes, $F(2,27) = 9.77$, $p < 0.001$, and the six-wire 0.125-mm prototype, $F(2,22) = 14.14$, $p < 0.001$. The Tukey's post-hoc test revealed that the slip ratio in 5%wt was significantly lower than the slip ratio in 5–10%wt ($p < 0.001$) for both prototypes.

Table 5.1. Results of the independent two-tailed t -tests. t - and p -values, and the corresponding degrees of freedom (df), are reported for each range of distance within each gelatine phantom.

Prototypes	Gelatine phantom	Range	t -value	df	p -value
W6-D0.25 vs. W6-D0.125	G5	1	-0.857	16	0.404
		2	-9.911	16	< 0.001
		3	-9.518	16	< 0.001
	G5-10	1	-3.010	17	0.008
		2	-5.057	17	< 0.001
		3	-4.795	17	< 0.001
	G5-10-5	1	-0.393	16	0.6993
		2	-5.483	16	< 0.001
		3	-5.680	16	< 0.001
W6-D0.25 vs. W3-D0.25	G5-10	1	-3.605	17	0.002
		2	-8.520	17	< 0.001
		3	-9.411	17	< 0.001

Note. A negative t -value indicates that the mean value of the first prototype is smaller than the second. $p < 0.001$ is annotated in bold.

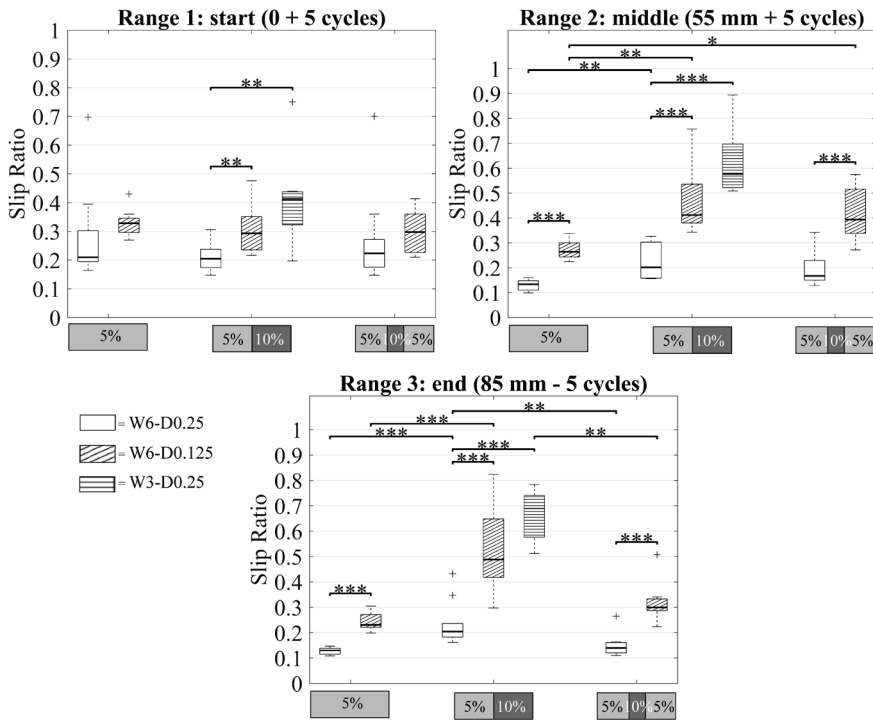


Figure 5.6. Slip ratio in Range 1, Range 2, and Range 3 for G5 (5%), G5-10 (5%-10%), and G5-10-5 (5%-10%-5%). W6-D0.25 (no hatches), W6-D0.125 (diagonal hatches), and W3-D0.25 (horizontal hatches) prototypes. *** $p < 0.001$, ** $p < 0.01$, * $p < 0.05$.

5.3.5. Additional experiments

We performed a series of additional experiments to investigate the needle behaviour inside tissue-mimicking phantoms:

1. We used a second actuation mode, called *continuous motion*, where all wires were actuated simultaneously and were always in motion: one wire moved forward while at the same time the other wires moved backward. When a wire reached the stroke value, it started to move backward while the second wire started to move forward and so on, thus creating a continuous needle motion. We performed ten measurements with the W6-D0.25 prototype inside a G5-10 multi-layered phantom (see Supplementary Material Fig. S4). The needle reached the reference depth of 55 mm in on average 266 s ($SD = 26$ s), 65 mm in 322 s ($SD = 27$ s), and 85 mm in 437 s ($SD = 40$ s). Considering that the motion is continuous, that is, there are no cycles as in the step-by-step motion, the slip ratio was calculated for the total motion

- (i.e., from the initial point to the final depth). The slip ratio was 0.28 at 55 mm depth, 0.29 at 65 mm depth, and 0.32 at 85 mm depth.
2. We used 15%wt gelatine phantoms (corresponding to 31 kPa) to assess the performance of the needle inside stiff tissues. We performed two tests with the six-wire 0.25-mm prototype actuated with step-by-step motion (speed = 2 mm/s, stroke = 4 mm). The results (see Supplementary Material Fig. S5) showed that the slip ratio increased from 0.2 to 0.8 when the needle moved from the 5% to the 15% layer. When the needle moved further inside the 15% layer (ca. 10 cycles), the slip ratio decreased, reaching a constant stable value.
 3. We investigated the behaviour of the needle inside a 5%wt gelatine phantom with a thin layer of plastic foil at the depth of 95 mm. The foil was used to mimic a serous membrane. The needle was able to penetrate the plastic foil in about 5 cycles (Figure 5.7a-b). After puncturing the plastic foil, the needle was able to move through the gelatine with a constant slip ratio of about 0.2 (see Supplementary Material Video S1).
 4. We performed a qualitative test to show the application potential and functionalization of the needle prototype. We replaced one Nitinol wire with a Nitinol tube ($\varnothing = 0.2$ mm) and we connected it to a syringe. Then, we manually inserted the needle into a gelatine phantom and push liquid through the Nitinol tube using the syringe. We could inject water inside the gelatine in the area around the needle tip, which indicates that the needle could be used as injection tool (Figure 5.7c). Additionally, we replaced one Nitinol wire ($\varnothing = 0.25$ mm) with an acrylate recoated optical fibre ($\varnothing = 0.2$ mm). Then, we actuated the needle using the step-by-step sequence. The measurement showed that the needle was still able to propel itself forward and the optical fibre could move through the gelatine phantom as well. The used fibre had a smaller diameter than the Nitinol wire, which means that there was a slightly smaller surface in contact with the substrate. The optical fibre could be also placed in the centre of the needle with the six Nitinol wires around it forming a circle (Figure 5.7d).

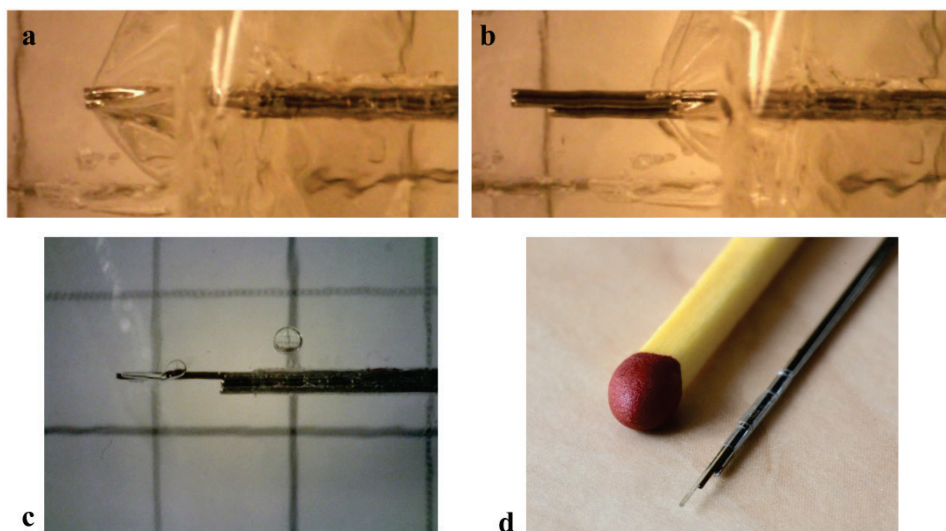


Figure 5.7. Six-wire 0.25-mm needle prototype moving through a plastic foil placed between two layers of 5% gelatine. (a) The needle is pushing the plastic foil without cutting it. (b) The needle cuts the plastic foil and moves forward. Photos made with a Digitale PC-Microscop Dino-Lite (AM73915MZTL 5 Megapixel, 10-140x). (c) Injection of water into a 5%wt phantom with the W6-D0.25 prototype where a Nitinol wires is replaced by a Nitinol tube. (d) Tip of the W6-D0.25 prototype with two Nitinol wires replaced by a Nitinol tube and an optical fibre.

5

5.4. DISCUSSION

In this work, we investigated the influence of the substrate properties (stiffness) and the needle design parameters (number of wires, outer needle diameter) on the self-propelling motion of a bio-inspired needle through tissue-mimicking phantoms. The results of the experiments showed that the slip ratio is significantly lower for a larger diameter (0.25 vs. 0.125 mm) and for a greater number of wires (six vs. three). Hypothesis 1 is not confirmed, as W6-D0.25 exhibited lower slip than W6-D0.125, which means that the difference between the forces acting on the protruding and non-protruding wires in W6-D0.25 was higher than in W6-D0.125. This might have happened because, during the incremental motion, the wires crack the gelatine in such a way that the contact between gelatine and the wire surface is partially lost for the thinner wires. Additionally, the friction of the ball bearing system used for the cart, albeit low, might play a larger role against the forward motion of the needle into the gelatine when using 0.125 mm compared to 0.25 mm. Moreover, at a length of 300 mm, the 0.125 mm wires are more flexible than 0.25 mm; (limited) buckling along the length (e.g., outside the gelatine) might occur more easily for the thinner wires. Summarizing, the self-propelling mechanism is theoretically size-independent because it relies to relative friction

differences, but in reality, side-effects related to the experimental setup have been likely at place, for which reason the results were not supportive to the first hypothesis. The results provided support to Hypothesis 2. The slip ratio was constant through a gelatine layer with the same stiffness, providing support to Hypothesis 3, with a visible increase of the value at the passage from 5% to 10% layer, consistent with Hypothesis 4. This is due to the fact that the needle had to puncture the new layer (10%) which is stiffer than the previous one (5%). When the needle passed from the 10% layer to the 5% layer, the slip ratio decreased. In this case, the needle does not encounter a high stiffness force and can easily penetrate the new layer. The peaks of the value of the slip ratio in Figure 5.6 are also a representation of what happens during the insertion of the needle into multi-layered tissue. Prior the puncture, the tissue deforms and the insertion force reaches a peak equal to the stiffness of the tissue. When the tissue layer is punctured, the insertion force value drops and the needle can penetrate the tissue [12, 13]. So, the change of slip during the needle insertion is an indication of the needle being in between two layers.

In previous work [24], the needle prototype was made of six-wires 0.25 mm in diameter, using the same material and dimensions as the wires used for the W6-0.25, placed around a seventh-fixed wire and kept together at the tip with a ring. The needle was let self-propel through a gelatine phantom (4%wt) using a step-by-step motion. The experiments showed that, when actuating one wire at the time, the mean slip ratio was 0.21. In this work, we replaced the ring with a shrinking tube, to reduce the diameter at the tip, and we used different gelatine concentrations (5%wt and 10%wt). The mean slip ratio for W6-0.25 in all three gelatine phantoms was 0.2, if we do not consider the increase of the value at the start of the experiment and at the interface between the different gelatine stiffness degrees.

One of the most common consequences of needle insertion into soft tissue is tissue displacement [38, 39]. The wasp-inspired motion mechanism presented in this work can reduce the tissue motion and deformation, as Leibinger et al. demonstrated in their work [27]. The wires are continuously pushing and pulling the material around them, applying a constant strain to the material. Any viscoelastic material, such as the gelatine phantom or the tissue, shows stress relaxation, meaning that the stress decreases over time when a constant strain is applied. In our additional experiments, the plastic foil deformed before needle puncturing. This effect reflects what would happen when a needle has to penetrate an organ. The tissue boundary of the organ will be deformed under the load of the needle before puncturing occurs [36].

The experiments have been done using tissue-mimicking phantoms made with porcine gelatine powder. In literature, various material for phantoms have been presented, among which agarose-, gelatine- or PVA-based phantoms are the most commonly used [40, 41]. The type of material used to create the phantom for the study is not relevant as long as the stiffness

of the phantom is comparable with that of soft tissues. In our study, we chose to use the gelatine-based phantoms, which are easy to fabricate and allowed us to create phantoms of different stiffness degrees in a fast manner.

In general, a phantom provides a controlled environment, allowing for performing repeatable experiments. However, in order to get a better understanding of the functionality of the needle in medical applications, experiments with real tissues are needed. For this reason, we also performed a brief *ex vivo* performance evaluation in porcine liver, kidney, and brain using the W6D0.25 needle prototype. The needle was able to self-propel through the different tissue types, although the slip was higher than in the gelatine phantom. We believe that the high slip values were caused by the presence of various hard structures into the real tissue, such as muscle fibres, and cavities of vessels or connective tissue, which interfered with the needle motion.

During the experiments, we noticed that the wires were sometimes getting entangled. The reason might be related to our connection mechanism: the wires were only connected at the tip with a 10 mm long shrinking tube, and there was no system that kept them in place along the body length. Therefore, the wires could change position during the experiment. In future prototypes, wire entanglement might be avoided by adding several shrinking tubes along the body of the needle, each connected to a different wire.

During percutaneous procedures, needles are visualized using X-ray or ultrasound. Despite the use of radiation, X-ray imaging is preferred over ultrasound, because of the ease of visualization of the needle in the image. To avoid insertion of multiple medical instruments and reduce the operation time, there is a need for needles that include visualization in real time and functionalities such as being able to take a sample or inject a drug. Our prototypes contain multiple wires, each of which can be easily replaced with an optical fibre to allow real-time visualization of the needle inside the body, and tubes to administer drugs or to perform biopsies.

Summarizing, in this study, we showed the advantage of using an ovipositor-inspired motion mechanism to prevent buckling of needles with high length-to-diameter ratio (>200) during deep insertion into tissue-mimicking phantoms. Additionally, we demonstrated that a thicker needle with more wires performs better than a thinner needle with fewer wires. Finally, we showed that the wires can be replaced with functional elements, such as optical fibres and tubes, to create a multifunctional needle without increasing the complexity of the design. The use of such a needle design and motion mechanism could improve the accuracy and safety during delicate medical procedures.

SUPPLEMENTARY MATERIAL

Supplementary information is available at <https://doi.org/10.1038/s41598-019-56403-0>.

REFERENCES

1. Volpe A, Kachura JR, Geddie WR, Evans AJ, Gharajeh A, Saravanan A, et al. Techniques, safety and accuracy of sampling of renal tumors by fine needle aspiration and core biopsy. *J Urol*. 2007; 178(2):379–86.
2. Maharaj B, Leary W, Naran A, Maharaj R, Cooppan R, Pirie D, et al. Sampling variability and its influence on the diagnostic yield of percutaneous needle biopsy of the liver. *The Lancet*. 1986; 327(8480):523–5.
3. Maddali P, Moisi M, Page J, Chamiraju P, Fisahn C, Oskouian R, et al. Anatomical complications of epidural anesthesia: A comprehensive review. *Clin Anat*. 2017.
4. Selander D, Dhunér KG, Lundborg G. Peripheral nerve injury due to injection needles used for regional anesthesia: an experimental study of the acute effects of needle point trauma. *Acta Anaesthesiol Scand*. 1977; 21(3):182–8.
5. Podder T, Clark D, Sherman J, Fuller D, Messing E, Rubens D, et al. In vivo motion and force measurement of surgical needle intervention during prostate brachytherapy. *Med Phys*. 2006; 33(8):2915–22.
6. Wan G, Wei Z, Gardi L, Downey DB, Fenster A. Brachytherapy needle deflection evaluation and correction. *Med Phys*. 2005; 32(4):902–9.
7. Okamura AM, Simone C, O’leary MD. Force modeling for needle insertion into soft tissue. *IEEE Trans Biomed Eng*. 2004; 51(10):1707–16.
8. Ng KW, Goh JQ, Foo SL, Ting PH, Lee TK, Esuvaranathan K, et al. Needle deflection studies for optimal insertion modeling. *International. J Biosci Biochem Bioinform*. 2013; 3(6):570.
9. Kataoka H, Washio T, Chinzei K, Mizuhara K, Simone C, Okamura AM. Measurement of the tip and friction force acting on a needle during penetration. In: Dohi T, Kikinis R (eds) *Medical Image Computing and Computer-Assisted Intervention — MICCAI 2002*. Lecture Notes in Computer Science, vol 2488. Berlin: Springer.
10. Blau PJ. *Friction science and technology: from concepts to applications*: CRC press; 2008.
11. Yang C, Xie Y, Liu S, Sun D. Force Modeling, Identification, and Feedback Control of Robot-Assisted Needle Insertion: A Survey of the Literature. *Sensors*. 2018; 18(2):561.
12. Jiang S, Li P, Yu Y, Liu J, Yang Z. Experimental study of needle–tissue interaction forces: effect of needle geometries, insertion methods and tissue characteristics. *J Biomech*. 2014; 47: 3344–53.
13. Carra A, Avila-Vilchis JC, editors. *Needle insertion modeling through several tissue layers*. 2nd International Asia Conference on Informatics in Control, Automation and Robotics (CAR 2010); 2010 Mar 6-7; Wuhan, China. IEEE; 2010.
14. Gerovichev O, Marayong P, Okamura AM. The effect of visual and haptic feedback on manual and teleoperated needle insertion. *Med Image Comput Comput Assist Interv*. 2002:147–154.
15. Narayan M, Choti MA, Fey AM. Data-driven detection of needle buckling events in robotic needle steering. *J Med Robot*. 2018; 4:1850005.
16. Reed KB, Majewicz A, Kallem V, Alterovitz R, Goldberg K, Cowan NJ, Okamura AM. Robot-Assisted Needle Steering. *IEEE Robot Autom Mag*. 2011; 18(4):35–46.

17. Chen W-F, Atsuta T. Theory of beam-columns, volume 2: space behavior and design: J. Ross Publishing; 2007.
18. Sakes A, Dodou D, Breedveld P. Buckling prevention strategies in nature as inspiration for improving percutaneous instruments: a review. *Bioinspir Biomim*. 2016; 11(2):021001.
19. Le Lannic J, Nénon J-P. Functional morphology of the ovipositor in *Megarhyssa atrata* (Hymenoptera, Ichneumonidae) and its penetration into wood. *Zoomorphology*. 1999; 119(2):73–9.
20. Cerkvenik U, Dodou D, van Leeuwen JL, Gussekloo SW. Functional principles of steerable multi-element probes in insects. *Biological Reviews*. 2018.
21. Vincent J, King M. The mechanism of drilling by wood wasp ovipositors. *Biomimetics (USA)* (1995).
22. Cerkvenik U, van de Straat B, Gussekloo SW, van Leeuwen JL. Mechanisms of ovipositor insertion and steering of a parasitic wasp. *PNAS*. 2017; 114: E7822–E7831.
23. Frasson L, Ko S, Turner A, Parittotokkaporn T, Vincent JF, y Baena FR. STING: a soft-tissue intervention and neurosurgical guide to access deep brain lesions through curved trajectories. *Proc Inst Mech Eng H J Eng Med*. 2010; 224(6):775–88.
24. Scali M, Pusch T, Breedveld P, Dodou D. Ovipositor-inspired steerable needle: design and preliminary experimental evaluation. *Bioinspir Biomim*. 2017; 13(1):016006.
25. Ko SY, Frasson L, y Baena FR. Closed-loop planar motion control of a steerable probe with a “programmable bevel” inspired by nature. *IEEE Trans Robot*. 2011; 27(5):970–83.
26. Virdyawan V, Oldfield M, y Baena FR. Laser Doppler sensing for blood vessel detection with a biologically inspired steerable needle. *Bioinspir Biomim*. 2018; 13(2):026009.
27. Leibinger A, Oldfield MJ, y Baena FR. Minimally disruptive needle insertion: a biologically inspired solution. *Interface focus*. 2016; 6(3):20150107.
28. Gill HS, Prausnitz MR. Does needle size matter? *Journal of diabetes science and technology*. 2007; 1(5):725–9.
29. Kroger AT, Atkinson WL, Marcuse EK, Pickering LK. General recommendations on immunization; recommendations of the advisory committee on immunization practices (ACIP). 2006.
30. Schwartz S, Hassman D, Shelmet J, Sievers R, Weinstein R, Liang J, et al. A multicenter, open-label, randomized, two-period crossover trial comparing glycemic control, satisfaction, and preference achieved with a 31 gauge× 6 mm needle versus a 29 gauge× 12.7 mm needle in obese patients with diabetes mellitus. *Clinical therapeutics*. 2004;26(10):1663–78.
31. Scali M, Kreeft D, Breedveld P & Dodou D. Design and evaluation of a wasp-inspired steerable needle. *Proc. SPIE Bioinspiration, Biomimetics, and Bioreplication 2017*: 1016207–1016213.
32. Scali M, Veldhoven PAH, Henselmans PWJ, Dodou D, Breedveld P. Design of an ultra-thin steerable probe for percutaneous interventions and preliminary evaluation in a gelatine phantom. *PloS one*. 2019.
33. Levental I, Georges PC, Janmey PA. Soft biological materials and their impact on cell function. *Soft Matter*. 2007; 3(3):299–306.
34. Mueller S, Sandrin L. Liver stiffness: a novel parameter for the diagnosis of liver disease. *Hepat Med*. 2010; 2:49.
35. Sprang T, Breedveld P and Dodou D. Wasp-inspired needle insertion with low net push force. In: Lepora N, Mura A, Mangan M, Verschure P, Desmulliez M, Prescott T (eds) *Biomimetic and*

- Biohybrid Systems. *Living Machines* 2016. *Lecture Notes in Computer Science*, vol 9793. 2016; Springer, Cham; p. 307–18.
36. Van Gerwen DJ, Dankelman J, van den Dobbelsteen JJ. Needle-tissue interaction forces - A survey of experimental data. *Med Eng Phys*. 2012; 34(6):665–80.
 37. Simone C, Okamura AM. Modeling of needle insertion forces for robot-assisted percutaneous therapy. *Proceedings 2002 IEEE International Conference on Robotics and Automation (Cat No 02CH37292)*; 2002 May 11-15; Washington, DC, USA, USA. IEEE; 2002.
 38. Dedong G, Yong L, Bin Y. Analysis of Dynamic Tissue Deformation during Needle Insertion into Soft Tissue. *IFAC Proceedings Volumes*. 2013; 46(5):684–91.
 39. Deurloo EE, Gilhuijs KG, Kool LJS, Muller SH. Displacement of breast tissue and needle deviations during stereotactic procedures. *Invest Radiol*. 2001; 36(6):347–53.
 40. Culjat MO, Goldenberg D, Tewari P, Singh RS. A review of tissue substitutes for ultrasound imaging. *Ultrasound Med Biol*. 2010; 36(6):861–73.
 41. De Jong TL, Pluymen LH, van Gerwen DJ, Kleinrensink G-J, Dankelman J, van den Dobbelsteen JJ. PVA matches human liver in needle-tissue interaction. *J Mech Behav Biomed*. 2017; 69:223–8.

Chapter 6

Behavior of an Ovipositor-Inspired Needle in Porcine Tissue: A Preliminary Ex Vivo Study

ABSTRACT

In this paper, we report on a preliminary ex vivo evaluation of an ovipositor-inspired needle prototype. The prototype was tested in porcine kidney, liver, and brain. The prototype consisted of six 0.25-mm diameter Nitinol wires kept together at the tip by a 10-mm long shrinking tube. Each of the six wires was connected to a linear stepper motor which enabled the motion of the wire forward and backward. The needle advanced through the tissue by reciprocally moving the wires using two different modes. The performance of the needle was evaluated in terms of the amount of slip of the needle with respect to the tissue. In 10 out of 18 measurements, the needle was able to advance through the tissue. The slip was considerably higher compared to a previous experimental evaluation we performed in gelatine phantoms. The main reason is likely that gelatine phantoms are homogenous and isotropic, whereas the biological tissue is heterogeneous and anisotropic. In future needle prototypes, a directional-friction pattern could be added on the surface of the wires to increase the gripping force and overcome the cutting force needed to move through biological tissue.

6.1. INTRODUCTION

In previous studies, we investigated the behaviour of an ovipositor-inspired needle prototype in gelatine phantoms of different concentrations: 4%wt (see Chapter 3), 5%wt (see Chapter 4 and Chapter 5), and 10%wt (see Chapter 5). We also evaluated the needle in multi-layer gelatine phantoms in Chapter 5. In this chapter, an ex vivo evaluation of the needle prototype is presented.

6.2. MATERIALS AND METHODS

6.2.1. Needle prototype and actuation unit

The needle prototype consisted of six 0.25-mm diameter Nitinol wires (Flexmet, Belgium) kept together at the tip by a 10-mm long shrinking tube (Vention Medical) with an inner diameter (ID) = 0.813 mm and a wall thickness (W) = 0.013 mm (see Chapter 5 for details about the needle design). Each of the six wires was connected to a linear stepper motor (RobotDigg Equip Makers) which enabled the motion of the wire forward and backward (Figure 6.1). The wires were guided with capillary tubes outside the actuation unit. The motors were controlled with an Arduino board (MEGA 2560).

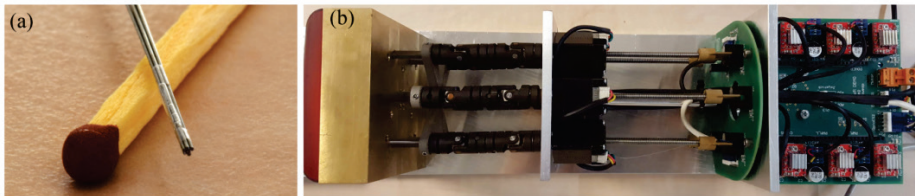


Figure 6.1. Needle and actuation unit. (a) Needle prototype with six 0.25-mm diameter Nitinol wires. (b) Actuation unit with the six linear stepper motors and a printed circuit board (PCB) on top of an Arduino board (MEGA 2560).

6.2.2. Actuation mode

The needle moved forward by reciprocally moving the wire using two different modes. In the first mode, called *step-by-step*, each wire moved forward one-by-one until a pre-defined *stroke*. After that, all wires were pulled backward simultaneously over the same stroke. We call each sequence of forward and backward motion a *cycle*. In the other mode, called *continuous*, one wire was moving forward until a pre-defined stroke, while at the same time the other wires were moving backward. When the stroke value was reached, the advancing wire started to move backward and one of the other wires started to move forward.

In order for the needle to advance through tissue, the static friction force of the stationary or pulling wires should be larger than the sum of the dynamic friction force and the cutting force of the wires moving forward.

6.2.3. Experimental setup

The experimental setup consisted of the needle connected to the actuation unit, an aluminium base, an aluminium cart with a customized box for the tissue sample, and a data acquisition system (Figure 6.2). An ultrasound (US) probe (Philips iE33 machine) was fixed to the cart by means of a frame and a holder, so that the probe was moving together with the cart once the latter was pulled by the needle during the actuation. A laser proximity sensor (MicroEpsilon optoNCDT ILD1420-200, range: 200 mm) was used to record the position of the cart during the measurements. The setup was designed in collaboration with LifeTec Group (Eindhoven, the Netherlands).

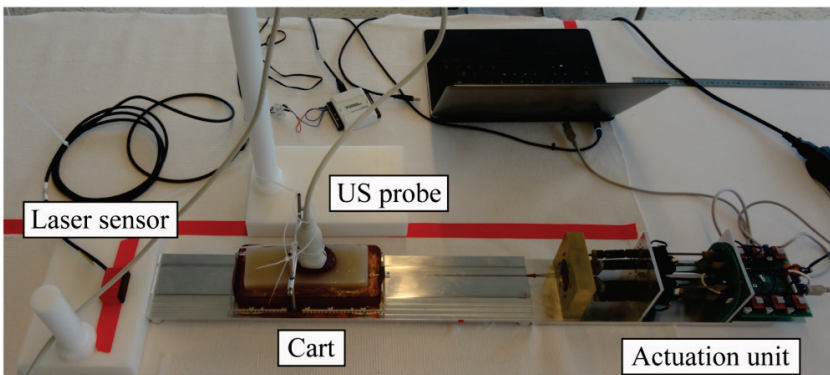


Figure 6.2. Experimental setup for the ex vivo evaluation. Experimental setup with the actuation unit, the aluminium cart on with a box containing the tissue sample, the ultrasound probe (US), and the laser distance sensor.

6.2.4. Biological tissue samples

The biological tissue samples were collected 4 hours before the start of the experiments from a local slaughterhouse and used during the course of the same day. The samples included porcine kidney, liver, and brain. These three tissues were chosen because of their differences in stiffness and internal structure. They represent a stiff (above 20 kPa), middle stiff (between 10 and 20 kPa), and soft tissue (below 10 kPa), respectively. The three stiffnesses were also comparable to the stiffnesses of gelatine phantoms we used in a previous evaluation of our prototype in Chapter 5.

Figure 6.3a shows the gross anatomy of porcine kidney with the renal cortex, renal medulla, and renal pelvis. The renal cortex has a granular structure, whereas the medulla

contains tubules that end up into the space or the renal pelvis [1]. The stiffness of kidney ranges between 15 and 40 kPa [2, 3]. The pieces of kidney used in our measurements were taken from the renal cortex, which has a uniform texture [4], and part of the renal medulla.

Liver is composed of structural and functional units called liver lobules. Liver cells composing each lobule radiate outwards from a central vein [1]. In porcine liver, the lobules are defined by a network of fibrous connective tissue, which is less visible in the human liver (Figure 6.3b) [5]. Porcine liver has a Young's modulus ranging between 15 and 20 kPa [6]. For the experiment, we cut two pieces from the part of the liver with the least number of vessels to limit the risk of having to puncture the stiff vessel wall with the needle.

Brain consists of white and grey matter. The white matter, bundles of axons, connects the grey matter areas (i.e., location of the nerve cell bodies) to each other as shown in Figure 6.3c [1]. Porcine brain is characterized by a stiffness between 1 and 5 kPa [7]. Porcine brain is quite small, therefore the entire organ was used in our measurements.

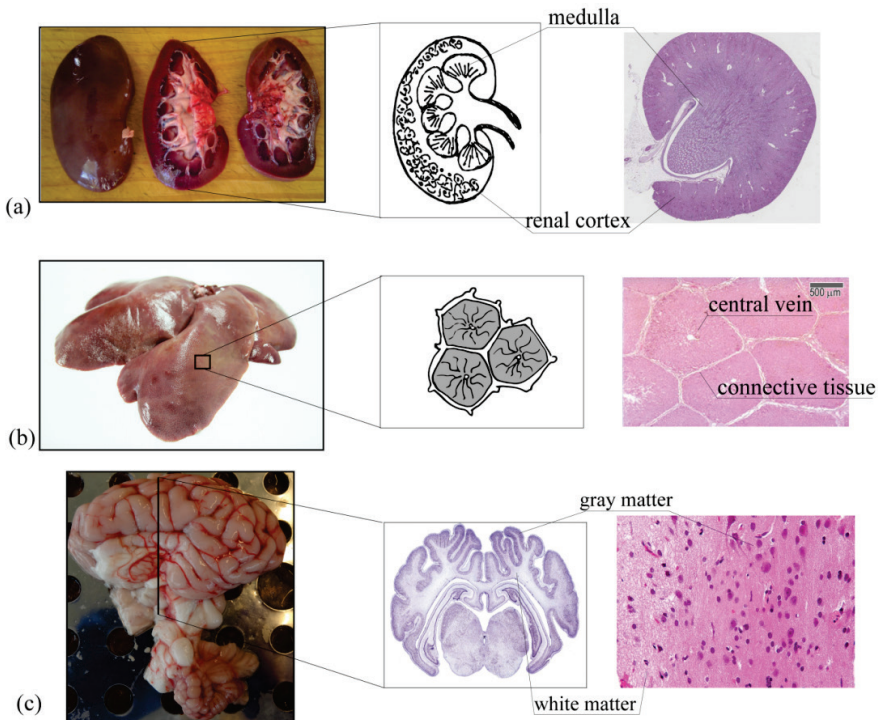


Figure 6.3. Porcine tissue and histology. (a) Porcine kidney photo [8], a schematic image and a histological image (adapted from [9]) showing the renal cortex and the medulla. (b) Porcine liver photo [10], a schematic image and a histologic image (adapted from [11]) of the lobules showing the central veins and the connective tissue between the lobules. (c) Porcine brain photo, histology of brain section (adapted from [12]) and micrograph showing white and grey matter (adapted from [13]).

6.2.5. Procedure

A piece of organ was placed in a box with liquid agar (4%) and stored it in the refrigerator for 30 minutes to solidify so that the tissue is fixed in place. The tissue-agar sample was then placed into the box on the cart (195 x 78 x 26 mm) (Figure 6.4). Tissue samples without agar were also used.

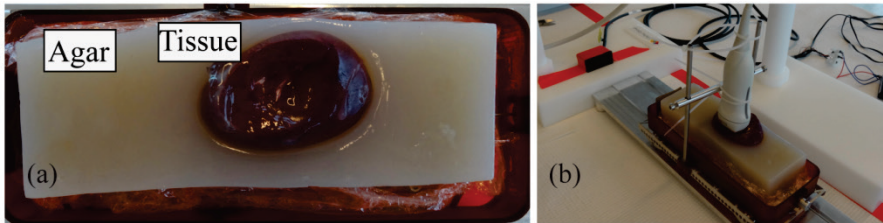


Figure 6.4. Tissue-agar sample. (a) Piece of porcine kidney inside solidified 4% agar. (b) Close-up of the tissue-agar sample on the cart with the US probe connected to a frame.

The needle was inserted manually in the tissue for about 30 mm. Next, the US probe was fixed at a position that ensured the visualization of the needle. Then, the laser sensor that recorded the distance travelled by the cart and the motors that actuated the needle were turned on. The needle was tested inside all three tissue types (i.e., kidney, liver, and brain) using a step-by-step motion at a speed of 2 mm/s with a stroke of 4 mm. Additionally, we tested the needle with continuous motion and speeds of 2 mm/s and 4 mm/s inside the liver. The motion of the needle was monitored by looking at the signal from the laser sensor and terminated when the cart stopped moving forward or kept moving back and forth around the same position, indicating that the needle stopped advancing through the tissue. In total, 18 measurements were performed: 5 in kidney tissue, of which 3 with agar and 2 without agar around the sample, 7 in liver tissue, of which 2 with agar and 5 without agar around the sample, and 6 in brain tissue, of which 1 with agar and 5 without agar around the sample.

6.2.6. Data analysis

The performance of the needle was evaluated in terms of the amount of slip of the needle with respect to the tissue (see Chapter 3). The data from the optical sensor were imported and processed in MATLAB 2016b. The travelled distance measured (d_{meas}) by the sensor was compared to the theoretical distance (d_{theor}) that corresponds to the travelled distance if there were no slip (i.e., the number of cycles multiplied by the stroke). The slip ratio was calculated over an entire measurement as $\text{slip}_{\text{ratio}} = 1 - \frac{d_{\text{meas}}}{d_{\text{theor}}}$. Figure 6.5 shows a typical graph retrieved by the sensor data. The local minima show the position of the cart when all wires are pushed

forward, and the local maxima represent the position of the cart when the wires are pulled backward during the step-by-step motion.

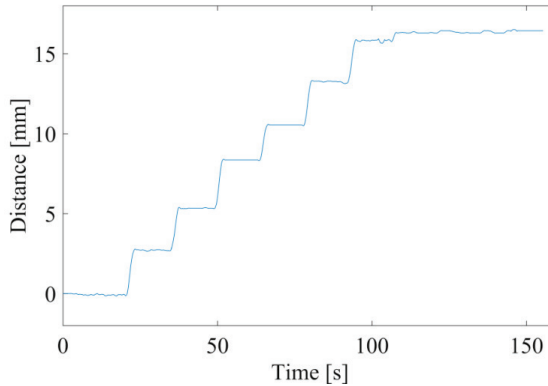


Figure 6.5. Travelled distance measured by the laser sensor.

6.3. RESULTS

Table 6.1 shows the measurements performed during the experiment. Information about the distance travelled by the cart with the corresponding number of cycles needed and the theoretical distance that the cart should have travelled if no slip had occurred are also reported. With the step-by-step motion, the needle was able to pull itself through the kidney in 3 out of 5 measurements, through the liver in 5 out of 7 measurements and through the brain in 2 out of 6 measurements. All 3 measurements performed into the liver using continuous motion were successful. Figure 6.6 shows the needle as visualized with the US probe during one of the measurements in the kidney.

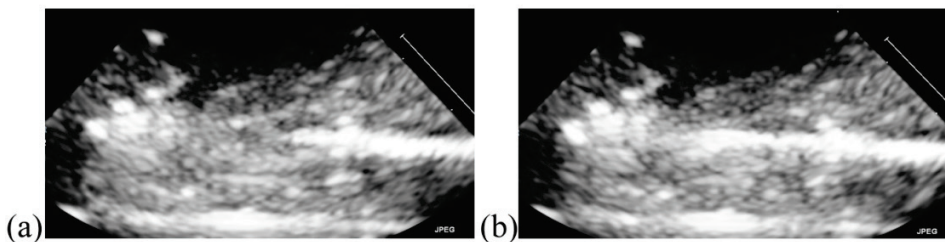


Figure 6.6. Ultrasound images of the needle inside kidney. (a) The initial frame and (b) the final frame of the video taken during the motion of the needle inside the kidney.

Table 6.1. Results of the ex vivo evaluation. For each measurement, the following information is reported: tissue type (kidney, liver, or brain), use of agar to contain the piece of tissue (yes or no), actuation mode (step-by-step or continuous motion), speed (2 or 4 mm/s), travelled distance [mm] of the cart, cycles (number of cycles needed to travel that distance), theoretical travelled distance [mm] (distance that the cart was supposed to travel if no slip occurred) and Slip_{ratio}.

Measurement #	Tissue	Agar	Actuation mode	Speed [mm/s]	Travelled distance [mm]	Cycles	Theoretical travelled distance [mm]	Slip _{ratio}
1	Kidney	Yes	Step-by-step	2	20.68	8	32	0.35
2	Kidney	Yes	Step-by-step	2	11.53	8	32	0.64
8	Liver	No	Step-by-step	2	9.31	20	80	0.88
9	Liver	No	Continuous	2	5.69	11	44	0.87
10	Liver	No	Continuous	4	17.01	35	142	0.88
11	Liver	No	Continuous	4	10.14	29	116	0.90
12	Liver	No	Step-by-step	2	5.76	13	52	0.88
13	Brain	No	Step-by-step	2	16.43	7	28	0.40
17	Brain	No	Step-by-step	2	5.88	9	36	0.83
18	Kidney	No	Step-by-step	2	5.05	21	84	0.93

*Only the measurements where the needle pulled itself through the tissue are reported in this table (see Appendix 6.A for the plots distance travelled by cart vs. time).

6.4. DISCUSSION

This study reported on a preliminary ex vivo evaluation of an ovipositor-inspired needle into porcine kidney, liver, and brain. In 10 out of 18 measurements, the needle was able to advance through the tissue. All 3 measurements performed into the liver using continuous motion were successful.

Table 6.1 shows that slip during the motion cycles was relatively low in measurements n.2 (Kidney, step-by-step) and n.13 (Brain, step-by-step), while it was quite high in measurements n.11 (Liver, continuous) and n.18 (Kidney, step-by-step). Compared to our previous evaluation of the same needle in gelatine phantoms in Chapter 3 and Chapter 5, the needle moved with considerably higher slip into the real tissue. The main reason is likely that gelatine phantoms are homogenous and isotropic, whereas the biological tissue is heterogeneous and anisotropic. The tissue contains fibres oriented in different directions (Figure 6.3). If the needle is penetrating the tissue in a direction perpendicular to the fibres, the needle will encounter more difficulty to cut the tissue than if the direction of insertion is parallel to the fibres.

In 8 out of 18 measurements, the needle was not able to penetrate the tissue. This means that the friction force on the stationary or pulling wires was not enough to overcome the sum of cutting force and dynamic friction force acting on the pushing wires. There are various reasons that could explain this result. The kidney sample contained a small part of renal pelvis (white part of the tissue in Figure 6.7). When the needle reached the depth where the renal pelvis was located, it stopped moving because it was not able to puncture that structure. In the liver sample, there are two elements that might have stopped the forward motion of the needle: (1) the network of connective tissue and (2) vessel walls. The first element might not be an issue in human liver where the connective tissue is less prominent (Figure 6.8). Brain is the softest between the three organs. The needle did not have to cut through fibres to move through the brain tissue. For this reason, the motion through the brain was smoother than the motion through the kidney and the liver. In some experiments, however, there was a gap between parts of the brain, in which cases there was insufficient contact areas for the stationary (or pulling) wires to generate grip and initiate the self-propelling motion.

The needle prototype had a blunt tip, which is an inefficient geometry for cutting [14]. In future prototypes, a conic shape of the needle tip can be considered, to facilitate tissue cutting. Additionally, to increase the gripping force of the stationary (or pulling) wires and overcome the cutting force needed to move through biological tissue, a directional-friction pattern could be added on the surface of the wires, similar to [15]. Finally, different actuation modes where wires are moved at higher speed can be tested, as cutting through the tissue might become easier with increasing the needle insertion speed [16].

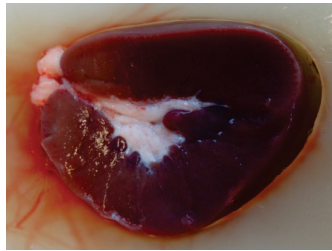


Figure 6.7. Piece of kidney used during the measurements. The red structure is the renal cortex and the medulla. The white structure is the renal pelvis.

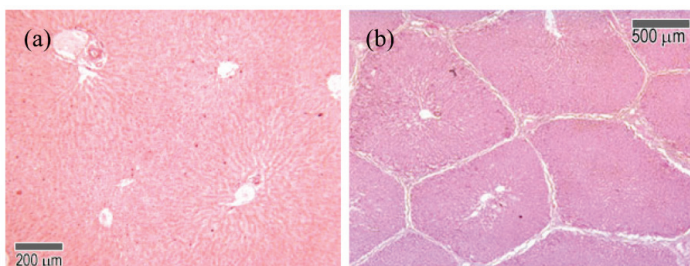


Figure 6.8. Histology of (a) rat liver, similar to human liver, and (b) pig liver (adapted from [11]).

ACKNOWLEDGMENTS

Thanks to Melanie Krüger and Bart Smeets from LifeTec Group (Eindhoven, the Netherlands) for their help in designing the setup and performing the experiment.

REFERENCES

1. Marieb EN and Hoehn K. Human anatomy & physiology: Pearson Education; 2007.
2. Snedeker JG, Niederer P, Schmidlin F, Farshad M, Demetropoulos C, Lee J and Yang KH. Strain-rate dependent material properties of the porcine and human kidney capsule. *J Biomech.* 2005; 38:1011-21.
3. Amador C, Urban MW, Chen S and Greenleaf JF Shearwave dispersion ultrasound vibrometry (SDUV) on swine kidney *IEEE Trans Ultrason Ferroelectr Freq Control.* 2011; 58: 2608-19.
4. Nasser S, Bilston LE and Phan-Thien N Viscoelastic properties of pig kidney in shear, experimental results and modelling. *Rheol acta.* 2002; 41:180-92.
5. Mazza G, Rombouts K, Hall AR, Urbani L, Luong TV, Al-Akkad W, et al. Decellularized human liver as a natural 3D-scaffold for liver bioengineering and transplantation. *Sci Rep.* 2015; 5: 13079.
6. Öpik R, Hunt A, Ristolainen A, Aubin PM and Krusmaa M. Development of high fidelity liver and kidney phantom organs for use with robotic surgical systems. 4th IEEE RAS & EMBS

- International Conference on Biomedical Robotics and Biomechanics (BioRob). 2012. p. 425-430.
7. Guertler CA, Okamoto RJ, Schmidt JL, Badachhape AA, Johnson CL and Bayly PV Mechanical properties of porcine brain tissue in vivo and ex vivo estimated by MR elastography. *J Biomech.* 2018; 69:10-8.
 8. 2012 Flickr (CC BY-NC-SA 2.0)
Available from: <https://www.flickr.com/photos/avlxyz/7552785284/in/photostream/>
 9. Histology laboratory manual 2018.
Available from: <https://www.seahawksfootballproshop.com/what-i-wish-everyone-knew-about-kidney-histology-slides-labeled-kidney-histology-slides-labeled/7266/histology-laboratory-manual-kidney-histology-slides-labeled/>
 10. Available from: <https://pixabay.com/photos/liver-pig-pigs-cook-fresh-food-3306256/>
 11. Histology guide University of Leeds
Available from: <https://www.histology.leeds.ac.uk/digestive/liver.php>
 12. Ulyanova AV, Koch PF, Cottone C, Grovola MR, Adam CD, Browne KD et al. Electrophysiological Signature Reveals Laminar Structure of the Porcine Hippocampus. *eNeuro* 2018; 5.
 13. White Matter. Available from: https://en.wikipedia.org/wiki/White_matter.
 14. Jiang S, Li P, Yu Y, Liu J and Yang Z. Experimental study of needle-tissue interaction forces: effect of needle geometries, insertion methods and tissue characteristics. *J Biomech.* 2014; 47: 3344-53.
 15. Parittotokkaporn T, Frasson L, Schneider A, Davies B, Degenaar P and y Baena FR Insertion experiments of a biologically inspired microtextured and multi-part probe based on reciprocal motion. 2010 Annual International Conference of the IEEE Engineering in Medicine and Biology Society (EMBC). 2010: p. 3190-3193.
 16. Mahvash M and Dupont PE. Fast needle insertion to minimize tissue deformation and damage 2009 IEEE International Conference on Robotics and Automation. 2009: p. 3097-31.

APPENDIX 6.A. MEASUREMENTS PLOTS

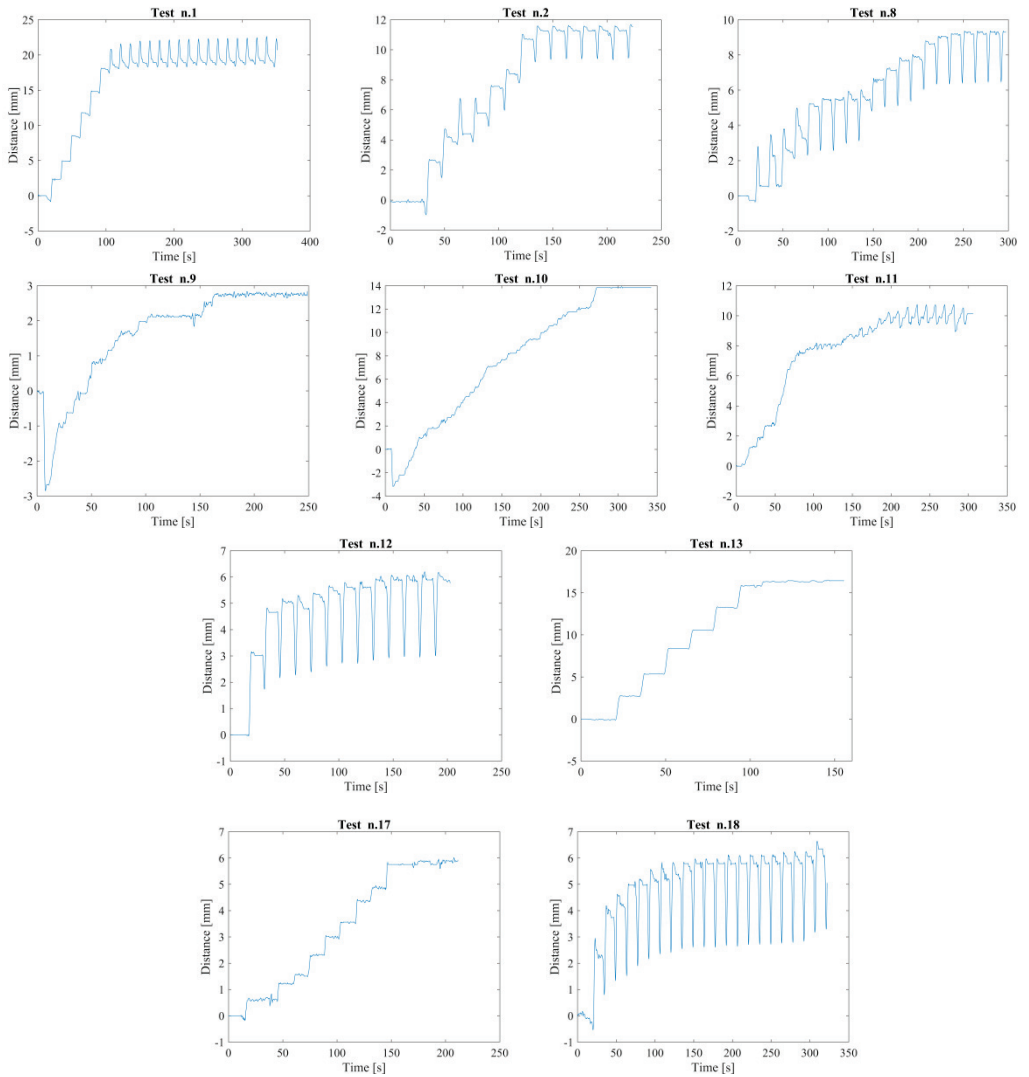


Figure 6.A1. Thumbnail of the plot of distance travelled by the cart [mm] vs. time of the experiment [s] for each of the 10 measurements where the needle pulled itself through the tissue.

Chapter 7

Design of an Ultra-Thin Steerable Probe and Preliminary Evaluation in a Gelatine Phantom

Published as:

Scali M*, Veldhoven PAH*, Henselmans PWJ, Dodou D, Breedveld P. Design of an ultra-thin steerable probe for percutaneous interventions and preliminary evaluation in a gelatine phantom. PloS ONE. 2019; 14(9): e0221165.

<https://doi.org/10.1371/journal.pone.0221165>

*Authors contributed equally to the realization of this paper

ABSTRACT

Needles with diameter under 1 mm are used in various medical applications to limit the risk of complication and patient discomfort during the procedure. Next to a small diameter, needle steerability is an important property for reaching targets located deep inside the body accurately and precisely. In this paper, we present a 0.5-mm prototype probe which is able to steer in three dimensions (3D) without the need of axial rotation. The prototype consists of three Nitinol wires (each with a diameter of 0.125 mm) with a pre-curved tip. The wires are kept together by a stainless steel tube. Each wire is clamped to a block which translates along a leadscrew, the rotation of the latter being controlled by a wheel connected at the distal end of the leadscrew. The tip bends upon retraction of one or two wires. When pushed through a soft solid structure (e.g., a soft tissue or soft tissue phantom), the probe deflects due to off-axis forces acting on its tip by the surrounding structure. We tested the performance of the prototype into a 10%wt gelatine phantom, in terms of the predictability of the steering direction and the controllability of the final position after steering inside the substrate. The results showed that the probe steered in the direction of the retracted wire and that the final position varied from small deflections from the straight path when the wires were slightly retracted, to sharp curvatures for large wire retraction. The probe could be used in various applications, from cases where only a small correction of the path in one direction is needed to cases where the path to be followed includes obstacles and curves in multiple directions.

7.1. INTRODUCTION

Medical needles are used in a variety of percutaneous procedures, including biopsy [1], drug delivery [2], and ablation [3]. Accurate and precise needle placement is required for the success of these procedures. During insertion, the needle can be misplaced due to tissue deformation and respiratory motion [4]. Often, in order to correct their trajectory, needles have to be withdrawn and re-inserted, which increases the procedure time and patient discomfort [5]. Additionally, poor control of the position and trajectory of a needle entails a risk of puncturing sensitive structures, such as blood vessels [6, 7].

7.2 STATE-OF-THE-ART STEERABLE NEEDLES AND PROBES

Over the last years, steerable needles and probes have been investigated in scientific works to enhance manoeuvrability through soft tissue [8–10]. Steerability helps the physician to correct misalignments and to reach the desired target while avoiding sensitive structures without the need of multiple insertions [11, 12].

A number of designs of steerable needles and probes have been proposed (see [9] for a review). A common steering method is by means of a needle tip with a pre-defined shape. Needles of this type typically consist of a cylindrical tube (body) and a tip with a bevel angle (i.e., bevel-tip needles) or a curve (i.e., pre-curved needles). Needles with multiple pre-curved cylindrical tubes combined in a telescopic way [13, 14] and needles with a tip that is both pre-curved and bevelled [15] have also been reported, and it has been shown that the latter achieves sharper steering curvatures than solely pre-curved or bevel-tip needles [16, 17]. Thanks to their simple design, it is possible to manufacture pre-defined shape needles with diameters smaller than 1 mm (see Table 1 in Scali et al. [18]). Konh et al. [19] tested bevel-tip needles with diameters of 0.38 mm, 0.51 mm, and 0.64 mm in gelatine phantoms and reported a maximum deflection of 36 mm achieved with the 0.38-mm needle at an insertion depth of 150 mm. Majewicz et al. [16] showed that a 0.58-mm pre-bent bevel-tip needle could bend inside goat liver with a small radius of curvature (34 mm), whereas a bevel-tip needle with the same diameter achieved a radius of curvature of around 667 mm, that is, a much flatter curve than the pre-bent bevel-tip needle.

A drawback of needles with a pre-defined shape is that the user does not have direct control over the needle curvature. Needles with a bevel tip rely on tissue interaction forces to steer. Steering in 3D is achieved with rotation of the needle body around its own axis to re-orient the bevel-tip towards the desired direction. In order to move straight, the needle has to be continuously rotated while being pushed forward. However, rotating a flexible long needle inside a soft organ generates torsional friction on the needle body, which might result

in discrepancy between the orientation of the needle tip and the needle body [20]. This discrepancy can cause a loss of control over the needle path [21]. Additionally, it has been shown that when a bevel-tip needle is continuously rotated, it opens a spiral track in the soft organ, which increases the risk of tissue damage [22]. Pre-curved needles are usually consisting of a pre-curved stylet that is fed through a straight cannula. When the stylet is inside the cannula it is forced to assume a straight shape, once the stylet is pushed out of the cannula, it regains its pre-set curve. When the pre-curved stylet is inside the tissue, the user cannot directly correct its position; the only way to do this is to retract the stylet inside the cannula, rotate it, and reinsert it into the tissue. This method not only increases the time of the procedure, but could also damage the surrounding tissue due to the creation of multiple paths [20].

There are also needles that can steer by means of cable actuation. This mechanism allows on-demand steering at the tip in one plane [23, 24] or in two perpendicular planes [25, 26] and therefore changing the direction of the needle trajectory “on the spot”. Cable-actuated needles have a central backbone (i.e., the needle body), which is bent by pulling flexible elements connected to it (i.e., cables). The cables are generally placed at the maximum possible distance from the neutral bending line in the needle centre to create a large moment arm so that the needle can bend with a relatively small actuation force [27]. The smaller the diameter of the needle, the smaller the generated moment arms and thus the higher the actuation force needed to generate sharp curvatures, resulting in high internal forces in the needle.

Rutigliano et al. [28] showed that a 21 G (0.82 mm) 17-cm long cable-driven steerable needle (Morrison, AprioMed AB, Uppsala, Sweden) performed better than a 20 G (0.91 mm) 15-cm long straight needle with a bevel-tip (Chiba; Cook Medical, Bloomington, Ind) in terms of both procedure time and needle placement during fine needle aspiration. The steerable needle was composed of a rigid straight cannula and a steerable stylet that was actuated by a friction-based lever lock. The maximum tip deflection was 10 mm. The same needle was tested during a neural plexus blockade procedure to avoid traversing the kidney [12]. The idea was that the needle tip curves when the lever is turned and stays in position when the lever is released. However, the needle distal end did not remain curved after the stylet was removed, which is unwanted during accurate positioning of the needle. Adebar et al. [23] developed a flexural conical tip needle (tip $\varnothing = 1.0$ mm, body $\varnothing = 0.8$ mm) with a one-degree-of-freedom joint ($\varnothing = 2.0$ mm) actuated via a Nitinol pull wire. Ryu et al. [29] designed an active needle ($\varnothing = 1.67$ mm) where a superelastic Nitinol tube with laser machined slits could bend in one direction upon actuation of a shape memory alloy wire. Similarly, Gerboni et al. [24] presented an articulated needle (tip $\varnothing = 1.35$ mm, body $\varnothing = 0.68$ mm) with multiple flexural elements that allow the tip to bend in one direction when a tendon

is pulled. These types of needles can change from a straight to a bent configuration once inside the tissue, but rotation of the needle body is needed to steer in 3D. The 2-mm diameter needle reported in Van de Berg et al. [25] used four actuation cables that run over a ball joint placed near the tip to deflect in two orthogonal planes, creating different steering trajectories once the needle is inserted into a substrate without the need of axial rotation. Summarizing, pre-defined shape needles can achieve small diameters due to their simple design which can be easily miniaturized (e.g., down to 0.4 mm [30]). However, pre-defined shape needles have limited steerability and usually require extra rotation of the needle body to steer in 3D. On the other hand, cable-actuated steerable needles allow for a high level of manoeuvrability, but they tend to have a more complex design than needles with a pre-defined shape. For this reason, the diameter of cable-actuated needles is usually larger than 1 mm.

7.3. AIM

Reaching targets located deep inside the body while limiting tissue damage requires steerable needles that (1) have a small diameter (preferably under 1 mm) and (2) are able to 3D steering without the use of axial rotation. In this work, we aimed to combine the manoeuvrability of the cable-actuated needles with the easy-to-downscale design of the pre-defined shape needles and accordingly design a miniaturized probe with a diameter of 0.5 mm (25 G) suitable for omnidirectional steering in 3D without the use of axial rotation. First, the design process of the steerable probe is described, from the design requirements to the manufacturing of the probe prototype. Next, an experimental evaluation of the prototype in homogeneous tissue-mimicking phantoms is presented. A preliminary version of this work has been briefly reported in a conference abstract [31].

7.4. DESIGN PROCESS

7.4.1. Design requirements

The probe should fulfil the following requirements:

1. The diameter should be under 1 mm. Typical diameters of a pre-defined needle found in literature are between 0.4 mm [30] and 0.9 mm [32] (see Table 1 in Scali et al. [18] for more examples).
2. The probe should be able to steer in 3D, with steering curvatures comparable to values presented in literature [18], where 34 mm is the smallest reported radius of curvature for a pre-curved needle with a diameter of 0.58 mm [16].

3. Current steerable needles with a diameter equal to or smaller than 1 mm are only able to steer in one direction, that is, one-degree of freedom (1-DOF), and axial rotation is thus needed to steer in different directions. The designed probe should be capable of omnidirectional steering in 3D without axial rotation of the probe, to avoid discrepancy between the orientation of the probe tip and the orientation of the probe body [20].

7.4.2. Probe design

To allow for sharp steering curvatures, we used a set of straight elastic elements connected at the tip. If one element is being pulled at, while the rest of the elements are kept in place, the system bends around a bending plane that runs through the central axis of the stationary elements. In this way, the moment arm is enlarged compared to that in a standard cable-actuated needle, because the neutral line is shifted to the outer periphery of the needle.

To enlarge the moment arm even more, we pre-bent the elements outward at the tip. By doing this, the bending plane is shifted further sideways, so that the moment arm increases compared to straight elements, resulting in smaller internal forces and larger bending angles.

Adding an outward pre-bent at the tip, however, can locally increase the diameter of the needle. To keep the diameter equal throughout the length of the needle, we ensured that the bent did not exceed the wall thickness of the shaft cover nor the thickness of the part that connects the elements at the tip.

The required number of pre-curved elements is a trade-off between the desired steering accuracy, the bending radius of the steering curvature, and the total diameter of the probe. In order to steer in 3D without axial rotation, a minimum of three elements is required. To fulfil our requirements of a diameter smaller than 1 mm and a small bending radius, we therefore opted for three elements.

Our final probe tip design consists of three flexible pre-curved elements connected together at the tip and covered with a sheath along their body (Figure 7.1a-b). Pulling one element straightens that element and gives freedom to the non-retracted elements to bend (Figure 7.1c). Additionally, the pulling element acts as a pulling cable, generating a force at the tip that helps the other two elements to bend. The bent elements make the probe steer upon insertion into a substrate. The more an element is pulled, the more the other two elements bend and the sharper the generated curve is.

7.4.3. Probe prototype

Our steerable probe (Figure 7.2) consists of three longitudinally aligned Nitinol wires ($\varnothing = 0.125$ mm). The wires are straight along their length and pre-curved at the tip. The curves at the tip are created by heating the wires up to 480°C with a rework station (Tenma SMD

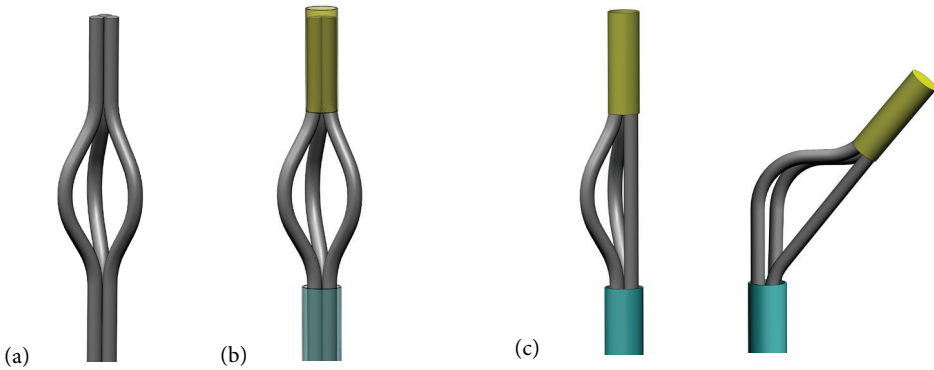


Figure 7.1. Schematic of the design of the probe tip. (a) Three elements with a pre-curve close to the tip. (b) The elements are connected at the tip and kept together along the body with a tubular sheath. (c) The element pulled is straightened and helps the other two pre-curved elements to bend, bringing the tip in a bent position.

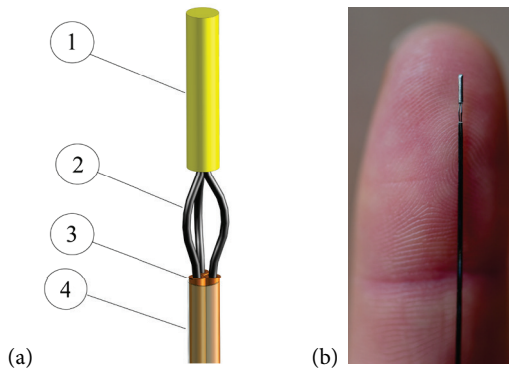


Figure 7.2. Probe tip. (a) 3D drawing of the probe tip showing the stainless steel tube (1), the Nitinol wires with the pre-curve (2), the Nitinol tubes (3), and the polyester shrinking tube (4). (b) A close-up of the probe tip in the straight configuration.

rework station 220V), while being manually curved around a 0.3-mm diameter rod (for details on the choice of the needle tip design see Supplementary Material: S1 Appendix). A 3-mm long stainless steel tube (inner diameter (ID) = 0.3 mm, outer diameter (OD) = 0.5 mm) is glued at the tip, to keep the three wires together at their end points. The curved section of the wires below the tube has a length of 2 mm and a width of 0.5 mm. The other part of each individual wire is fed through an individual superelastic Nitinol tube (Johnson Matthey, ID = 0.15 mm, OD = 0.24 mm) up to the location of the pre-curve. The three Nitinol tubes (1) increase the bending stiffness of the probe shaft to facilitate insertion of the probe into a solid structure (e.g., soft tissue or soft tissue phantom), (2) guide the Nitinol wires without

buckling from the probe base to the probe tip where the actual bending action takes place, similar to a Bowden cable, and (3) keep the wires in place over almost the entire needle length, preventing them from getting entangled. The tubes are fixed to the main body of the system, while the wires can slide freely through them. An ultrathin-walled polyester shrinking tube (Vention Medical, ID = 1.1 mm, wall thickness = 0.0076 mm) is put around the three Nitinol tubes, to keep them together without limiting their flexibility while only minimally increasing the diameter. The total diameter of the probe is 0.5 mm, the overall length of the steerable tip is 5 mm (i.e., the length of the stainless steel tube plus the length of the curves), and the total length of the probe is 180 mm.

The retraction of each wire is controlled by a manual leadscrew mechanism (Figure 7.3). Each wire is clamped to a block which can translate along a leadscrew, the rotation of which is controlled by a steering wheel connected at the distal end of the leadscrew. An M2x20 screw with a pitch of 0.4 mm is used, meaning that one full rotation of the wheel leads to a 0.4 mm translation of the block and the connected wire. There are large and small grooves on the wheels, serving as a visual indication corresponding to a 1/4 rotation (0.1 mm translation of the block) and a 1/24 rotation (0.017 mm translation of the block), respectively. When the block translates, a part of the wire is exposed and become prone to buckling. A rigid tube glued to the block through which the Nitinol wire with its surrounding Nitinol tube is fed prevents buckling.

The main body of the actuation unit has a cylindrical shape with rectangular slots to accommodate the blocks and prevent them from rotating (Figure 7.4). A star-shape plate is positioned between the blocks and the internal wall of the slot to guide the leadscrew. A guidance cap with inner grooves is used to guide the Nitinol tubes from the back to the front of the actuation unit, from where they are kept together by the shrinking tube for the whole length of the probe body. The Nitinol tubes are glued to a flat ring-shaped object positioned at the top of the main body and at the top of a guidance cap to prevent their motion. The actuation unit is covered with a protection cap with rounded edges to avoid damaging the probe at the point of entry into the actuation unit.

The body of the actuation unit is 3D printed in stainless steel (type 316L) using laser metal fusion (Sisma, type Mysint100). The wheels and the cap are 3D printed from polymeric material (acrylate, R05 red). The actuation unit is designed to accommodate up to six Nitinol wires.

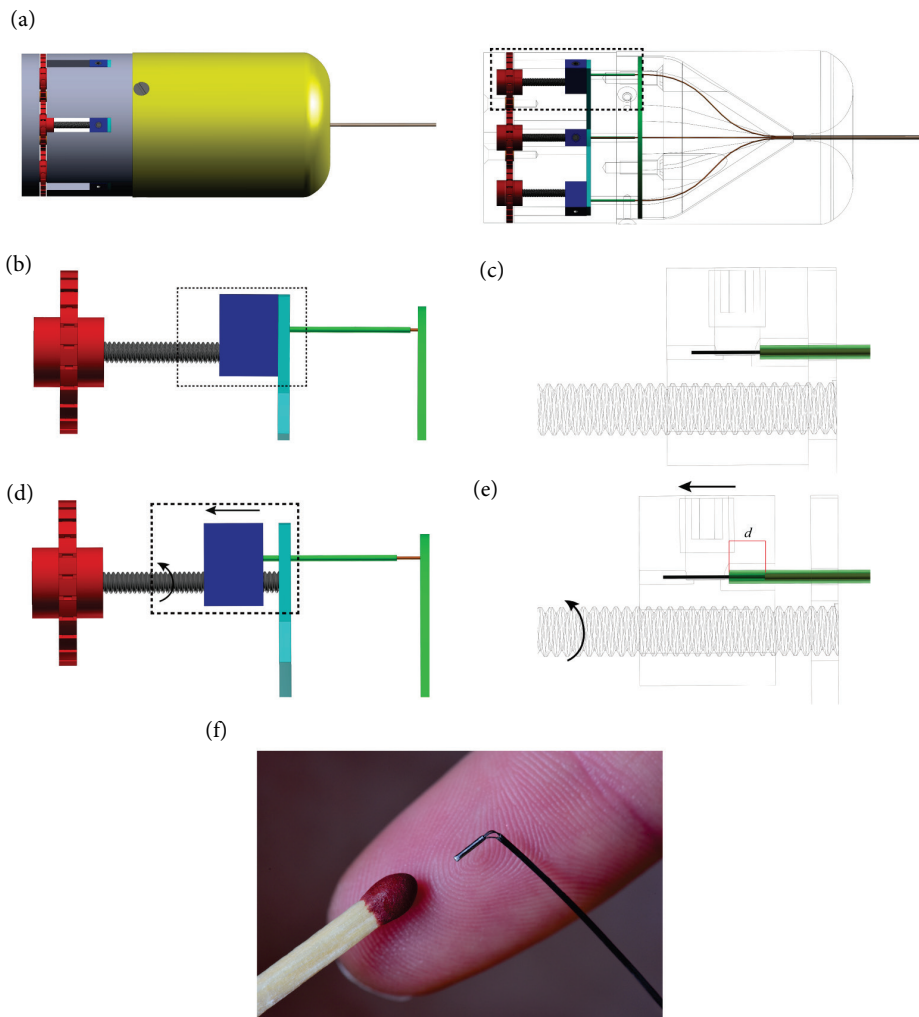


Figure 7.3. Actuation mechanism of the probe prototype. (a) 3D drawing of the actuation unit (left) and the leadscrew mechanisms with the wires surrounded by the tubes visible inside the main body (right). (b) Close-up of one leadscrew mechanism at the initial position. (c) Close-up of the wire clamped inside the block surrounded by the Nitinol tube (orange) and the rigid tube (green), which is glued inside the block. (d) Close-up of one leadscrew mechanism after the wheel has been turned and the block with the wires clamped inside translated. (e) Close-up showing the position of the wire, Nitinol tube, and rigid tube after the block translation. When the block translates, the wire is retracted leaving behind the Nitinol tube that is glued to the ring-shaped object (green). The rigid tube protects the length of the wire d that is not supported by the Nitinol tube. (f) Photograph of the tip bent after retraction of one wire. Dashed rectangular windows highlight the areas of interest. Arrows show the directions of motion of the parts.

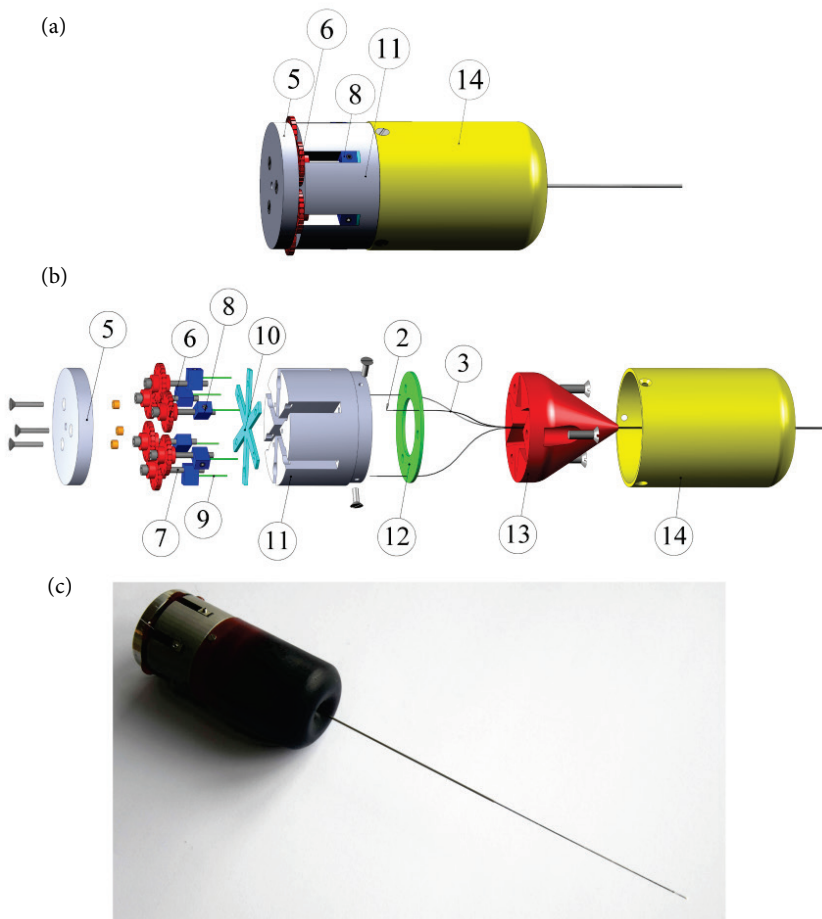


Figure 7.4. Prototype of the ultra-thin probe. (a) 3D drawing of the actuation unit showing the back plate (5), wheels (6), block (8), main body of the unit (11), and protection cap (14). (b) Exploded view of the actuation unit showing the back plate (5), wheel (6), lead screw M2x20 (7), block (8), rigid tube (9), star-shape plate (10), main body (11), Nitinol wire (2), Nitinol tube (3), ring-shaped object (12), conical guidance cap (13) and protection cap (14). (c) Photograph of the probe prototype.

7.5. EXPERIMENTAL EVALUATION

We performed two experiments to evaluate the performance of the probe, assessing the predictability of the steering direction and the controllability of the final position after steering, respectively. The experimental setup was the same for both experiments.

7.5.1. Gelatine phantom

The probe was tested in 10%wt gelatine phantoms. These phantoms were prepared by mixing hot water and gelatine powder (Dr. Oetker Professional, the Netherlands) and casting the mixture into transparent boxes (12 cm x 8 cm x 12 cm). The liquid gelatine was left at 4°C overnight to solidify.

The stiffness of 10%wt gelatine phantom was characterized using a rheometer (AR-G2 Rheometer, TA Instruments Ltd) with a parallel-disc geometry (diameter of 25 mm). First, the response of the gelatine to a strain change (range 0.01–10%) at a constant velocity of 10 rad/s was measured, to find the linear viscoelastic region of the material. After that, the response of the gelatine to a frequency change between 100Hz and 0.1 Hz at 0.5% strain (value within the linear viscoelastic region) was measured.

From these tests, we obtained values for the storage modulus (G') and the loss modulus (G''). The moduli were averaged across frequencies to calculate the dynamic shear modulus $G^* = G' + G''$. The absolute value of G^* was calculated as $G = \sqrt{G'^2 + G''^2}$. The Young's modulus E was estimated by the shear modulus G using the equation $E=2G(1+\nu)$, where ν is the Poisson's ratio ($E = 3G$, for $\nu = 0.5$). Based on these data, we estimated a Young's modulus of 17 kPa for 10%wt gelatine phantom. Usually, the Young's modulus of the soft tissues is characterized by a range of values [33, 34], which might vary depending on the measurement method [35, 36]. The Young's modulus of the gelatine in our study approximates skeletal muscle tissue (12–32 kPa) [37], healthy liver (10–20 kPa) [38], or breast glandular tissue (7.5–66 kPa) [39].

7.5.2. Experimental setup

A linear stage (Aerotech ACT115, model MTC300) was used to insert the probe inside a block of gelatine with a constant speed of 2 mm/s. The probe was mounted on the linear stage by means of an aluminium block. To avoid buckling of the probe outside the gelatine during insertion, two concentric tubes were placed over the probe. The outer tube (OD=2 mm, ID=1.1 mm, length=50 mm) and the inner tube (OD=1 mm, ID=0.6 mm, length=65 mm) were both made of stainless steel. When the probe is pushed inside the gelatine, the tubes slide into one another, restricting the lateral motion of the probe. Two video cameras (Panasonic HC-V250) were used to acquire a front and a side view image during insertion (Figure 7.5).

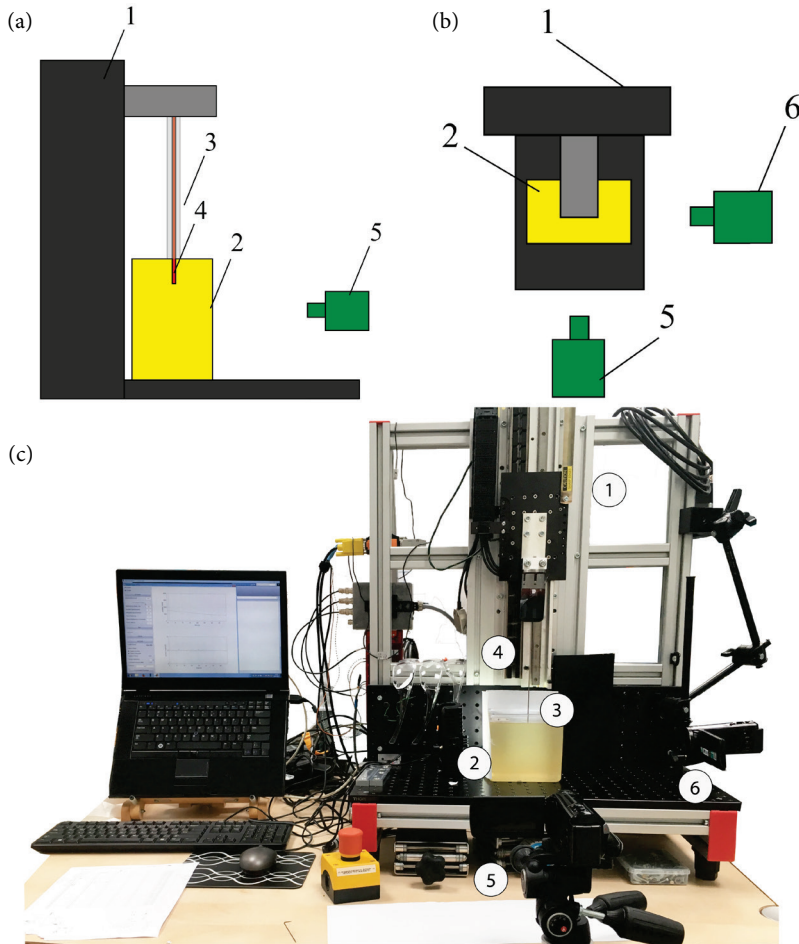


Figure 7.5. Experimental setup. (a) Schematic illustration of the setup in side view, with the linear stage (1), the gelatine box (2), the concentric tubes for the insertion of the probe (3), the probe itself (4), and the front view camera (5). (b) Schematic illustration of the setup in top view, with two cameras, the front view camera (5) and the side view camera (6). (c) Photograph of the experimental setup.

7.5.3. Actuation modes

The tip can be bent by pulling at one or more wires. In order to bend the tip, the operator rotates one or more of the wheels described in the previous section, which leads to the translation of the block in which the wire is clamped, and via that translation to the bending of the tip. The amount of pulling depends on the translation of the block, which is controlled by the number of turns of the wheel. In our experiments we distinguished three levels of pulling (Figure 7.6):

- Level 1 (L1): one turn of the wheel, which corresponds to a 0.4-mm block translation and 10° bending of the tip.
- Level 2 (L2): two turns of the wheel, which corresponds to a 0.8-mm block translation and 20° bending of the tip.
- Level 3 (L3): three turns of the wheel, which corresponds to a 1.2-mm block translation and 50° bending of the tip.

Note that these levels of pulling have been measured in free space. Once the needle is inserted into a substrate, the degree of tip bending might be smaller than these values, due to resistance forces by the tissue [29].

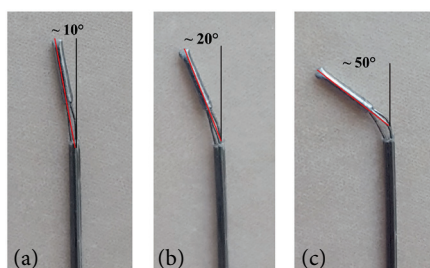


Figure 7.6. Positions of the tip after the three level of retraction. (a) L1, (b) L2, and (c) L3 retraction (see text for the definitions of L1, L2, and L3).

7.5.4. Experiment 1: Steering direction

Experimental design and procedure description

In Experiment 1, the predictability of the steering direction was assessed as a function of which wire was retracted (W1, W2, or W3) and the number of wires that were retracted simultaneously (one or two). In order to measure the steering direction, we used a polar coordinate system, in which each point on a plane is determined by the distance from a reference point and the angle from a reference direction. The wires are positioned 120° from each other, therefore when one or two wires are retracted, the theoretical difference between the two resulting steering directions of the probe is 120°. The difference between the two resulting steering directions when one wire is retracted and when two wires are retracted is therefore 60°.

The level of retraction was set at 0.8 mm (L2) for all conditions, because the steering direction is not expected to depend on the level of retraction. A total of six conditions were tested (Figure 7.7). Each condition was tested five times.

Before each test, the probe was inserted for about 10 mm inside the gelatine phantom using the linear stage and photographed with the front and side cameras. The initial insertion

was done to reduce the effects of cutting and friction forces acting on the tip when punching the substrate. Next, the wheels of the actuation unit were turned to obtain the tip configuration corresponding to the desired condition. Once the tip was set, the linear stage pushed the probe inside the gelatine for 65 mm. At the end of each measurement, a photograph from both sides was taken. After that, the probe was retracted using the linear stage. All measurements were performed over the course of one day.







Condition	W1	W2	W3	
1	L2	0	0	
2	L2	L2	0	
3	0	L2	0	
4	0	L2	L2	
5	0	0	L2	
6	L2	0	L2	

Figure 7.7. Conditions for Experiment 1. W1, W2, and W3 indicate which wire was retracted, and L2 is the chosen level of retraction in the experiment (0.8 mm).

Data analysis

The photographs of the initial and final position of both front and side view were imported to MATLAB (R2016b). After cropping the photographs around the area of interest, we increased the contrast and converted them to binary images. Next, we extracted the skeleton of the binary images, from which we took the coordinates (x, y) of the last point of the probe (i.e., the probe tip) (Figure 7.8). After that, we calculated the difference between the x - and y -coordinates of the last point in the final image and in the initial image, for both front and side view as:

$$\begin{aligned}\Delta x_{\text{front}} &= x_{\text{front}} - x_{\text{INfront}} & \Delta x_{\text{side}} &= x_{\text{side}} - x_{\text{INside}} \\ \Delta y_{\text{front}} &= y_{\text{front}} - y_{\text{INfront}} & \Delta y_{\text{side}} &= y_{\text{side}} - y_{\text{INside}}\end{aligned}$$

Where $(x_{\text{front}}, y_{\text{front}})$ and $(x_{\text{side}}, y_{\text{side}})$ are the coordinates of the last point of the probe in the final image of the front view and side view, respectively, and $(x_{\text{INfront}}, y_{\text{INfront}})$ and $(x_{\text{INside}}, y_{\text{INside}})$ are the coordinates of the last point of the probe in the initial image of the front view and side view, respectively (Figure 7.9). The differences along the y -axis (Δy_{front} and Δy_{side}) represent the projection of the final point reached by the probe along the axis of insertion in front and side view, and the differences along the x -axis (Δx_{front} and Δx_{side}) represent the deflection in front and side view.

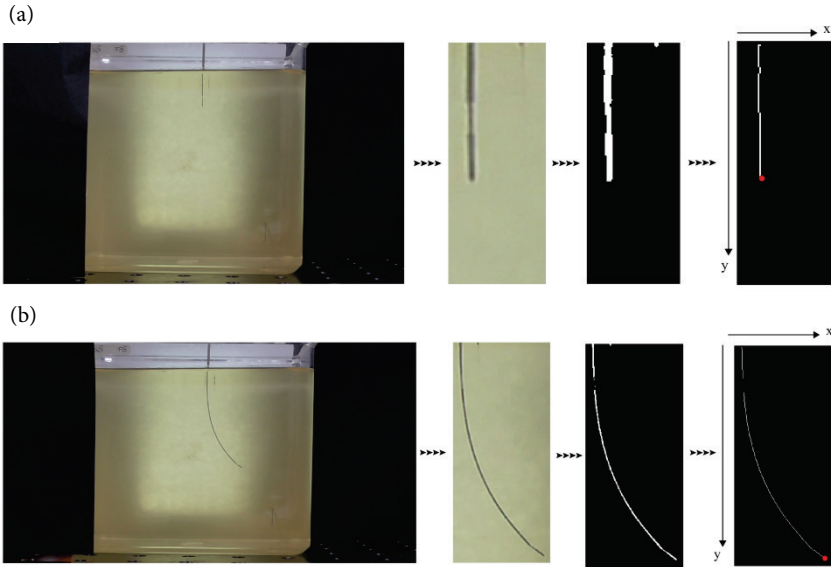


Figure 7.8. Image processing of the photographs. (a) Initial front view photograph. (b) Final front view photograph. In this example, we used the images for Condition 1, Measurement 3. First, the original photograph was read in MATLAB and cropped around the area of interest. After that, the photograph was converted to a binary image, and the skeleton of the image and the coordinates (x, y) of the last point of the probe were retrieved.

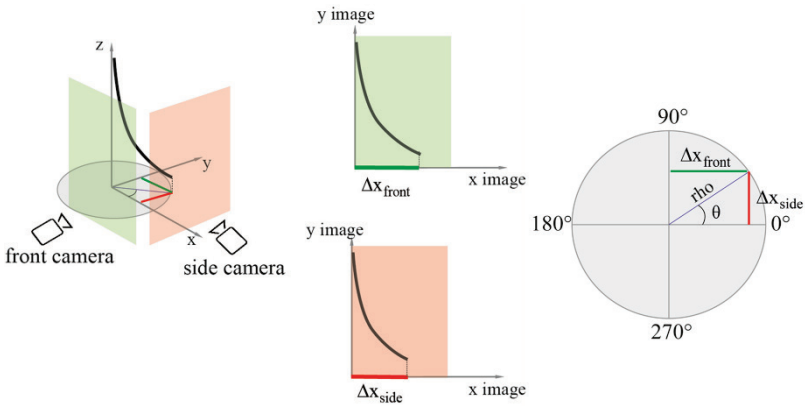


Figure 7.9. Schematic representation of the probe on the 3D plane. In red, the y -coordinate of the final point of the probe (Δx_{side}). In green, the x -coordinate of the final point of the probe (Δx_{front}). The angle θ is equal to $\arctan(\Delta x_{side}[\text{mm}], \Delta x_{front}[\text{mm}])$, and the distance ρ is $\sqrt{(\Delta x_{front}[\text{mm}]^2 + \Delta x_{side}[\text{mm}]^2)}$.

To calculate the actual difference in mm we used a scaling factor (SF). The scaling factor for the front view (SF_{front}) was estimated by using the length dimension of the gelatine box ($l \times w \times h$, 120 x 80 x 120 mm), knowing that the SF is equal to the box length in [mm] divided by the box length in pixels. The scaling factor of the side view (SF_{side}) was estimated knowing that the depth of the box in front and side view should be the same.

$$SF_{\text{side}} = \frac{(\Delta y_{\text{front}} \cdot SF_{\text{front}})}{\Delta y_{\text{side}}} \quad (7.1)$$

From the coordinates of the probe tip we can calculate the angle θ , which indicates the direction of steering of the probe, and the distance rho, which indicates the radius of curvature of the circular path described by the probe (Figure 7.9). The value of rho can be used as a measure of the deviation of the probe from the straight path. We calculated the two parameters, θ and rho, as:

$$\theta = \arctan(\Delta x_{\text{side}}[\text{mm}], \Delta x_{\text{front}}[\text{mm}]) \quad (7.2)$$

$$\text{rho} = \sqrt{(\Delta x_{\text{front}}[\text{mm}]^2 + \Delta x_{\text{side}}[\text{mm}]^2)} \quad (7.3)$$

7.5.5. Experiment 2: Final position after steering

Experimental design and procedure description

In Experiment 2, the final position after steering was assessed as a function of the number of retracted wires (one or two), and the level of retraction ($L1 = 0.4$ mm, $L2 = 0.8$ mm, or $L3 = 1.2$ mm, corresponding to one, two, or three turns of the wheel, respectively). For one-wire retraction, W1 was retracted, and for two-wire retraction, W1 and W2 were retracted. The combinations used for the experiments are shown in Figure 7.10. The experiment was performed following the same procedure of Experiment 1.

Condition	W1	W2	W3	
1	L1	0	0	
2	L2	0	0	
3	L3	0	0	
4	L1	L1	0	
5	L2	L2	0	
6	L3	L3	0	
7	L2	L1	0	
8	L3	L1	0	
9	L3	L2	0	

Figure 7.10. Conditions for Experiment 2. W1, W2, and W3 indicate which wire was retracted, and L1, L2, and L3 indicate the level of retraction (0.4 mm, 0.8 mm, and 1.2 mm). The three circles represent the three wires. Light grey, medium grey, and black indicate retraction by 0.4 (L1), 0.8 (L2), and 1.2 mm (L3), respectively.

Data analysis

The photographs were processed in MATLAB (R2016b) following the same procedure as described for Experiment 1. From the coordinates of the end point of the probe tip, we calculated the difference between the position of the end point in the initial image and in the final image. These values were used to calculate the angle θ and the distance ρ . The angle θ indicates the direction of steering of the probe, and ρ indicates the deflection of the probe from the straight path as described earlier. The final position after steering was assessed as a function of the amount of deflection from the straight path and the projection of the final point reached by the probe along the axis of insertion, called henceforth insertion depth. We used the ratio between deflection and insertion depth to evaluate the steerability of the prototype:

$$\text{ratio} = \frac{\text{deflection}}{\text{insertion_depth}} \tag{7.4}$$

A small curvature was defined by a ratio < 1 , meaning that the probe deflection was smaller than the insertion depth. A sharp curvature was defined by a ratio > 1 , meaning that the probe deflection was larger than the insertion depth.

7.6. RESULTS

7.6.1. Experiment 1

Figure 7.11 shows the angles achieved for all (6x5) measurements. In Table 7.1, the median and interquartile range of the steering direction angles for each condition are presented. Table 7.2 shows the differences between the median values of the steering direction among the conditions. It can be seen that Conditions 1 and 4 had the lowest and the highest variability, respectively. The conditions in which two wires were retracted exhibited a larger variability than the conditions in which only one wire was retracted.

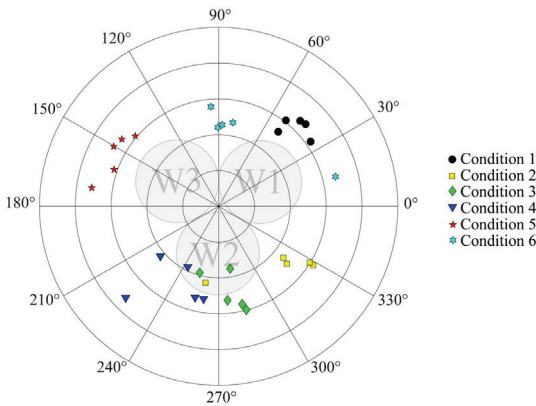


Figure 7.11. Polar plot showing the angle of the steering direction of the probe measurements.

Table 7.1. Median and interquartile range of the steering direction angle for each condition.

Condition	Median	Interquartile range
1	46.2°	10.2°
2	321.6°	23.2°
3	280.5°	13.8°
4	243.0°	33.3°
5	150.3°	19.5°
6	87.6°	27.7°

Table 7.2. Differences between the medians of the steering direction angle among conditions.

Conditions	1	2	3	4	5
2	84.7°				
3	125.7°	41.0°			
4	163.2°	78.6°	37.5°		
5	104.0°	171.3°	130.2°	92.7°	
6	41.4°	126.0°	167.1°	155.4°	62.7°

7.6.2. Experiment 2

In Condition 6, one out of the five measurements was excluded because the probe moved upwards during bending, meaning that the start and the final position could not be properly compared.

The ratio between deflection and insertion depth was below 1 for Conditions 1 and 4, and above 1 for the remainder of the conditions (Table 7.3 and Figure 7.12). For one-wire retraction with L1 (Condition 1), the ratio was under 1 (0.60) and increased with an increasing level of retraction. The same holds for two-wire retraction with the same level of retraction (L1, L2, or L3). The ratio was 0.79 for W1-L1 and W2-L1 (Condition 4), 1.24 for W1-L2 and W2-L2 (Condition 5), and 7.49 for W1-L3 and W2-L2 (Condition 6). Condition 6 had the highest ratio value (7.49), followed by Condition 8 (5.03), and Condition 3 (4.10). Conditions 3 and 8 had the highest variance.

Table 7.3. Median and interquartile range (IQR) of the deflection, insertion depth and ratio deflection to insertion depth for each condition.

Condition	Deflection [mm]	Insertion depth [mm]	Ratio
	Median (IQR)	Median (IQR)	Median (IQR)
1	33.25 (14.71)	51.95 (29.54)	0.60 (2.69)
2	47.36 (5.35)	36.21 (9.87)	1.26 (0.48)
3	49.45 (8.17)	13.52 (21.03)	4.10 (8.27)
4	39.41 (6.54)	48.70 (11.58)	0.79 (0.41)
5	43.70 (4.41)	35.14 (6.23)	1.24 (0.20)
6	56.43 (16.10)*	8.04 (10.89)*	7.49 (3.60)*
7	45.49 (6.41)	35.10 (7.31)	1.30 (0.39)
8	50.27 (29.99)	9.77 (4.96)	5.03 (6.05)
9	53.20 (6.70)	15.66 (8.35)	3.45 (3.08)

*number of measurements n = 4

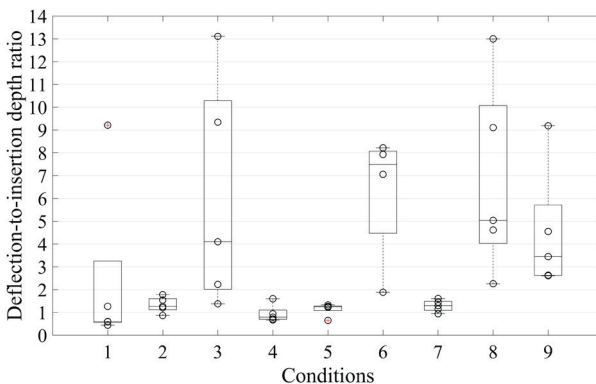


Figure 7.12. Deflection-to-insertion depth ratio for each condition. For Condition 6 only four out of five measurements are displayed.

7.7. DISCUSSION

In this study, we presented a new design of a steerable probe that is able to steer in 3D without the need of axial rotation. With a diameter of 0.5 mm (25 G), this is the smallest reported probe that steers in 3D without the need of axial rotation [18]. Combining the simple design of a pre-curved needle [40] with the steering capability of a cable-actuated steerable needle [25] allowed us to miniaturize the needle without losing the omnidirectionality of the steering. Our probe does not have any additional means of actuation; the Nitinol wires, which the probe consists of, act both as pre-curved elements and as pulling cables.

Once the probe with the bent tip is inserted into the gelatine phantom, the probe follows a curved trajectory due to off-axis reaction forces generated at the tip. The probe is able to steer omnidirectionally following the direction of the retracted wire(s), and the sharpness of the curvature increases with the level of wire retraction.

7.7.1. Probe performance

Our aim was to evaluate the performance of the prototype in terms of predictability and controllability of steering. In order to know the path followed by the probe, direct vision of the probe inside the phantom was needed. Options to do this include (electromagnetic) tracking and direct visualization from outside the phantom. Since the probe was not designed to contain sensors at the tip or in the body, direct visualisation was chosen, for which a transparent substrate (i.e., gelatine) with mechanical properties similar to soft tissue was used. In literature, gelatine, polyvinyl alcohol, and agar are commonly used to mimic tissue [41, 42], because of their versatility in terms of shape and stiffness modification. Doing the tests in such controlled environment allowed us to get data on the performance of the prototype and set the requirements for future improvements of the prototype.

In Experiment 1, we assessed the predictability of the steering direction as a function of which wire was retracted. The probe performed more accurately (i.e., exhibited less variation) for one- than for two-wire retraction. One possible explanation is that, in order to achieve the direction wanted with two-wire retraction, the wires should be retracted by the same amount. The actuation was done manually and there was no locking of the system in position once the wires were pulled. This might have caused mismatch between the input (wheel rotation) and the output (tip bending). If one element is retracted more than the other one, the steering direction is not exactly in the middle of the two retracted wires but rather shifted towards the direction of the wire that is more retracted. Additionally, when one wire is retracted, the bending force generated is in line with the direction of the desired bending motion, whereas when two wires are retracted, the bending forces are not in line with the direction of motion making the system unstable.

In Experiment 2, we assessed the final position after steering as a function of the deflection and the insertion depth. The deflection-to-insertion depth ratio increases with the level of retraction of the wire. This behaviour can be seen in both one-wire retraction and two-wire retraction. The more a wire is retracted, the sharper the bend and the higher the deflection-to-insertion depth ratio. This result is in line with observations in the literature. Specifically, Wedlick et al. [43] analysed the curvature of a series of pre-curved needle with various arc lengths. These authors showed that a needle with a large arc length follows curves with a smaller radius of curvature than a needle with a small arc length. Sitzman et al. [44] compared the deflection of needles with diameters of 0.64 mm (22G), 0.47 mm (25G), 0.36 mm (27G), and 0.28 mm (29 G) and with a 5° versus a 10° bend. At 60 mm depth, the deflection with the 10° bend was greater than the deflection of the needle with 5° bend, and this deflection increased for smaller needle diameters. Increasing the tip angle is not always related to an increase of the needle curvature. Adebar et al. [23] analysed the influence of the tip angle on curvature of a bent-tip needle. They used three needles (diameter = 0.8 mm) with a tip angle of 30°, 45°, and 60° and tip length of 12 mm. The curvature of the needle increased when increasing the tip angle from 30° to 45°, whereas there was no change in the curvature when increasing the tip angle further, from 45° and 60°. Additionally, our results showed that the variability of the ratio between deflection and insertion depth among conditions is relatively high compared to state-of-the-art needle designs. However, in literature, 4-mm pre-bent tip length also showed a large variability in deflection [16]. A way to reduce this variability could be to increase the pre-bent tip length [23].

Condition 6 exhibited the highest deflection-to-insertion depth ratio (7.49), followed by Condition 8 (5.03) and Condition 3 (4.10). These are the conditions in which wire 1 was retracted with the highest level of retraction ($L_3 = 1.2$ mm), which means that the tip was highly bent (~50°), resulting in high curvature once the probe was pushed through the gelatine.

During the experiments the probe was inserted in the gelatine using a constant wire retraction. For this reason, the probe followed only one curve in one direction. By changing the configuration of the wires during the insertion, the probe was able to follow a multi-curved path as shown in Figure 7.13 (Supplementary Material: S1 Video).



Figure 7.13. Probe following a multi-curve path.

7.7.2. Limitations and future work

In order to prevent buckling during the insertion of the probe in the gelatine phantom, two concentric tubes were used to support the shaft of the probe that was outside the gelatine. To avoid friction between the probe and these tubes, we chose 0.6 mm as inner diameter of the smallest tube. This left room for some small lateral displacement of the probe, which might have led to inaccuracy in the needle insertion.

We investigated the performance of the probe in homogeneous 10%wt gelatine phantoms (17 kPa, which might correspond to skeletal muscle tissue [37]). However, biological tissue is rather non-homogeneous, with common stiffness degrees ranging between 1 kPa (corresponding to brain tissue [33, 34]) and 50 kPa (corresponding to tendons [33, 34]). Multi-layered phantoms using different gelatine concentrations might mimic better the human anatomy. Additionally, after further development of the prototype, ex vivo and in vivo experiments are needed to test the performance in a more realistic situation.

In some of the photographs we had difficulties in retrieving the probe because of low contrast or incorrect image focus. We performed a manual analysis of all the photographs, which limits the reproducibility of the study. When the probe was inserted into the gelatine with a high level of retraction (e.g., L3), we could notice that the probe was slicing through the substrate laterally along the path (Figure 7.14). This effect mostly occurred when the probe was following sharp curvatures and needs to be avoided during medical procedures [21].

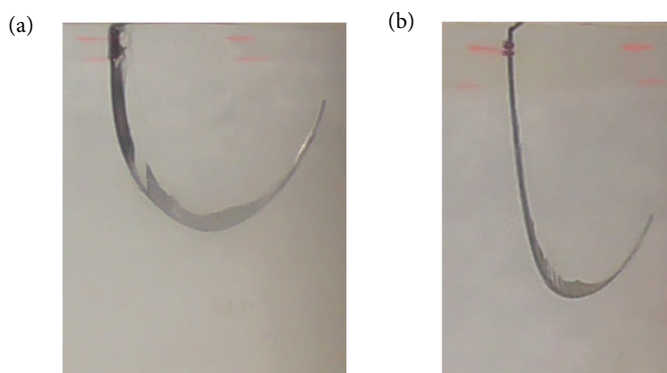


Figure 7.14. Probe cutting the gelatine during insertion (Experiment 2). (a) Condition 6 ($W1=L3$, $W2=L3$, and $W3=0$). (b) Condition 8 ($W1=L3$, $W2=L1$, and $W3=0$).

The angle of the tip was set at the beginning of each test based on the turn of the wheel at the handle. However, during the insertion of the probe inside the gelatine, the tip angle might change because of the resistance forces acting from the gelatine on the tip. In future developments, a real-time measurement of the position of the probe tip could be used to investigate this aspect.

The tip of the probe consists of three wires bent and connected together. This design choice might not be ideal for a clinical setting. The empty space between the wires could entrap tissue during the insertion of the probe and in case of biopsy, healthy tissue could be contaminated. In future versions of the probe prototype, tissue trapping can be avoided by adding a cover around the tip (e.g., plastic sheath).

The tip of the prototype did not show any plastic deformation during all the measurements. It might be possible that because of the continuous retraction and bending, the wires will encounter plastic deformation over time. However, considering that the probe is meant for single use only, this possible effect is deemed not critical. Another risk for plastic deformation might occur when the probe encounters a stiff substrate (the yield load of the used Nitinol wires is 0.721 Kg as reported by the manufacturer). Future versions of the prototype would need to include a locking mechanism that protects the tip once a very stiff tissue is encountered.

In both experiments, a constant speed of 2 mm/s was used. In literature, there is not much information about the needle insertion speed used in clinical practice. Van Gerwen et al. [45] reported recorded speeds between 0.4 mm/s and 10 mm/s for epidural procedures [46] and much higher speeds of about 500 mm/s measured during brachytherapy interventions [47]. It is known that the friction force between the substrate and the needle increases with the insertion speed. Kaboyashi et al. [48] showed that when inserting a 17 G needle into porcine

liver at different speeds, the friction force increased with speeds up to 2 mm/s, reaching a constant value for higher speeds. Mahvash et al. [49] observed that high needle insertion speeds are related to low tissue deformation and damage. However, safely insertion of a needle manually at high speeds might entail a risk of imprecise movement.

In this work, we assessed the performance of the probe by looking at the final position reached at the end of each measurement. In future work a fine-grained analysis of the entire path followed by the prototype could be also conducted, to gain a better understanding of the behaviour of the probe inside the substrate.

In our prototype, steering is achieved by rotating a wheel. In future prototypes, an ergonomic handle can be added, with which the end user intuitively steers the probe, similar to the handle that Van de Berg et al. [25] used in their cable-actuated needle design. Additionally, there should be a rigid telescopic tube system connected to the handle to guide the probe when the probe is outside the substrate and to prevent buckling during the insertion phase.

7.7.3. Possible applications of the steerable probe

7

Needles with diameters between 22 G (0.71 mm) and 27 G (0.41 mm) are used in a number of procedures, such as fine needle aspiration (FNA) [50] and regional or peripheral anaesthesia [51]. In FNA, 25-G or 22-G needles have exhibited higher diagnostic accuracy than the 19-G needles that are typically used in core biopsy [52]. Thin needles are generally less traumatic than thick needles, and complications, due to the accidental puncture of a vessel for example, are also reduced in the former case [50]. In spinal anaesthesia, needles ranging between 22 G (0.72 mm) and 27 G (0.41 mm) are commonly used [51]. It has been shown that the smaller puncture created by smaller spinal needles is associated with a decrease in incidences of postdural puncture headache caused by cerebral spinal fluid leakage [53]. Steinfeldt et al. [54] showed a correlation between larger needle diameter and increased nerve damage during nerve block procedures. In biopsy procedures, the size of the needle influences the size of the sample that can be retrieved. Small diameter (under 1 mm) needle are commonly used for fine needle aspiration cytology, where a very small sample for cytological exams is needed [55].

The probe design demonstrated in this paper can be combined with a guiding outer needle, as it is currently done in the coaxial technique for FNA [56]. In this case, a standard 18–19 G rigid needle can be used to penetrate the first layers of tissues, after which the proposed probe, surrounded by a flexible tube, could be fed through the needle, pushed out of the tube and steered towards the target. In order to continuously track the position of the probe, CT imaging or ultrasound could be used, as with standard needles. Once the needle

reaches the target, the flexible tube could be advanced and the probe could be withdrawn. The empty tube left in place could be used to extract tissue sample and inject drugs.

Next to a small diameter, needle steerability is an important property for improving accuracy and precision in reaching the desired target inside the body. The ability of changing the needle tip direction on-demand once the needle has been inserted into the tissue, without the need of axial rotation, could be beneficial for controllability. Steering can also be used to correct for unwanted needle deflection upon insertion into the tissue, or to adjust the trajectory if the target is moving due to tissue motion (e.g., breathing or heart beating).

Having an ultra-thin probe (diameter below 1 mm) that is able to steer, such as the probe presented in this work, can open new possibilities for the physician during complex procedures. One example is the celiac plexus blockage or neurolysis [57]. This is a procedure where medication is injected to relieve abdominal pain caused, for example, by pancreas cancer. The needle is inserted either from the back or the abdomen of the patient to reach the area behind the vertebra, avoiding to puncture organs and major vessels [58]. In the future, a needle as the one presented in our work could be used in combination with a thin-walled cannula, to access the fat space around the celiac plexus block, while avoiding to puncture organs or major blood vessels.

7.8. CONCLUSION

This paper presents the design and evaluation of a 0.5-mm steering probe. The novel prototype combines the simple design of pre-curved needles with the steering method of cable-actuated needles. We showed that the probe was able to penetrate a gelatine phantom (10%wt) and steer omnidirectionally without the need of axial rotation. The probe was able to steer in the direction of the retracted wire, and the final position reached varied between small deflections from the straight path when the wires were slightly retracted and sharp curvatures when the wires were retracted more. The probe could be used in percutaneous procedures, such as spinal anaesthesia and fine needle aspiration, where a diameter smaller than 1 mm is desired. The ability to steer allows for correcting for small deviations from the path and for avoiding obstacles while navigating towards a target.

SUPPLEMENTARY MATERIAL

S1 Appendix. Probe tip selection.

<https://doi.org/10.1371/journal.pone.0221165.s001>

S1 Video. Video of the probe following a multi-curved path.

<https://doi.org/10.1371/journal.pone.0221165.s002>

REFERENCES

1. Welker JA, Henshaw RM, Jelinek J, Shmookler BM, Malawer MM. The percutaneous needle biopsy is safe and recommended in the diagnosis of musculoskeletal masses. *Cancer*. 2000; 89(12):2677–86.
2. Prausnitz MR, Mitragotri S, Langer R. Current status and future potential of transdermal drug delivery. *Nat Rev Drug Discov*. 2004; 3(2):115.
3. Mauri G, Cova L, Monaco CG, Sconfienza LM, Corbetta S, Benedini S, et al. Benign thyroid nodules treatment using percutaneous laser ablation (PLA) and radiofrequency ablation (RFA). *Int J Hyperthermia*. 2017; 33(3):295–9.
4. Riviere C, Thakral A, Iordachita I, Mitroi G, Stoianovici D. Predicting respiratory motion for active canceling during percutaneous needle insertion. Proceedings of the 23rd Annual International Conference of the IEEE Engineering in Medicine and Biology Society; 2001 Oct 25–28; Istanbul, Turkey. IEEE; 2001 p. 3477–80.
5. Torabi M, Gupta R, Walsh CJ. Compact robotically steerable image-guided instrument for multi-adjacent-point (MAP) targeting. *IEEE Trans Robot*. 2014; 30(4):802–15.
6. Binder DK, Rau G, Starr PA. Hemorrhagic complications of microelectrode-guided deep brain stimulation. *Stereotact Funct Neurosurg*. 2003; 80(1–4):28–31.
7. Gupta S, Nguyen HL, Morello Jr FA, Ahrar K, Wallace MJ, Madoff DC, et al. Various approaches for CT-guided percutaneous biopsy of deep pelvic lesions: anatomic and technical considerations. *Radiographics*. 2004; 24(1):175–89.
8. Van De Berg NJ, Van Gerwen DJ, Dankelman J, Van Den Dobbelsteen JJ. Design choices in needle steering – A Review. *IEEE ASME Trans Mechatron*. 2015; 20(5):2172–83.
9. Scali M, Pusch TP, Breedveld P, Dodou D. Needle-like instruments for steering through solid organs: A review of the scientific and patent literature. *Proc Inst Mech Eng H*. 2017; 231(3):250–265.
10. Abolhassani N, Patel R, Moallem M. Needle insertion into soft tissue: A survey. *Med Eng Phys*. 2007; 29(4):413–31.
11. Glzman D, Shoham M. Flexible needle steering for percutaneous therapies. *Comput Aided Surg*. 2006; 11(4):194–201.
12. Kriegshauser JS, Knuttinen MG, Zhang N, Oklu R. Use of a steerable needle for CT-guided nerve plexus blockade. *Abdom Radiol (NY)*. 2018:1–6.
13. Webster RJ, Okamura AM, Cowan NJ. Toward active cannulas: Miniature snake-like surgical robots. Proceedings of the 2006 IEEE/RSJ International Conference on Intelligent Robots and Systems; 2006 Oct 9–15; Beijing, China. IEEE; 2006 p.2857–63.
14. Sears P, Dupont P. A steerable needle technology using curved concentric tubes. Proceedings of the 2006 IEEE/RSJ International Conference on Intelligent Robots and Systems; 2006 Oct 9–15; Beijing, China. IEEE; 2006 p.2850–56.
15. Kaplan EJ, inventor; Microspherix LLC, assignee. Deflectable implantation device and method of use. United States patent US 7282020. 2007 Oct 16.
16. Majewicz A, Wedlick TR, Reed KB, Okamura AM. Evaluation of robotic needle steering in ex vivo tissue. Proceedings of the 2010 IEEE International Conference on Robotics and Automation; 2010 May 3–7; Anchorage, AK, USA. IEEE; 2010 p. 2068–73.
17. Majewicz A, Marra SP, van Vledder MG, Lin M, Choti MA, Song DY, et al. Behavior of tip-steerable needles in ex vivo and in vivo tissue. *IEEE Trans Biom Eng*. 2012; 59(10):2705–15.

18. Scali M, Kreeft D, Breedveld P, Dodou D. Design and evaluation of a wasp-inspired steerable needle. Proceedings Volume 10162, Bioinspiration, Biomimetics, and Bioreplication; 2017 Apr 17; Portland, Oregon, United States. SPIE; 2017 p. 1016207.
19. Konh B, Honarvar M, Darvish K, Hutapea P. Simulation and experimental studies in needle-tissue interactions. *J Clin Monit Comput*. 2017; 31(4):861–72.
20. Reed KB, Okamura AM, Cowan NJ. Modeling and control of needles with torsional friction. *IEEE Trans Biomed Eng*. 2009; 56(12):2905–16.
21. Reed KB, Majewicz A, Kalleem V, Alterovitz R, Goldberg K, Cowan NJ, et al. Robot-assisted needle steering. *IEEE Robot Autom Mag*. 2011; 18(4):35–46.
22. Meltsner M, Ferrier N, Thomadsen B. Observations on rotating needle insertions using a brachytherapy robot. *Phys Med Biol*. 2007; 52(19):6027.
23. Adebar TK, Greer JD, Laeseke PF, Hwang GL, Okamura AM. Methods for improving the curvature of steerable needles in biological tissue. *IEEE Trans Biomed Eng*. 2016; 63(6):1167–77.
24. Gerboni G, Greer JD, Laeseke PF, Hwang GL, Okamura AM. Highly articulated robotic needle achieves distributed ablation of liver tissue. *IEEE Robot Autom Lett*. 2017; 2(3):1367–74.
25. Van de Berg NJ, Dankelman J, van den Dobbelsteen JJ. Design of an actively controlled steerable needle with tendon actuation and FBG-based shape sensing. *Med Eng Phys*. 2015; 37(6):617–22.
26. Losey DP, York PA, Swaney PJ, Burgner J, Webster Iii RJ, editors. A flexure-based wrist for needle-sized surgical robots. Proc SPIE 8671, Medical Imaging 2013: Image-Guided Procedures, Robotic Interventions, and Modeling; 2013 Mar 14; Lake Buena Vista (Orlando Area), Florida, United States. SPIE; 2013 p. 86711G.
27. Swaney PJ, York PA, Gilbert HB, Burgner-Kahrs J, Webster RJ. Design, fabrication, and testing of a needle-sized wrist for surgical instruments. *J Med Devices*. 2017; 11(1):014501.
28. Rutigliano S, Abraham JA, Kenneally BE, Zoga AC, Nevalainen M, Roedl JB. Analysis of a Steerable needle for fine needle aspiration and biopsy: efficiency and radiation dose compared with a conventional straight needle. *J Comput Tomogr*. 2017; 41(6):957–61.
29. Ryu SC, Quek ZF, Koh J-S, Renaud P, Black RJ, Moslehi B, et al. Design of an optically controlled MR-compatible active needle. *IEEE Trans Robot*. 2015; 31(1):1–11.
30. Misra S, Reed KB, Schafer BW, Ramesh K, Okamura AM. Observations and models for needle-tissue interactions. *IEEE International Conference on Robotics and Automation*; 2009 May 12–17; Kobe, Japan. IEEE; 2009 p. 2687–92.
31. Veldhoven P, Scali M, Henselmans P, Dodou D, Breedveld P. Ultra-thin steerable needle: an experimental prototype. 29th International Conference of the Society for Medical Innovation and Technology (iSMIT); Turin, Italy. 2017, Nov 9–10.
32. Swaney PJ, Burgner J, Gilbert HB, Webster RJ. A flexure-based steerable needle: high curvature with reduced tissue damage. *IEEE Trans Biomed Eng*. 2013; 60(4):906–9.
33. Arda K, Ciledag N, Aktas E, Aribas BK, Köse K. Quantitative assessment of normal soft-tissue elasticity using shear-wave ultrasound elastography. *AJR Am J Roentgenol*. 2011;197(3):532–6.
34. Liu J, Zheng H, Poh P, Machens H-G, Schilling A. Hydrogels for engineering of perfusable vascular networks. *Int J Mol Sci*. 2015; 16(7):15997–6016.
35. McKee CT, Last JA, Russell P, Murphy CJ. Indentation versus tensile measurements of Young's modulus for soft biological tissues. *Tissue Eng Part B Rev*. 2011; 17(3):155–64.
36. Akhtar R, Sherratt MJ, Cruickshank JK, Derby B. Characterizing the elastic properties of tissues. *Mater Today*. 2011; 14(3):96–105.

37. Kot BCW, Zhang ZJ, Lee AWC, Leung VYF, Fu SN. Elastic modulus of muscle and tendon with shear wave ultrasound elastography: variations with different technical settings. *PloS one*. 2012; 7(8):p.e44348.
38. Basdogan C. Dynamic material properties of human and animal livers. In: Payan Y, editor. *Soft Tissue Biomechanical Modeling for Computer Assisted Surgery*. Studies in Mechanobiology, Tissue Engineering and Biomaterials, vol 11. Springer, Berlin, Heidelberg; 2012. Pp. 229–41.
39. Gefen A, Dilmoney B. Mechanics of the normal woman's breast. *Technol Health Care*. 2007; 15(4):259–71.
40. Okazawa S, Ebrahimi R, Chuang J, Salcudean SE, Rohling R. Hand-held steerable needle device. *IEEE-ASME T Mech*. 2005; 10(3):285–96.
41. De Jong TL, Pluymen LH, van Gerwen DJ, Kleinrensink G-J, Dankelman J, van den Dobbelsteen JJ. PVA matches human liver in needle-tissue interaction. *Journal of the mechanical behavior of biomedical materials*. 2017; 69:223–8.
42. Leibinger A, Forte AE, Tan Z, Oldfield MJ, Beyrau F, Dini D, et al. Soft tissue phantoms for realistic needle insertion: a comparative study. *Ann Biomed Eng*. 2016; 44(8):2442–52.
43. Wedlick TR, Okamura AM. Characterization of pre-curved needles for steering in tissue. *Proceedings of 31st Annual International Conference of the IEEE Engineering in Medicine and Biology Society*; 2009 Sept 3–6; Minneapolis, USA. IEEE; 2009 p. 1200–3.
44. Sitzman BT, Uncles DR. The effects of needle type, gauge, and tip bend on spinal needle deflection. *Anesth Analg*. 1996; 82(2):297–301.
45. Van Gerwen DJ, Dankelman J, van den Dobbelsteen JJ. Needle-tissue interaction forces – A survey of experimental data. *Med Eng Phys*. 2012; 34(6):665–680.
46. Healey AE, Evans JC, Murphy MG, Powell S, How TV, Groves D, et al. In vivo force during arterial interventional radiology needle puncture procedures. In: Westwood JD, Haluck RS, Hoffman HM, editors. *Medicine Meets Virtual Reality: The Magical Next Becomes the Medical Now*. Vol. 111: IOS Press; 2005. P. 178–84.
47. Podder T, Clark D, Sherman J, Fuller D, Messing E, Rubens D, et al. In vivo motion and force measurement of surgical needle intervention during prostate brachytherapy. *Med Phys*. 2006; 33(8):2915–22.
48. Kobayashi Y, Sato T, Fujie MG. Modeling of friction force based on relative velocity between liver tissue and needle for needle insertion simulation. *Annual International Conference of the IEEE Engineering in Medicine and Biology Society*; 2009 Sept 3–6; Minneapolis, USA. IEEE; 2009 p. 5274–78.
49. Mahvash M, Dupont PE, editors. Fast needle insertion to minimize tissue deformation and damage. *IEEE International Conference on Robotics and Automation*; 2009 May 12–17; Kobe, Japan. IEEE; 2009 p.3097–102.
50. Wu M, Burstein DE. Fine needle aspiration. *Cancer Invest*. 2004;22(4):620–28.
51. Tsen LC, Hepner DL. Needles used for spinal anesthesia. *Expert Rev Med Devices*. 2006; 3(4):499–508.
52. Sakamoto H, Kitano M, Komaki T, Noda K, Chikugo T, Dote K, et al. Prospective comparative study of the EUS guided 25-gauge FNA needle with the 19-gauge Trucut needle and 22-gauge FNA needle in patients with solid pancreatic masses. *J Gastroenterol Hepatol*. 2009; 24(3):384–90.
53. Halpern S, Preston R. Postdural puncture headache and spinal needle design. *Metaanalyses. Anesthesiology*. 1994; 81(6):1376–83.

54. Steinfeldt T, Nimphius W, Werner T, Vassiliou T, Kill C, Karakas E, et al. Nerve injury by needle nerve perforation in regional anaesthesia: does size matter? *Br J Anaesth.* 2009; 104(2):245–53.
55. Stewart C, Coldewey J, Stewart I. Comparison of fine needle aspiration cytology and needle core biopsy in the diagnosis of radiologically detected abdominal lesions. *J Clin Pathol.* 2002; 55(2):93–7.
56. Gupta S, Ahrar K, Morello Jr FA, Wallace MJ, Madoff DC, Hicks ME. Using a coaxial technique with a curved inner needle for CT-guided fine-needle aspiration biopsy. *Am J Roentgenol.* 2002; 179(1):109–12.
57. Brown DL, Bulley CK, Quiel EL. Neurolytic celiac plexus block for pancreatic cancer pain. *Anesth Analg.* 1987; 66(9):869–73.
58. Kambadakone A, Thabet A, Gervais DA, Mueller PR, Arellano RS. CT-guided celiac plexus neurolysis: a review of anatomy, indications, technique, and tips for successful treatment. *Radiographics.* 2011; 31(6):1599–621.

Chapter 8

Discussion

*“Il piacere più nobile
è la gioia della comprensione”
(The noblest pleasure
is the joy of understanding)*

Leonardo da Vinci

8.1. MAIN FINDINGS OF THIS THESIS

The aim of this thesis was the design, development, and evaluation of a new biologically inspired needle that can steer and self-propel at a submillimeter scale. A series of needles were developed that combined morphological and functional features inspired by the ovipositor of parasitic wasps. The work can be summarized in the following research contributions:

To investigate the state-of-the-art of mechanical working principles of steerable needle-like instruments.

A classification of mechanical working principles used to steer needles through solid organs has been created (Chapter 2). The classification showed that there are needles that steer due to a pre-defined shape (e.g., bevel tip or pre-bent needles) or due to a means of actuation (e.g., cable-actuated needles). The design of bevel tip and pre-bent needles is simple and therefore easy to manufacture at a small scale, but to steer in 3D they need to be rotated around their body axis, which might result in a discrepancy between the rotation given outside the body and the actual rotation of the needle inside the body. Cable-actuated needles have a more complex design, which allows them to rotate in 3D without the need of axial rotation but inhibits their miniaturization.

To investigate how the mechanical working principles of the wasp ovipositor can be translated into the design of needles able to self-propel and steer through solid structures.

The anatomical and mechanical features of the ovipositor of a parasitic wasp were used as inspiration for the development of a 1.2-mm diameter, 160-mm long needle prototype (Chapter 3). We demonstrated that a six-wires needle self-propelled through a tissue-mimicking phantom substrate with stiffness similar to brain tissue (~5 kPa). Additionally, the needle was able to steer by means of a “discrete bevel”, made by moving adjacent wires in order to approximate a bevel-tip. In a second prototype, we demonstrated that pre-directing the wires increased the steerability of the needle (Chapter 4).

To develop self-propelling and steerable needles with a diameter smaller than 1 mm and to evaluate their self-propelling behaviour in single- and multi-layered phantoms.

We developed three prototypes with diameters 0.8 mm, 0.6 mm and 0.4 mm, and a length of 300 mm (Chapter 5). We demonstrated that the needle prototypes were able to self-propel through single- and multi- layer tissue-mimicking phantoms without buckling. Additionally, the 0.8 mm needle was able to puncture a plastic thin layer placed between two pieces of gelatine, which was used to simulate the outer membrane of an organ. As we replaced Nitinol wires with a Nitinol tube and a fiber optic, the needle was still able to self-propel. This is an indication that the needle can be made out of different elements, each of them used for a

specific function, without compromising the motion. Preliminary tests in porcine tissues showed that the needle was able to self-propel through different tissues types (Chapter 6). The needle self-propelled better through the brain than the other tissue types, possibly, because the brain tissue is more homogeneous than the other organs. Finally, we showed that a 0.5 mm diameter hand-held probe was able to steer in 3D without the need of axial rotation. This was possible by combining the simplicity of the pre-curved needle design with the steering capabilities of cable-actuated needles (Chapter 7).

8.2. TOWARDS CLINICAL USE

In percutaneous procedures, thin needles are used to reduce tissue damage and pain. Superficial targets are easily reachable with standard needles, but when the targets are located deep into the body, long needles are needed to reach these areas. However, thin and long needles are subjected to buckling and thus need to be equipped with buckling prevention mechanisms.

The reciprocal mechanism of the wasp ovipositor that was implemented in our needles allowed the needles to self-propel through different types of substrates without buckling. We showed that the needles could move through gelatine phantoms of various stiffness degrees. In order for the mechanism to work, continuous contact between the outer needle surface and the tissue is required. In air or liquid, the needle would not be able to self-propel. For this reason, before starting the experiments, the needles were manually inserted over a few centimetres into the gelatine phantom. Manual insertion is also possible in clinical practice; for example, the physician could use a rigid assistive insertion tool (e.g., a short cannula with a sharp tip) to cut through the skin. Alternatively, we could add a layer of gelatine on top of the skin of the patient and, after manually inserting the needle into the gelatine, let the needle self-propel through the soft tissue of the patient.

Getting deep into the body is not the only challenge that a needle encounters. From the insertion point to the target area, there are sensitive structures such as vessels and organs that should be avoided. Steerable needles can be used to negotiate movement around such structures. Bevel-tip and pre-curved needles have the advantage that they are easy to use in case of superficial targets or when high accuracy is not required. For reaching deep targets inside the body, the needle described in this thesis could be very useful. The ovipositor-inspired needle can change direction without the need of axial rotation of the body, which means that there is no need to withdraw and re-insert the needle several times. Additionally, during needle insertion, clinicians often face unwanted deviations from the trajectory because of needle deflections inside the tissue and motion of the target due to, for example, breathing. This type of error is experienced by the majority of interventional radiologists [1].

The proposed steering mechanism in this thesis could correct for these errors by actively steering back to the pre-planned trajectory.

In percutaneous intervention the physician uses needles to access areas inside the body in order to perform a specific task (e.g., collecting samples or delivering a drug). Our needles are made out of six Nitinol wires; each of these wires could be replaced by a tube for liquid injection or tissue sampling, fibre optics for real time visualization, or any other systems needed for the procedure (Figure 8.1). One of the wires could be used for measuring tissue stiffness in situ, for example by using a micro-indenter placed at the tip [2]. Ultimately, it could be possible to have diagnosis and therapy in one single intervention.

Our bio-inspired needle could have a positive impact during brachytherapy or delicate procedures in the brain. In brachytherapy, multiple needles are used to place radioactive seeds into the prostate. Our needle could allow for the insertion of multiple seeds with a single insertion. In deep brain stimulation, needles can be used as delivery device to place electrodes for the treatment of Parkinson's disease [3]. The electrodes need to be placed accurately inside a very delicate environment. The bio-inspired self-propelling motion will allow needle insertion with zero net push force and the possibility of on the spot correction of the needle path while limiting tissue damage.

The steering angles of our needles are still rather limited as compared to the sharp curves that the wasp can achieve with its ovipositor. Nonetheless, we expect that a small diameter needle that can be inserted with zero net push force and steer in 3D without the need of axial rotation could open the doors to new clinical applications that are nowadays considered challenging or not even possible.



Figure 8.1. Multi-functional needle prototype containing one fiber optic, a Nitinol tube and Nitinol wires.

8.3. OTHER APPLICATIONS

The bio-inspired reciprocal mechanism depends on the relative difference between friction forces acting on the elements that are moved forward versus the stationary/pulled backwards elements and because of this it can theoretically work both at small (μm – mm) and at large scales (m).

In a side project of this research, the ovipositor-mechanism has inspired the development of a self-propelling endoscopic device intended for locomotion through the large intestine (colon) [4]. The actuation mechanism of the device consists of a motor and a rotor consisting of a cylindrical cam. Six elements, called sliders, are placed around the cam and move back and forward following the path defined by the cam (Figure 8.2a-b). The basic working principle of this mechanism is that multiple stationary sliders create sufficient friction to allow for a single slider to move forward. In each step, one slider moves forward, whereas the others remain stationary with respect to the environment. The frame moves forward with 1/6 of the speed of a moving slider to create a smooth and continuous forward motion of the device. To enhance grip, experiments were carried out with 3D-printed structures attached to the outer surface of each slider (Figure 8.2c). The 3D-printed structures were designed with the idea to generate direction-dependent friction in order to increase grip in one direction (backward) and decrease it in the other (forward). We tested the propulsion mechanism of the device in plastic tubes and *ex vivo* in porcine colons. The device was able to propel through the plastic tubes with zero external push force. However, it did not propel through the colon with the chosen 3D-printed structures, because the colonic wall is very flexible and moved elastically with the structures without any sliding. Therefore, improved 3D-printed structures were developed in which the tangential spacing between the structures was decreased so that the colonic wall does not flex between them (Figure 8.2d). The improved prototype was able to self-propel *ex vivo* through the porcine colon, without causing visual damage to the colonic wall.

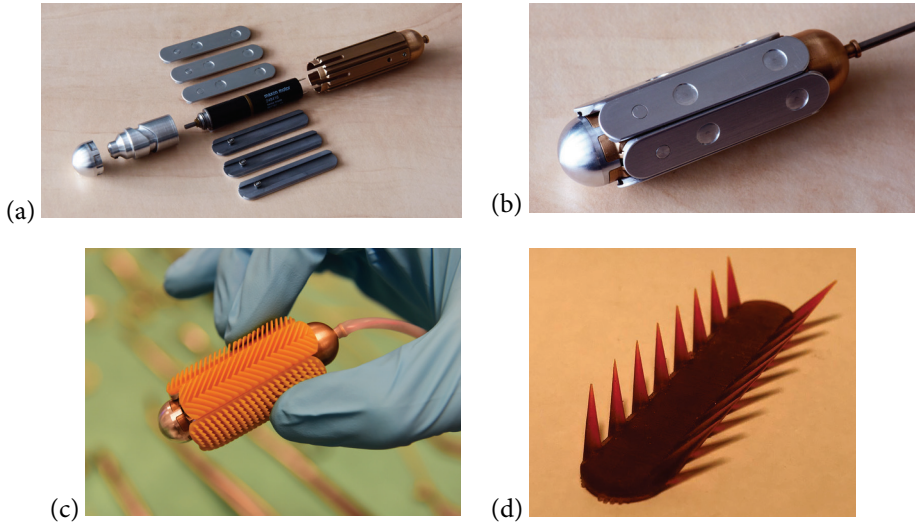


Figure 8.2. Endoscopic self-propelling device prototype. (a) Assembly view showing the different parts. (b) Assembled device. (c) 3D-printed structures attached to the surface of the device. (d) 3D-printed structure with texture only at its sides.

At a much larger scale, the ovipositor mechanism could be used, for example, for earth drilling applications in which tunnels have to be drilled through soil to reach underground gas or oil layers or for planetary drilling [5]. The most common technique for drilling is rotatory drilling, where a rotatory motion of the drill tip creates a hole inside the ground. In order to break the substrate into pieces, sufficient forward force needs to be applied by the drill bit, usually generated by the weight of the drill itself. In environments where the gravity force is lower than on Earth, for example on Mars, generating enough force will require a heavier drill than the one used on Earth. Using a mechanism inspired by the wasp ovipositor might allow for a more compact and energy efficient drill. Recently, prototypes of ovipositor-inspired drills for low gravity environments have been proposed [6].

8.4. TECHNICAL CHALLENGES STILL AHEAD

Image guidance systems can be used to visualize the motion of needles inside tissue. Commonly, ultrasound (US), CT or MRI guidance are used. US guidance is usually preferred over CT guidance because of the real-time visualization and the lack of exposure to radiation. MRI guidance has limited use in percutaneous interventions, due to high costs of the equipment and need of MR compatible needles. In the future, for ex vivo and in vivo experiments, the image guidance needs to be integrated in the design of the experimental setup. The needle could be used in combination with CT or with an US probe held either by

the doctor or a robotic arm. To correct the trajectory of the needle in real-time, a feedback control system could be implemented. The needle position data merged with the images from the visualization system will provide the physician with continuous information about the motion of the needle inside the body. This will allow to correct in real-time for deviations of the needle path.

The actuation unit used in this thesis has been designed with the purpose of performing experiments in which a cart with tissue-mimicking gelatine moves towards the base of the needle. In reality, the needle will have to self-propel inside the body while the tissue remains at its place. The actuation unit could be miniaturized and included in a handle that automatically moves forward following the motion of the needle. The handle can be placed on a tripod held by a robotic arm for a precise and accurate motion of the needle. Instead of linear stepper motors with an additional transmission mechanism, small piezoelectric actuators could be used for actuation of the needle elements.

Creating complex shapes at a submillimetre scale, such as the tongue-and-groove mechanism of the ovipositor in a wasp, is challenging with the currently available manufacturing technology. Recently, needles at a microscale made with polymer material have been presented as substitute of stainless steel needles because of the ease of fabrication, biocompatibility and MRI-compatibility of the former [7]. Such microneedles have been manufactured using micro-molding, micro-milling or micro-stereolithography [8], allowing also the creation of multiple channels. In the near future, we expect that some of the challenges described in this thesis, such as the manufacturability of the internal interlocking mechanism, can be overcome by the continuous development of high-tech manufacturing techniques.

8.5. TOWARDS FUTURE BIO-INSPIRED NEEDLES

The hypothesis that the wasp uses a push-pull mechanism to move the ovipositor through a substrate where one valve is pushed forward while the other valves are pulled backward, as previously described by Vincent et al. [9], has only recently been experimentally validated. Cerkvenik et al. [10] recorded the probing of the parasitic wasp *Diachasmimorpha longicaudata* with high speed cameras. The motion analysis showed that the wasp could probe and steer in different directions and that the push-pull mechanism was used into stiff and not into soft substrates [10].

The ovipositor of the parasitic wasp *D. longicaudata* has a stiffness gradient, due to a change in material properties, which is considered partly responsible for the steering of the ovipositor [11]. The ovipositor of the wasp *D. longicaudata* contains an S-shaped region proximal to the tip. This region has a lower stiffness than the rest of the ovipositor (Figure

8.3). As a result, protraction of the ventral valves causes incurving of the ventral valves towards the dorsal one, which results in a change in probing direction. This might help the wasp to achieve sharp curvatures and a wide range of directions.

In future needle prototypes, using a combination of stiff and deformable sections could improve the steering achieved by asymmetry at the tip. Inspired by the material gradient of the wasp ovipositor, a prototype could be developed with the use of multi-material 3D printing creating a stiff needle body to maintain the shape and avoid buckling, a flexible area behind the tip to allow sharp curves, and a stiff tip to facilitate puncturing of the tissue.

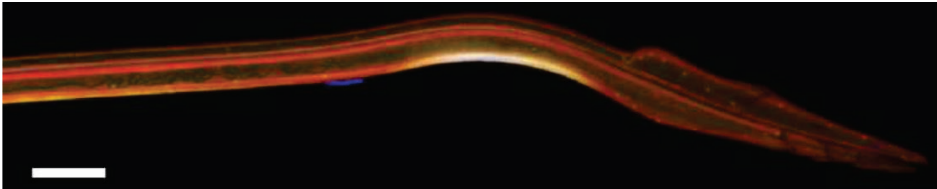


Figure 8.3. Stiffness gradient of the ovipositor of the wasp *D. longicaudata*. The picture shows the autofluorescence of the ovipositor in a confocal laser scanning microscope, the dorsal valves being at the top and the ventral valve at the bottom. The fluorescence signal at the area at the bottom of the curve indicates the presence of a softer material. Scale bar: 10 μm (adapted from [11]).

The parasitic wasp *D. longicaudata* is able to change the steering direction up to 180° [12]. This might be possible because of a local twisting of the valves observed during the ovipositor insertion [12], the origin of this movement being still unknown. The twist motion could be implemented in future needle prototypes, perhaps using bi-stable mechanisms, to achieve a wider range of directions during steering. Recently, the muscles in the abdomen of the wasp have been analysed to understand which of them are involved in the pushing and pulling of the valves during the insertion of the ovipositor [12, 13]. The ventral valve slides independently, whereas the motion of the two dorsal valves is actuated by shared muscles in the abdomen. A thorough understanding on how the wasp uses its muscles to actuate the ovipositor could be another source of inspiration for the improvement of the actuation system of our needles.

In nature, there are many other needle-like structures similar to the ovipositor of a wasp, such as the proboscis of mosquitos and honeybees' stingers [14, 15]. The mosquitos' proboscis is made out of six slender elements used to probe into a host. First, mosquitos pierce the skin and anchor to that with the outer elements that contain a saw-like surface. Then, a vibratory motion is employed to move the other elements inside the skin with limited insertion force [16]. Typical diameters of the proboscis are 20-30 μm with a length of few mm. These slender structures have been used as inspiration for the development of

microneedles [15, 17, 18]. Honeybees are able to insert their stingers with a low insertion force into tissue due to backward-facing harpoon-like barbs on the surface that reduce friction forces during insertion while increasing the force in the opposite direction making it difficult to pull out the needle [19]. In the literature, honeybee-inspired needles are presented as a possible solution to reduce the insertion force during needle insertion [20].

Combining the insertion mechanism of the mosquitos' proboscis and the honeybees' stingers with the propelling mechanism of the ovipositor could lead to new bio-inspired needles that can be inserted into the skin with low insertion force and that can self-propel towards any target inside the body. Nature contains an ubiquity of mechanisms; it is up to us to understand and translate these mechanisms to develop the technology of the future.

REFERENCES

1. De Jong TL, van de Berg NJ, Tas L, Moelker A, Dankelman J, van den Dobbelsteen JJ. Needle placement errors: do we need steerable needles in interventional radiology? *Med Devices (Auckl)*. 2018; 11:259.
2. Beekmans SV, Emanuel KS, Smit TH, Iannuzzi D. Minimally Invasive Micro-Indentation: mapping tissue mechanics at the tip of an 18G needle. *Sci Rep*. 2017; 7(1):11364.
3. Machado A, Rezai AR, Kopell BH, Gross RE, Sharan AD, Benabid AL. Deep brain stimulation for Parkinson's disease: surgical technique and perioperative management. *Mov Disord*. 2006; 21(S14):S247–S58.
4. Posthoorn P. The design of a self-propelling mechanism for an endoluminal robot. Master thesis. Delft University of Technology, 2017.
5. Gouache T, Gao Y, Gourinat Y, Coste P. Wood wasp inspired planetary and Earth drill. *Biomimetics Learning from Nature: InTech*; 2010.
6. Gao Y, Ellery A, Sweeting M, Vincent J. Bioinspired Drill for Planetary Sampling: Literature Survey, Conceptual Design, and Feasibility Study. *Journal of Spacecraft and Rockets*. 2007; 44(3):703–9.
7. Wang M, Hu L, Xu C. Recent advances in the design of polymeric microneedles for transdermal drug delivery and biosensing. *Lab on a Chip*. 2017; 17(8):1373–87.
8. Ali Z, Türeyen E, Karpat Y, Çakmakçı M. Fabrication of polymer micro needles for transdermal drug delivery system using DLP based projection stereo-lithography. *Procedia CIRP*. 2016; 42:87–90.
9. Vincent J, King M. The mechanism of drilling by wood wasp ovipositors. *Biomimetics (USA)*. 1995.
10. Cerkvėnik U, van de Straat B, Gussekloo SW, van Leeuwen JL. Mechanisms of ovipositor insertion and steering of a parasitic wasp. *PNAS*. 2017; 114(37):E7822–E31.
11. Cerkvėnik U, Van Leeuwen JL, Kovalev A, Gorb SN, Matsumura Y, Gussekloo SW. Stiffness gradients facilitate ovipositor bending and spatial probing control in a parasitic wasp. *J Exp Biol*. 2019; 222(9):jeb195628.
12. Cerkvėnik U. Biomechanics of a parasitic wasp ovipositor: Probing for answers. PhD Thesis: Wageningen University; 2019.

13. Eggs B, Birkhold AI, Röhrle O, Betz O. Structure and function of the musculoskeletal ovipositor system of an ichneumonid wasp. *BMC Zoology*. 2018; 3(1):12.
14. Sakes A, Dodou D, Breedveld P. Buckling prevention strategies in nature as inspiration for improving percutaneous instruments: a review. *Bioinspir Biomim*. 2016; 11(2):021001.
15. Gurera D, Bhushan B, Kumar N. Lessons from mosquitoes' painless piercing. *J Mech Behav Biomed*. 2018; 84:178–87.
16. Lenau TA, Hesselberg T, Drakidisa A, Silvaa P, Gomesa S. Mosquito inspired medical needles. In *Bioinspiration, Biomimetics, and Bioreplication*; 2017 Apr 17: p. 1016208.
17. Ramasubramanian MK, Barham OM, Swaminathan V. Mechanics of a mosquito bite with applications to microneedle design. *Bioinspir Biomim*. 2008; 3(4):046001.
18. Suzuki M, Sawa T, Terada Y, Takahashi T, Aoyagi S. Fabrication of microneedles precisely imitating mosquito's proboscis by nanoscale tree dimensional laser lithography and its characterization. 8th International Conference on Solid-State Sensors, Actuators and Microsystems (Transducers); 2015 Jun 21. IEEE; 2015 p. 121–124.
19. Ling J, Song Z, Wang J, Chen K, Li J, Xu S, et al. Effect of honeybee stinger and its microstructured barbs on insertion and pull force. *J Mech Behav Biomed*. 2017; 68:173–9.
20. Sahlabadi M, Hutapea P. Novel design of honeybee-inspired needles for percutaneous procedure. *Bioinspir Biomim*. 2018; 13(3):036013.

Acknowledgments

When I moved to the Netherlands, I received a bell for my future bike, with written:

“Life is like riding a bicycle” (cit. A. Einstein)

This is exactly how I would describe my life in the last five years. Good days, when everything goes as planned and there is progress, like biking with the wind in your back; bad days when a prototype doesn't work, a code keeps giving an error, and it feels like biking against the wind. Sometimes, pushing through doesn't help and the best is to step off the bike and walk. I learnt that it is not relevant how fast we move forward, the important is to keep going and eventually we will reach the destination.

This book is the result of good and bad days, of ideas and prototyping, of reading and writing papers, but is also the result of collaborations with great people, conference trips, coffee and lunch breaks with colleagues, and many other things.

First, I would like to thank Paul Breedveld and Dimitra Dodou. My promotors, my guides and my supporters during these years. Paul, I admire your contagious creativity and the fun you have while brainstorming about novel designs. Thank you for your trust and for challenging me in my research. Dimitra, I appreciate your attention to details and prompt feedback. Thank you for understanding my personality behind the lines and for being there for any little doubt I had. It might have been hard sometimes to manage my “Italian temper”, but you both did a great job in helping me grow as a researcher and as a person.

Thanks to the “WASP team” for the interesting discussions during our periodical meetings, your questions and comments have helped me a lot during the process. This project truly brought two worlds together, biology and technology. Thanks Uros, your outstanding discoveries about the wasp and the use of its ovipositor made also my project more exciting.

My thanks are extended to the colleagues at DEMO. The place where the word “impossible” doesn't exist. Remi, David, and in particular Menno and Danny, thanks for helping to solve problems along the way. Every prototype and set-up that I describe in this thesis has your signature on it.

Thanks to all MSc and BSc students I had the pleasure to meet and work with during these years. As supervisor I learnt something new every day. Special thanks to Tim, Paulien, Davey and Perry, I am very proud of being able to present some of your work in this thesis.

Thanks to my office-mates Paul, Ewout, Aimée, Awaz, Juan and to the BmE crew: Nadia, Ingrid, Peter, Elise, Annetje, Frédérique, Bram, Jeroen, Eline, Bastiaan, Henri, Tricia, Milton, Costanza, Marco, Nazli, Hoda, Tonke, Roos, Nick, David... Every one of you have helped me in this 5-years period. If not directly, you did that with a word, a smile, a coffee, a dinner, a

party. One of the first Dutch words I learnt when I arrived at TU Delft was “gezellig!”. It is a perfect word to describe the period spent with all of you. Dank jullie wel, het was gezellig!

I would like to thank especially my paronyms. Ingrid, we started our PhD adventures at the same time and year-by-year we kept celebrating our achievements together. You are my PhD-buddy, my party-buddy, you are my buddy! Peter, you have been my “shoulder” in the past years. You were there during my last summer of endless tests in our shared lab-corner-in-the-basement. Together we founded the *PhD dreamworks*, and it was so much fun to share those unforgettable moments with you. Ingrid and Peter, we grew from being colleagues to being good friends, I am happy to have you at my side during the last step of this journey.

Gabri, during these years you were there to “offer” me a coffee and listen to my monologues. You knew how to cheer me up with a risotto or a whole Easter lunch. Thanks for reminding me that I don’t need to be home to feel at home.

Going through ups and downs was not possible without playing some beach volleyball with amazing people that share this passion with me. Thank you girls, for letting me feel part of a family! Playing this sport with you was a stress-relief during intense periods and it helped me become more confident about myself. I learnt that hard work, perseverance and resilience will lead to a positive performance. This book is an example on how I applied these lessons in my research.

Thanks to my friends in Trequanda, Pisa and in the rest of my home country, and to the people I have met in Munich and Trondheim, my homes for short periods of time. In some way each of you guided me here. Visiting each other during these years gave me that extra energy I needed to complete my PhD research.

Thanks to my family. You might not be able to understand my work, but you understand me. Grazie per essermi stati vicini anche se lontani!

Along the journey, I received the most precious and unexpected gift. I met my best friend, my partner, the person who can always make me laugh. Lieve Teun, thanks for being there even when my flow of emotions takes over. No matter which language I speak you are always able to get me, even when you think you don’t. You showed me that biking against the wind can be easy and fun if we ride a tandem. There are no words to describe how grateful I am for your help during this challenging period. Grazie di tutto!

Marta Scali
Delft, 2020

Curriculum Vitae



Marta Scali

16 – 01 – 1988

Born in Sinalunga, Italy

WORK EXPERIENCE

2019 – present

R&D Engineer, D.O.R.C. International

2015 – 2019

PhD researcher, Department of Biomechanical Engineering,
Delft University of Technology, Delft, the Netherlands

2014

Early stage researcher, Technical University of Munich,
Munich, Germany

2013

Early stage researcher, SINTEF Medical Technology,
Trondheim, Norway

2012

Internship SINTEF Medical Technology, Trondheim, Norway

EDUCATION

2009 – 2012

Master *cum laude* in Biomedical Engineering,
University of Pisa, Pisa, Italy

2006 – 2009

Bachelor in Biomedical Engineering,
University of Pisa, Pisa, Italy

2001 – 2006

High School, Liceo Scientifico A. da Sangallo,
Montepulciano, Italy

AWARDS

2017

Best Student Paper Award, SPIE Smart Structures and Materials +
Nondestructive Evaluation and Health Monitoring conference on
Bioinspiration, Biomimetics and Bioreplication, Portland, United
States.

2018

Best oral presentation, International Conference of Society for
Medical innovation and Technology (SMIT), Seoul, South Korea.

PUBLICATIONS

Publications part of this thesis:

- **Scali M**, Breedveld P and Dodou D. Experimental evaluation of a self-propelling bio-inspired needle in single- and multi-layered phantoms. *Scientific Reports*. 2019; 9: p. 19988. <https://doi.org/10.1038/s41598-019-56403-0>
- **Scali M**, Veldhoven PAH, Henselmans PWJ, Dodou D, Breedveld P. Design of an ultra-thin steerable probe for percutaneous interventions and preliminary evaluation in a gelatine phantom. *PLoS ONE*. 2019. 14(9): e0221165. <https://doi.org/10.1371/journal.pone.0221165>.
- **Scali M**, Kreeft D, Breedveld P, Dodou D. Design and evaluation of a wasp inspired steerable needle. *Proc. SPIE 10162, Bioinspiration, Biomimetics, and Bioreplication*. 2017: 1016207. <https://doi.org/10.1117/12.2259978>.
- **Scali M**, Pusch TP, Breedveld P, Dodou D. Ovipositor-inspired steerable needle: design and preliminary experimental evaluation, *Bioinspiration & Biomimetics*. 2017; 13(1): 016006. <https://doi.org/10.1088/1748-3190/aa92b9>.
- **Scali M**, Pusch TP, Breedveld P, Dodou D. Needle-like instruments for steering through solid organs: a review of the scientific and patent literature. *Proc. of the Institution of Mechanical Engineers Part H: Journal of Engineering in Medicine*. 2017; 231(3): 250-265. <https://doi.org/10.1177/0954411916672149>.

Other publications:

- Sakes A, van de Steeg I, Kater E, **Scali M**, Breedveld P. Development of a Novel Wasp-Inspired Friction-Based Tissue Transportation System, submitted to *Nature Biomedical Engineering*.
- Sendrowicz A, **Scali M**, Culmone C, Breedveld P. Surgical drilling of curved holes in bone – a patent review. *Expert Review of Medical Devices*. 2019; 16(4): 287-298. <https://doi.org/10.1080/17434440.2019.1596794>
- Culmone C, Ali A, **Scali M**, Menciassi A, Breedveld P. ChoRe: a device for trans-catheter chordae tendineae repair. *Proc. of the Institution of Mechanical Engineers Part H: Journal of Engineering in Medicine*. 2019: 11 p. <https://doi.org/10.1177/0954411919848856>
- Reynisson PJ, **Scali M**, Smistad E, Hofstad EF, Leira HO, et al. Airway segmentation and centerline extraction from thoracic CT–comparison of a new method to state of the art commercialized methods. *PLoS ONE*. 2015; 10(12). <https://doi.org/10.1371/journal.pone.0144282>
- Reynisson PJ, Leira HO, Hernes TN, Hofstad EF, **Scali M**, et al. Navigated bronchoscopy: a technical review. *Journal of bronchology & interventional pulmonology*. 2014; 21(3): 242-264. <https://doi.org/10.1097/LBR.000000000000064>

Conferences contributions:

- Culmone C, Bazuin L, Scali M, Breedveld P. Towards Non-Assembly 3D Printed Medical Instruments. 41st Conference of the IEEE Engineering in Medicine and Biology Society. 2019. Jul. 23-27, Berlin, Germany. (poster)
- Scali M, Dodou D, Breedveld P. Bio-inspired self-propelling needle. 30th International Conference of Society for Medical innovation and Technology (SMIT). 2018, Nov. 8-9, Seoul, South Korea. (abstract)
- Scali M, Kreeft D, Breedveld P, Dodou D. Design and evaluation of a wasp inspired steerable needle. SPIE Smart Structures and Materials + Nondestructive Evaluation and Health Monitoring, 2017, Portland, Oregon, United States. (oral presentation)
- Scali M, Pusch T, Breedveld P, Dodou D. Ovipositor-inspired needle for solid organ interventions. Proc. 6th Dutch Conference of Biomedical Engineering. 2017. Jan. 26-27, Egmond aan Zee, the Netherlands, 1 p. (abstract)
- Veldhoven PAH, Scali M, Henselmans PWJ, Dodou D, Breedveld P. Ultra-thin steerable needle: an experimental prototype. Proc. 29th International Conference of Society for Medical innovation and Technology (SMIT). 2017, Nov. 09-10, Turin, Italy, 1 p. (abstract)
- Scali M, Pusch PT, Dodou D, Breedveld P. Design and preliminary evaluation of a bio-inspired steerable needle. Proc. 28th International Conference of Society for Medical innovation and Technology (SMIT). 2016, Oct. 05-08, Delft, the Netherlands, 1 p. (abstract)

Press:

- NWO Resultaat – Natuur inspireert techniek:
<https://www.nwo.nl/algemeen/actueel/social-media/resultaat-online/medische-instrumenten>
- TU Delft Fame Lab Competition, popular science presentation:
<https://www.tudelft.nl/famelab/contestants/marta-scali/>
- NOW Actueel – <https://www.nwo.nl/onderzoek-en-resultaten/cases/hoe-biologen-en-ingenieurs-leren-van-dieren>
- ASME – Alliance of Advanced BioMedical Engineering –
<https://aabme.asme.org/posts/ovipositor-inspires-new-needle-for-surgery>
- EOS wetenschap – <https://www.eoswetenschap.eu/technologie/sluipwesp-inspiratie-voor-flinterdunne-chirurgische-naald>
- Wageningen University & Research <https://weblog.wur.eu/spotlight/parasitic-wasp-inspires-advancements-in-surgery/>
- TU Delft – <https://www.tudelft.nl/en/2018/3me/november/surgical-tool-inspired-by-parasitoid-wasp/>
- De Ingenieur – <https://www.deingenieur.nl/artikel/new-needle-reaches-deep-into-the-body>

